

# **An Efficient Full-Potential Linearized Augmented-Plane-Wave Electronic Structure Method for Charge and Spin Transport through realistic Nanoferronic Junctions**

Von der Fakultät für Mathematik, Informatik und Naturwissenschaften  
der Rheinisch-Westfälischen Technischen Hochschule Aachen  
zur Erlangung des akademischen Grades eines Doktors der Naturwissenschaften  
genehmigte Dissertation

vorgelegt von  
Diplom-Physiker  
Frank Freimuth  
aus Ellern

Berichter: Universitätsprofessor Dr. S. Blügel  
Universitätsprofessor Dr. P. H. Dederichs

Tag der mündlichen Prüfung: 02.02.2011

Diese Dissertation ist auf den Internetseiten der Hochschulbibliothek online verfügbar.



# Abstract

The full-potential linearized augmented-plane-wave (FLAPW) electronic structure method, a precise relativistic all-electron method enabling the description of the electronic structure and ground-state properties of multi-component complex bulk solids and low-dimensional systems from the first principles of quantum mechanics, has been extended along two research lines:

(A) An efficient order- $N$  implementation of the FLAPW method was developed to perform *ab initio* calculations of electronic transport properties in magnetic tunnel junctions (MTJs) and all-metallic spin-valves within the spin-density and vector spin-density formulations of the local density approximation (LDA) and the generalized gradient approximation (GGA) to the density functional theory (DFT), whose computational effort scales not proportionally to the conventional cubic power ( $N^3$ ), but linearly with the number of layers  $N$  of the system. The method is based on the Green-function embedding technique, which allows to treat open systems and to solve the scattering problem of electronic transport. In order to achieve the order- $N$  scaling behavior, the system is partitioned into layers, which are calculated separately. Due to its order- $N$  scaling, the implementation allows to profit from the high precision of the FLAPW method at a low computational cost. Computational efficiency is an important aspect in calculations of electronic transport as the scattering region often exceeds 2-5 nm in thickness and may contain several hundreds of atoms per unit cell. The applicability of the order- $N$  FLAPW electronic structure method is much more general and allows the efficient investigation of quantities based on the self-consistent solution of the electron charge and vector magnetization densities such as the electronic structure, the total energy and other ground state properties. The method is ideally suited to heterostructures and has been extended to treat surfaces and thin films. A particular asset is the possibility to investigate quantities slowly varying in space such as a charge or spin-density wave. The implementation was validated for the electronic, magnetic and structural properties of films and surfaces as well as their electronic transport properties.

The method was applied to the investigation of the spin-transfer torque (STT), an alternative to the conventionally used Oersted field to switch the magnetization in spin-valves and tunnel junctions, whose strength scales favorably with the increasing integration density of the actual devices. Within the order- $N$  Green function embedding method, two formulations of the spin torque were implemented: The spin torque is calculated (i) from the variation of the spin current and (ii) directly as the torque, which the exchange field

exerts on the non-equilibrium spin density. The second formulation allows the calculation of the spin-torque in the presence of spin-orbit coupling. Calculations of the spin-torque were performed for Co/Cu/Co and Fe/Ag/Fe spin-valves and for the Fe/MgO/Fe MTJ. For the all-metallic spin-valves the asymmetries of the torque per current were determined and found to be in good agreement with the theory of Slonczewski and in the case of the Fe/Ag/Fe spin-valve also in good agreement with experiments. In contrast to Slonczewski's model, the out-of-plane torque is available from the *ab initio* calculations of the spin-torque. It is found to be negligible for thick free layers. In the case of the Fe/MgO/Fe MTJ good quantitative agreement with experiments is found.

(B) For the description of many properties in condensed matter physics, the Wannier function is superior over the Bloch function, which is the underlying concept of most electronic structure methods describing periodic solids, including the FLAPW method. The Wannier function approach to electronic structure provides a real-space description of solid-state properties and enables for example a very intuitive picture on bonding properties. In the context of electronic transport, Wannier functions have advantages in several respects: (i) They may be used to set up realistic single particle or many-body model Hamiltonians with parameters as determined from *ab initio* calculations. (ii) They are intimately related to the Berry phase, a quantity entering the modern theory of ferroelectric polarization, orbital magnetism and the Hall conductivities. (iii) They provide an efficient basis set of localized functions, which is optimal for the study of local correlation effects on electronic transport. Within the FLAPW formalism, maximally localized Wannier functions were implemented. The implementation was validated for bulk, films and one-dimensional systems, with and without spin-orbit coupling. The ferroelectric polarization was computed from the Wannier functions for several ferroelectric and multiferroic materials (e.g.  $\text{HoMnO}_3$ ) and found to be in good agreement with experimental data, where available.



# Contents

<b>1</b>	<b>Introduction</b>	<b>1</b>
<b>2</b>	<b>Density Functional Theory and Beyond</b>	<b>9</b>
2.1	Density Functional Theory . . . . .	9
2.1.1	The Hohenberg-Kohn Theorems . . . . .	10
2.1.2	The Kohn-Sham Equations . . . . .	11
2.1.3	Spin Density Functional Theory . . . . .	12
2.1.4	The Local Spin Density Approximation . . . . .	13
2.1.5	The full-potential linearized augmented-plane-wave method . . . . .	13
2.1.6	The APW+lo method . . . . .	17
2.1.7	Non-Collinear Magnetism . . . . .	17
2.2	Dynamical Mean-Field Theory . . . . .	18
2.2.1	Perturbation Theory in Infinite Dimensions . . . . .	19
2.2.2	Mapping onto the Anderson Impurity Model . . . . .	20
2.2.3	Exact Diagonalization . . . . .	24
<b>3</b>	<b>Ballistic Transport and Beyond</b>	<b>27</b>
3.1	Ballistic Transport . . . . .	28
3.1.1	The Conductance Quantum . . . . .	28
3.1.2	Landauer Formulation of Ballistic Transport . . . . .	29
3.1.3	Calculation of electronic transport within ground-state DFT . . . . .	30
3.2	NEGF Formalism . . . . .	30
3.2.1	The Meir-Wingreen formula . . . . .	33
<b>4</b>	<b>The embedding method</b>	<b>35</b>
4.1	Derivation of the Embedding Method . . . . .	37
4.1.1	The embedding potential . . . . .	38
4.1.2	Variational principle for the embedded region . . . . .	40
4.2	Embedding within the FLAPW method . . . . .	43
4.3	The surface projector . . . . .	44
4.4	Scattering States and Conductance . . . . .	45
4.5	Transfer Matrix and Embedding Potential . . . . .	47
4.6	The embedding-based order-N concept . . . . .	49

4.7	The surface projector for a curvy surface . . . . .	51
4.8	An alternative expression for the curvy surface projector . . . . .	54
4.9	Step Functions . . . . .	56
4.10	Transformation of the Potential and the Charge Density . . . . .	57
4.11	Computation of Surfaces within the embedding method . . . . .	59
4.12	Flow chart: Non-Self-Consistent Embedding . . . . .	59
<b>5</b>	<b>Self-Consistent Embedding</b>	<b>61</b>
5.1	Generation of the charge density . . . . .	61
5.2	Construction of the Coulomb Potential . . . . .	63
5.2.1	The Pseudocharge Method . . . . .	63
5.2.2	Construction of the Coulomb Potential in the Interstitial . . . . .	64
5.2.3	Construction of the Coulomb potential (Surface Calculations) . . . . .	66
5.3	Self-Consistency scheme . . . . .	67
5.4	Evaluation of total energy . . . . .	68
5.5	Evaluation of atomic forces . . . . .	68
5.5.1	Atomic Forces within standard FLAPW . . . . .	68
5.5.2	Atomic Forces within the Embedding Method . . . . .	71
<b>6</b>	<b>Efficient Embedding</b>	<b>73</b>
6.1	Solution of a linear system of equations . . . . .	73
6.2	Spectral representation of the Green function . . . . .	74
6.3	Dyson equation . . . . .	75
6.3.1	Propagation of the embedding potential . . . . .	76
6.3.2	Calculation of the full Green function . . . . .	78
6.3.3	Charge density (Equilibrium case) . . . . .	79
6.3.4	Charge density (Nonequilibrium case) . . . . .	79
<b>7</b>	<b>Order-N Embedding</b>	<b>83</b>
7.1	Order-N Self-Consistency Scheme . . . . .	83
7.2	Order-N for films and surfaces . . . . .	84
7.2.1	An order-N implementation for the film geometry . . . . .	85
7.3	Parallelization . . . . .	86
7.3.1	Parallelization of the Potential Generation . . . . .	87
7.3.2	Parallelization of the Embedding potential propagation . . . . .	88
7.4	A simple test case: Cu/Vacuum/Cu . . . . .	89
<b>8</b>	<b>Applications of the Embedding Method</b>	<b>91</b>
8.1	(001) Surface of bct Cobalt . . . . .	91
8.2	Surface State of Antimony . . . . .	94
8.3	Electronic Transport in Fe/MgO/Fe . . . . .	94
8.4	Electronic Transport in Co/MgO/Co . . . . .	95
8.5	Electronic Transport in Fe/Co/MgO/Co/Fe . . . . .	98

8.6	Anisotropy of a surface layer of EuO . . . . .	98
<b>9</b>	<b>Spin-Transfer Torque</b>	<b>101</b>
9.1	Calculation of the spin-transfer torque from first principles . . . . .	104
9.1.1	Current induced torques in the presence of spin orbit coupling . . .	107
9.2	Current induced Torques and magnetization Dynamics in Model systems .	108
9.2.1	The interface between a normal metal and a ferromagnetic metal .	108
9.2.2	Modeling a complete four-layer structure . . . . .	110
9.2.3	Macrospin model of current induced magnetization switching . . . .	113
9.2.4	Slonczewski's model . . . . .	114
9.2.5	Interpretation of GMR and STT data . . . . .	115
9.3	Calculation of the spin-transfer torque within the Embedding method . .	117
9.4	Computational procedure . . . . .	119
9.5	GMR and STT in Co-Cu-Co nanopillars . . . . .	120
9.6	GMR and STT in Fe-Ag-Fe nanopillars . . . . .	125
9.7	GMR and STT in Fe-Au-Fe nanopillars . . . . .	133
9.8	TMR and STT in Fe-MgO-Fe . . . . .	134
9.8.1	Co instead of Fe in the magnetic layers . . . . .	141
<b>10</b>	<b>Wannier Functions</b>	<b>143</b>
10.1	Maximally localized Wannier functions . . . . .	144
10.1.1	One dimensional example . . . . .	144
10.1.2	Maximal localization procedure . . . . .	147
10.1.3	First-guess Wannier functions . . . . .	149
10.2	Implementation within the FLAPW method . . . . .	150
10.2.1	Calculation of $M_{mn}^{(\mathbf{k},\mathbf{b})}$ within the FLAPW formalism . . . . .	150
10.2.2	Local orbital contributions to the $M_{mn}^{(\mathbf{k},\mathbf{b})}$ matrix . . . . .	151
10.2.3	Calculation of $A_{mn}^{(\mathbf{k})}$ within the FLAPW formalism . . . . .	152
10.2.4	The $M_{mn}^{(\mathbf{k},\mathbf{b})}$ matrix in case of film calculations . . . . .	153
10.2.5	The $M_{mn}^{(\mathbf{k},\mathbf{b})}$ matrix in case of one dimensional calculations . . . . .	154
10.3	Wannier Representation of the Hamiltonian . . . . .	155
10.4	Spin-orbit coupling . . . . .	156
10.5	Use of symmetry in Wannier function calculations . . . . .	158
10.6	The Berry Phase . . . . .	160
10.7	Ferroelectric Polarization . . . . .	161
10.7.1	Wannier Picture of Ferroelectric Polarization . . . . .	167
10.8	Examples of Wannier functions . . . . .	169
10.8.1	Diamond . . . . .	169
10.8.2	SrVO <sub>3</sub> . . . . .	170
10.8.3	Graphene . . . . .	173
10.8.4	Platinum . . . . .	174
10.8.5	Ferroelectricity of BaTiO <sub>3</sub> . . . . .	178
10.8.6	Ferroelectricity of PbTiO <sub>3</sub> . . . . .	179

---

10.8.7 Ferroelectricity of $\text{HoMnO}_3$ . . . . .	182
10.8.8 Bi(111) Ultrathin Film: Topological Insulator . . . . .	186
10.9 Intrinsic anomalous Hall effect . . . . .	187
<b>11 Summary and Conclusions</b>	<b>191</b>
<b>A Spherical Harmonics</b>	<b>195</b>
A.1 Gaunt Coefficients . . . . .	195
A.2 Wigner $D$ -matrix . . . . .	196
<b>B Coordinate Frame Transformations</b>	<b>197</b>
B.1 Definition of and need for local coordinate frames . . . . .	197
B.2 Transformation of cartesian vectors and cartesian vector operators . . . . .	198
B.3 Transformation of spinors . . . . .	198
<b>C MPI subroutines</b>	<b>199</b>
<b>D JUGENE</b>	<b>201</b>
<b>Acknowledgement</b>	<b>215</b>
<b>Curriculum Vitae</b>	<b>219</b>

# Chapter 1

## Introduction

With the discovery of the giant magnetoresistance (GMR) effect by Peter Grünberg *et al.* [1] and Albert Fert *et al.* [2] in 1988, spintronics was born as a new, exciting and very active research field. In these experiments it was found that an electrical current passing through ferromagnetic films separated by non-magnetic metallic spacer layers is subject to a resistivity, which changes unexpectedly largely (gigantically at those days) with the change of the relative alignment of the magnetization in these films from ferromagnetic to antiferromagnetic. Obviously GMR made it possible to turn the information of a two-state magnetic configuration (parallel or anti-parallel associated with bit 0 or 1) into an electrical one, or in a more abstract sense, turn spin information into charge current information. Already 8 years after the discovery, this effect was used for example in sensors embodied in read heads of hard disks of common PCs. Thus, in contrast to standard electronics, which makes use of the charge of the electron, spintronic devices exploit also the electron spin degree of freedom. The most widely used spintronic effect – the GMR – has revolutionized the computer hard drive technology, as it allowed to achieve much higher data storage densities, which currently approach 1 Tbit/in<sup>2</sup>. In 2007 Albert Fert and Peter Grünberg were awarded the Nobel Prize in physics for this discovery.

Soon after this discovery, experiments have been carried out in which the non-magnetic metallic spacer layer was replaced by a non-magnetic semiconductor and insulator. In this set-up spin-polarized electrons tunnel from one ferromagnetic layer through an insulating barrier film into the second ferromagnetic layer, and again a strong dependence of the resistance upon the relative orientation of the magnetization was found. The effect is called the tunneling magnetoresistance (TMR) and the set-up is called a magnetic tunnel junction (MTJ). In difference to previous GMR systems, TMR systems exhibit a large voltage drop across the MTJ in a geometry, where the current flows perpendicular to the plane of the device and operates with small electrical currents. This allows high integration densities and is the origin of device concepts for the nonvolatile magnetic random access memories (MRAM) that are made from an array of MTJs. Although the TMR effect was first observed by Jullière in 1975 [3] at low temperatures, its rediscovery with much higher TMR ratio (an important figure of merit) by Miyazaki and Tekuza [4], and Moodera and co-workers [5] opened the prospect of realizing the MRAM. Today, the most success-

ful MTJs are made of MgO insulators sandwiched between ferromagnetic electrodes, e.g. Co<sub>2</sub>FeAl/MgO/CoFe, that show extremely large TMR ratios that approach 400% at room temperature with record-breaking output voltage of 425 mV [6].

The MRAM has the prospective to become the mainstream memory technology as it has the potential to achieve the high integration density of the Dynamical Random Access Memory (DRAM), the operation speed of the Static Random Access Memory (SRAM) combined with the non-volatility of the Flash memory by high endurance and low-voltage operations. An important issue, which remains to be resolved is the reliable, memory-cell selective writing process at high speed and low power consumption. The writing of such a cell is traditionally done by applying an electrical current to create a magnetic field, which reverses one of the magnetizations of the two electrodes. This type of writing is a very energy inefficient and slow process, with writing currents that increase unfavorably with the reduction of the memory cell size, which has limited the use of this type of memory in today's electronics. A much more elegant and efficient way relies on the transfer of electronic spins between the two layers. Currents sent through an MRAM device create a torque on the magnetization of the individual layers which is called spin transfer torque (STT). If this spin transfer torque is strong enough it can switch the magnetization direction. The resulting memory element is called a spin transfer torque MRAM or, in short, STT-MRAM. It promises to greatly reduce the current needed to switch these memory elements, which should reduce the size of these elements, and to increase their speed. Much scientific and engineering effort is geared towards reducing the threshold current density for switching and increasing switching speed and theory can assist to optimize the design of the cell by understanding which materials combination leads to a large torque by low current density. The concept of spin-transfer torque goes back to two theoretical predictions of Berger [7] and Slonczewski[8] in 1996 and was confirmed by early experiments [9, 10, 11]. It may be interpreted as inverse of the GMR effect: In the GMR effect, at a given voltage, the strength of the electron current depends on the magnetic configuration. In the STT effect, due to the exchange interaction between the spin current and the localized magnetic moments, a magnetic torque on the localized magnetic moments is produced. This spin torque can oppose the intrinsic damping of the magnetic layer exciting spin waves and, for sufficient current strengths, reverses the direction of the magnetization. Besides the practical importance, spin-transfer effects provide a probe of the interactions between spins and magnetism and strengthen our fundamental understanding of magnetic materials. Not only do these effects arise from spin interactions at interfaces but they also occur from current flowing through non-uniformities of the magnetization (such are domain walls, vortices or skyrmions). Thus, spin transfer links the physical phenomena of magnetic excitations, damping, reversal and micromagnetic configurations with spin transport and may open a path to high frequency non-linear oscillators.

Intrigued by the success of metal-based tunnel junctions such as Fe/MgO/Fe, currently it is aimed at the advancement of a new field named *nanoferronics*, in which ferroelectric, multiferroic or in general electronically active, hysteretic oxides replace electronically passive binary oxide barriers in conventional tunneling elements. This may open up the way to multifunctional tunneling contacts, providing an electric field control of spin-dependent

transport properties. Interesting transport concepts such as the tunneling electroresistance (TER) and the tunneling electro-magnetic resistance (TEMR) [12] have been suggested. The ferromagnetic lead may be a conventional transition metal or a ferromagnetic oxide leading to all-oxide tunnel junctions entering the realm of oxide heterostructures and oxide electronics. Due to the fact that these are mostly oxide compounds including transition elements, a number of challenges arise in their study, both experimentally and theoretically.

Thus, in the past and even more so in the future, we deal with devices made of artificial multicomponent heterostructures, whose functionality derives from the modification of (spin-dependent) transport properties by external parameters such as electric and magnetic fields, strain, pressure or light as well as the inverse processes where spin-dependent electrical currents modify quantities characterizing the state of a device such as the ferroelectric polarization or the magnetization. In the future we will deal with materials, which support the response by the intrinsic electronic properties, for example materials exhibiting strong electron correlation.

The aim of this thesis is to develop and apply electronic structure methods that lay the foundations to realistically describe the physical properties and processes in these junctions from the first-principles of quantum mechanics of the many-electron system. This is a difficult task due to the underlying non-equilibrium quantum mechanical many-body problem, the complexity and the diversity of the chemical elements, the structural geometry and the size of the systems.

The quantum mechanical many particle problem cannot be solved exactly for large systems due to the exponential increase of the size of the Hilbert space. Density-functional theory (DFT) developed by Hohenberg and Kohn [13] and Kohn and Sham [14] circumvents the exponential growth of the size of the Hilbert space by using charge density and spin density as fundamental variables of a universal yet unknown exchange-correlation functional. The quantum mechanical many-particle problem is mapped onto an effective single-particle one. Unfortunately, the exact exchange-correlation functional is not known, but the success of the density-functional theory lies in the practical observation that the exchange correlation functional approximated by the one of the homogeneous electron gas gives encouraging if not excellent results on the level of predictive power. Since the introduction of the density-functional theory, the quantitative description of the properties of solids has made great advances. Systems that are so large and complex that they cannot be treated anymore with any correlated quantum chemistry method (e.g. Hartree-Fock) may still be amenable to DFT. Moreover, owing to the development of ever better exchange correlation potentials the quantitative reliability of predictions based on parameter-free DFT has for some properties reached the level that computer-aided material design substantially supports the experimental quest for materials exhibiting a desired functionality. The Nobel prize in chemistry of 1998 awarded to Walter Kohn and John A. Pople acknowledged the large success of density functional theory. Today we deal with a highly developed array of different first-principles DFT implementations, which all have their right on their own mostly geared addressing particular properties or material classes most efficiently. The full-potential linearized augmented-plane-wave (FLAPW) method [15, 16, 17, 18], which is used in this work, is known to be an all-electron method avoiding the construction of pseu-



dopotentials, and is applicable to all elements in the periodic table even in open structures, low-symmetries such as surfaces or thin films, with complex magnetic structures including spin-orbit interaction allowing structural optimizations on the basis of forces exerted on the atoms. It is known for its high precision, but also for its methodological complexity and numerical expense.

While DFT allows to calculate ground state properties for many solids quantitatively correct in a parameter free way, it also has limitations. The excited states are usually not well described by the effective single-particle eigenstates, e.g. the gap of semiconductors or insulators is often underestimated. Where electronic transport is concerned it has to be stressed that even at zero applied bias voltage the electronic transport properties are not ground state properties. One option to overcome these limitations is to perform a many-body calculation for a correlated subspace of the full Hilbert space. Such calculations are motivated or guided by realistic many-body Hamiltonians. The link between these models and the density-functional approach is given by the Wannier functions, which are a natural basis for model Hamiltonians. However, such a localized basis set is not available intrinsically within most electronic structure methods for periodic solids and this holds also for the FLAPW method. Most methods are based on Bloch functions. In recent years, maximally localized Wannier functions [19, 20], optimally spatially localized functions related to the Bloch functions by a unitary transformation, have become the preferred basis set to study local correlations [21, 22, 23]. A second asset of the Wannier function is closely related to the modern theory of the ferroelectric polarization [24] in which quantities that depend on the quantum mechanical position operator in an infinite periodic solid, can be formulated by means of the Berry phase. In this theory the ferroelectric polarization is connected to the centers of the Wannier functions. At last the Wannier function is an efficient basis set to express quantities in real space, which provides frequently a new look on physical properties. For all those and more reasons Wannier functions were implemented within the FLAPW method suitable for bulk, film and one-dimensional geometries. As examples results are provided for the metallic  $\text{SrVO}_3$ , ferroelectric  $\text{BaTiO}_3$  grown on  $\text{SrTiO}_3$ , multiferroic  $\text{HoMnO}_3$ , ferroelectric  $\text{PbTiO}_3$ , diamond, covalently bonded graphene, a one-dimensional Pt-chain, and a double layer of  $\text{Bi}(111)$ . Tight-binding parameters for the topological insulator  $\text{Bi}(111)$  and  $\text{SrVO}_3$  were determined. The effect of spin-orbit coupling on the Wannier functions for the cases of  $\text{SrVO}_3$  and platinum is discussed. The dependency of the Wannier functions on the choice of the localized trial orbitals as well as the difference between the maximally localized and first-guess Wannier functions are discussed. Our results are compared to results published elsewhere, where available, and found to be in excellent agreement.

A non-trivial problem is the calculation of the electronic structure and the derived properties within the DFT applying the appropriate approximations to the unknown exchange correlation functional for the actual device geometry of spin-valves and magnetic or nanoferroic tunnel junctions. In many instances the thickness of the active devices is in the order of a few nanometers and can involve hundreds of atoms per unit cell. As said above the FLAPW method is comparatively demanding concerning the required computational resources. The computational time obeys a cubic scaling law with system size. In the



present thesis an implementation of the FLAPW method was developed which exhibits an order- $N$  scaling behavior with the number of layers  $N$  and which is particularly well-suited for determining the ground state properties of systems in the geometry of junctions for calculations of electronic and spin transport properties. By order- $N$  scaling it is meant that the computational time needed for  $N \cdot M$  layers is larger than the time needed for  $M$  layers by a factor of  $N$  provided all layers are of the same size. The order- $N$  scaling is obtained on the basis of the Green function embedding method [25, 26, 27, 28, 29] by partitioning the system into layers, which are computed separately. A central quantity of the embedding method is the embedding potential. The embedding potential contains the information on the boundary condition, which the Green function satisfies. It can be interpreted as a generalized logarithmic derivative. The embedding method allows to calculate the Green function of a finite region of space, which is embedded into an environment, by adding the embedding potential of the environment to the Hamiltonian of the finite region. In order to calculate the layers individually within the order- $N$  implementation the embedding potentials of the individual layers are needed. They are obtained in a preceding step by layer-wise propagation through the system. The partitioning of the system into  $N$  layers reduces the computational cost by roughly a factor of  $N^2/8$  when compared to an embedding calculation of the system as a whole. A difficult technical issue is how to optimally define the embedding surface, on which the embedding potential is defined. In this respect, a technical breakthrough, which made the order- $N$  scaling possible, was the development of surface projectors on a curvy surface originating from muffin-tin spheres embedded in an interstitial region. The efficiency of the method relies also on the Dyson equation and the spectral representation of the Hamiltonian, which allow e.g. to implement the energy-contour integration more efficiently.

The Landauer formula is the most widely applied tool to study electronic transport. It solves the electronic transport problem by mapping it onto a scattering problem. In the present work the scattering problem is solved within the effective single particle description of DFT using the Green function embedding technique. Strictly speaking, out of equilibrium it is incorrect to calculate the many-body current from the effective single-particle eigenstates of static DFT: Electronic transport is a non-equilibrium problem, which is very difficult to solve for interacting electrons. Nevertheless, evaluating the Landauer formula for the effective single particle channels of DFT often allows to predict qualitative trends correctly, while a quantitative agreement cannot be expected and is not found in general. Using the ballistic Landauer formulation electronic transport in MgO-based MTJs with Fe, FeCo, and Co as metallic leads was calculated.

In the case of strongly correlated materials the applicability of the ballistic Landauer formulation is particularly questionable. In contrast to static DFT, in time-dependent versions of density functional theory, e.g. time-dependent density functional theory (TDDFT) and time-dependent current density-functional theory (TDCDFT) the calculated single-particle total current is equal to the many-body total current [30]. However, finding appropriate dynamical exchange correlation potentials for TDDFT and TDCDFT is difficult and a current research topic. With the implementation of Wannier functions within the FLAPW method the foundation was laid to describe the electronic transport properties of

interacting electrons within a realistic many-body model-Hamiltonian approach.

Understanding the switching of the magnetization in magnetic tunneljunctions in particular requires the understanding of the spin-transport. In contrast to the charge-transport, for which the conservation of the charge current is fundamental, the spin-current is not conserved in non-collinear magnetic configurations and in the presence of spin-orbit coupling. The spatial dependence of the spin-current gives rise to the spin torque. In order to calculate the spin torque the scattering states are evaluated using the Green function embedding method. From the scattering states the spin-current is obtained. The spin-torque exerted on a region is given by the net flow of spin-current into that region. In addition to the spin-current based implementation of the spin-torque a second way of calculating the spin-torque was implemented: From the scattering states the non-equilibrium charge and spin densities are available. The spin-torque is calculated from the exchange field and the non-equilibrium spin density. In contrast to the spin-current based implementation the second method is also valid in the presence of spin-orbit coupling: In the presence of spin-orbit coupling the spin-current is not even conserved in a collinear magnetic system, suggesting that the exchange field is not the only source of spatial dependence of the spin-current in this case. We calculated the spin-torque in the all-metallic spin-valves Co/Cu/Co, Fe/Ag/Fe and Fe/Au/Fe as well as in MgO-based MTJs. Where possible, we compared our results to existing calculations of these systems, which were carried out using the Korringa-Kohn-Rostocker (KKR) method. In the case of the Co/Cu/Co spin-valve very good agreement was found between our results and those of the KKR-calculations. In the case of the MgO-based MTJs differences are found especially for the out-of-plane torque. The results for the Fe/Ag/Fe and Fe/Au/Fe spin-valves are compared to Slonczewski's model.

The present thesis is organized as follows. In chapter two a brief introduction into density functional theory and the full-potential linearized augmented-plane-wave method is given. The limitations of density functional theory are discussed and dynamical mean field theory is presented as a way to go beyond density functional theory. The third chapter discusses the electronic transport problem. For the case of non-interacting electrons the Landauer formulation is presented. How to calculate transport properties of interacting electron systems is discussed in the framework of the NEGF formalism. Chapter four introduces the embedding method. The main equations of the embedding method are derived, the embedding potential is defined and the surface projector is introduced. In chapter five the basic concepts of self-consistent embedding are introduced. Self-consistent embedding opens the way to calculate electronic transport in the presence of a finite bias. Additionally, it is a major ingredient of the order-N embedding implementation. In chapter six the formal structure of the embedding method is investigated with the purpose of finding equations which allow to perform the calculations within the embedding method particularly efficiently. Chapter seven deals with order-N embedding. The parallelization of the order-N implementation is discussed in detail. Several applications of the embedding method in surface and transport calculations will be presented in chapter eight. The spin-torque is the topic of chapter nine. The theory of the spin-torque and its calculation within the embedding method are discussed and applications are shown. Chapter ten is devoted

to the Wannier functions. The details of the implementation are discussed and applications are shown. The thesis is summarized in chapter eleven.



## Chapter 2

# Density Functional Theory and Beyond

For a complete and satisfactory theoretical investigation of solids a quantum mechanical treatment is indispensable. This amounts to formulating and solving the many-body Schrödinger equation for the nucleons and electrons comprising the solid. In order to simplify this complex problem, one may consider the nucleons to be static at first and dealing with the electrons only. If necessary, the effect of the nuclear degrees of freedom may be considered in a second step. This simplification is known as the Born-Oppenheimer approximation and justified by the fact that the characteristic time scale of the nuclear motion is much longer than its electronic counterpart. Consequently, we are left with the electronic Schrödinger equation

$$\left[ -\frac{1}{2} \sum_{i=1}^N \Delta_i + \sum_{i,j=1}^N \frac{e^2}{|\mathbf{r}_i - \mathbf{r}_j|} - \sum_{i=1}^N \sum_{\mu=1}^M \frac{e^2 Z_\mu}{|\mathbf{r}_i - \boldsymbol{\tau}_\mu|} \right] \Psi(\mathbf{r}_1, \dots, \mathbf{r}_N) = E \Psi(\mathbf{r}_1, \dots, \mathbf{r}_N) \quad (2.1)$$

for  $N$  electrons with position vectors  $\mathbf{r}_i$ , where we denote the number of nucleons by  $M$  and their charge and position by  $Z_\mu$  and  $\boldsymbol{\tau}_\mu$ , respectively. Unfortunately, the direct solution of this equation is only possible for small values of  $N$  as the dimension of the Hilbert space of  $\Psi(\mathbf{r}_1, \dots, \mathbf{r}_N)$  grows like  $V^N$  with the system size  $V$  and the number  $N$  of electrons. Very often  $V \propto N$  and the dimension of the Hilbert space grows like  $N^N$ .

### 2.1 Density Functional Theory

Density functional theory has been developed by Hohenberg and Kohn [13] and Kohn and Sham [14]. It avoids the dramatic increase of the Hilbert space with system size by replacing the complex many-body wave function  $\Psi(\mathbf{r}_1, \dots, \mathbf{r}_N)$  by the simpler charge density as basic object of the theory.

### 2.1.1 The Hohenberg-Kohn Theorems

As outlined above, the standard procedure of treating a quantum mechanical system is to set up its Hamiltonian and to find the wave functions that solve the corresponding Schrödinger equation. Any measurable quantity of this system may then be calculated from the expectation values of a corresponding operator for these wave functions. It can be shown that the knowledge of the ground state wave function alone suffices to identify the quantum mechanical system to which it belongs, i.e., it determines the Hamiltonian up to a constant. To put it another way, any measurable quantity is a unique functional of the ground state wave function.

The first Hohenberg-Kohn theorem states that the knowledge of the ground state density alone is sufficient to determine the Hamiltonian up to a constant. Consequently, any measurable quantity is a unique functional of the ground state density. For example, there is a unique energy functional  $E[n(\mathbf{r})]$ , which allows to compute the ground state energy from the density  $n(\mathbf{r})$ . As the kinetic energy and the Coulomb interaction between electrons are universal functionals, we may write for the energy functional

$$E[n(\mathbf{r})] = F[n(\mathbf{r})] + \int v(\mathbf{r})n(\mathbf{r})d^3r, \quad (2.2)$$

where the external potential

$$v(\mathbf{r}) = - \sum_{\mu=1}^M \frac{e^2 Z_{\mu}}{|\mathbf{r} - \boldsymbol{\tau}_{\mu}|} \quad (2.3)$$

is generated by the nucleons and  $F[n(\mathbf{r})]$  is the unique functional of kinetic energy plus Coulomb interaction energy between electrons. Combining this result with the Ritz variational principle leads to the second Hohenberg-Kohn theorem: Given the external potential  $v(\mathbf{r})$ , the corresponding ground state density  $n(\mathbf{r})$  minimizes the functional

$$E_v[n(\mathbf{r})] = F[n(\mathbf{r})] + \int v(\mathbf{r})n(\mathbf{r})d^3r, \quad (2.4)$$

under the constraint that the total number of electrons is kept fixed. Thus, the second Hohenberg-Kohn theorem provides a recipe for the calculation of the ground state density.

It is convenient to separate out the classical Coulomb energy from  $F[n(\mathbf{r})]$  and to write

$$F[n(\mathbf{r})] = \frac{1}{2} \int \frac{n(\mathbf{r})n(\mathbf{r}')}{|\mathbf{r} - \mathbf{r}'|} d^3r' d^3r + G[n(\mathbf{r})], \quad (2.5)$$

where  $G[n(\mathbf{r})]$  is likewise a universal functional. Then, the expression for the energy functional (2.2) becomes

$$E_v[n(\mathbf{r})] = G[n(\mathbf{r})] + \int v(\mathbf{r})n(\mathbf{r})d^3r + \frac{1}{2} \int \frac{n(\mathbf{r})n(\mathbf{r}')}{|\mathbf{r} - \mathbf{r}'|} d^3r' d^3r. \quad (2.6)$$

### 2.1.2 The Kohn-Sham Equations

Unfortunately, the functional  $G[n(\mathbf{r})]$  is not known exactly and has to be approximated. In order to construct such an approximation, it has been proposed by Kohn and Sham [14] to introduce a reference system of  $N$  non-interacting electrons moving in an effective potential  $V_{\text{eff}}$ , where the electron density  $n(\mathbf{r})$  agrees with the one of the interacting system. The ground state wave function of this reference system is simply given by the Slater determinant of a set of  $N$  single-particle wave functions,  $\{\psi_i(\mathbf{r})\}$ , which satisfy the set of Schrödinger-like equations

$$\left[-\frac{1}{2}\nabla^2 + V_{\text{eff}}(\mathbf{r})\right]\psi_i(\mathbf{r}) = \epsilon_i\psi_i(\mathbf{r}), \quad (2.7)$$

which are called Kohn-Sham equations. The wave functions  $\psi_i$  are called Kohn-Sham wave functions. Clearly, the ground-state density of this system is calculated in the following way:

$$n(\mathbf{r}) = \sum_{i=1}^N |\psi_i(\mathbf{r})|^2. \quad (2.8)$$

The expression for the energy functional of the non-interacting reference system is

$$E_s[n] = T_s[n] + \int V_{\text{eff}}(\mathbf{r})n(\mathbf{r})d^3r, \quad (2.9)$$

where the subscript “s” stands for “single particle”. According to the second Hohenberg-Kohn theorem, the ground state of the reference system minimizes the energy functional  $E_s[n]$  under the constraint of fixed electron number. Using Lagrange-multipliers  $\epsilon_i$  to take these constraints into account the minimization of the energy functional  $E_s[n]$  reproduces the set of differential equations (2.7).

For the energy functional of the interacting system we may write

$$E_v[n] = T_s[n] + \frac{1}{2} \int \frac{n(\mathbf{r})n(\mathbf{r}')}{|\mathbf{r} - \mathbf{r}'|} d^3r' d^3r + \int v(\mathbf{r})n(\mathbf{r})d^3r + E_{xc}[n], \quad (2.10)$$

where we introduced the exchange-correlation functional

$$E_{xc}[n] = G[n] - T_s[n]. \quad (2.11)$$

The exact exchange-correlation functional is unknown like  $G[n]$  is unknown, but in fact very reliable approximations have been developed for  $E_{xc}[n]$ . Minimization of the energy functional Eq. (2.10) under the constraint of fixed electron number yields a second set of Schrödinger-like equations. If the effective potential is chosen according to

$$V_{\text{eff}}(\mathbf{r}) = \int \frac{n(\mathbf{r}')}{|\mathbf{r} - \mathbf{r}'|} d^3r' + v(\mathbf{r}) + \frac{\delta E_{xc}[n]}{\delta n(\mathbf{r})}, \quad (2.12)$$

the first set of equations, Eq. (2.7), becomes equivalent to this second set of Schrödinger-like equations, and the ground-state density of the non-interacting reference system is

identical to the ground-state density of the interacting system. The equation for the effective potential, Eq. (2.12), has to be solved self-consistently together with Eq. (2.7) and Eq. (2.8): For a given density  $n(\mathbf{r})$  one sets up the effective potential according to Eq. (2.12) and solves the Kohn-Sham equations, Eq. (2.7), which provides the wave functions  $\phi_i$  needed to calculate a new density  $n(\mathbf{r})$  according to Eq. (2.8), which is used to calculate the effective potential again. When self-consistency is reached, the input density, which is used to calculate the effective potential, is equal to the output density, which is calculated from the Kohn-Sham wave functions  $\psi_i$ . The ground-state energy of the interacting system is given by

$$E = \sum_i n_i \epsilon_i - \int n(\mathbf{r}) V_{\text{eff}}(\mathbf{r}) d^3 r + \frac{1}{2} \int \frac{n(\mathbf{r})n(\mathbf{r}')}{|\mathbf{r} - \mathbf{r}'|} d^3 r' d^3 r + \int v(\mathbf{r})n(\mathbf{r})d^3 r + E_{xc}[n], \quad (2.13)$$

where  $n_i$  specifies the occupation of state  $i$ .

### 2.1.3 Spin Density Functional Theory

For magnetic systems the preceding discussion has to be extended. Instead of the electron density alone we now use electron density  $n(\mathbf{r})$  and *spin density*  $\mathbf{m}(\mathbf{r})$  as fundamental variables of the theory. If the occupied states are given in terms of the two component spinor wave functions

$$\boldsymbol{\psi}_i(\mathbf{r}) = \begin{pmatrix} \psi_{\uparrow,i}(\mathbf{r}) \\ \psi_{\downarrow,i}(\mathbf{r}) \end{pmatrix}, \quad (2.14)$$

electron and spin-density are given by

$$\begin{aligned} n(\mathbf{r}) &= \sum_{i,\sigma=\uparrow,\downarrow} |\psi_{\sigma,i}(\mathbf{r})|^2, \\ \mathbf{m}(\mathbf{r}) &= \sum_i (\boldsymbol{\psi}_i(\mathbf{r}))^\dagger \boldsymbol{\sigma} \boldsymbol{\psi}_i(\mathbf{r}). \end{aligned} \quad (2.15)$$

The exchange-correlation functional  $E_{xc}[n, \mathbf{m}]$  depends on both electron density and spin density. As Kohn-Sham equations we now obtain the set of Pauli-like equations

$$\left[ -\frac{1}{2}\Delta + V_{\text{eff}}(\mathbf{r}) + \boldsymbol{\sigma} \cdot \mathbf{B}^{\text{xc}}(\mathbf{r}) \right] \boldsymbol{\psi}_i(\mathbf{r}) = E_i \boldsymbol{\psi}_i(\mathbf{r}), \quad (2.16)$$

where  $\mathbf{B}^{\text{xc}}(\mathbf{r})$  is the *exchange field*

$$\mathbf{B}^{\text{xc}}(\mathbf{r}) = \frac{\delta E_{xc}[n, \mathbf{m}]}{\delta \mathbf{m}(\mathbf{r})}. \quad (2.17)$$

In this general form, Eq. (2.16) may be used to treat *noncollinear magnetism*. If  $\mathbf{B}^{\text{xc}}(\mathbf{r})$  has a fixed direction in space, e.g.  $\mathbf{B}^{\text{xc}}(\mathbf{r}) = B^{\text{xc}}(\mathbf{r})\hat{\mathbf{e}}_z$ , Eq. (2.16) describes *collinear magnetism*



and may be written as two equations, one for each spinor component:

$$\begin{aligned} \left[ -\frac{1}{2}\Delta + V_{\text{eff}}(\mathbf{r}) + B^{\text{xc}}(\mathbf{r}) \right] \psi_{\uparrow,i}(\mathbf{r}) &= E_{\uparrow,i} \psi_{\uparrow,i}(\mathbf{r}), \\ \left[ -\frac{1}{2}\Delta + V_{\text{eff}}(\mathbf{r}) - B^{\text{xc}}(\mathbf{r}) \right] \psi_{\downarrow,i}(\mathbf{r}) &= E_{\downarrow,i} \psi_{\downarrow,i}(\mathbf{r}). \end{aligned} \quad (2.18)$$

### 2.1.4 The Local Spin Density Approximation

While the density functional theory provides an exact theoretical framework for the treatment of many-body systems, practical applications suffer from the lack of knowledge of the exact exchange-correlation functional, for which approximations have to be developed. Despite this drawback many solids may be described surprisingly well by these approximations to density functional theory. One widely used approximation is the local spin density approximation (LSDA). Within LSDA the exchange correlation energy is approximated as follows:

$$E_{\text{xc}}[n, \mathbf{m}] = \int n(\mathbf{r}) \epsilon_{\text{xc}}(n(\mathbf{r}), m(\mathbf{r})) d^3r, \quad (2.19)$$

where  $\epsilon_{\text{xc}}(n(\mathbf{r}), m(\mathbf{r}))$  is the *exchange correlation density* of the free electron gas with parameters  $n(\mathbf{r})$  and  $m(\mathbf{r})$ .

Within LSDA the exchange field is parallel to the magnetization:

$$\mathbf{B}^{\text{xc}}(\mathbf{r}) = \frac{\delta E_{\text{xc}}[n, \mathbf{m}]}{\delta \mathbf{m}(\mathbf{r})} = n(\mathbf{r}) \frac{\partial \epsilon_{\text{xc}}(n(\mathbf{r}), m(\mathbf{r}))}{\partial m(\mathbf{r})} \hat{\mathbf{m}}, \quad (2.20)$$

i.e., we may write

$$\mathbf{B}^{\text{xc}}(\mathbf{r}) = B^{\text{xc}}(n(\mathbf{r}), m(\mathbf{r})) \hat{\mathbf{m}}(\mathbf{r}). \quad (2.21)$$

### 2.1.5 The full-potential linearized augmented-plane-wave method

In order to solve the Kohn-Sham equations, Eq. (2.7), numerically, one needs to calculate matrix elements of the Hamilton operator for a given basis set. While the choice of plane waves as basis functions is very appealing, describing the rapid oscillations of the wave function close to the nucleus in a plane wave basis set is inefficient. It is natural to distinguish between the region of space where plane waves provide a good description of the wave functions and the regions of space around the atoms, where the wave functions are atom-like. We denote the former by *interstitial region* (INT) and the latter by *muffin-tin regions* (MT). The augmented plane wave (APW) approach, originally proposed by Slater [15, 31], uses a mixed basis set for INT and MT regions: In the interstitial region plane waves are used to represent the wave functions, while inside the MT-spheres the wave functions are expanded in terms of the solutions of the scalar relativistic Dirac equation, which is solved for a set of energy parameters and for the spherically symmetric component of the potential. The basis functions are labeled by the interstitial plane wave indices. Inside the MT-spheres the plane waves are replaced by a linear combination of the radial

solutions of the scalar relativistic Dirac equation in such a way that the basis function is continuous at the MT-sphere boundary. Hence, the APW basis functions are

$$\phi_{\mathbf{g}}^{(\mathbf{k})}(\mathbf{r}) = \begin{cases} \frac{1}{\sqrt{V}} e^{i(\mathbf{k}+\mathbf{g})\cdot\mathbf{r}} & \mathbf{r} \in \text{INT} \\ \sum_L a_L^{\mu\mathbf{g}} u_{1,l}^{\mu}(r') Y_L(r') & \mathbf{r} \in \text{MT}_{\mu} \end{cases}, \quad (2.22)$$

where we denoted the radial solutions of the scalar relativistic Dirac equation for atom  $\mu$  by  $u_{1,l}^{\mu}(r)$ ,  $\mathbf{r}' = (\mathbf{r} - \boldsymbol{\tau}^{\mu})$  is the position vector with respect to the center  $\boldsymbol{\tau}^{\mu}$  of atom  $\mu$ , and  $L = (l, m)$  is a compact notation for angular momentum. To keep the notation simple, we do not explicitly write the  $k$ -dependence of the coefficient  $a_L^{\mu\mathbf{g}}$ . However, an energy-independent APW basis set like in Eq. (2.22) does not provide sufficient variational freedom. The use of an energy-dependent APW-basis set is possible but entails a non-linear energy dependence of the Hamiltonian operator, which dramatically increases the complexity of the eigenvalue problem. Andersen proposed [16] to linearize this non-linear eigenvalue problem by using linear combinations of both the radial functions  $u_{1,l}^{\mu}(r)$  and their derivatives  $\dot{u}_{1,l}^{\mu}(r)$  with respect to energy in such a way that the basis function and its first derivative are continuous at the MT-sphere boundary. The resulting basis functions are called *linearized* augmented plane waves (LAPW) and are given by

$$\phi_{\mathbf{g}}^{(\mathbf{k})}(\mathbf{r}) = \begin{cases} \frac{1}{\sqrt{V}} e^{i(\mathbf{k}+\mathbf{g})\cdot\mathbf{r}} & \mathbf{r} \in \text{INT} \\ \sum_L [a_L^{\mu\mathbf{g}} u_{1,l}^{\mu}(r') + b_L^{\mu\mathbf{g}} \dot{u}_{1,l}^{\mu}(r')] Y_L(\hat{\mathbf{r}}') & \mathbf{r} \in \text{MT}_{\mu} \end{cases}. \quad (2.23)$$

The radial function  $u_{1,l}^{\mu}(r)$  is a solution of the scalar relativistic Dirac equation at the energy  $E_{1,l}^{\mu}$ , which may be computed from eigenvalues and corresponding partial charges (see e.g. Ref. [32]).

In order to describe semi-core states, the LAPW basis set may be supplemented with local orbitals (LOs) [33]. In contrast to the LAPW basis functions defined in Eq. (2.23) a local orbital is zero everywhere in space with the exception of the interior of the MT-sphere of that atom the semi-core states of which it describes. Within the FLAPW method, local orbitals for a given angular momentum  $l$  are constructed as a linear combination of a solution  $u_{2,l}^{\mu}$  of the scalar relativistic wave equation at the energy  $E_{2,l}^{\mu}$  of the semi-core state and the radial solutions  $u_{1,l}$  and  $\dot{u}_{2,l}$  used to describe the valence window. The coefficients of this linear combination are determined in such a way that the resulting basis functions and their radial derivative are zero at the muffin-tin boundary:

$$\phi_{LO}^{(\mathbf{k})}(\mathbf{r}) = \begin{cases} 0 & \mathbf{r} \in \text{INT} \\ \sum_L [a_L^{\mu,LO} u_{1,l}^{\mu}(r') + b_L^{\mu,LO} \dot{u}_{1,l}^{\mu}(r') + c_L^{\mu,LO} u_{2,l}^{\mu}(r')] Y_L(\hat{\mathbf{r}}') & \mathbf{r} \in \text{MT}_{\mu} \end{cases}. \quad (2.24)$$

The radial solutions  $u_{1,l}^\mu(r)$  and their energy derivatives  $\dot{u}_{1,l}^\mu(r)$  solve the equations<sup>1</sup>

$$\begin{aligned} \left[ \hat{H}^{\mu,\text{sph}} - E_{1,l} \right] r u_{1,l}^\mu(r) &= \left[ -\frac{1}{2} \frac{\partial^2}{\partial r^2} + \frac{l(l+1)}{2r^2} + V^{\mu,\text{sph}}(r) - E_{1,l} \right] r u_{1,l}^\mu(r) = 0, \\ \left[ \hat{H}^{\mu,\text{sph}} - E_{1,l} \right] r \dot{u}_{1,l}^\mu(r) &= \left[ -\frac{1}{2} \frac{\partial^2}{\partial r^2} + \frac{l(l+1)}{2r^2} + V^{\mu,\text{sph}}(r) - E_{1,l} \right] r \dot{u}_{1,l}^\mu(r) = r u_{1,l}^\mu(r). \end{aligned} \quad (2.25)$$

The energy derivative  $\dot{u}_{1,l}^\mu(r)$  and the radial function  $u_{1,l}^\mu(r)$  are orthogonal and  $u_{1,l}^\mu(r)$  is normalized:

$$\begin{aligned} \int r^2 u_{1,l}^\mu(r) u_{1,l}^\mu(r) dr &= 1, \\ \int r^2 u_{1,l}^\mu(r) \dot{u}_{1,l}^\mu(r) dr &= 0, \\ \int r^2 \dot{u}_{1,l}^\mu(r) \dot{u}_{1,l}^\mu(r) dr &= N_l^\mu. \end{aligned} \quad (2.26)$$

The Hamilton operator  $\hat{H}^{\mu,\text{sph}}$  in Eq. (2.25) contains the term  $-1/2\Delta$ , which acts as operator for the kinetic energy. When we compute matrix elements we use instead a symmetrized form of the kinetic energy operator in order to obtain a Hermitian Hamiltonian matrix:

$$-\frac{1}{2} \overleftrightarrow{\Delta} \rightarrow -\frac{1}{4} \overleftarrow{\Delta} - \frac{1}{4} \overrightarrow{\Delta}, \quad (2.27)$$

where the double-arrow indicates whether the Laplace operator differentiates objects to its left or to its right. Consequently, the spherical part of Hamiltonian matrix is given by

$$\begin{aligned} H_{\mathbf{g},\mathbf{g}'}^{\mu,\text{sph}} &= \sum_L \int dr r^2 \left[ a_L^{\mu,\mathbf{g}} u_{1,l}^\mu + b_L^{\mu,\mathbf{g}} u_{1,l}^\mu \right]^* \hat{H}^{\mu,\text{sph}} \left[ a_L^{\mu,\mathbf{g}'} u_{1,l}^\mu + b_L^{\mu,\mathbf{g}'} u_{1,l}^\mu \right] \\ &= \sum_L \left[ (a_L^{\mu,\mathbf{g}})^* a_L^{\mu,\mathbf{g}'} E_{1,l} + \frac{1}{2} (a_L^{\mu,\mathbf{g}})^* b_L^{\mu,\mathbf{g}'} + \frac{1}{2} (b_L^{\mu,\mathbf{g}})^* a_L^{\mu,\mathbf{g}'} + (b_L^{\mu,\mathbf{g}})^* b_L^{\mu,\mathbf{g}'} E_{1,l} N_l^\mu \right] \end{aligned} \quad (2.28)$$

The non-spherical part of the potential is expanded into a product of radial functions and spherical harmonics:

$$V^{\mu,\text{NS}}(\mathbf{r}) = \sum_L V_L^\mu(r) Y_L(\hat{\mathbf{r}}) \quad (2.29)$$

---

<sup>1</sup>For simplicity we discuss here only the non-relativistic Schrödinger equation. In practice the radial functions are obtained as solutions of the scalar relativistic Dirac equation.

Defining the matrix elements

$$\begin{aligned}
I_{l',l,L''}^{\mu,u,u} &= \int dr r^2 u_{1,l'}^\mu u_{1,l}^\mu V_{L''}^\mu(r), \\
I_{l',l,L''}^{\mu,u,\dot{u}} &= \int dr r^2 u_{1,l'}^\mu \dot{u}_{1,l}^\mu V_{L''}^\mu(r), \\
I_{l',l,L''}^{\mu,\dot{u},u} &= \int dr r^2 \dot{u}_{1,l'}^\mu u_{1,l}^\mu V_{L''}^\mu(r), \\
I_{l',l,L''}^{\mu,\dot{u},\dot{u}} &= \int dr r^2 \dot{u}_{1,l'}^\mu \dot{u}_{1,l}^\mu V_{L''}^\mu(r)
\end{aligned} \tag{2.30}$$

and their contractions with the Gaunt coefficients (see App. A)

$$\begin{aligned}
t_{L',L}^{\mu,u,u} &= \sum_{L''} I_{l',l,L''}^{\mu,u,u} G(L', L, L''), \\
t_{L',L}^{\mu,u,\dot{u}} &= \sum_{L''} I_{l',l,L''}^{\mu,u,\dot{u}} G(L', L, L''), \\
t_{L',L}^{\mu,\dot{u},u} &= \sum_{L''} I_{l',l,L''}^{\mu,\dot{u},u} G(L', L, L''), \\
t_{L',L}^{\mu,\dot{u},\dot{u}} &= \sum_{L''} I_{l',l,L''}^{\mu,\dot{u},\dot{u}} G(L', L, L''),
\end{aligned} \tag{2.31}$$

we may write the non-spherical contribution to the Hamiltonian as follows:

$$\begin{aligned}
H_{\mathbf{g},\mathbf{g}'}^{\mu,\text{NS}} &= \sum_{L,L'} \left[ (a_{L'}^{\mu,\mathbf{g}})^* t_{L',L}^{\mu,u,u} a_L^{\mu,\mathbf{g}'} + (b_{L'}^{\mu,\mathbf{g}})^* t_{L',L}^{\mu,\dot{u},\dot{u}} b_L^{\mu,\mathbf{g}'} + \right. \\
&\quad \left. + (a_{L'}^{\mu,\mathbf{g}})^* t_{L',L}^{\mu,u,\dot{u}} b_L^{\mu,\mathbf{g}'} + (b_{L'}^{\mu,\mathbf{g}})^* t_{L',L}^{\mu,\dot{u},u} a_L^{\mu,\mathbf{g}'} \right].
\end{aligned} \tag{2.32}$$

In Eq. (2.28) and Eq. (2.32) we specified the MT-contributions to the LAPW-LAPW matrix elements. The local orbitals lead to additional LO-LO, LO-LAPW and LAPW-LO matrix elements, which are obtained analogously to the LAPW-LAPW matrix elements. The interstitial contribution to the Hamiltonian matrix is given by

$$H_{\mathbf{g},\mathbf{g}'}^{\text{INT}} = \frac{1}{V} \int_{\text{INT}} d r^3 e^{-i(\mathbf{g}+\mathbf{k})\cdot\mathbf{r}} \left( -\frac{1}{4} \overleftarrow{\Delta} - \frac{1}{4} \overrightarrow{\Delta} + V(\mathbf{r}) \right) e^{i(\mathbf{g}'+\mathbf{k})\cdot\mathbf{r}}. \tag{2.33}$$

The LAPW basis functions are not orthogonal and hence the overlap matrix  $S$  needs to be computed. The MT contributions to the overlap matrix run

$$S_{\mathbf{g},\mathbf{g}'}^\mu = \sum_L \left[ (a_L^{\mu,\mathbf{g}})^* a_L^{\mu,\mathbf{g}'} + (b_L^{\mu,\mathbf{g}})^* b_L^{\mu,\mathbf{g}'} N_l^\mu \right] \tag{2.34}$$

and the interstitial contribution is

$$S_{\mathbf{g},\mathbf{g}'}^{\text{INT}} = \frac{1}{V} \int_{\text{INT}} d r^3 e^{i(\mathbf{g}'-\mathbf{g})\cdot\mathbf{r}}. \tag{2.35}$$

### 2.1.6 The APW+lo method

An obvious advantage of the APW basis set, Eq. (2.22), over the LAPW basis set, Eq. (2.23), is that the APW basis set does not suffer from the rigidity due to imposing the constraint of continuity on the first derivative of the LAPW basis functions. Local orbitals may be used to substitute the missing variational freedom of the APW basis. The resulting basis set is called APW+lo [34]. In contrast to the local orbitals described above (and abbreviated LOs), which serve to describe semi-core states, the local orbitals for APW+lo (which are abbreviated los), are generated from the radial wave function and its energy derivative, evaluated at the same energy parameters as the APWs:

$$R_L^{lo}(\mathbf{r}) = a_L^{lo} u_{1,l}(r) + b_L^{lo} \dot{u}_{1,l}(r), \quad (2.36)$$

where the coefficient  $a_L^{lo}$  is set to one and  $b_L^{lo}$  is chosen such that  $R_L^{lo} = 0$  at the MT boundary. The resulting basis function

$$\phi_{lo}^{(\mathbf{k})}(\mathbf{r}) = \begin{cases} 0 & \mathbf{r} \in \text{INT} \\ \sum_L [a_L^{lo} u_{1,l}^\mu(r') + b_L^{lo} \dot{u}_{1,l}^\mu(r')] Y_L(\hat{\mathbf{r}}') & \mathbf{r} \in \text{MT}_\mu \end{cases} \quad (2.37)$$

exhibits a kink at the MT-boundary like the APWs. This kink contributes the term

$$\int_{\partial\text{MT}} \frac{1}{2} (\phi_{\mathbf{G}}(\mathbf{r}))^* \left( \frac{\partial \phi_{\mathbf{G}'}^{\text{MT}}}{\partial r} - \frac{\partial \phi_{\mathbf{G}'}^{\text{INT}}}{\partial r} \right) dS \quad (2.38)$$

to the kinetic energy, where the superscripts MT and INT mean that the derivatives are evaluated using the muffin-tin and the interstitial form of the basis functions, respectively, and the integration is performed on the muffin-tin surface. Using the nabla operator instead of the laplacian to express the kinetic energy in the interstitial, the interstitial contribution to the surface integral drops out:

$$-\frac{1}{2} \left[ \int_{\text{INT}} (\phi_{\mathbf{G}}(\mathbf{r}))^* \Delta \phi_{\mathbf{G}'}(\mathbf{r}) d^3 r + \int (\phi_{\mathbf{G}}(\mathbf{r}))^* \frac{\partial \phi_{\mathbf{G}'}^{\text{INT}}}{\partial r} dS \right] = \frac{1}{2} \int_{\text{INT}} (\nabla \phi_{\mathbf{G}}(\mathbf{r}))^* \nabla \phi_{\mathbf{G}'}(\mathbf{r}) d^3 r. \quad (2.39)$$

In order to calculate the MT-contribution to the kinetic energy, it is more convenient to use the laplacian. In this case the surface term from Eq. (2.38) has to be added:

$$-\frac{1}{2} \left[ \int_{\text{MT}} (\phi_{\mathbf{G}}(\mathbf{r}))^* \Delta \phi_{\mathbf{G}'}(\mathbf{r}) d^3 r + \int_{\partial\text{MT}} (\phi_{\mathbf{G}}(\mathbf{r}))^* \frac{\partial \phi_{\mathbf{G}'}(\mathbf{r})}{\partial r} dS \right]. \quad (2.40)$$

### 2.1.7 Non-Collinear Magnetism

The density matrix  $\boldsymbol{\rho}(\mathbf{r})$  corresponding to the density  $n(\mathbf{r})$  and the vector spin-density  $\mathbf{m}(\mathbf{r})$  is given by

$$\boldsymbol{\rho}(\mathbf{r}) = \frac{1}{2} \begin{pmatrix} n(\mathbf{r}) + m_z(\mathbf{r}) & m_x(\mathbf{r}) - im_y(\mathbf{r}) \\ m_x(\mathbf{r}) + im_y(\mathbf{r}) & n(\mathbf{r}) - m_z(\mathbf{r}) \end{pmatrix} = \frac{1}{2} [n(\mathbf{r}) \sigma_0 + \mathbf{m}(\mathbf{r}) \cdot \boldsymbol{\sigma}]. \quad (2.41)$$

Accordingly, the charge density and the components of the spin-density are obtained from the density matrix as follows:

$$\begin{aligned} n(\mathbf{r}) &= \text{Tr} [\sigma_0 \boldsymbol{\rho}(\mathbf{r})], \\ m_1(\mathbf{r}) &= \text{Tr} [\sigma_1 \boldsymbol{\rho}(\mathbf{r})], \\ m_2(\mathbf{r}) &= \text{Tr} [\sigma_2 \boldsymbol{\rho}(\mathbf{r})], \\ m_3(\mathbf{r}) &= \text{Tr} [\sigma_3 \boldsymbol{\rho}(\mathbf{r})]. \end{aligned} \quad (2.42)$$

Similarly, the potential of a non-collinear magnetic system may be written as a  $2 \times 2$  matrix:

$$\mathbf{V}(\mathbf{r}) = \begin{pmatrix} V(\mathbf{r}) + \mu_B B_z(\mathbf{r}) & \mu_B (B_x(\mathbf{r}) - iB_y(\mathbf{r})) \\ \mu_B (B_x(\mathbf{r}) + iB_y(\mathbf{r})) & V(\mathbf{r}) - \mu_B B_z(\mathbf{r}) \end{pmatrix}. \quad (2.43)$$

Within the FLAPW program FLEUR [35] non-collinear magnetism is implemented [36] using an approximation, which neglects the intra-atomic non-collinearity within the MT-spheres, i.e., only in the interstitial region the full matrix Eq. (2.43) is used and for each MT-sphere a fixed direction  $\hat{\mathbf{e}}_z^\mu$  of the exchange field is assumed. Ideally, this fixed direction  $\hat{\mathbf{e}}_z^\mu$  points in the direction of the magnetic moment of atom  $\mu$ . The exchange field inside the MT-spheres is calculated assuming a collinear spin-density  $m^\mu(\mathbf{r}')$ , which is obtained from the non-collinear spin-density  $\mathbf{m}(\mathbf{r})$  by projection onto the direction  $\hat{\mathbf{e}}_z^\mu$  of the magnetic moment:

$$m^\mu(\mathbf{r}') = \mathbf{m}(\mathbf{r}' + \boldsymbol{\tau}_\mu) \cdot \hat{\mathbf{e}}_z^\mu. \quad (2.44)$$

Clearly, this approximation has the consequence that the potential is not continuous at the MT-sphere boundary in general. In each MT-sphere a local coordinate system (see App. B) is introduced with the  $z$ -axis pointing in the direction  $\hat{\mathbf{e}}_z^\mu$  of the magnetic moment. The local coordinate system is used for the representation of the spin degrees of freedom in the MT-sphere. Concerning the position degrees of freedom only one coordinate system is used everywhere in space.

## 2.2 Dynamical Mean-Field Theory

Predictions of spectral properties, e.g. the gap of insulating materials, derived from density functional theory are usually much less satisfactory than predictions of e.g. structural properties. For weakly correlated materials spectral properties may be improved to a satisfactory level by using the GW approximation, which is based on many-body perturbation theory. For strongly localized electrons, such as  $d$ - and  $f$ - electrons, the ratio of the Coulomb-repulsion to the band width may be so large, that perturbation theory fails. For these strongly correlated materials, spectral properties are predicted satisfactorily by dynamical mean-field theory [37, 38, 39, 40, 41, 42].

The Hubbard model constitutes a very simple formulation of the physics of strongly correlated fermions. Despite its simplicity, the Hubbard model can only be solved exactly in one dimension and in infinite dimensions. In infinite dimensions the many-body diagrammatics simplifies considerably leading to a local self-energy. This locality of the

self-energy allows to map the lattice problem onto a single-impurity Anderson model, which can be solved exactly. Dynamical mean-field theory is based on the assumption that a local self-energy is an accurate approximation for finite dimensional systems.

### 2.2.1 Perturbation Theory in Infinite Dimensions

In the following we consider the one-band Hubbard model on a  $d$ -dimensional hypercubic lattice with nearest neighbor hopping  $t_{ij}$  and on-site interaction  $U$ . The Hamiltonian of this model is given by

$$\hat{H} = \sum_{i,j,\sigma} t_{ij} \hat{c}_{i\sigma}^\dagger \hat{c}_{j\sigma} + U \sum_i \hat{n}_{i\uparrow} \hat{n}_{i\downarrow}. \quad (2.45)$$

While taking the limit  $d \rightarrow \infty$ , the hoppings  $t_{ij}$  have to be scaled as  $1/\sqrt{d}$  in order to keep the energy per site finite. [37] This can be seen from the behavior of the density of states

$$D_\sigma(E) = \int \frac{d^d k}{(2\pi)^d} \delta(E - \epsilon_{\mathbf{k}}) \quad (2.46)$$

in the limit  $d \rightarrow \infty$ : Assume the hoppings to be given explicitly by the expression

$$t_{ij} = \frac{t}{\sqrt{2d}}, \quad (2.47)$$

for example. In this case, the kinetic energy is given by

$$\epsilon_{\mathbf{k}} = \frac{2t}{\sqrt{2d}} \sum_{i=1}^d \cos k_i, \quad (2.48)$$

and according to the central limit theorem, the density of states, Eq. (2.46), assumes the form of a normal distribution with the mean value  $\langle \epsilon_{\mathbf{k}} \rangle = 0$  and the variance  $\langle \epsilon_{\mathbf{k}}^2 \rangle = t^2$  in the limit  $d \rightarrow \infty$ :

$$D_\sigma(E) = \frac{1}{\sqrt{2\pi t^2}} e^{-E^2/2t^2}. \quad (2.49)$$

Hence, the scaling, Eq. (2.47), ensures that the density of states remains finite as  $d \rightarrow \infty$ .

With this scaling, Eq. (2.47), the nearest-neighbor matrix elements of the non-interacting Green function

$$\mathbf{G}^0(E) = (E - \mathbf{t})^{-1} \quad (2.50)$$

behave like

$$G_{ij}^0 \propto 1/\sqrt{d} \quad (2.51)$$

in the limit  $d \rightarrow \infty$ . It can be shown that the same is true for the interacting Green function, i.e.,  $G_{ij} \propto 1/\sqrt{d}$ . Figure 2.1 shows a self-energy diagram that has three propagating lines. If  $i$  and  $j$  are nearest neighbors, this diagram scales like  $d^{-\frac{3}{2}}$ . Consider, for example, the contribution of this kind of diagram to the nearest-neighbor matrix elements of the Green function. It scales like  $d^{-\frac{3}{2}}$ , which is smaller by a factor of  $1/d$  compared to

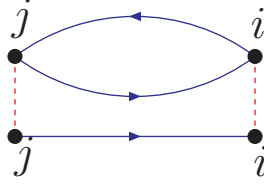


Figure 2.1: Self-energy diagram that is irrelevant in the limit  $d \rightarrow \infty$  for  $i \neq j$ .

Eq. (2.51). Consequently, this kind of diagram is irrelevant in the limit  $d \rightarrow \infty$  for  $i \neq j$ . The above argument can be extended to include all self-energy diagrams, and hence the self-energy is local in the limit  $d \rightarrow \infty$ , i.e.,

$$\Sigma_{ij} = \delta_{ij} \Sigma, \quad (2.52)$$

where translational invariance was assumed in addition.

## 2.2.2 Mapping onto the Anderson Impurity Model

Within dynamical mean-field theory the self-energy of the lattice model (e.g. the Hubbard model) is approximated by a local self-energy  $\Sigma_{\text{lat},\sigma}(E)$ . Consequently, the interacting Green function  $\mathbf{G}_{\sigma}(E)$  of the lattice model is related to the non-interacting one  $\mathbf{G}_{\sigma}^0(E)$  by the Dyson equation

$$G_{ij,\sigma}(E) = G_{ij,\sigma}^0(E) + \sum_l G_{il,\sigma}^0(E) \Sigma_{\sigma}(E) G_{lj,\sigma}(E), \quad (2.53)$$

which runs in  $k$ -space:

$$G_{\sigma}(\mathbf{k}, E) = [E - \epsilon_{\mathbf{k},\sigma} - \Sigma_{\text{lat},\sigma}(E)]^{-1}. \quad (2.54)$$

A model system, which is easier to solve than the Hubbard model, and the self-energy of which is local, is the Anderson impurity model. Mapping the Hubbard model onto the Anderson impurity model allows to determine the self-energy of the Hubbard model (within the DMFT approximation). The Hamiltonian of the Anderson impurity model is given by

$$\hat{H}_{\text{And}} = \hat{H}_0 + \hat{H}_{\text{imp}} + \hat{H}_{\text{hyb}} + \hat{H}_{\text{int}}, \quad (2.55)$$

where

$$\hat{H}_0 = \sum_{\nu,\sigma} \xi_{\nu,\sigma} \hat{c}_{\nu,\sigma}^{\dagger} \hat{c}_{\nu,\sigma} \quad (2.56)$$

describes a non-interacting fermionic bath,

$$\hat{H}_{\text{imp}} = \sum_{\sigma} \xi_{0,\sigma} \hat{d}_{\sigma}^{\dagger} \hat{d}_{\sigma} \quad (2.57)$$



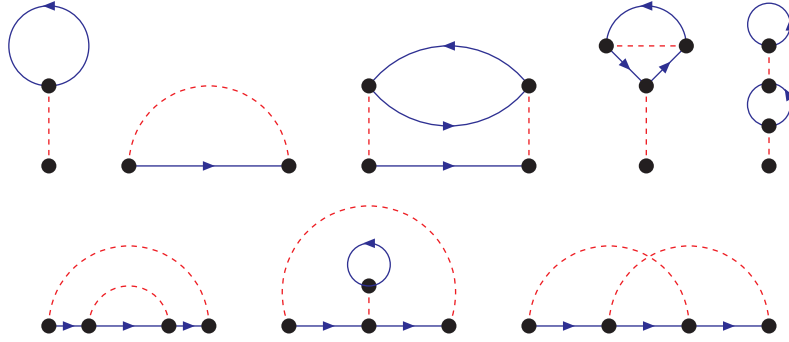


Figure 2.2: Self-energy diagrams of first and second order of the Anderson impurity model.

describes the localized level,

$$\hat{H}_{\text{hyb}} = \sum_{\nu,\sigma} (V_{\nu,\sigma}^* \hat{c}_{\nu,\sigma}^\dagger \hat{d}_\sigma + V_{\nu,\sigma} \hat{d}_\sigma^\dagger \hat{c}_{\nu,\sigma}) \quad (2.58)$$

describes the hybridization between the localized level and the bath, and

$$\hat{H}_{\text{int}} = U \hat{n}_{0,\uparrow} \hat{n}_{0,\downarrow} \quad (2.59)$$

describes the interaction at the impurity site, where  $\hat{n}_{0,\sigma} = \hat{d}_\sigma^\dagger \hat{d}_\sigma$  measures the occupation at the impurity site. For zero interaction the Green function of the impurity site may be calculated from the coupled system of equations of motion

$$\begin{aligned} (E - \xi_{0,\sigma}) \mathcal{G}_{00,\sigma}^0(E) - \sum_{\nu} V_{\nu,\sigma} \mathcal{G}_{\nu 0,\sigma}^0(E) &= 1 \\ (E - \xi_{\nu,\sigma}) \mathcal{G}_{\nu 0,\sigma}^0(E) - V_{\nu,\sigma}^* \mathcal{G}_{00,\sigma}^0(E) &= 0 \end{aligned} \quad (2.60)$$

and is given by

$$\mathcal{G}_\sigma^0(E) := \mathcal{G}_{00,\sigma}^0(E) = \frac{1}{E - \xi_{0,\sigma} - \sum_{\nu} \frac{|V_{\nu,\sigma}|^2}{E - \xi_{\nu,\sigma}}}. \quad (2.61)$$

It is related to the interacting Green function  $\mathcal{G}_\sigma(E)$  by the Dyson equation

$$(\mathcal{G}_\sigma(E))^{-1} = (\mathcal{G}_\sigma^0(E))^{-1} - \Sigma_{\text{And},\sigma}(E), \quad (2.62)$$

where  $\Sigma_{\text{And},\sigma}(E)$  is the self-energy of the impurity model. To simplify the notation we assume the Green functions and self-energies to be spin-independent in the following. Figure 2.2 shows the self-energy diagrams of the Anderson impurity model up to second order. Note that all interaction vertices in these diagrams correspond to the impurity site. Interpreting the propagating lines in the diagrams of Figure 2.2 to be given by the site-diagonal element of the non-interacting Green function of the lattice model,  $\mathbf{G}_{00}^0(E)$ , these diagrams constitute a part of the self-energy of the lattice model. Obviously, the diagrams of the

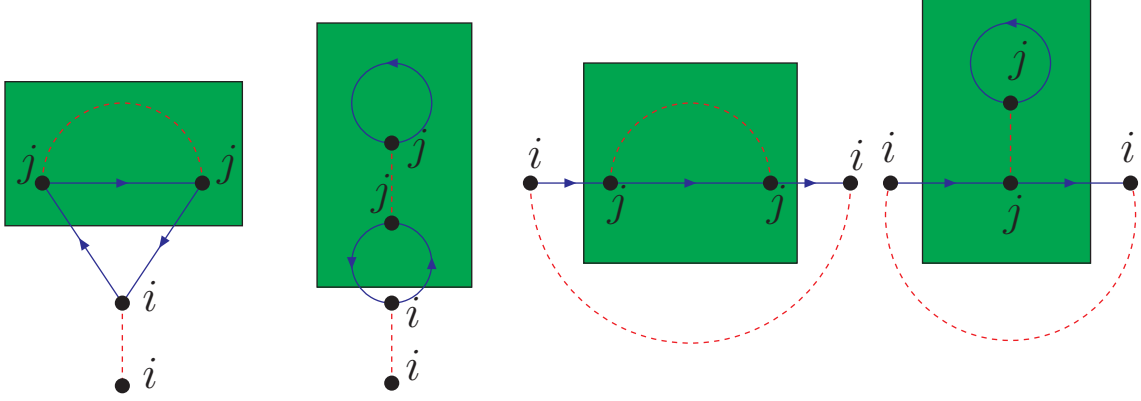


Figure 2.3: Self-energy diagrams of the lattice model, which are not contained in Figure 2.2 for  $i \neq j$ . Since the self-energy is assumed local the outer vertices correspond to the same lattice site. The green boxes contain self-energy diagrams occurring also in figure 2.2. Hence, these diagrams can be generated from the first-order diagrams in figure 2.2 by adding the term  $G_{ij}^0(E)\Sigma(E)G_{ji}^0(E)$  to the propagator of the diagrams in figure 2.2.

Hubbard model and the diagrams of the Anderson impurity model differ by the fact that in the latter case all vertices always correspond to the same site. This is why there are self-energy diagrams of the lattice model, which are not contained in figure 2.2. A few of them are shown in figure 2.3. However, by choosing an appropriate propagator for the propagating lines of the diagrams of the Anderson impurity model one can generate these missing diagrams: The diagrams in figure 2.3 can be constructed from the first order diagrams in figure 2.2 by adding the term  $G_{ij}^0(E)\Sigma(E)G_{ji}^0(E)$  to the propagating line. For  $i = j$  the diagrams in figure 2.3 already occur in figure 2.2. Consequently, to avoid overcounting of these diagrams the correct term to add to the propagating line is  $\sum_{j \neq i} G_{ij}^0(E)\Sigma(E)G_{ji}^0(E)$ . Considering all orders, one finds [38]:

$$\Sigma(E) := \Sigma_{\text{lat}}[\mathbf{G}^0](E) = \Sigma_{\text{And}}[\mathcal{G}^0](E), \quad (2.63)$$

where the propagator  $\mathcal{G}^0$  of the Anderson impurity model is connected to the non-interacting Green function  $\mathbf{G}^0$  of the Hubbard model by the Dyson equation

$$G'_{ij}(E) = G_{ij}^0(E) + \sum_k G_{ik}^0(E)\Sigma(E)(1 - \delta_{0k})G'_{kj} \quad (2.64)$$

and

$$\mathcal{G}^0(E) = G'_{00}(E). \quad (2.65)$$

The above equations allow to calculate  $\Sigma(E)$  self-consistently: One starts with a guess for  $\Sigma(E)$  and calculates  $\mathcal{G}^0(E)$  from Eqns. (2.64,2.65). Then, one solves the Anderson impurity model for this  $\mathcal{G}^0(E)$ , which yields a new  $\Sigma(E)$ . From the new  $\Sigma(E)$  a new  $\mathcal{G}^0(E)$  is calculated using again Eqns. (2.64,2.65). These steps are repeated until convergence of

the self-energy  $\Sigma(E)$  is reached. The factor  $(1 - \delta_{0k})$  in Eq. (2.64) is needed to avoid overcounting of diagrams, as explained above.

The DMFT selfconsistency condition Eqns. (2.64, 2.65) may be cast into a form more suitable for efficient numerical computations: Defining the matrix

$$\tilde{\Sigma}(E) := \Sigma(E) - \sigma(E), \quad (2.66)$$

where  $\Sigma_{ij}(E) = \delta_{ij}\Sigma(E)$  and  $\sigma_{ij}(E) = \delta_{0i}\delta_{ij}\Sigma(E)$ , the Dyson equation, Eq. (2.64), runs in matrix notation:

$$\begin{aligned} \mathbf{G}'(E) &= \mathbf{G}^0(E)[1 - \tilde{\Sigma}(E)\mathbf{G}^0]^{-1} \\ &= \mathbf{G}^0(E)[1 + [1 - \Sigma(E)\mathbf{G}^0(E)]^{-1}\sigma(E)\mathbf{G}^0(E)]^{-1}[1 - \Sigma(E)\mathbf{G}^0(E)]^{-1}. \end{aligned} \quad (2.67)$$

Using the identity

$$[1 - \Sigma(E)\mathbf{G}^0(E)]^{-1} = (\mathbf{G}^0(E))^{-1}\mathbf{G}(E) \quad (2.68)$$

and expanding the second factor in a power series yields

$$\begin{aligned} \mathbf{G}'(E) &= \mathbf{G}^0(E)[1 + (\mathbf{G}^0(E))^{-1}\mathbf{G}(E)\sigma(E)\mathbf{G}^0(E)]^{-1}(\mathbf{G}^0(E))^{-1}\mathbf{G}(E) \\ &= \mathbf{G}(E) - \mathbf{G}(E)\sigma(E)\mathbf{G}(E) + \mathbf{G}(E)\sigma(E)\mathbf{G}(E)\sigma(E)\mathbf{G}(E) - \dots, \end{aligned} \quad (2.69)$$

and hence

$$\begin{aligned} \mathcal{G}^0(E) &= G_{00}(E) - G_{00}(E)\Sigma(E)G_{00}(E) + G_{00}(E)\Sigma(E)G_{00}(E)\Sigma(E)G_{00}(E) - \dots \\ &= G_{00}(E)[1 + \Sigma(E)G_{00}(E)]^{-1}. \end{aligned} \quad (2.70)$$

This is equivalent to

$$(\mathcal{G}^0(E))^{-1} = (G_{00}(E))^{-1} + \Sigma(E). \quad (2.71)$$

Comparing this formulation of the DMFT self-consistency condition with Eq. (2.62) one finds that its meaning is

$$\mathcal{G}(E) = G_{00}(E), \quad (2.72)$$

i.e., equality between the interacting Green function of the Anderson impurity model and the site diagonal elements of the interacting Green function of the lattice model. In this case the self-consistency cycle could be chosen as follows: Calculate the site-diagonal element of the interacting Green function with the help of Eq. (2.54) and the (old) self-energy, i.e.,

$$G_{00}(E) = \sum_{\mathbf{k}} [E - \epsilon_{\mathbf{k}} - \Sigma(E)]^{-1}. \quad (2.73)$$

Calculate  $\mathcal{G}^0(E)$  according to Eq. (2.71). Solve the Anderson impurity model for this Green function  $\mathcal{G}^0(E)$  and obtain the (new) self-energy. Iterate these steps until convergence of the self-energy is achieved.

### 2.2.3 Exact Diagonalization

The quantum impurity problem may be solved in various ways: Density matrix renormalization group (DMRG), iterated perturbation theory (IPT), non-crossing approximation (NCA), exact diagonalization (ED), numerical renormalization group (NRG) and quantum Monte Carlo (QMC) are the most popular methods. In the following we discuss the use of exact diagonalization to solve the quantum impurity problem, which is conceptually a particularly simple way to do this. To simplify the notation, we discuss only the one-band case. Within the ED approach, the impurity site is coupled to a finite cluster of bath sites. The non-interacting Green function of the impurity site coupled to the cluster is given by

$$\mathcal{G}_{\text{cl}}^0(i\omega_n) = \left( i\omega_n + \mu - \sum_j \frac{|t_j|^2}{i\omega_n + \mu - \epsilon_j} \right)^{-1} \quad (2.74)$$

on the Matsubara axis, where  $t_j$  is the hopping from the bath site  $j$  to the impurity site and  $\epsilon_j$  is the energy of the bath level  $j$ . The hoppings  $t_j$  and the bath site energies  $\epsilon_j$  are chosen such that the deviation  $\Delta$ ,

$$\Delta = \sum_n |\mathcal{G}^0(i\omega_n) - \mathcal{G}_{\text{cl}}^0(i\omega_n)|^2, \quad (2.75)$$

from  $\mathcal{G}^0(i\omega_n)$ , as obtained from Eq. (2.71), is minimized. The hoppings  $t_j$ , the bath site energies  $\epsilon_j$  and the Coulomb interaction  $U$  on the impurity site define the many-body Hamiltonian. This Hamiltonian conserves the number of particles with spin up,  $n_\uparrow$ , and the number of particles with spin down,  $n_\downarrow$ . Consequently, it may be diagonalized for given particle numbers  $n_\uparrow$  and  $n_\downarrow$ . The thermal Green function of the impurity is defined by

$$G_\sigma(\tau, \tau') = -\langle T_\tau \hat{d}_\sigma(\tau) \hat{d}_\sigma^\dagger(\tau') \rangle, \quad (2.76)$$

where  $\hat{d}_\sigma$  and  $\hat{d}_\sigma^\dagger$  denote annihilation and creation operators at the impurity site in the imaginary-time Heisenberg representation, respectively:

$$\begin{aligned} \hat{d}_\sigma(\tau) &= e^{(\hat{H} - \mu \hat{N})\tau} \hat{d}_\sigma e^{-(\hat{H} - \mu \hat{N})\tau}, \\ \hat{d}_\sigma^\dagger(\tau) &= e^{(\hat{H} - \mu \hat{N})\tau} \hat{d}_\sigma^\dagger e^{-(\hat{H} - \mu \hat{N})\tau}. \end{aligned} \quad (2.77)$$

Defining the partition function  $\Xi$  as

$$\Xi = \text{Tr}[e^{-\beta(\hat{H} - \mu \hat{N})}], \quad (2.78)$$

the thermal average  $\langle \hat{\mathcal{O}} \rangle$  of any operator  $\hat{\mathcal{O}}$  is given by

$$\langle \hat{\mathcal{O}} \rangle = \frac{1}{\Xi} \text{Tr}[e^{-\beta(\hat{H} - \mu \hat{N})} \hat{\mathcal{O}}]. \quad (2.79)$$

The above traces are performed in Fock space. The thermal Green function  $G_\sigma(\tau, \tau')$  depends only on the difference between times  $\tau$  and  $\tau'$ :

$$G_\sigma(\tau, \tau') = G_\sigma(\tau - \tau', 0) = G_\sigma(0, \tau' - \tau) =: G_\sigma(\tau - \tau'). \quad (2.80)$$

Denoting the  $i$ -th eigenvector of  $\hat{H} - \mu\hat{N}$  that has  $n_\uparrow$  electrons with spin up and  $n_\downarrow$  electrons with spin down by  $|n_\uparrow, n_\downarrow, i\rangle$  and the corresponding eigenvalue by  $E_{n_\uparrow, n_\downarrow, i}$  one may write

$$G_\uparrow(\tau) = - \sum_{n_\uparrow, n_\downarrow} \sum_{i, j} e^{-\beta E_{n_\uparrow, n_\downarrow, i}} e^{(E_{n_\uparrow, n_\downarrow, i} - E_{n_\uparrow+1, n_\downarrow, j})\tau} \times \quad (2.81)$$

$$\times \langle n_\uparrow, n_\downarrow, i | d_\uparrow | n_\uparrow+1, n_\downarrow, j \rangle \langle n_\uparrow+1, n_\downarrow, j | d_\uparrow^\dagger | n_\uparrow, n_\downarrow, i \rangle$$

for the spin-up component of the thermal Green function of the impurity site. The expression for the spin-down component is analogous. The occupancies are given by

$$n_\sigma = 1 + G_\sigma(0). \quad (2.82)$$

The solution of the many-body cluster Hamiltonian yields the self-energy

$$\Sigma_\sigma(E) = (\mathcal{G}_{\text{cl}, \sigma}^0(E))^{-1} - (G_\sigma(E))^{-1}. \quad (2.83)$$

This self-energy may be used to obtain a new lattice Green function according to Eq. (2.73). From the new lattice Green function a new non-interacting Green function is obtained using Eq. (2.71). Minimizing the deviation  $\Delta$ , Eq. (2.75), yields a new set of parameters of the cluster many-body Hamiltonian, which closes the self-consistency cycle.



## Chapter 3

# Ballistic Transport and Beyond

A typical setup of a transport junction is shown in Fig. 3.1: By means of a voltage source a voltage difference is established between the *left reservoir*  $L$  and the *right reservoir*  $R$ . The left and right reservoirs are connected by the central *scattering region*  $\Omega$ , which gives rise to a current flow. In reality, this setup can be used to model a *tunnel junction* in order to investigate the TMR-effect theoretically. Also, it may be used to investigate the GMR-effect in an *all-metallic junction*. We assume that the system is periodic in the  $X$ - and  $Y$ -directions everywhere. Additionally, we assume a *local periodicity* also in  $Z$ -direction in the left and right reservoirs,  $L$  and  $R$ . The latter assumption can be justified as follows for *idealized homogeneous* reservoirs  $L$  and  $R$ : As  $L$  and  $R$  are far away from the central scattering region  $\Omega$  and the regions where the device is connected to the voltage supply,  $LSR$  and  $RSR$ , the charge density in  $L$  and  $R$  is almost identical to the one of perfect crystals of the respective reservoir materials. Consequently, also the Kohn-Sham effective potential is almost perfectly bulk-like everywhere in  $L$  and  $R$ . The *local periodicity* of the reservoirs greatly simplifies the calculation of the transport properties of the system, because the incident wave function of an electron incident from left (right) in  $L$  ( $R$ ) may be determined from a single unit cell of  $L$  ( $R$ ). Likewise the channels accessible to the transmitted and reflected electrons may be calculated from a single unit cell each. In chapter 4 we will see that this means that the *embedding potential* may be calculated from a single unit cell.

In order to calculate the electronic transport properties for this example, usually one more step of idealization is performed: The reservoirs  $L$  and  $R$  are assumed to be *semi-infinite* and periodic and the voltage difference between the left and right reservoirs is taken into account by using two different Fermi energies,  $E_{F,l}$  and  $E_{F,r}$ , for left- and right-going scattering states, respectively, as shown in Fig. 3.2. In contrast to the setup of Fig. 3.1, where a *stationary* current is only possible in the presence of *dissipation*, this latter description has the advantage that there is no conceptual need to include dissipation explicitly in the calculation.

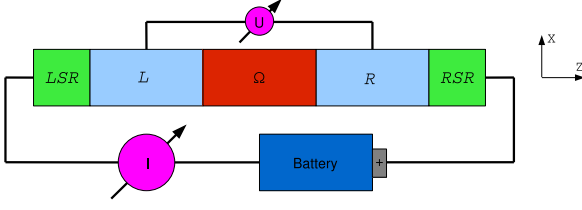


Figure 3.1: Typical setup to measure electronic transport. An electron current  $I$  flows from the left reservoir  $L$  to the right reservoir  $R$  through the central scattering region  $\Omega$ . A voltage difference  $U$  between the reservoirs is associated with the current flow.

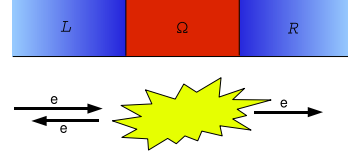


Figure 3.2: Typical setup to calculate electronic transport: The reservoirs  $L$  and  $R$  are semi-infinite periodic and the Fermi energy  $E_{F,l}$  in the left reservoir is higher than the Fermi energy  $E_{F,r}$  in the right reservoir. In the energy window  $[E_{R,r}, E_{F,l}]$  only scattering states going from  $L$  to  $R$  are occupied.

## 3.1 Ballistic Transport

In the following we discuss general properties regarding the transport of non-interacting electrons moving subject to a potential, which is constant in time. We describe the electrons by single-particle wave functions with well-defined energies. The usefulness of this strongly simplified picture for realistic electron transport, where the interaction of the electrons cannot be neglected, is discussed at the end of this section.

### 3.1.1 The Conductance Quantum

Consider the case where LR, RR and CSR all consist of the same metal and where CSR is an atomic wire with a cross-section of a few or even only one bulk unit cells. We would like to calculate the *conductance* per unit cell through the atomic wire. At first we assume that there is only a single band, with dispersion  $E(k)$ . The current  $dI$  per unit cell due to the infinitesimal voltage  $dU$  between the left and right reservoirs is given by

$$dI = \frac{1}{L} \frac{dN}{dE} v_G dU, \quad (3.1)$$

where  $L$  is the length of one unit cell in the direction of current flow.  $dN/dE$  and  $v_G$  are the density of states and the group velocity, respectively, associated with the single band. Consequently, the conductance per unit cell of the atomic wire is

$$\Gamma(E) = \frac{dI}{dU} = \frac{1}{L} \frac{dN}{dE} v_G. \quad (3.2)$$

Inserting the definition of the group velocity,

$$v_G = \frac{dE(k)}{dk}, \quad (3.3)$$



and the following identity for the density of states

$$\frac{dN}{dE} = \frac{L}{2\pi} \frac{dk}{dE} \quad (3.4)$$

one obtains

$$\Gamma(E) = \frac{1}{2\pi} \quad (3.5)$$

as the conductance of a single band. If  $\nu(E)$  is the number of bands at the energy  $E$ , the conductance  $\Gamma(E)$  of the atomic wire is simply an integer multiple of  $1/(2\pi)$ :

$$\Gamma(E) = \frac{\nu(E)}{2\pi}, \quad (3.6)$$

Assuming spin-degeneracy, the conductance is an integer multiple of  $1/\pi = 2e^2/h$ . The quantity  $2e^2/h$  is known as the *conductance quantum*. Its value in SI-units is  $2e^2/h \approx 77.5\mu\text{S} \approx 1/(12.9k\Omega)$ . At first glance it might appear surprising that the conductance of an atomic wire at zero temperature is not infinite, as one would expect for a perfect crystal at absolute zero. The solution to this puzzle is that the resistance is generated by the *contacts* of the wire with the reservoirs. Thus, the origin of the resistance is not the volume of the atomic wire but the *interfaces* to the reservoirs. In fact, for Eq. (3.6) to hold, it is crucial to measure the voltage drop between the reservoirs and not along the atomic wire itself.

### 3.1.2 Landauer Formulation of Ballistic Transport

We now consider the case of a general scattering region SRC in Fig. 3.2 and also the reservoirs  $L$  and  $R$  may be composed of different metals. The assumption of *local periodicity* in  $Z$ -direction in  $L$  and  $R$  allows us to use bulk states  $\psi_{L,\nu}^{(\bar{\mathbf{k}})}(E)$  and  $\psi_{R,\nu}^{(\bar{\mathbf{k}})}(E)$  as basis sets in  $L$  and  $R$ , respectively. We label the bulk states at energy  $E$  by a *two-dimensional*  $\bar{\mathbf{k}}$ -vector and the band-index  $\nu$ . In general the Bloch state  $\psi_{L,\nu}^{(\bar{\mathbf{k}})}(E)$  incident from the left reservoir  $L$  is transmitted as follows into the right reservoir  $R$ :

$$\Psi_{\nu}^{(\bar{\mathbf{k}})}(E, \mathbf{r}) = \sum_{\nu'} t_{\nu,\nu'} \psi_{R,\nu'}^{(\bar{\mathbf{k}})}(E, \mathbf{r}), \quad (3.7)$$

where  $t_{\nu,\nu'}$  are the *transmission coefficients* and the  $\nu'$ -summation includes both *right-going Bloch* and *right-decaying evanescent* states of  $R$ . The state  $\Psi_{\nu}^{(\bar{\mathbf{k}})}(E, \mathbf{r})$  contributes the following conductance per unit cell:

$$\Gamma_{\nu}^{(\bar{\mathbf{k}})}(E) = \frac{e^2}{h} \sum_{\nu'} |t_{\nu,\nu'}|^2 \theta_{\nu'}^{\text{B,R}}, \quad (3.8)$$

where  $\theta_{\nu'}^{\text{B,R}}$  is equal to one for a right-going Bloch state in  $R$  and zero otherwise. Summing over the incident Bloch states of the left reservoir we obtain

$$\Gamma^{(\bar{\mathbf{k}})}(E) = \frac{e^2}{h} \sum_{\nu,\nu'} |t_{\nu,\nu'}|^2 \theta_{\nu'}^{\text{B,R}} \theta_{\nu}^{\text{B,L}}, \quad (3.9)$$

where  $\theta_{\nu}^{B,L}$  is equal to one for a right-going Bloch state in  $L$  and zero otherwise. In order to obtain the transmission coefficients  $t_{\nu,\nu'}$  one has to solve the quantum mechanical scattering problem for the system composed of left lead  $L$ , scattering region  $\Omega$  and right lead  $R$ .

### 3.1.3 Calculation of electronic transport within ground-state DFT

If the exact exchange-correlation potential was known, ground-state density-functional theory would allow to calculate the density of the ground state exactly. In practice, very good approximations of the exchange-correlation potential are available. Thus, it is tempting to apply the single-particle picture of electronic transport described in the preceding subsections to the Kohn-Sham reference system of non-interacting particles. However, in contrast to the charge-density, there is no theorem relating the current in the interacting many-particle system to the current calculated in the Kohn-Sham reference system. Nevertheless, the vast majority of electronic transport calculations of realistic junctions have been performed exactly this way, despite the lack of a solid theoretical foundation. Even if the exact exchange-correlation potential was known and even in the limit of zero bias this procedure is an approximation. Unfortunately, it is very difficult to estimate the error due to this approximation. However, one finds empirically, that qualitative predictions based on ground-state DFT of trends in transport junctions are often correct, while quantitative agreement between theory and experiment cannot be expected in general.

In order to improve the description of electronic transport beyond DFT, one may choose between two rather different routes. The first way is to replace static DFT by a dynamical DFT, i.e., time-dependent density-functional theory (TDDFT) or time-dependent current density-functional theory (TDCDFT). It can be shown [30] that within the dynamical versions of DFT the many-body total current is equal to the calculated one-electron total current. Thus, the dynamical DFTs offer a solid theoretical framework to tackle the problem of electron transport. Like in the case of static DFT, the major difficulties concern finding a powerful exchange correlation potential. However, this is more difficult in the case of dynamical DFTs. Very often simply the exchange correlation potential of static DFT is used, which in many cases does not lead to significant improvements in comparison to static DFT calculations. The second way is to give up the single particle picture of transport and to perform a many-body calculation. This is usually done within the framework of the non-equilibrium Green function (NEGF) formalism to be presented in the next section.

## 3.2 NEGF Formalism

At zero temperature the Green function is defined as

$$G(t_1, t_2) = -i\langle T[\hat{A}(t_1)\hat{B}(t_2)] \rangle, \quad (3.10)$$

where  $\hat{A}(t_1)$  and  $\hat{B}(t_2)$  are Heisenberg operators and  $T$  is the time-ordering operator. Suppose the Hamilton operator of the system is

$$\hat{H}(t) = \hat{H}_0 + \hat{V}(t), \quad (3.11)$$

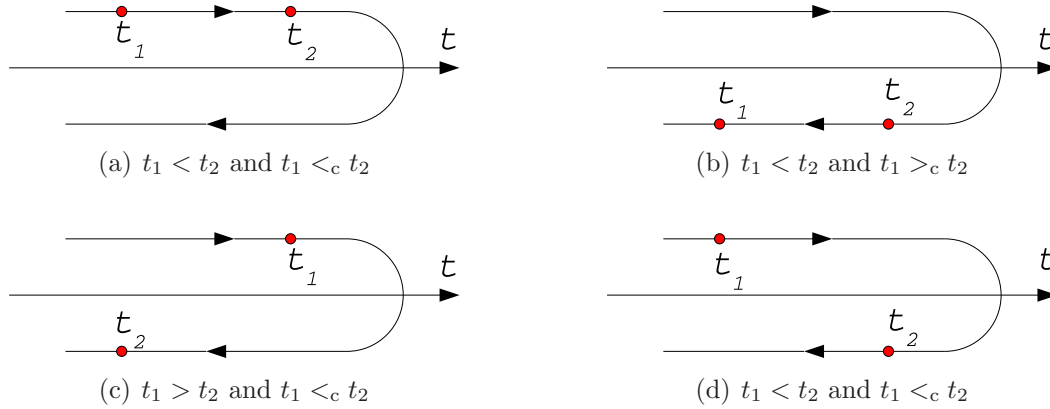


Figure 3.3: “Closed time path” contour of the NEGF formalism. Each point on the contour belongs either to the upper branch or the lower branch. (a) For two points on the upper branch contour-ordering  $<_c$  is equivalent to time-ordering  $<$ . (b) For both points on the lower branch contour-ordering is equivalent to anti-time-ordering. (c),(d) For one point on the upper branch and one point on the lower branch the point on the lower branch is always ahead with respect to contour-ordering irrespective of time-order.

where  $\hat{V}(t)$  is a perturbation and the exact eigenstates of  $\hat{H}_0$  are known. In order to calculate the Green function perturbatively, it is convenient to use the interaction picture. Within the interaction picture, the operators are

$$\begin{aligned}\hat{A}_I(t) &= \exp\left(i\hat{H}_0(t-t_0)\right) \hat{A} \exp\left(-i\hat{H}_0(t-t_0)\right) \Big|_{t_0=-\infty}, \\ \hat{B}_I(t) &= \exp\left(i\hat{H}_0(t-t_0)\right) \hat{B} \exp\left(-i\hat{H}_0(t-t_0)\right) \Big|_{t_0=-\infty}\end{aligned}\quad (3.12)$$

and the Green function is

$$G(t_1, t_2) = -i\langle \hat{S}^\dagger T[\hat{A}_I(t_1)\hat{B}_I(t_2)\hat{S}] \rangle, \quad (3.13)$$

where the  $\hat{S}$ -operator is defined as follows:

$$\hat{S} = T \exp\left(-i \int_{-\infty}^{\infty} \hat{V}_I(t') dt'\right). \quad (3.14)$$

We first consider the case of an interacting many-body system in equilibrium, i.e., a static perturbation  $\hat{V}$ , which we switch on adiabatically:

$$\hat{V}_I(t) = \hat{V}_0 e^{-|t|\eta}, \quad (3.15)$$

where  $\eta$  is a small positive quantity, and the limit  $\eta \rightarrow 0$  is considered at the end of the calculation. Denoting the ground state of  $\hat{H}_0$  as  $|0\rangle$  we know that

$$\begin{aligned}\hat{S}|0\rangle &= e^{i\varphi}|0\rangle, \\ \langle 0|\hat{S}^\dagger &= \langle 0|e^{-i\varphi},\end{aligned}\quad (3.16)$$

i.e., the ground state  $|0\rangle$  develops into a state, which differs only by a phase factor. Definitely, this is only true because the interaction is switched on and off adiabatically in Eq. (3.15). This allows to rewrite Eq. (3.13) as

$$G(t_1, t_2) = -i \frac{\langle 0 | T[\hat{A}_I(t_1) \hat{B}_I(t_2) \hat{S}] | 0 \rangle}{\langle 0 | \hat{S} | 0 \rangle}. \quad (3.17)$$

In the diagrammatic representation of Eq. (3.17) the denominator cancels exactly the disconnected diagrams of the numerator and we finally obtain the well-known result [43]:

$$G(t_1, t_2) = -i \langle 0 | T[\hat{A}_I(t_1) \hat{B}_I(t_2) \hat{S}] | 0 \rangle_{\text{connected}}. \quad (3.18)$$

Clearly, in non-equilibrium situations Eq. (3.16) does not hold. Consider for example the transport setup in Fig. 3.1. Imagine an additional switch in the circuit: At times  $t < t_0$  the battery is disconnected and no current flows. At times  $t \geq t_0$  the battery is connected and a current flows. Even if we disconnect the battery again at a later time, the system will not return into its initial state. As a second example consider the excitation of a system by light. In this case the perturbation is given by a time-dependent electromagnetic field. In order for the system to reach again the state of the remote past in the remote future it would be necessary that the perturbation is ramped down in a special way. While this might be possible in special cases, in the general case it is not. However, Eq. (3.16) was used to obtain Eq. (3.17, 3.18), on which the diagrammatic expansion is based. In order to arrive at a formulation of perturbation theory for non-equilibrium systems analogous to the equilibrium case, one introduces a time-contour which starts at time  $-\infty$ , goes to time  $\infty$ , and then goes back to time  $-\infty$ . This idea dates back to Schwinger [44] and the time-contour is illustrated in Fig. 3.3. Introducing the contour order operator  $T_c$  we define the contour Green function of the complex field  $\psi(\mathbf{r}, t)$  as follows:

$$G_c(\mathbf{r}_1, t_1; \mathbf{r}_2, t_2) = -i \langle T_c[\psi(\mathbf{r}_1, t_1) \psi^\dagger(\mathbf{r}_2, t_2)] \rangle. \quad (3.19)$$

It can be shown that the contour Green function may be obtained from

$$G_c(\mathbf{r}_1, t_1; \mathbf{r}_2, t_2) = \frac{-i \langle T_c[\hat{S}' \hat{S}^i \psi(\mathbf{r}_1, t_1) \psi^\dagger(\mathbf{r}_2, t_2)] \rangle}{\langle T_c[\hat{S}' \hat{S}^i] \rangle}, \quad (3.20)$$

which has the same structure as Eq. (3.17). Consequently, a diagrammatic representation of the contour Green function is possible, which is formally analogous to the diagrammatic representation of the equilibrium Green function. The operators  $\hat{S}'$  and  $\hat{S}^i$  are time evolution operators on the time-contour.

For given *physical* times  $t_1$  and  $t_2$  there are four corresponding situations on the time-contour:

- Both times are on the upper time contour. In this case the contour Green function is equal to the time ordered Green function:

$$G_T(\mathbf{r}_1, t_1; \mathbf{r}_2, t_2) = -i \langle T[\psi(\mathbf{r}_1, t_1) \psi^\dagger(\mathbf{r}_2, t_2)] \rangle. \quad (3.21)$$

- Both times are on the lower time contour. In this case the contour Green function is equal to the anti time ordered Green function:

$$G_{\tilde{T}}(\mathbf{r}_1, t_1; \mathbf{r}_2, t_2) = -i\langle \tilde{T}[\psi(\mathbf{r}_1, t_1)\psi^\dagger(\mathbf{r}_2, t_2)] \rangle. \quad (3.22)$$

- The first time is on the lower time contour and the second time is on the upper time contour:

$$G_+(\mathbf{r}_1, t_1; \mathbf{r}_2, t_2) = i\langle [\psi^\dagger(\mathbf{r}_2, t_2)\psi(\mathbf{r}_1, t_1)] \rangle. \quad (3.23)$$

- The first time is on the upper time contour and the second time is on the lower time contour:

$$G_-(\mathbf{r}_1, t_1; \mathbf{r}_2, t_2) = -i\langle [\psi(\mathbf{r}_1, t_1)\psi^\dagger(\mathbf{r}_2, t_2)] \rangle. \quad (3.24)$$

The contour Green function  $G_c$  or, equivalently, the set of Green functions  $G_T, G_{\tilde{T}}, G_+, G_-$  are needed for the calculations within the NEGF formalism. The connection to the physical Green functions, which are needed to obtain measurable quantities, is provided by the following identities:

$$\begin{aligned} G_r &= G_- - G_{\tilde{T}}, \\ G_a &= G_+ - G_{\tilde{T}}, \\ G &= G_+ + G_-, \end{aligned} \quad (3.25)$$

where  $G_r$  is the retarded Green function,  $G_a$  is the advanced Green function and  $G$  is the causal Green function.

In order to evaluate the Dyson equation on the time contour,

$$\mathbf{G}(\tau_1, \tau_2) = \mathbf{G}^0(\tau_1, \tau_2) + \int d\tau \int d\tau' \mathbf{G}^0(\tau_1, \tau) \boldsymbol{\Sigma}(\tau, \tau') \mathbf{G}^0(\tau', \tau_2), \quad (3.26)$$

one may use the so-called Langreth's rules. The Langreth's rules for the convolution

$$\mathbf{A}(\tau_1, \tau_2) = \int d\tau \mathbf{B}(\tau_1, \tau) \mathbf{C}(\tau, \tau_2) \quad (3.27)$$

on the time contour are:

$$\begin{aligned} \mathbf{A}_-(t_1, t_2) &= \int dt [\mathbf{B}_r(t_1, t) \mathbf{C}_-(t, t_2) + \mathbf{B}_-(t_1, t) \mathbf{C}_a(t, t_2)], \\ \mathbf{A}_r(t_1, t_2) &= \int dt \mathbf{B}_r(t_1, t) \mathbf{C}_r(t, t_2). \end{aligned} \quad (3.28)$$

### 3.2.1 The Meir-Wingreen formula

Using the NEGF formalism presented above one obtains the following expression for the current through an interacting region at equilibrium:

$$I = \frac{4}{\pi} \int dE \text{Tr} [(f_L(E) \Im \boldsymbol{\Sigma}_L(E) - f_R(E) \Im \boldsymbol{\Sigma}_R(E)) \mathbf{A}(E) + i(\boldsymbol{\Sigma}_L(E) - \boldsymbol{\Sigma}_R(E)) \mathbf{G}_-(E)], \quad (3.29)$$

where  $f_L(E)$  and  $f_R(E)$  are the Fermi distribution functions of the left and right leads, respectively,  $\mathbf{A}(E)$  is the spectral function of the scattering region and  $\mathbf{\Sigma}_{L,R}(E)$  are the lead self energies, which describe the coupling of the scattering region to the leads. This expression is called Meir-Wingreen formula [45].

In general, the lesser Green function  $\mathbf{G}_-(E)$  in the Meir-Wingreen formula cannot be obtained easily by considering only the stationary situation which evolves after the current has been switched on in the past: In the general case time propagations along the NEGF time contour are needed to obtain  $\mathbf{G}_-(E)$  even when we are only interested in the stationary current. In Ref. [46] an approximation is proposed which allows to set up a closed system of equations involving only quantities of the stationary system. The approximation is based on the ansatz

$$\begin{aligned}\mathbf{\Sigma}_-(E) &= \mathbf{\Sigma}_{0,-}(E)\mathbf{\Lambda}(E), \\ \mathbf{\Sigma}_+(E) &= \mathbf{\Sigma}_{0,+}(E)\mathbf{\Lambda}(E),\end{aligned}\tag{3.30}$$

where  $\mathbf{\Lambda}(E)$  is determined from the requirement of current conservation and found to be

$$\mathbf{\Lambda}(E) = 1 + \frac{\Im \mathbf{\Sigma}_{\text{corr}}}{\Im \mathbf{\Sigma}_{0,R} + \Im \mathbf{\Sigma}_{0,L}},\tag{3.31}$$

where  $\mathbf{\Sigma}_{\text{corr}}$  is the self-energy of the scattering region in equilibrium in the presence of the many-body interaction and  $\mathbf{\Sigma}_{0,R/L}$  are the lead self-energies needed to describe non-equilibrium in the absence of many-body interactions.

Using this approximation one obtains a Landauer-like expression for the current [47]:

$$I = \frac{e}{h} \int dE (f_L(E) - f_R(E)) \text{Tr} [G^\dagger(E) \Gamma_L(E) G(E) \Gamma_R(E) \mathbf{\Lambda}(E)].\tag{3.32}$$

An efficient basis-set to implement the many-body transport formalism described above is provided by maximally localized Wannier functions, which will be discussed in chapter 10.

# Chapter 4

## The embedding method

In condensed matter theory one frequently encounters the problem of calculating the properties of *open* systems, i.e., systems which are in touch with an outside world, which one does not want to include explicitly in the calculation. Clearly, an open system can in general *interchange* particles, energy, angular momentum, etc. with its *environment*. This has the consequence that particles, energy, etc. may be *transported through* the open system, if one can distinguish between different *boundaries* of the open system.

In chapter 3 we started already the discussion on one important class of open systems: The calculation of the transport setup shown in Fig. 3.2 requires techniques to tackle open systems, since the scattering states, which carry the current, cannot be determined from the knowledge of the finite scattering region alone, but depend on the properties of the *infinite* system. The need to consider the infinite system is a consequence of the absence of periodicity in the present scattering problem, which prohibits to impose periodic boundary conditions. In order to clarify this point we consider a one-dimensional model, where an electron with energy  $E > 0$  moves in the potential

$$V(x) = \begin{cases} 0 & x < 0 \\ V_0 & 0 \leq x \leq a \\ 0 & x > a \end{cases} . \quad (4.1)$$

In order to find the scattering state corresponding to an electron coming from the left we have to determine the coefficients  $c_1$ ,  $c_2$ ,  $r$  and  $t$  in

$$\Psi(x) = \begin{cases} e^{ik_1x} + re^{-ik_1x} & x < 0 \\ c_1e^{ik_2x} + c_2e^{-ik_2x} & 0 \leq x \leq a \\ te^{ik_1x} & x > a \end{cases} \quad (4.2)$$

such that the resulting wave function  $\Psi(x)$  and its derivative are continuous at  $x = 0$  and  $x = a$ . Definitely, we only need to evaluate  $\Psi(x)$  and its derivative at  $x = 0 - \epsilon$ ,  $x = 0 + \epsilon$ ,  $x = a - \epsilon$  and  $x = a + \epsilon$  in order to establish the system of linear equations for the unknown coefficients  $c_1$ ,  $c_2$ ,  $r$  and  $t$ . Nevertheless, information about the infinite system is present already in our *ansatz*: The incoming wave  $e^{ik_1x}$ , the reflected wave  $re^{-ik_1x}$  and the

transmitted wave  $te^{ik_1x}$  correspond to the potential  $V(x)$ , Eq. (4.1). If the potential is not  $V(x)$ , but instead e.g.

$$V_1(x) = \begin{cases} -\sin^2(x) & x < 0 \\ V_0 & 0 \leq x \leq a \\ -\sin^2(x-a) & x > a \end{cases}, \quad (4.3)$$

the ansatz Eq. (4.2) is not appropriate. Even though the regions  $x < 0$  and  $x > a$  are *semi-infinite*, one can nevertheless take their effect on the wave function in the region  $0 \leq x \leq a$  into account rather easily, as we will now discuss. Let us consider again the potential  $V(x)$ , Eq. (4.1). We first consider *bound states*, i.e., we assume  $0 > E > V_0$  at first. The wave function is now

$$\Psi(x) = \begin{cases} c_0 e^{\kappa_1 x} & x < 0 \\ c_1 e^{ik_2 x} + c_2 e^{-ik_2 x} & 0 \leq x \leq a \\ c_3 e^{-\kappa_1 x} & x > a \end{cases} \quad (4.4)$$

instead of Eq. (4.2). At  $x = 0 - \epsilon$  the *logarithmic normal derivative* is

$$-\frac{d}{dx} \log \Psi(x)|_{x=0-\epsilon} = -\frac{1}{\Psi(x)} \frac{d}{dx} \Psi(x)|_{x=0-\epsilon} = -\kappa_1 \quad (4.5)$$

and at  $x = a + \epsilon$  it is likewise

$$\frac{d}{dx} \log \Psi(x)|_{x=a+\epsilon} = -\kappa_1. \quad (4.6)$$

We define the *embedding potentials*  $\Sigma_l(E)$  and  $\Sigma_r(E)$  of the left and right sides of the central region  $0 \leq x \leq a$  as  $-1/2$  times the respective logarithmic normal derivatives, i.e.,

$$\Sigma_r(E) = \Sigma_l(E) = \frac{\kappa_1}{2}(E) = \frac{\sqrt{2|E|}}{2}. \quad (4.7)$$

In section 4.1 it will be proven that with the help of the embedding potentials one can set up a Schrödinger equation for the wave function involving *only the central region*  $0 \leq x \leq a$ : The properties of the environment, which consists of the semi-infinite regions  $x < 0$  and  $x > a$ , enter this effective Schrödinger equation via the embedding potentials. Using heuristic arguments we will now set up this effective Schrödinger equation for our one-dimensional model. The wave function and its derivative have to be continuous at  $x = 0$  and  $x = a$ . Let us assume that we can enforce this by using the delta function to introduce a penalty for wave functions that violate the smoothness requirement. Concretely, we enforce smoothness on the left boundary of the central region by adding the term

$$\frac{1}{2} \delta(x) [2\Sigma_l(E) - \frac{d}{dx}] \quad (4.8)$$

to the Hamiltonian. Likewise, on the right boundary smoothness is enforced by the term

$$\frac{1}{2} \delta(x-a) [2\Sigma_r(E) + \frac{d}{dx}]. \quad (4.9)$$



Now, the complete effective Schrödinger equation for the wave function in the central region is

$$\left[ -\frac{1}{2} \frac{d^2}{dx^2} + V_0 + \frac{1}{2} \delta(x) [2\Sigma_l(E) - \frac{d}{dx}] + \frac{1}{2} \delta(x-a) [2\Sigma_r(E) + \frac{d}{dx}] \right] \Psi(x) = E\Psi(x). \quad (4.10)$$

Next, we consider the case of *scattering states*,  $E > 0$ . From the ansatz in Eq. (4.2) it is clear that we cannot proceed in the same way as for the bound states: While we know the logarithmic derivative on the right boundary of the central region, we do not know it for the left boundary, because in the left region ( $x < 0$ ) the scattering state is a superposition of an in-coming and an out-going wave and the logarithmic derivative depends on the ratio of the amplitudes of the in-coming and out-going waves, which is not known a priori. Clearly, for the *retarded Green function*, which satisfies *out-going boundary conditions*, this problem does not occur and we can formulate an effective equation for the Green function of the central region:

$$\left[ -\frac{1}{2} \frac{d^2}{dx^2} + V_0 + \frac{1}{2} \delta(x) [2\Sigma_l(E) - \frac{d}{dx}] + \frac{1}{2} \delta(x-a) [2\Sigma_r(E) + \frac{d}{dx}] \right] G(x, x') = \delta(x - x'). \quad (4.11)$$

This is an important finding, because for a realistic three dimensional scattering setup it is much easier to determine the Green function in the central region only than to solve the complete scattering problem in a single step. From now on the central region will be referred to as *embedded region*.

However, there is still one problem left: The determination of the embedding potentials is expected to be more complicated for a realistic system than for our simple model. Our model potentials,  $V(x)$  and  $V_1(x)$ , are *periodic within the semi-infinite* regions  $x < 0$  and  $x > a$ , which greatly simplifies the task of setting up the ansatz for the scattering wave function. We argued in our discussion of Fig. 3.1 at the beginning of chapter 3 that the assumption of a *local periodicity* within the reservoirs may be fulfilled also by realistic systems. If this is the case the embedding potentials may be calculated from the *complex band structure* of the reservoir materials, as will be explained below. We will see that the procedure in the general case is similar in spirit to the above treatment of our one dimensional model system.

Clearly, electronic transport is not the only case, where one encounters an *open* system. One more important example is the *surface* of a semi-infinite slab: We wish to compute the properties of the surface region and need to eliminate the semi-infinite substrate of the surface for this purpose in order to be able to tackle the problem numerically.

## 4.1 Derivation of the Embedding Method

Based on the variational principle Inglesfield [25, 48] has derived a set of equations which allow to *embed* a limited region of space (region I in Fig. 4.1) into an *environment* (region II in Fig. 4.1). The environment is taken into account implicitly via an energy-dependent non-local *embedding potential*, which is defined on the *embedding surface*  $S$ . We illustrated the

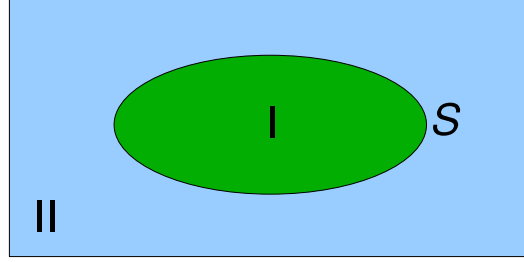


Figure 4.1: Region I is embedded into region II. The embedding surface  $S$  separates both.

principle of this method already in our discussion of the one-dimensional model of quantum transport in Eq. (4.10) and Eq. (4.11) and sketch now the derivation. In contrast to the derivations given by Inglesfield [25, 48] we pay attention to the order of operators. Thereby, we implicitly treat also the case of spin-orbit coupling and non-collinear magnetism. While we formulate the equations for a scalar potential  $V(\mathbf{r})$  to keep the notation simple, the derivation remains valid when we perform the generalization to the noncollinear case. Consequently, in order to obtain the equations in the noncollinear case, we only need to replace as follows:

$$\begin{aligned} V(\mathbf{r}) &\rightarrow V_{\sigma,\sigma'}(\mathbf{r}), \\ G(\mathbf{r}, \mathbf{r}'; E) &\rightarrow G_{\sigma,\sigma'}(\mathbf{r}, \mathbf{r}'; E), \\ \Sigma(\mathbf{r}, \mathbf{r}'; E) &\rightarrow \Sigma_{\sigma,\sigma'}(\mathbf{r}, \mathbf{r}'; E). \end{aligned} \quad (4.12)$$

#### 4.1.1 The embedding potential

Consider the wave function  $\psi(\mathbf{r})$ , which satisfies the Schrödinger equation

$$\left[ -\frac{1}{2}\Delta_{\mathbf{r}} + V(\mathbf{r}) - E \right] \psi(\mathbf{r}) = 0 \quad (4.13)$$

at energy  $E$  in regions I and II. We attempt to express  $\psi(\mathbf{r})$  in region II in terms of its boundary values on  $S$  with the help of the Green function. The Green function  $G_0(\mathbf{r}, \mathbf{r}')$  is a solution of

$$\left[ -\frac{1}{2}\Delta_{\mathbf{r}} + V(\mathbf{r}) - E \right] G_0(\mathbf{r}, \mathbf{r}') = -\delta(\mathbf{r} - \mathbf{r}') \quad (4.14)$$

and of

$$G_0(\mathbf{r}', \mathbf{r}) \left[ -\frac{1}{2}\overleftarrow{\Delta}_{\mathbf{r}} + V(\mathbf{r}) - E \right] = -\delta(\mathbf{r} - \mathbf{r}'), \quad (4.15)$$

where the arrow indicates that the Laplace operator differentiates the functions to its left side. Multiplying Eq. (4.13) from the left by  $G_0(\mathbf{r}', \mathbf{r})$  and Eq. (4.15) from the right by  $\psi(\mathbf{r})$  and integrating over region II and subtracting both we obtain

$$\psi(\mathbf{r}') = \frac{1}{2} \int_I d^3r G_0(\mathbf{r}', \mathbf{r}) \left[ \overleftarrow{\Delta}_{\mathbf{r}} - \overrightarrow{\Delta}_{\mathbf{r}} \right] \psi(\mathbf{r}). \quad (4.16)$$

Using Green's theorem it is now straightforward to express the wave function  $\Psi(\mathbf{r})$  in II in terms of the Green function in II and the boundary values of the wave function on the embedding surface  $S$ :

$$\psi(\mathbf{r}) = \frac{1}{2} \int_S d^2 r_S \left[ G_0(\mathbf{r}, \mathbf{r}_S) \frac{\partial \psi(\mathbf{r}_S)}{\partial n_S} - \frac{\partial G_0(\mathbf{r}, \mathbf{r}_S)}{\partial n_S} \psi(\mathbf{r}_S) \right], \quad (4.17)$$

where  $\mathbf{r}_S$  is a point on  $S$  and we denoted the surface normal derivative by  $\partial/\partial n_S$ :

$$\frac{\partial \psi(\mathbf{r}_S)}{\partial n_S} = \hat{\mathbf{n}}(\mathbf{r}_S) \cdot \nabla \Psi(\mathbf{r})|_{\mathbf{r}=\mathbf{r}_S}, \quad (4.18)$$

where  $\hat{\mathbf{n}}(\mathbf{r}_S)$  points outward from I into II. If we construct  $G_0(\mathbf{r}, \mathbf{r}')$  to have zero normal derivative on  $S$ , Eq. (4.17) simplifies as follows:

$$\psi(\mathbf{r}) = \frac{1}{2} \int_S d^2 r_S G_0(\mathbf{r}, \mathbf{r}_S) \frac{\partial \psi(\mathbf{r}_S)}{\partial n_S}. \quad (4.19)$$

In particular, we can use the Green function to calculate the wave function on the surface from the surface derivative of the wave function:

$$\psi(\mathbf{r}_S) = \frac{1}{2} \int_S d^2 r'_S G_0(\mathbf{r}_S, \mathbf{r}'_S) \frac{\partial \psi(\mathbf{r}'_S)}{\partial n_S}. \quad (4.20)$$

The inverse of the integration kernel in Eq. (4.20) is the *embedding potential* multiplied by (-1):

$$\Sigma(\mathbf{r}_S, \mathbf{r}'_S) = -G_0^{-1}(\mathbf{r}_S, \mathbf{r}'_S). \quad (4.21)$$

The embedding potential allows to calculate the normal derivative of the wave function from its values on  $S$  as follows

$$\hat{\mathbf{n}}(\mathbf{r}_S) \cdot \nabla \Psi(\mathbf{r})|_{\mathbf{r}=\mathbf{r}_S} = -2 \int_S d^2 r'_S \Sigma_S(\mathbf{r}_S, \mathbf{r}'_S) \psi(\mathbf{r}'_S). \quad (4.22)$$

As we did not explicitly write out the energy dependence of the Green function in this section, we point out here, that the embedding potential is energy-dependent like the Green function. We may choose  $\Sigma_S(\mathbf{r}_S, \mathbf{r}'_S)$  to correspond either to incoming or outgoing boundary conditions on  $S$ . We choose outgoing boundary conditions with respect to region I.

In the next section we will need the following identity, which involves the derivative of the embedding potential with respect to energy:

$$\int_{\text{II}} d^3 r |\psi(\mathbf{r})|^2 = - \int_S d^2 r_S \int_S d^2 r'_S (\psi(\mathbf{r}_S))^* \frac{\Sigma(\mathbf{r}_S, \mathbf{r}'_S, E)}{\partial E} \psi(\mathbf{r}'_S). \quad (4.23)$$

The volume integral on the left hand side is over the region II. Eq. (4.23) allows to calculate the overlap in region II from the boundary values on  $S$ .

### 4.1.2 Variational principle for the embedded region

We consider a wave function  $\psi(\mathbf{r})$ , which is an exact eigenfunction of the Schrödinger equation in region II with eigenvalue  $E_{\text{II}}$  and a trial function in region I. It is assumed that  $\psi(\mathbf{r})$  is continuous on the *embedding surface*  $S$ , however its first derivative may exhibit a discontinuity. Denoting the *outward normal* of region I as  $\hat{\mathbf{n}}(\mathbf{r}_S)$  and the overlap integrals of  $\psi(\mathbf{r})$  in region I and II as  $S_{\text{I}}$  and  $S_{\text{II}}$ ,

$$\begin{aligned} S_{\text{I}} &= \int_{\text{I}} d^3r \psi^*(\mathbf{r})\psi(\mathbf{r}), \\ S_{\text{II}} &= \int_{\text{II}} d^3r \psi^*(\mathbf{r})\psi(\mathbf{r}), \end{aligned} \quad (4.24)$$

the expectation value of the energy,  $E$ , of the wave function  $\psi(\mathbf{r})$  is given by

$$\begin{aligned} E &= \frac{\int d^3r \psi^*(\mathbf{r})\hat{H}\psi(\mathbf{r})}{\int d^3r \psi^*(\mathbf{r})\psi(\mathbf{r})} \\ &= \frac{\int_{\text{I}} d^3r \psi^*(\mathbf{r})\hat{H}\psi(\mathbf{r}) + E_{\text{II}}S_{\text{II}} + \frac{1}{2} \int_S d^2r_S \psi^*(\mathbf{r}_S)\hat{\mathbf{n}}(\mathbf{r}_S) \cdot [\nabla\psi(\mathbf{r}_S)|_{\text{I}} - \nabla\psi(\mathbf{r}_S)|_{\text{II}}]}{S_{\text{I}} + S_{\text{II}}}, \end{aligned} \quad (4.25)$$

where  $\mathbf{r}_S$  is a point on the embedding surface  $S$  and the surface integral in the numerator is the kinetic energy associated with kinks of the wave function on  $S$ . In order to formulate the variational principle only in terms of the wave function *inside* the embedded region I, two terms have to be reformulated: The normal derivative  $\hat{\mathbf{n}}(\mathbf{r}_S) \cdot \nabla\psi(\mathbf{r}_S)|_{\text{II}}$  in region II and the overlap  $S_{\text{II}}$ . Using Eq. (4.22) we may express the normal derivative in terms of the *embedding potential* according to

$$\hat{\mathbf{n}}(\mathbf{r}_S) \cdot \nabla\psi(\mathbf{r}_S)|_{\text{II}} = -2 \int_S d^2r'_S \Sigma_S(\mathbf{r}_S, \mathbf{r}'_S; E)\psi(\mathbf{r}'_S). \quad (4.26)$$

Furthermore, we use Eq. (4.23) to eliminate the overlap  $S_{\text{II}}$ . We finally obtain a formulation of the variational principle which only involves  $\psi(\mathbf{r})$  in region I:

$$\begin{aligned} &ES_{\text{I}} - (E - E_{\text{II}}) \int_S d^2r_S \int_S d^2r'_S (\psi(\mathbf{r}_S))^* \frac{\Sigma(\mathbf{r}_S, \mathbf{r}'_S; E_{\text{II}})}{\partial E_{\text{II}}} \psi(\mathbf{r}'_S) \\ &= \int_{\text{I}} d^3r \psi^*(\mathbf{r})\hat{H}\psi(\mathbf{r}) + \\ &+ \frac{1}{2} \int_S d^2r_S \psi^*(\mathbf{r}_S) \left[ \hat{\mathbf{n}}(\mathbf{r}_S) \cdot \nabla\psi(\mathbf{r}_S)|_{\text{I}} + 2 \int_S d^2r'_S \Sigma_S(\mathbf{r}_S, \mathbf{r}'_S; E_{\text{II}})\psi(\mathbf{r}'_S) \right]. \end{aligned} \quad (4.27)$$

In order to derive an effective Schrödinger equation for  $\psi(\mathbf{r})$ , we require the energy  $E$  to be constant under small variations of  $\psi(\mathbf{r})$ . The effective Schrödinger equation runs

$$\begin{aligned} &[E + \frac{1}{2}\Delta - V(\mathbf{r})]\psi(\mathbf{r}) - \frac{1}{2} \sum_{S=S_L, S_R} \int_S d^2r_S \delta(\mathbf{r} - \mathbf{r}_S) \times \\ &\times [2 \int_S d^2r'_S \Sigma_S(\mathbf{r}_S, \mathbf{r}'_S; E)\psi(\mathbf{r}'_S) + \mathbf{n}(\mathbf{r}_S) \cdot \nabla_{\mathbf{r}''}\psi(\mathbf{r}'')|_{\mathbf{r}''=\mathbf{r}_S}] = 0. \end{aligned} \quad (4.28)$$

Likewise, the Green function  $G(\mathbf{r}, \mathbf{r}'; E)$  of the scattering region at energy  $E$  is the solution of the integro-differential equation

$$\begin{aligned} & [E + \frac{1}{2}\Delta - V(\mathbf{r})]G(\mathbf{r}, \mathbf{r}'; E) - \frac{1}{2} \sum_{S=S_L, S_R} \int_S d^2 r_S \delta(\mathbf{r} - \mathbf{r}_S) \times \\ & \times \left[ 2 \int_S d^2 r'_S \Sigma_S(\mathbf{r}_S, \mathbf{r}'_S; E) G(\mathbf{r}'_S, \mathbf{r}'; E) + \mathbf{n}(\mathbf{r}_S) \cdot \nabla_{\mathbf{r}''} G(\mathbf{r}'', \mathbf{r}'; E)|_{\mathbf{r}''=\mathbf{r}_S} \right] = \delta(\mathbf{r} - \mathbf{r}'), \end{aligned} \quad (4.29)$$

which has a simple interpretation: The condition

$$2 \int_S d^2 r'_S \Sigma_S(\mathbf{r}_S, \mathbf{r}'_S; E) G(\mathbf{r}'_S, \mathbf{r}'; E) + \mathbf{n}(\mathbf{r}_S) \cdot \nabla_{\mathbf{r}''} G(\mathbf{r}'', \mathbf{r}'; E)|_{\mathbf{r}''=\mathbf{r}_S} = 0 \quad (4.30)$$

ensures that the Green function satisfies the correct boundary condition on the embedding surface  $S$ . This condition is enforced in Eq. (4.29) by the delta function  $\delta(\mathbf{r} - \mathbf{r}_S)$ , which is a prefactor of this condition. As is well known [49, 50] the permutation symmetry  $G(\mathbf{r}, \mathbf{r}') = G(\mathbf{r}', \mathbf{r})$  is in general not a property of the Green function and the question of the symmetries of the Green function requires additional investigation. Clearly, the following is equivalent to Eq. (4.29):

$$\begin{aligned} & G(\mathbf{r}', \mathbf{r}; E)[E + \frac{1}{2}\Delta_{\mathbf{r}} - V(\mathbf{r})] - \frac{1}{2} \sum_{S=S_L, S_R} \int_S d^2 r_S \delta(\mathbf{r} - \mathbf{r}_S) \times \\ & \times \left[ 2 \int_S d^2 r'_S G(\mathbf{r}', \mathbf{r}'_S; E) \Sigma_S(\mathbf{r}'_S, \mathbf{r}_S; E) + \mathbf{n}(\mathbf{r}_S) \cdot \nabla_{\mathbf{r}''} G(\mathbf{r}', \mathbf{r}''; E)|_{\mathbf{r}''=\mathbf{r}_S} \right] = \delta(\mathbf{r} - \mathbf{r}'). \end{aligned} \quad (4.31)$$

Interpreting the boundary term in brackets in the same fashion as Eq. (4.30) completes our knowledge on the boundary values of the Green function:

$$\begin{aligned} \mathbf{n}(\mathbf{r}_S) \cdot \nabla_{\mathbf{r}''} G(\mathbf{r}'', \mathbf{r}'; E)|_{\mathbf{r}''=\mathbf{r}_S} &= -2 \int_S d^2 r'_S \Sigma_S(\mathbf{r}_S, \mathbf{r}'_S; E) G(\mathbf{r}'_S, \mathbf{r}'; E), \\ \mathbf{n}(\mathbf{r}_S) \cdot \nabla_{\mathbf{r}''} G(\mathbf{r}', \mathbf{r}''; E)|_{\mathbf{r}''=\mathbf{r}_S} &= -2 \int_S d^2 r'_S G(\mathbf{r}', \mathbf{r}'_S; E) \Sigma_S(\mathbf{r}'_S, \mathbf{r}_S; E). \end{aligned} \quad (4.32)$$

We now consider the case where an incident wave  $\Psi_{\text{in}}(\mathbf{r})$  is scattered by region I. The full wave function is

$$\Psi(\mathbf{r}) = \Psi_{\text{in}}(\mathbf{r}) + \Psi_{\text{out}}(\mathbf{r}). \quad (4.33)$$

Using Eq. (4.17) we may express the wave function in region I in terms of the values of the

incident wave on the embedding surface,  $\Psi_{\text{in}}(\mathbf{r}_S)$ :

$$\begin{aligned}
\psi(\mathbf{r}) &= -\frac{1}{2} \int_S d^2 r_S \left[ G(\mathbf{r}, \mathbf{r}_S) \frac{\partial \psi(\mathbf{r}_S)}{\partial n_S} - \frac{\partial G(\mathbf{r}, \mathbf{r}_S)}{\partial n_S} \psi(\mathbf{r}_S) \right] = \\
&= -\frac{1}{2} \int_S d^2 r_S \left[ G(\mathbf{r}, \mathbf{r}_S) \frac{\partial \psi_{\text{in}}(\mathbf{r}_S)}{\partial n_S} - \frac{\partial G(\mathbf{r}, \mathbf{r}_S)}{\partial n_S} \psi_{\text{in}}(\mathbf{r}_S) \right] \\
&\quad - \frac{1}{2} \int_S d^2 r_S \left[ G(\mathbf{r}, \mathbf{r}_S) \frac{\partial \psi_{\text{out}}(\mathbf{r}_S)}{\partial n_S} - \frac{\partial G(\mathbf{r}, \mathbf{r}_S)}{\partial n_S} \psi_{\text{out}}(\mathbf{r}_S) \right] = \\
&= -\frac{1}{2} \int_S d^2 r_S \left[ G(\mathbf{r}, \mathbf{r}_S) \frac{\partial \psi_{\text{in}}(\mathbf{r}_S)}{\partial n_S} - \frac{\partial G(\mathbf{r}, \mathbf{r}_S)}{\partial n_S} \psi_{\text{in}}(\mathbf{r}_S) \right] = \\
&= -2i \int_S d^2 r_S d^2 r'_S G(\mathbf{r}, \mathbf{r}_S) \Im [\Sigma_S(\mathbf{r}_S, \mathbf{r}'_S; E)] \psi_{\text{in}}(\mathbf{r}'_S),
\end{aligned} \tag{4.34}$$

where we made use of

$$\Psi'_{\text{in}}(\mathbf{r}_S) = -2 \int_S d^2 r'_S \Sigma_S^*(\mathbf{r}'_S, \mathbf{r}_S; E) \Psi_{\text{in}}(\mathbf{r}'_S). \tag{4.35}$$

Note that the sign in Eq. (4.34) differs from the sign in Eq. (4.17) because  $\mathbf{r}$  is lying now inside region I and  $\hat{\mathbf{n}}(\mathbf{r}_S)$  is pointing out of region I. When writing the third equality in Eq. (4.34) we made use of

$$\begin{aligned}
&\int_S d^2 r_S \left[ G(\mathbf{r}, \mathbf{r}_S) \frac{\partial \psi_{\text{out}}(\mathbf{r}_S)}{\partial n_S} - \frac{\partial G(\mathbf{r}, \mathbf{r}_S)}{\partial n_S} \psi_{\text{out}}(\mathbf{r}_S) \right] = \\
&= \int_S d^2 r_S d^2 r'_S [G(\mathbf{r}, \mathbf{r}_S) (\Sigma(\mathbf{r}_S, \mathbf{r}'_S) \psi_{\text{out}}(\mathbf{r}'_S)) - (G(\mathbf{r}, \mathbf{r}_S) \Sigma(\mathbf{r}_S, \mathbf{r}'_S)) \psi_{\text{out}}(\mathbf{r}'_S)] = 0.
\end{aligned} \tag{4.36}$$

Summarizing, the value of Eq. (4.29) is that we may compute the Green function of the embedded region  $\Omega$  without including the environment, region II, explicitly in the calculation. However, the boundary conditions of the Green function are needed on the embedding surface  $S$ . These boundary conditions are provided indirectly by the embedding potential  $\Sigma_S(E)$ , an energy dependent non-local potential, which allows to obtain the normal derivative  $\Psi'(\mathbf{r}_S) := \hat{\mathbf{n}}(\mathbf{r}_S) \cdot \nabla \Psi(\mathbf{r})|_{\mathbf{r}=\mathbf{r}_S}$  of a wave function  $\Psi(\mathbf{r})$  on the embedding surface  $S$  with surface normal  $\hat{\mathbf{n}}(\mathbf{r}_S)$  according to

$$\Psi'(\mathbf{r}_S) = -2 \int_S d^2 r'_S \Sigma_S(\mathbf{r}_S, \mathbf{r}'_S; E) \Psi(\mathbf{r}'_S), \tag{4.37}$$

where  $\mathbf{r}_S$  is a point on the embedding surface  $S$ . The surface normal is chosen to point out of the embedded region  $\Omega$ . Evidently, the embedding potential is a *generalized logarithmic derivative* and a *Dirichlet-to-Neumann operator*. If the scattered wave function is needed in region I, it may be obtained from Eq. (4.34).

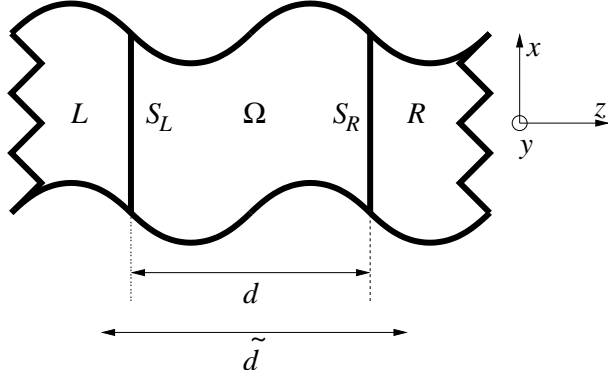


Figure 4.2: Two semi-infinite metallic leads  $L$  and  $R$  are separated by a scattering region  $\Omega$ . If a bias is applied between  $R$  and  $L$ , a current flows through the system, and transport properties may be studied. The scattering region  $\Omega$  contacts the leads at the left and the right boundaries,  $S_L$  and  $S_R$ . Translational invariance is lost in the horizontal  $z$  direction, but persists in the  $x$  and  $y$  directions. The thickness of the central scattering region is denoted  $d$ . For the expansion of wave functions and Green functions of the scattering region, plane waves are used, which are periodic in  $\tilde{d}$ .

## 4.2 Embedding within the FLAPW method

We now express the equations of the embedding formalism in terms of the FLAPW basis functions and continue the discussion of the embedding method in this basis set. To be concrete we consider the transport setup illustrated in Fig. 4.2 and work out the embedding method for this kind of system. Fig. 4.2 shows a typical transport geometry: A *central scattering region*  $\Omega$  sandwiched between two *semi-infinite metallic leads*  $L$  and  $R$ . If a bias voltage is applied between the left and right leads, a current flows through the system, and the transport properties of the system may be investigated. In-plane translational invariance is assumed. Later on we will exploit the fact that the central scattering region  $\Omega$  may be chosen to contain also several buffer layers of lead material, so that the electron density distribution in the leads,  $L$  and  $R$ , can be approximated by the corresponding bulk distribution, and the potential in the leads may be approximated by the unperturbed bulk potential.

In the present transport setup, two embedding potentials,  $\Sigma_{S_L}(E)$  and  $\Sigma_{S_R}(E)$ , are needed to impose boundary conditions on the Green function on the left and right embedding surfaces. We now recast Eq. (4.29) into a matrix equation in the space of the LAPW basis functions. In the interstitial region, the LAPW basis function  $\phi_{\mathbf{g}}^{(\bar{\mathbf{k}})}(\mathbf{r})$  is given by

$$\phi_{\mathbf{g}}^{(\bar{\mathbf{k}})}(\mathbf{r}) = \frac{1}{\sqrt{\tilde{d}A}} e^{i(\mathbf{g}+\bar{\mathbf{k}})\cdot\mathbf{r}} \quad (4.38)$$

for the present transport setup, which exhibits in-plane translational invariance. Here,  $A$  is the area of the in-plane unit cell,  $\bar{\mathbf{k}}$  is a point in the two-dimensional Brillouin zone, and  $\tilde{d}$  is the length of the normalization volume in  $z$  direction. The in-plane component of

$\mathbf{g}$ , which labels the LAPW basis functions, is a two-dimensional reciprocal lattice vector and the out of plane component of  $\mathbf{g}$  is given by  $g_{\perp} = 2\pi m/\tilde{d}$ , with  $m$  an integer. As illustrated in Fig. (4.2),  $\tilde{d}$  is larger than the length of the central region  $d$ , to enable an efficient expansion of the Green function, which is nonperiodic in  $z$ -direction. Frequently, we will refer to the volume between  $-\tilde{d}/2$  and  $\tilde{d}/2$  as  $\tilde{\Omega}$ . Clearly, the size of  $\tilde{\Omega}$  is  $\tilde{d}A$ . We expand the Green function in terms of the LAPW basis functions as follows:

$$G(\mathbf{r}, \mathbf{r}'; E) = \frac{1}{N} \sum_{\bar{\mathbf{k}}} \sum_{\mathbf{g}, \mathbf{g}'} \Phi_{\mathbf{g}}^{(\bar{\mathbf{k}})}(\mathbf{r}) (\Phi_{\mathbf{g}'}^{(\bar{\mathbf{k}})}(\mathbf{r}'))^* G_{\mathbf{g}, \mathbf{g}'}^{(\bar{\mathbf{k}})}(E), \quad (4.39)$$

where  $N$  is the number of  $\bar{\mathbf{k}}$ -points. Inserting this expansion into Eq. (4.29), multiplying with  $(\Phi_{\mathbf{g}}^{(\bar{\mathbf{k}})}(\mathbf{r}))^*$  and  $\Phi_{\mathbf{g}'}^{(\bar{\mathbf{k}})}(\mathbf{r}')$ , integrating  $\mathbf{r}$  and  $\mathbf{r}'$  over the volume of the scattering region, and simplifying, yields the following expression for the Green function matrix:

$$\mathbf{G}^{(\bar{\mathbf{k}})}(E) = [E\mathbf{S}^{(\bar{\mathbf{k}})} - \mathbf{H}^{(\bar{\mathbf{k}})} - \Sigma_{S_L}^{(\bar{\mathbf{k}})}(E) - \Sigma_{S_R}^{(\bar{\mathbf{k}})}(E)]^{-1}, \quad (4.40)$$

where the matrix elements of the overlap matrix  $\mathbf{S}^{(\bar{\mathbf{k}})}$ , the Hamiltonian matrix  $\mathbf{H}^{(\bar{\mathbf{k}})}$ , and the embedding potential matrix  $\Sigma_S^{(\bar{\mathbf{k}})}$  are given by

$$\begin{aligned} S_{\mathbf{g}, \mathbf{g}'}^{(\bar{\mathbf{k}})} &= \int_{\Omega} d^3 r (\Phi_{\mathbf{g}}^{(\bar{\mathbf{k}})}(\mathbf{r}))^* \Phi_{\mathbf{g}'}^{(\bar{\mathbf{k}})}(\mathbf{r}) \\ H_{\mathbf{g}, \mathbf{g}'}^{(\bar{\mathbf{k}})} &= \int_{\Omega} d^3 r \left[ \frac{1}{2} (\nabla \Phi_{\mathbf{g}}^{(\bar{\mathbf{k}})}(\mathbf{r}))^* \nabla \Phi_{\mathbf{g}'}^{(\bar{\mathbf{k}})}(\mathbf{r}) + (\Phi_{\mathbf{g}}^{(\bar{\mathbf{k}})}(\mathbf{r}))^* V(\mathbf{r}) \Phi_{\mathbf{g}'}^{(\bar{\mathbf{k}})}(\mathbf{r}) \right] \\ \Sigma_{S, \mathbf{g}, \mathbf{g}'}^{(\bar{\mathbf{k}})}(E) &= \int_S d^2 r_S \int_S d^2 r'_S (\Phi_{\mathbf{g}}^{(\bar{\mathbf{k}})}(\mathbf{r}_S))^* \Sigma_S(\mathbf{r}_S, \mathbf{r}'_S; E) \Phi_{\mathbf{g}'}^{(\bar{\mathbf{k}})}(\mathbf{r}'_S). \end{aligned} \quad (4.41)$$

Calculating the Green function according to Eq. (4.40) using the matrices defined in Eq. (4.41) allows to obtain for example the equilibrium charge density within the scattering volume from the density matrix

$$\rho^{(\bar{\mathbf{k}})} = -\frac{1}{\pi} \Im \int_{-\infty}^{\infty} f(E) \mathbf{G}^{(\bar{\mathbf{k}})}(E + i0^+) dE, \quad (4.42)$$

where  $f(E)$  denotes the Fermi-Dirac distribution at given Fermi energy and temperature.

### 4.3 The surface projector

We now discuss quantities defined on the embedding surface  $S$ , such as the embedding potential  $\Sigma_S(\mathbf{r}_S, \mathbf{r}'_S; E)$ . For this purpose, it is convenient, to introduce a set of basis functions  $\phi_{\bar{\mathbf{g}}}^{(\bar{\mathbf{k}})}(\mathbf{r}_S)$  defined on this surface. Specification of the explicit form of the surface basis functions  $\phi_{\bar{\mathbf{g}}}^{(\bar{\mathbf{k}})}(\mathbf{r}_S)$  is postponed to section 4.7. For a nonorthonormal set of functions  $\phi_{\bar{\mathbf{g}}}^{(\bar{\mathbf{k}})}(\mathbf{r}_S)$ , their overlap matrix elements

$$\bar{\mathbf{S}}_{S, \bar{\mathbf{g}}, \bar{\mathbf{g}}'} = \int_S d^2 r_S (\phi_{\bar{\mathbf{g}}}^{(\bar{\mathbf{k}})}(\mathbf{r}_S))^* \phi_{\bar{\mathbf{g}}'}^{(\bar{\mathbf{k}})}(\mathbf{r}_S) \quad (4.43)$$



will be needed in the following. Introducing the overlap  $\tilde{\mathbf{P}}_S$  of the surface projection of the LAPW basis function  $\phi_{\mathbf{g}}^{(\bar{\mathbf{k}})}(\mathbf{r}_S)$  with the surface basis function  $\phi_{\bar{\mathbf{g}}}^{(\bar{\mathbf{k}})}(\mathbf{r}_S)$

$$\tilde{P}_{S,\bar{\mathbf{g}},\mathbf{g}} = \int_S (\phi_{\bar{\mathbf{g}}}^{(\bar{\mathbf{k}})}(\mathbf{r}_S))^* \phi_{\mathbf{g}}^{(\bar{\mathbf{k}})}(\mathbf{r}_S) d^2 r_S, \quad (4.44)$$

we define the surface projector  $\mathbf{P}_S$  onto the embedding surface  $S$ :

$$\mathbf{P}_S = (\bar{\mathbf{S}}_S)^{-1} \tilde{\mathbf{P}}_S. \quad (4.45)$$

The surface projector  $\mathbf{P}_S$  is used to obtain the expansion coefficients of the surface projection  $\Psi^{(\bar{\mathbf{k}})}(\mathbf{r}_S)$  of a wave function

$$\Psi^{(\bar{\mathbf{k}})}(\mathbf{r}) = \sum_{\mathbf{g}} \Psi_{\mathbf{g}}^{(\bar{\mathbf{k}})} \phi_{\mathbf{g}}^{(\bar{\mathbf{k}})}(\mathbf{r}) \quad (4.46)$$

with respect to the surface basis functions  $\phi_{\bar{\mathbf{g}}}^{(\bar{\mathbf{k}})}(\mathbf{r}_S)$  according to

$$\Psi^{(\bar{\mathbf{k}})}(\mathbf{r}_S) = \sum_{\mathbf{g}, \bar{\mathbf{g}}} P_{S,\bar{\mathbf{g}},\mathbf{g}} \Psi_{\mathbf{g}}^{(\bar{\mathbf{k}})} \phi_{\bar{\mathbf{g}}}^{(\bar{\mathbf{k}})}(\mathbf{r}_S). \quad (4.47)$$

Using the matrix elements

$$\bar{\Sigma}_{S,\bar{\mathbf{g}},\bar{\mathbf{g}}'}^{(\bar{\mathbf{k}})}(E) = \int_S \int_S (\phi_{\bar{\mathbf{g}}}^{(\bar{\mathbf{k}})}(\mathbf{r}_S))^* \Sigma_S^{(\bar{\mathbf{k}})}(\mathbf{r}_S, \mathbf{r}'_S; E) \phi_{\bar{\mathbf{g}}'}^{(\bar{\mathbf{k}})}(\mathbf{r}'_S) d^2 r_S d^2 r'_S \quad (4.48)$$

of the embedding potential in the basis set of the surface wave functions  $\phi_{\bar{\mathbf{g}}}^{(\bar{\mathbf{k}})}(\mathbf{r}_S)$ , we recast the expression for the matrix elements of the embedding potential given in Eq. (4.41) as

$$\Sigma_{S,\mathbf{g},\mathbf{g}'}^{(\bar{\mathbf{k}})}(E) = \sum_{\bar{\mathbf{g}}, \bar{\mathbf{g}}'} (P_{S,\bar{\mathbf{g}},\mathbf{g}})^* \bar{\Sigma}_{S,\bar{\mathbf{g}},\bar{\mathbf{g}}'}^{(\bar{\mathbf{k}})}(E) P_{S,\bar{\mathbf{g}}',\mathbf{g}'}. \quad (4.49)$$

## 4.4 Scattering States and Conductance

For a given wave function  $\Psi^{(\bar{\mathbf{k}})}(\mathbf{r})$  the current density is given by

$$\mathbf{J}(\mathbf{r}) = \frac{1}{2i} \left[ (\Psi^{(\bar{\mathbf{k}})}(\mathbf{r}))^* \nabla \Psi^{(\bar{\mathbf{k}})}(\mathbf{r}) - \Psi^{(\bar{\mathbf{k}})}(\mathbf{r}) \nabla (\Psi^{(\bar{\mathbf{k}})}(\mathbf{r}))^* \right] \quad (4.50)$$

and the resulting currents through the embedding surfaces  $S = S_L, S_R$  are:

$$I_S = \int_S \hat{\mathbf{n}}(\mathbf{r}_S) \cdot \mathbf{J}(\mathbf{r}_S) d^2 r_S, \quad (4.51)$$

where our convention for  $\hat{\mathbf{n}}(\mathbf{r}_S)$  (pointing outward from  $\Omega$ ) implies that currents are positive, when electrons flow from  $\Omega$  into the lead contacting  $\Omega$  on  $S$ . We now assume that

the wave function  $\Psi^{(\bar{\mathbf{k}})}(\mathbf{r})$  satisfies out-going boundary conditions on  $S$ . This allows us to rewrite Eq. (4.51) as follows:

$$\begin{aligned} I_S &= i \int_S d^2 r_S \int_S d^2 r'_S \left[ (\Psi^{(\bar{\mathbf{k}})}(\mathbf{r}_S))^* \Sigma_S(\mathbf{r}_S, \mathbf{r}'_S) \Psi^{(\bar{\mathbf{k}})}(\mathbf{r}'_S) - \Psi^{(\bar{\mathbf{k}})}(\mathbf{r}_S) (\Sigma_S(\mathbf{r}_S, \mathbf{r}'_S))^* (\Psi^{(\bar{\mathbf{k}})}(\mathbf{r}'_S))^* \right] \\ &= i \int_S d^2 r_S \int_S d^2 r'_S (\Psi^{(\bar{\mathbf{k}})}(\mathbf{r}_S))^* [\Sigma_S(\mathbf{r}_S, \mathbf{r}'_S) - (\Sigma_S(\mathbf{r}'_S, \mathbf{r}_S))^*] \Psi^{(\bar{\mathbf{k}})}(\mathbf{r}'_S), \end{aligned} \quad (4.52)$$

where we made use of Eq. (4.37). As we assume both the embedding potential  $\Sigma_S(\mathbf{r}_S, \mathbf{r}'_S)$  and the wave function  $\Psi^{(\bar{\mathbf{k}})}(\mathbf{r})$  to satisfy out-going boundary conditions,  $I_S$  as given by Eq. (4.52) is positive. We may use Eq. (4.46, 4.47, 4.48) to express Eq. (4.52) in terms of the APW basis functions:

$$\begin{aligned} I_S &= i(\Psi^{(\bar{\mathbf{k}})})^\dagger \mathbf{P}_S^\dagger \left[ \overline{\Sigma}_S^{(\bar{\mathbf{k}})} - \left( \overline{\Sigma}_S^{(\bar{\mathbf{k}})} \right)^\dagger \right] \mathbf{P}_S \Psi^{(\bar{\mathbf{k}})} = \\ &= -2(\Psi^{(\bar{\mathbf{k}})})^\dagger \mathbf{P}_S^\dagger \Im \left[ \overline{\Sigma}_S^{(\bar{\mathbf{k}})} \right] \mathbf{P}_S \Psi^{(\bar{\mathbf{k}})}, \end{aligned} \quad (4.53)$$

where  $\Psi^{(\bar{\mathbf{k}})}$  is the vector of expansion coefficients of the wave function  $\Psi^{(\bar{\mathbf{k}})}(\mathbf{r})$  in the APW basis set (see Eq. (4.46)). Thus, the current through the embedding surface  $S$  may be expressed in terms of the imaginary part of the embedding potential.

Clearly, the imaginary part of the embedding potential,  $\Im \overline{\Sigma}_S^{(\bar{\mathbf{k}})}(E)$ , is a Hermitian operator and as such it may be diagonalized and all its eigenvalues are real-valued. Hence, we may write:

$$\Im \overline{\Sigma}_S^{(\bar{\mathbf{k}})}(E) = \sum_j \alpha_{S,j}^{(\bar{\mathbf{k}})}(E) \mathbf{v}_{S,j}^{(\bar{\mathbf{k}})}(E) \left( \mathbf{v}_{S,j}^{(\bar{\mathbf{k}})}(E) \right)^\dagger, \quad (4.54)$$

where  $\mathbf{v}_{S,j}^{(\bar{\mathbf{k}})}(E)$  are the normalized eigenvectors and  $\alpha_{S,j}^{(\bar{\mathbf{k}})}(E)$  are the eigenvalues. If we choose the projected wave function  $\mathbf{P}_S \Psi^{(\bar{\mathbf{k}})}$  in Eq. (4.53) to be equal to the eigenvector  $\mathbf{v}_{S,j}^{(\bar{\mathbf{k}})}(E)$  of  $\Im \overline{\Sigma}_S^{(\bar{\mathbf{k}})}(E)$ , we obtain a condition on the eigenvalue  $\alpha_{S,j}^{(\bar{\mathbf{k}})}(E)$ :

$$0 \leq I_S = -2\alpha_{S,j}^{(\bar{\mathbf{k}})}(E). \quad (4.55)$$

Consequently, the imaginary part of the embedding potential is a Hermitian negative semi-definite operator [51]. The normalized eigenvectors  $\mathbf{v}_{S,j}^{(\bar{\mathbf{k}})}(E)$  serve as a natural definition of the lead channel states. Negative eigenvalues  $\alpha_{S,j}^{(\bar{\mathbf{k}})}(E)$  correspond to open channels while zero eigenvalues correspond to closed channels.

The scattering state due to the open channel state  $j$  with energy  $E$  incident from the left is given by [51] (see also Eq. (4.34))

$$\Psi_{L,j}^{(\bar{\mathbf{k}})}(E) = 2i\alpha_{S_L,j}^{(\bar{\mathbf{k}})}(E) \mathbf{G}^{(\bar{\mathbf{k}})}(E) \mathbf{P}_{S_L}^\dagger \mathbf{v}_{S_L,j}^{(\bar{\mathbf{k}})}(E). \quad (4.56)$$

Clearly, the scattering state Eq. (4.56) is a solution of the Schrödinger equation inside  $\Omega$ :

$$\left[ E\mathbf{S}^{(\bar{\mathbf{k}})} - \mathbf{H}^{(\bar{\mathbf{k}})} - \Sigma_L^{(\bar{\mathbf{k}})}(E) - \Sigma_R^{(\bar{\mathbf{k}})}(E) \right] \Psi_{L,j}^{(\bar{\mathbf{k}})}(E) = 0. \quad (4.57)$$

Using Eq. (4.55) and the result that each open channel contributes  $1/(2\pi) = e^2/h$  (one half of the conductance quantum) to the conductance of the lead (see section 3.1.1) we may conclude that the density of states of the  $j$ -th channel,  $D_{S_{Lj}}^{(\bar{\mathbf{k}})}(E)$ , is given by

$$D_{S_{Lj}}^{(\bar{\mathbf{k}})}(E) = \frac{1}{4\pi|\alpha_{S_{Lj}}^{(\bar{\mathbf{k}})}(E)|} = \frac{e^2}{2h|\alpha_{S_{Lj}}^{(\bar{\mathbf{k}})}(E)|}. \quad (4.58)$$

Starting from Eq. (4.53) one finds that the  $\bar{\mathbf{k}}$ -resolved conductance through the scattering region due to states going from left to right is

$$\begin{aligned} \Gamma^{(\bar{\mathbf{k}})}(E) &= -2 \sum_j D_{S_{Lj}}^{(\bar{\mathbf{k}})}(E) (\Psi_{Lj}^{(\bar{\mathbf{k}})}(E))^\dagger \mathbf{P}_{S_R}^\dagger \Im \left[ \bar{\Sigma}_{S_R}^{(\bar{\mathbf{k}})}(E) \right] \mathbf{P}_{S_R} \Psi_{Lj}^{(\bar{\mathbf{k}})}(E) = \\ &= \frac{e^2}{h} \sum_j \frac{1}{\alpha_{S_{Lj}}^{(\bar{\mathbf{k}})}(E)} (\Psi_{Lj}^{(\bar{\mathbf{k}})}(E))^\dagger \mathbf{P}_{S_R}^\dagger \Im \left[ \bar{\Sigma}_{S_R}^{(\bar{\mathbf{k}})}(E) \right] \mathbf{P}_{S_R} \Psi_{Lj}^{(\bar{\mathbf{k}})}(E) = \\ &= 4 \frac{e^2}{h} \sum_j \alpha_{S_{Lj}}^{(\bar{\mathbf{k}})}(E) (\mathbf{v}_{S_{L,j}}^{(\bar{\mathbf{k}})}(E))^\dagger \mathbf{P}_{S_L} (\mathbf{G}^{(\bar{\mathbf{k}})}(E))^\dagger \mathbf{P}_{S_R}^\dagger \Im \left[ \bar{\Sigma}_{S_R}^{(\bar{\mathbf{k}})}(E) \right] \mathbf{P}_{S_R} \mathbf{G}^{(\bar{\mathbf{k}})}(E) \mathbf{P}_{S_L}^\dagger \mathbf{v}_{S_{L,j}}^{(\bar{\mathbf{k}})}(E) = \\ &= 4 \frac{e^2}{h} \text{Tr} \left[ \Im \left[ \bar{\Sigma}_{S_L}^{(\bar{\mathbf{k}})}(E) \right] \mathbf{P}_{S_L} (\mathbf{G}^{(\bar{\mathbf{k}})}(E))^\dagger \mathbf{P}_{S_R}^\dagger \Im \left[ \bar{\Sigma}_{S_R}^{(\bar{\mathbf{k}})}(E) \right] \mathbf{P}_{S_R} \mathbf{G}^{(\bar{\mathbf{k}})}(E) \mathbf{P}_{S_L}^\dagger \right]. \end{aligned} \quad (4.59)$$

In the last equality we used Eq. (4.54) to replace the spectral representation of the imaginary part of the embedding potential by the imaginary part of the embedding potential itself. Defining the surface projections of the Green function

$$\bar{\mathbf{G}}_{S,S'}^{(\bar{\mathbf{k}})}(E) = \mathbf{P}_S \mathbf{G}^{(\bar{\mathbf{k}})}(E) \mathbf{P}_{S'}^\dagger, \quad (4.60)$$

we finally obtain the following result for the conductance:

$$\Gamma^{(\bar{\mathbf{k}})}(E) = 4 \frac{e^2}{h} \text{Tr} \left[ \bar{\mathbf{G}}_{S_L,S_R}^{(\bar{\mathbf{k}})}(E) \Im \bar{\Sigma}_{S_R}^{(\bar{\mathbf{k}})}(E) (\bar{\mathbf{G}}_{S_L,S_R}^{(\bar{\mathbf{k}})}(E))^\dagger \Im \bar{\Sigma}_{S_L}^{(\bar{\mathbf{k}})}(E) \right]. \quad (4.61)$$

Various different derivations of Eq. (4.61) can be found in Refs [28, 51].

## 4.5 Transfer Matrix and Embedding Potential

The transfer matrix  $\mathbf{T}^{(\bar{\mathbf{k}})}(E)$  allows to calculate the value and the normal derivative of the wave function on the right boundary of the scattering region from the corresponding values on the left boundary of the scattering region according to

$$\begin{pmatrix} \psi_{S_R} \\ \bar{\mathbf{S}}_{S_R} \psi'_{S_R} \end{pmatrix} = \mathbf{T}^{(\bar{\mathbf{k}})}(E) \begin{pmatrix} \psi_{S_L} \\ -\bar{\mathbf{S}}_{S_L} \psi'_{S_L} \end{pmatrix}, \quad (4.62)$$

where the vectors  $\psi_S$  and  $\psi'_S$  are the coefficient vectors of the expansion of the surface projected wave function and its normal derivative in the basis of the surface wave functions on the embedding surface  $S$ . The minus sign occurs because the surface normal on the left embedding surface points to the left and not to the right. By applying Green's theorem on the scattering region, it is straightforward to show that from the Green function of the scattering region with von Neumann's boundary conditions,  $\mathbf{G}^{0(\bar{\mathbf{k}})}(E)$ , the four components of the transfer matrix of the scattering region,

$$\mathbf{T}^{(\bar{\mathbf{k}})}(E) = \begin{pmatrix} \mathbf{T}_{11}^{(\bar{\mathbf{k}})}(E) & \mathbf{T}_{12}^{(\bar{\mathbf{k}})}(E) \\ \mathbf{T}_{21}^{(\bar{\mathbf{k}})}(E) & \mathbf{T}_{22}^{(\bar{\mathbf{k}})}(E) \end{pmatrix}, \quad (4.63)$$

are calculated as follows [29, 27]:

$$\begin{aligned} \mathbf{T}_{11}^{(\bar{\mathbf{k}})} &= \bar{\mathbf{G}}_{S_R S_R}^{0(\bar{\mathbf{k}})} \left( \bar{\mathbf{G}}_{S_L S_R}^{0(\bar{\mathbf{k}})} \right)^{-1} \\ \mathbf{T}_{12}^{(\bar{\mathbf{k}})} &= \frac{1}{2} \left[ \bar{\mathbf{G}}_{S_R S_L}^{0(\bar{\mathbf{k}})} - \bar{\mathbf{G}}_{S_R S_R}^{0(\bar{\mathbf{k}})} \left( \bar{\mathbf{G}}_{S_L S_R}^{0(\bar{\mathbf{k}})} \right)^{-1} \bar{\mathbf{G}}_{S_L S_L}^{0(\bar{\mathbf{k}})} \right] \\ \mathbf{T}_{21}^{(\bar{\mathbf{k}})} &= -2 \left( \bar{\mathbf{G}}_{S_L S_R}^{0(\bar{\mathbf{k}})} \right)^{-1} \\ \mathbf{T}_{22}^{(\bar{\mathbf{k}})} &= \left( \bar{\mathbf{G}}_{S_L S_R}^{0(\bar{\mathbf{k}})} \right)^{-1} \bar{\mathbf{G}}_{S_L S_L}^{0(\bar{\mathbf{k}})}. \end{aligned} \quad (4.64)$$

Setting the embedding potentials equal to zero in Eq. (4.40) yields the Green function with von Neumann's boundary conditions, which we denote by  $\mathbf{G}^{0(\bar{\mathbf{k}})}(E)$ .

From the transfer matrix  $\mathbf{T}^{(\bar{\mathbf{k}})}(E)$  of a principal layer of a periodic system, the *complex band structure* (CBS) and the embedding potential may be calculated [27]: Let  $\mathbf{b}$  be the translation that moves a principal layer into the position of its neighboring principal layer on its right side, and  $\mathbf{U}^{(\bar{\mathbf{k}})}(\mathbf{b}_{\parallel})$  the matrix of phase shifts due to the translation in  $xy$ -direction. Then, a Bloch wave of the crystal with energy  $E$  and wave vector  $\mathbf{k} = (\mathbf{k}_{\parallel}, k_z)$  corresponds to an eigenvalue  $\lambda = e^{ib_z k_z}$  of the eigenvalue equation

$$\lambda(\psi, \psi') = \tilde{\mathbf{T}}^{(\bar{\mathbf{k}})}(\psi, \psi'), \quad (4.65)$$

where

$$\tilde{\mathbf{T}}^{(\bar{\mathbf{k}})}(E) = \mathbf{U}^{(\bar{\mathbf{k}})}(\mathbf{b}_{\parallel}) \mathbf{T}^{(\bar{\mathbf{k}})}(E). \quad (4.66)$$

Likewise, an evanescent wave with complex wave vector  $\mathbf{k} = (\mathbf{k}_{\parallel}, k_z + i\kappa_z)$  corresponds to an eigenvalue  $\lambda = e^{ib_z k_z - b_z \kappa_z}$ . If  $N_{2D}$  denotes the number of basis functions on the two-dimensional embedding surface, then the number of eigenvectors of the matrix  $\tilde{\mathbf{T}}^{(\bar{\mathbf{k}})}(E)$  is  $2N_{2D}$ . Out of these  $2N_{2D}$  eigenvectors,  $N_{2D}$  correspond to outgoing states with respect to the left side of the principal layer. From these eigenvectors the left embedding potential is calculated as

$$\bar{\Sigma}_L(E) = \Psi(\Psi')^{-1}, \quad (4.67)$$

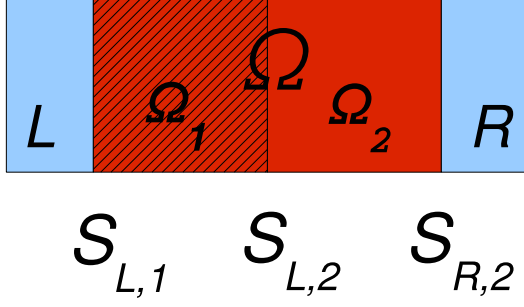


Figure 4.3: The embedded region  $\Omega$  is divided into two parts,  $\Omega_1$  and  $\Omega_2$ . The embedding surfaces of  $\Omega_2$  are  $S_{L,2}$  (on the left) and  $S_{R,2}$  (on the right).

where

$$\begin{aligned}\Psi &= [\psi_1, \dots, \psi_{N_{2D}}], \\ \Psi' &= [\psi'_1, \dots, \psi'_{N_{2D}}]\end{aligned}\tag{4.68}$$

are matrices composed of the eigenvectors. Analogously, the right embedding potential is calculated from the remaining  $N_{2D}$  eigenvectors, which are outgoing with respect to the right side of the principal layer. In section 6.3.1 we will describe an alternative calculational scheme for the embedding potential, which is due to Inglesfield [25], and prove the equivalence with the scheme described above.

## 4.6 The embedding-based order- $N$ concept

In the transport setup of Fig. 4.2, the embedding surfaces  $S_L$  and  $S_R$  may be chosen arbitrarily. Positioning them in the left and right leads, respectively, is only one possible choice. If this choice is made, the embedding potentials,  $\bar{\Sigma}_{S_L}^{(\bar{\mathbf{k}})}(E)$  and  $\bar{\Sigma}_{S_R}^{(\bar{\mathbf{k}})}(E)$ , may be calculated from a principal layer of bulk lead material, as described following Eq. (4.62). The computational effort needed to evaluate the conductance, Eq. (4.61), scales with the third power of the thickness of the region which is bounded by the embedding surfaces  $S_L$  and  $S_R$ , because the Green function has to be calculated for this region. Consequently, it is an intriguing idea to reduce the distance of the surfaces  $S_L$  and  $S_R$ , e.g. by moving the left embedding surface  $S_L$  towards the right one. As soon as the surface  $S_L$  enters the scattering region, the embedding potential  $\bar{\Sigma}_{S_L}^{(\bar{\mathbf{k}})}(E)$  starts to deviate from its value in the left lead and has to be propagated. We divide the embedding region  $\Omega$  into two parts,  $\Omega_1$  and  $\Omega_2$ , as shown in Fig. 4.3. The propagation of the left embedding potential through the region  $\Omega_1$  may be performed using the transfer matrix, Eq. (4.62), of region  $\Omega_1$ : On the initial embedding surface  $S_{L,1} = S_L$ , the normal derivative, with the surface normal pointing to the left, is given by  $-2\bar{\Sigma}_{S_{L,1}}^{(\bar{\mathbf{k}})}(E)\Psi_{S_{L,1}}^{(\bar{\mathbf{k}})}$ , while it is given by  $-2\bar{\Sigma}_{S_{L,2}}^{(\bar{\mathbf{k}})}(E)\Psi_{S_{L,2}}^{(\bar{\mathbf{k}})}$  on

the left embedding surface  $S_{L,2}$  of region  $\Omega_2$ . Entering this into Eq. (4.62) yields

$$\begin{pmatrix} \psi_{S_{L,2}} \\ 2\overline{\Sigma}_{S_{L,2}}^{(\bar{\mathbf{k}})} \psi_{S_{L,2}} \end{pmatrix} = \mathbf{T}_{\Omega_1}^{(\bar{\mathbf{k}})}(E) \begin{pmatrix} \psi_{S_{L,1}} \\ 2\overline{\Sigma}_{S_{L,1}}^{(\bar{\mathbf{k}})} \psi_{S_{L,1}} \end{pmatrix}. \quad (4.69)$$

Eliminating  $\Psi_{S_{L,1}}^{(\bar{\mathbf{k}})}$  and  $\Psi_{S_{L,2}}^{(\bar{\mathbf{k}})}$ , one obtains the following relationship between the left embedding potential on the initial surface  $S_{L,1}$  and the left embedding potential on the new surface  $S_{L,2}$ :

$$\overline{\Sigma}_{S_{L,2}}^{(\bar{\mathbf{k}})}(E) = \frac{1}{2} \left( \mathbf{T}_{21}^{(\bar{\mathbf{k}})}(E) + 2\mathbf{T}_{22}^{(\bar{\mathbf{k}})}(E)\overline{\Sigma}_{S_{L,1}}^{(\bar{\mathbf{k}})}(E) \right) \left( \mathbf{T}_{11}^{(\bar{\mathbf{k}})}(E) + 2\mathbf{T}_{12}^{(\bar{\mathbf{k}})}(E)\overline{\Sigma}_{S_{L,1}}^{(\bar{\mathbf{k}})}(E) \right)^{-1}. \quad (4.70)$$

Using the embedding potentials  $\overline{\Sigma}_{S_{L,2}}^{(\bar{\mathbf{k}})}(E)$  and  $\overline{\Sigma}_{S_{R,2}}^{(\bar{\mathbf{k}})}(E)$  of region  $\Omega_2$  we may compute the Green function of region  $\Omega_2$  and from the Green function and the embedding potentials also the conductance by applying Eq. (4.61) to region  $\Omega_2$ . As the regions  $\Omega_1$  and  $\Omega_2$  are smaller than the region  $\Omega$  the computational effort to calculate the conductance is generally smaller, if  $\Omega$  is divided into pieces as described above.

As an alternative to calculating the conductance by applying Eq. (4.61) to a region of finite thickness, it is also possible to propagate the left embedding potential further through  $\Omega_2$ , so that the left and right embedding surfaces coincide. In this case, the Green function in Eq. (4.61) is given by [52]

$$\mathbf{G}^{(\bar{\mathbf{k}})}(E) = - \left[ \overline{\Sigma}_{S_{L,3}}^{(\bar{\mathbf{k}})}(E) + \overline{\Sigma}_{S_{R,2}}^{(\bar{\mathbf{k}})}(E) \right]^{-1}, \quad (4.71)$$

where  $\overline{\Sigma}_{S_{L,3}}^{(\bar{\mathbf{k}})}(E)$  is the left embedding potential of the embedding surface  $S_{L,3}$ , which lies on top of  $S_{R,2}$ .

Instead of dividing  $\Omega$  into only two pieces, we may divide it into  $M$  layers. Using Eq. (4.70) the embedding potential  $\overline{\Sigma}_{S_L}^{(\bar{\mathbf{k}})}(E)$  may be propagated layer by layer towards the right lead until the distance to the right embedding surface  $S_R$  is only one layer. Then, the computational cost for the calculation of the conductance, Eq. (4.61), is that for a single layer. Alternatively, we may propagate the left embedding potential one layer further so that it is defined on the right embedding surface  $S_R$  of  $\Omega$ . The computational cost for the propagation of the embedding potential scales linearly with the number of layers, if the embedding potential is propagated layer by layer.

Similarly, for the self consistent calculation of the charge density a computational scheme may be devised, the computational burden of which scales linearly with the number of layers [26]. In this case, the left embedding potential is propagated layer by layer to the right side and the right embedding potential is propagated layer by layer to the left side. After this preparative step, a pair of suitable embedding potentials is available for each layer, and the charge density of each layer is evaluated using Eq. (4.42). This order- $N$  scheme for self-consistent embedding will be described in detail in chapter 7.

## 4.7 The surface projector for a curvy surface

The embedding potential and the transfer-matrix are defined on the two-dimensional embedding surface. As illustrated in Fig. 4.4, any planar embedding surface will cut MT-spheres in the general case. However, cut MT-spheres cannot be treated easily, due to the expansion of basis functions, charge density and potential in terms of spherical harmonics, as common within FLAPW. Besides these technical difficulties, one might anticipate also numerical ones due to the rapidly oscillating behavior of the wave function close to the nuclear cores. Consequently, if cutting through muffin-tins is to be avoided, the physical embedding surface is curvy in the general case.

In order to circumvent the use of curvy physical embedding planes, planar effective embedding planes have been proposed. This idea is illustrated in Fig. 4.4: Auxiliary volumes are added on both sides of the embedded region to generate planar effective boundaries. A formalism that allows to calculate effective embedding potentials, defined on the effective embedding planes, has been proposed by Ishida [53, 54]. For a planar embedding surface  $S$ , we define basis functions as follows:

$$\phi_{\bar{\mathbf{g}}}^{p(\bar{\mathbf{k}})}(\mathbf{r}_S) = \frac{1}{\sqrt{A}} e^{i(\bar{\mathbf{g}} + \bar{\mathbf{k}}) \cdot \mathbf{r}_S}, \quad (4.72)$$

where  $A$  is the area of the two-dimensional unit cell,  $\mathbf{r}_S$  is a point on the surface  $S$ ,  $\bar{\mathbf{k}}$  is a point in the two dimensional Brillouin zone, and  $\bar{\mathbf{g}}$ , which labels the basis functions, is a reciprocal lattice vector of the two-dimensional unit cell. These two-dimensional basis functions are orthonormal:

$$\int_S (\phi_{\bar{\mathbf{g}}}^{p(\bar{\mathbf{k}})}(\mathbf{r}_S))^* \phi_{\bar{\mathbf{g}}'}^{p(\bar{\mathbf{k}})}(\mathbf{r}_S) d^2 r_S = \delta_{\bar{\mathbf{g}}, \bar{\mathbf{g}}'}, \quad (4.73)$$

where the integration is over the two dimensional embedding surface  $S$ , the area of which is  $A$ . Consequently, the overlap matrix  $\bar{\mathbf{S}}_S$  defined in Eq. (4.43) is given by the unit matrix in the case of planar embedding surfaces and the choice Eq. (4.72) for the basis set. In accordance with Eq. (4.45), the projection of the LAPW basis function  $\Phi_{\mathbf{g}}^{(\bar{\mathbf{k}})}(\mathbf{r})$ , defined in Eq. (4.38), onto the embedding surface  $S$  has the expansion coefficients

$$P_{S, \bar{\mathbf{g}}, \mathbf{g}}^p = \int_S (\phi_{\bar{\mathbf{g}}}^{p(\bar{\mathbf{k}})}(\mathbf{r}_S))^* \Phi_{\mathbf{g}}^{(\bar{\mathbf{k}})}(\mathbf{r}_S) d^2 r_S = \frac{1}{\sqrt{d}} e^{i g_{\perp} z_S} \delta_{\bar{\mathbf{g}}, \mathbf{g}_{\parallel}}, \quad (4.74)$$

where  $z_S$  is the  $z$ -coordinate of the embedding plane  $S$ ,  $g_{\perp}$  is the component of  $\mathbf{g}$  normal to  $S$ , and  $\mathbf{g}_{\parallel}$  is the component of  $\mathbf{g}$  parallel to  $S$ . The matrix  $\mathbf{P}_S^p$  is the surface projector Eq. (4.45) in the case of planar embedding surfaces.

Fig. 4.4 illustrates how we choose the curvy surface: Away from MT-spheres, the curvy surface is given by a plane. Where the plane cuts the MT-spheres, it is replaced by a cup, which forms part of the surface of the MT-sphere which is cut. Concerning the set of basis functions, we opt again for plane waves, with their wave vector in the  $xy$ -plane. The

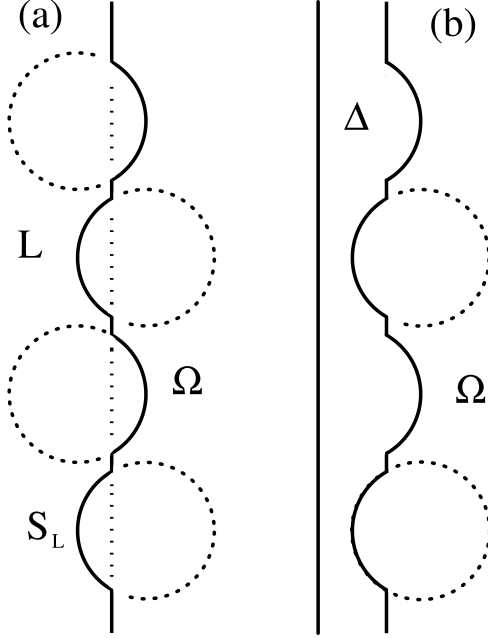


Figure 4.4: The left embedding surface  $S_L$  divides the left lead,  $L$ , from the left side of the scattering region,  $\Omega$ . a) The curvy surface (solid line) winds between the muffin-tin spheres (dotted circles) of the scattering region and those of the left lead. A planar embedding surface (dotted line) cuts the muffin-tin spheres. b) An auxiliary unphysical volume,  $\Delta$ , is added to the physical scattering region. The left boundary of the auxiliary volume is planar, which allows to use a very simple basis set for the definition of surface operators on this effective embedding plane.

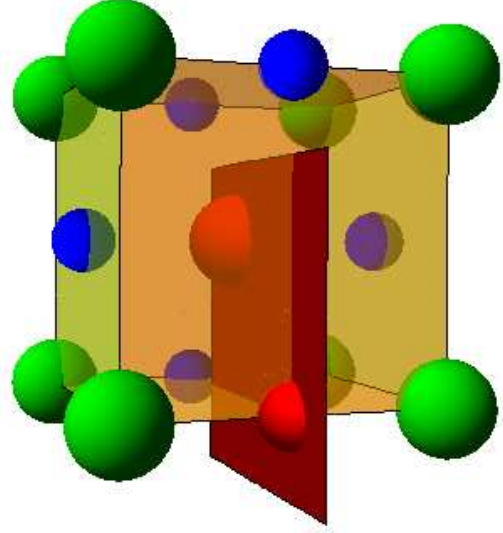


Figure 4.5: Three dimensional illustration of a curvy surface (red dividing surface). To be concrete, we chose a compound composed of two atomic species,  $A$  (green, large MT radius) and  $B$  (blue, small MT radius). Both species,  $A$  and  $B$ , are located on a bcc sub-lattice. The sublattices are displaced with respect to each other by half a lattice constant. The atom in the center belongs to species  $A$ . In the situation of the figure the curvy surface may be avoided if it is moved into the middle between adjacent atomic planes. If the radius of species  $A$  exceeds a quarter of the lattice constant, this is not possible any more. If species  $B$  is absent, we are left with a bcc structure. Usually the radius of species  $A$  exceeds a quarter of the lattice constant in this case.



mathematical expression for this curvy surface basis function

$$\phi_{\bar{\mathbf{g}}}^{c(\bar{\mathbf{k}})}(\mathbf{r}_S) = \frac{1}{\sqrt{A}} e^{i(\bar{\mathbf{g}}+\bar{\mathbf{k}})\cdot\mathbf{r}_{S,\parallel}} \quad (4.75)$$

resembles Eq. (4.72). The only difference is that  $\mathbf{r}_S$  is now defined on the curvy surface, i.e., it has in general both a component  $\mathbf{r}_{S,\parallel}$  parallel to the  $xy$  plane and a component  $r_{S,\perp}$  in  $z$  direction. In order to calculate the surface projector for the curvy embedding surface according to Eq. (4.45), we split up the surface integrations into three parts. First, we integrate over a plane. Second, we subtract the integrals over the disks, which are inside the MT-spheres cutting the plane. Third, we add the surface integrals over parts of the MT-spheres. The first contribution is given by Eq. (4.74). For the second contribution one obtains

$$I_2(\bar{\mathbf{g}}, \mathbf{g}) = -\frac{2\pi}{A\sqrt{\tilde{d}}} e^{ig_{\perp}z_S} \sum_{\mu} e^{i\bar{\mathbf{v}}\cdot\mathbf{p}_{\mu}} \frac{\bar{r}_{\mu}}{\bar{v}} J_1(\bar{r}_{\mu}\bar{v}), \quad (4.76)$$

where the position of the center of the MT-sphere of atom  $\mu$  is given by  $\mathbf{p}_{\mu}$ , and  $\bar{\mathbf{v}} = \mathbf{g}_{\parallel} - \bar{\mathbf{g}}$  is a two-dimensional reciprocal lattice vector.  $J_1$  is a cylindrical Bessel function. If we denote the radius of the MT-sphere of atom  $\mu$  by  $R_{\mu}$ , the radius of the disk that the MT-sphere cuts out of the plane is given by  $\bar{r}_{\mu} = \sqrt{R_{\mu}^2 - (z_S - p_{\mu,3})^2}$ . The expression for the third contribution is

$$I_3(\bar{\mathbf{g}}, \mathbf{g}) = \frac{2\pi}{A\sqrt{\tilde{d}}} \sum_{\mu} \int_0^{\bar{r}_{\mu}} \frac{R_{\mu}}{\sqrt{R_{\mu}^2 - r^2}} e^{i\mathbf{v}\cdot\mathbf{p}_{\mu}} r J_0(\bar{v}r) e^{ig_{\perp}\text{sig}(z_S - p_{3,\mu})\sqrt{R_{\mu}^2 - r^2}} dr, \quad (4.77)$$

where  $\mathbf{v} = \mathbf{g} - \bar{\mathbf{g}}$ , and a one dimensional integration is left over. Summing the contributions Eq. (4.74), Eq. (4.76), and Eq. (4.77), the complete expression for the overlap defined in Eq. (4.44) is given by

$$\tilde{P}_{\bar{\mathbf{g}},\mathbf{g}}^c = P_{\bar{\mathbf{g}},\mathbf{g}}^p + I_2(\bar{\mathbf{g}}, \mathbf{g}) + I_3(\bar{\mathbf{g}}, \mathbf{g}), \quad (4.78)$$

where the  $\bar{\mathbf{g}}$  and the  $\mathbf{g}$  label the basis functions on the embedding surface and the LAPW basis functions, respectively. Applying the overlap matrix  $\tilde{P}_{\bar{\mathbf{g}},\mathbf{g}}^c$  given in Eq. (4.78) onto a wave function  $\Psi^{(\bar{\mathbf{k}})}(\mathbf{r})$ , one obtains the matrix elements between the surface projection  $\Psi_S^{(\bar{\mathbf{k}})}(\mathbf{r}_S)$  of the wave function and the basis functions on the curvy surface:

$$\int_S (\phi_{\bar{\mathbf{g}}}^c(\mathbf{r}_S))^* \Psi_S^{(\bar{\mathbf{k}})}(\mathbf{r}_S) d^2 r_S = \sum_{\mathbf{g}} \tilde{P}_{\bar{\mathbf{g}},\mathbf{g}} \Psi_{\mathbf{g}}^{(\bar{\mathbf{k}})}, \quad (4.79)$$

where  $\Psi_{\mathbf{g}}^{(\bar{\mathbf{k}})}$  are the components of the wave function  $\Psi^{(\bar{\mathbf{k}})}(\mathbf{r})$  with respect to the LAPW basis set. In order to obtain an expression for the coefficients of the surface projection  $\Psi_S^{(\bar{\mathbf{k}})}(\mathbf{r}_S)$  of the wave function in terms of the basis functions on the embedding surface, one has to take account of the fact that the basis functions of the embedding surface are not orthonormal. Their overlap matrix Eq. (4.43) is given by

$$S_{\bar{\mathbf{g}},\bar{\mathbf{g}}'}^c = \sqrt{\tilde{d}} \tilde{P}_{\bar{\mathbf{g}},\bar{\mathbf{g}}'}^c = \delta_{\bar{\mathbf{g}},\bar{\mathbf{g}}'} + \sqrt{\tilde{d}} I_2(\bar{\mathbf{g}}, \bar{\mathbf{g}}') + \sqrt{\tilde{d}} I_3(\bar{\mathbf{g}}, \bar{\mathbf{g}}'). \quad (4.80)$$

Consequently, the surface projector, which yields the coefficients of the surface projection  $\Psi_S^{(\mathbf{k})}(\mathbf{r}_S)$  when applied to the wave function  $\Psi^{(\mathbf{k})}(\mathbf{r})$  is given by

$$\mathbf{P}^c = (\mathbf{S}^c)^{-1} \tilde{\mathbf{P}}^c. \quad (4.81)$$

## 4.8 An alternative expression for the curvy surface projector

In the following we discuss an alternative way to calculate the surface projector for the curvy surface. The present formulation uses the MT-representation of the wave function. We assume that the surface projector is used to calculate a current. The current densities are integrated on the curvy surface which divides the unit cell. We write the surface integral as a sum of two terms: The contribution of the MT-cups and the interstitial contribution. In order to evaluate the contribution of the MT-cup of atom  $\mu$  we use the expansion of the scattering state on the muffin-tin boundary in terms of spherical harmonics,  $F_\mu^{(\mathbf{k})}(j, E, L, s)$ , where  $j$  labels the channel,  $s$  is the spin component,  $L = (l, m)$  is the angular momentum and  $E$  is the energy. The analogous expansion of the radial derivative of the scattering state on the muffin-tin surface is denoted  $G_\mu^{(\mathbf{k})}(j, E, L, s)$ . We assume in the following that the expansion with respect to spherical harmonics is done in a coordinate frame the  $z$ -axis of which is oriented parallel to the direction of current-flow. If this is not the case, the expansions of the scattering state on the MT-sphere boundary are transformed into the coordinate frame whose  $z$ -axis points into the direction of current-flow by means of the Wigner rotation (see Appendix A):

$$\begin{aligned} F_\mu^{(\mathbf{k})}(j, E, L, s) &\rightarrow \sum_{L'} D(\mathbf{R})_{L,L'} F_\mu^{(\mathbf{k})}(j, E, L', s) \\ G_\mu^{(\mathbf{k})}(j, E, L, s) &\rightarrow \sum_{L'} D(\mathbf{R})_{L,L'} G_\mu^{(\mathbf{k})}(j, E, L', s). \end{aligned} \quad (4.82)$$

The radial components of the vector fields of the current ( $j^0$ ) and spin-current ( $j^m, m = 1, 2, 3$ ) density due to channel  $j$  on the muffin-tin boundary are given by

$$\begin{aligned} \frac{\partial j_\mu^\gamma(j, E, \hat{\mathbf{r}})}{\partial E} &= \frac{1}{2i} \sum_{\mathbf{k}} w_{\mathbf{k}} \sum_{L,L',L''} \sum_{s',s} G(L', L, L'') D_j^{(\mathbf{k})}(E) \times \\ &\times [(F_\mu^{(\mathbf{k})}(j, E, L'', s))^* \sigma_{s,s'}^\gamma G_\mu^{(\mathbf{k})}(j, E, L', s') - F_\mu^{(\mathbf{k})}(j, E, L', s) \sigma_{s,s'}^\gamma (G_\mu^{(\mathbf{k})}(j, E, L'', s'))^*] Y_L(\hat{r}), \end{aligned} \quad (4.83)$$

where  $G(L', L, L'')$  are the Gaunt coefficients (see Appendix A). Due to the relations

$$\int_0^\pi d\theta \sin(\theta) \int_0^{2\pi} d\phi Y_{lm}(\theta, \phi) = \delta_{0,m} \delta_{0,l} \sqrt{4\pi} \quad (4.84)$$

and

$$G(L', 0, L'') = \frac{1}{\sqrt{4\pi}} \delta_{l',l''} \delta_{m',m''} \quad (4.85)$$

the complete radial currents through the muffin-tin boundary are found to be

$$\begin{aligned} \frac{\partial I_\mu^\gamma(j, E)}{\partial E} &= \int R_\mu^2 \frac{\partial j_\mu^\gamma(j, E, \hat{\mathbf{r}})}{\partial E} d\Omega \\ &= \sum_{\mathbf{k}} w_{\mathbf{k}} \sum_{L, s, s'} D_j^{(\mathbf{k})}(E) R_\mu^2 \Im[(F_\mu^{(\mathbf{k})}(j, E, L, s))^* \sigma_{s, s'}^\gamma G_\mu^{(\mathbf{k})}(j, E, L, s')]. \end{aligned} \quad (4.86)$$

For the present purpose of calculating the current through the MT-cup of atom  $\mu$  the polar angle  $\theta$  is not integrated from 0 to  $\pi$  like in Eq. (4.84), but only from 0 to  $\theta_{\text{cut}}$ . If the plane cuts the MT-sphere of atom  $\mu$  at  $z_\mu$ , then the polar angle  $\theta$ , which describes the MT-cup, is restricted to lie within the interval  $[0, \theta_{\text{cut}, \mu} = \arccos((z_\mu - \tau_{3, \mu})/R_\mu)]$ , and instead of Eq. (4.84) we have to evaluate

$$\begin{aligned} H_\mu(L) &= \int_0^{\theta_{\text{cut}, \mu}} d\theta \sin(\theta) \int_0^{2\pi} d\phi Y_{lm}(\theta, \phi) \\ &= \delta_{0, m} h_l(\theta_{\text{cut}, \mu}), \end{aligned} \quad (4.87)$$

where

$$\begin{aligned} h_l(\theta_{\text{cut}, \mu}) &= \sqrt{(2l+1)\pi} \int_0^{\theta_{\text{cut}, \mu}} d\theta \sin(\theta) P_l(\cos(\theta)) \\ &= \sqrt{(2l+1)\pi} \int_0^{\cos(\theta_{\text{cut}, \mu})} dx P_l(x). \end{aligned} \quad (4.88)$$

In the case of many simple bulk materials one can choose the dividing plane in such a way that it cuts the MT-sphere in the middle. For this situation one may easily obtain an analytic expression for  $h_l(\pi/2)$ :

$$\begin{aligned} h_l(\pi/2) &= \sqrt{(2l+1)\pi} \int_0^{\pi/2} d\theta \sin(\theta) P_l(\cos(\theta)) \\ &= \sqrt{(2l+1)\pi} \int_0^1 dx P_l(x) \\ &= \sqrt{(2l+1)\pi} \times \left\{ \begin{array}{ll} 1 & (l=0) \\ 0 & (l \neq 0 \text{ and } l \text{ even}) \\ \frac{(-1)^{(l-1)/2} l!}{2^{l-1} l(l+1) ((\frac{1}{2}(l-1))!)^2} & (l \text{ odd}) \end{array} \right\}. \end{aligned} \quad (4.89)$$

Clearly, the  $h_l(\pi/2)$  are the coefficients of the expansion of the Heaviside step function  $H(\theta)$  in terms of spherical harmonics:

$$H(\theta) = \sqrt{\pi} [Y_{0,0}(\theta) + \frac{\sqrt{3}}{2} Y_{1,0}(\theta) - \frac{\sqrt{7}}{8} Y_{3,0}(\theta) + \frac{\sqrt{11}}{16} Y_{5,0}(\theta) + \dots]. \quad (4.90)$$

Using Eq. (4.83,4.87,4.88) we obtain the following MT-contribution of atom  $\mu$  to the current  $I_\mu^\gamma(j, E)$  of channel  $j$  at energy  $E$ :

$$\begin{aligned} \frac{\partial I_\mu^\gamma(j, E)}{\partial E} &= \int_0^{\theta_{\text{cut},\mu}} d\theta \sin(\theta) \int_0^{2\pi} d\phi R_\mu^2 \frac{\partial j_\mu^\gamma(j, E, \hat{\mathbf{r}})}{\partial E} \\ &= \sum_{\mathbf{k}} w_{\mathbf{k}} \sum_{L', L'', l} \sum_{s, s'} D_j^{(\mathbf{k})}(E) G_{l', l, l''}^{m', 0, m''} R_\mu^2 \Im[(F_\mu^{(\mathbf{k})}(j, E, L'', s))^* \sigma_{s, s'}^\gamma G_\mu^{(\mathbf{k})}(j, E, L', s')] h_l(\theta_{\text{cut},\mu}), \end{aligned} \quad (4.91)$$

where we now switched to the notation  $G_{l', l, l''}^{m', m, m''}$  for the Gaunt coefficients (see Appendix A). We now turn to the interstitial contribution. In the interstitial it is straightforward to expand the scattering state and its normal derivative on a real space mesh. Denoting the resulting expansions  $F^{(\mathbf{k})}(j, E, \mathbf{x}_S, s)$  and  $G^{(\mathbf{k})}(j, E, \mathbf{x}_S, s)$ , respectively, we may write the interstitial contribution as follows:

$$\frac{\partial I_{\text{INT},m}^\gamma(j, E)}{\partial E} = \sum_{\mathbf{k}} w_{\mathbf{k}} \sum_{s, s'} D_j^{(\mathbf{k})}(E) \int_{MT} \Im[(F^{(\mathbf{k})}(j, E, \mathbf{x}_S, s))^* \sigma_{s, s'}^\gamma G^{(\mathbf{k})}(j, E, \mathbf{x}_S, s')] d x_S^2. \quad (4.92)$$

## 4.9 Step Functions

For the interstitial contributions to the overlap and Hamiltonian matrices given in Eq. (4.41) we need step functions, which cut out everything but the interstitial inside  $\Omega$ . The fourier transform of the step function which cuts out the MT-spheres is given by [36, 32]:

$$\theta_{\mathbf{G}} = \delta_{\mathbf{G},0} - \sum_{\mu \in \Omega} e^{-i\mathbf{G} \cdot \boldsymbol{\tau}_\mu} \frac{4\pi R_\mu^3}{\tilde{\Omega}} \frac{j_1(GR_\mu)}{GR_\mu}. \quad (4.93)$$

This step function does not yet subtract that part of  $\tilde{\Omega}$ , which lies outside of the region  $-d/2 \leq z \leq d/2$ . Consequently, we subtract

$$D_{\mathbf{G}} = \left( \frac{\tilde{d} - d}{\tilde{d}} \delta_{0,\mathbf{G}} - 2(1 - \delta_{0,\mathbf{G}}) \frac{\sin(G_\perp d/2)}{\mathbf{G}_\perp \tilde{d}} \right) \delta_{0,\mathbf{G}_\parallel} \quad (4.94)$$

from Eq. (4.93). The complications due to the curvy embedding surface  $S$  (see Fig. 4.4) do not only affect the surface projector (section 4.7), but also the step functions: We need the step functions for the caps of the MT-spheres, which either stick out of the region  $-d/2 \leq z \leq d/2$  or which atoms in the leads cut out of  $\Omega$ . We have to add the step functions of the caps of the MT-spheres, which stick out of the region  $-d/2 \leq z \leq d/2$ , because they are subtracted in Eq. (4.93) and Eq. (4.94). We have to subtract the step functions of the caps of the MT-spheres, which lie outside of  $\Omega$ , because these regions do not belong to the interstitial of  $\Omega$ . If the MT of atom  $\mu$  sticks out of the region  $-d/2 \leq z \leq d/2$

by  $R_\mu - |z_S - \tau_{3,\mu}|$  and the radius of the disk cut out of the plane at  $z_S = \pm d/2$  by the MT-sphere is  $\bar{r}_\mu = \sqrt{R_\mu^2 - (z_S - \tau_{3,\mu})^2}$  the required integral is given by

$$\begin{aligned}
K_{\mathbf{g}}^\mu &= \frac{1}{\Omega} e^{-ig_\perp \tau_{3,\mu}} \int_{|z_S - \tau_{3,\mu}|}^{R_\mu} dz \int_0^{\sqrt{R_\mu^2 - z^2}} r dr \int_0^{2\pi} d\phi e^{-ig_\perp z \text{sig}(z_S - \tau_{3,\mu})} e^{ig_\parallel r \cos \phi} = \\
&= \frac{2\pi}{\Omega} e^{-ig_\perp \tau_{3,\mu}} \int_{|z_S - \tau_{3,\mu}|}^{R_\mu} dz \int_0^{\sqrt{R_\mu^2 - z^2}} r dr e^{-ig_\perp z \text{sig}(z_S - \tau_{3,\mu})} J_0(g_\parallel r) = \\
&= \frac{2\pi}{\Omega} e^{-ig_\perp \tau_{3,\mu}} \int_{|z_S - \tau_{3,\mu}|}^{R_\mu} dz e^{-ig_\perp z \text{sig}(z_S - \tau_{3,\mu})} \frac{\sqrt{R_\mu^2 - z^2}}{g_\parallel} J_1\left(g_\parallel \sqrt{R_\mu^2 - z^2}\right),
\end{aligned} \tag{4.95}$$

where  $J_0(z)$  and  $J_1(z)$  are cylindrical Bessel functions. The complete step function is given by

$$\Xi_{\mathbf{g}} = \theta_{\mathbf{g}} - D_{\mathbf{G}} - \sum_{\mu \notin \Omega} K_{\mathbf{g}}^\mu + \sum_{\mu \in \partial\Omega} K_{\mathbf{g}}^\mu. \tag{4.96}$$

For the overlap matrix and in the kinetic energy term of the Hamiltonian matrix we need the overlap integrals between plane waves. The integration region is exactly the interstitial region inside  $\Omega$  and consequently these overlap integrals are given by  $\Xi_{\mathbf{g}}$  of Eq. (4.96). For the potential energy term of the Hamiltonian matrix we need the convolution of the Kohn-Sham potential with the step function  $\Xi_{\mathbf{g}}$ . The convolution is performed efficiently by the fast-fourier-transform (FFT) [36, 32].

## 4.10 Transformation of the Potential and the Charge Density

From Eq. (4.42) one may obtain the charge density within the scattering region self-consistently. This self-consistent embedding will be discussed in detail in chapter 5. However, for some applications it is easier or necessary to take the potential or the charge density from a standard FLAPW calculation. For example, the potential of a principal layer of bulk lead material is needed to calculate the transfer matrix of the lead according to section 4.5, which allows to obtain the embedding potential of the lead and its complex band structure. In these cases it is necessary to transform the potential or the charge density from the standard FLAPW calculation to the embedding geometry. Clearly, this transformation does not concern the MT-spheres since the radial grid and the point group symmetry operations of the atoms may be chosen identical in standard FLAPW and the embedding setup. However, as  $\Omega$  and  $\tilde{\Omega}$  differ within the embedding setup (see Fig. 4.2), the expansions of potential and charge density in the interstitial are different for the two geometries. In the interstitial region potential and charge density are expanded in terms of two-dimensional stars (5.4), i.e., symmetrized plane waves. As the symmetrization of two-dimensional stars involves only the  $x$  and  $y$  directions while the transformation from standard FLAPW to the embedding geometry concerns the out-of-plane direction, we are

left with the problem of transforming one-dimensional plane-waves between the two geometries. Consider the function  $f(z)$  expanded in terms of the bulk FLAPW interstitial plane-wave basis:

$$\begin{aligned} f(z) &= \sum_n \tilde{c}_n e^{i\tilde{g}_n z}, \\ \tilde{g}_n &= \frac{2\pi n}{L}. \end{aligned} \quad (4.97)$$

We seek the coefficients  $c_m$  of the expansion of  $f(z)$  in terms of the plane-wave basis used within the embedding setup:

$$\begin{aligned} f(z) &= \sum_m c_m e^{ig_m z}, \\ g_m &= \frac{2\pi m}{\tilde{d}}. \end{aligned} \quad (4.98)$$

In general the transformation to the embedding geometry can only be exact if an infinite number of plane waves are used. However, in practice we impose a cutoff on the range of the wave vector  $g_m$  and the transformation is approximate. As we need the potential and the charge density only in the physical region  $\Omega$  and not in the larger normalization volume  $\tilde{\Omega}$ , we determine the coefficients  $c_m$  in such a way, that the deviation between  $f(z)$  and its approximate expansion is minimal over the region  $z \in [-d/2, d/2]$ . The quadratic deviation is

$$\begin{aligned} \Delta(\{c_m\}) &= \int_{-d/2}^{d/2} |f(z) - \sum_m c_m e^{ig_m z}|^2 dz \\ &= \int_{-d/2}^{d/2} |f(z)|^2 dz - \sum_m c_m^* f_m - \sum_m c_m f_m^* + \sum_{m,n} c_n \mathcal{O}_{n,m} c_m^*, \end{aligned} \quad (4.99)$$

where we defined the integrals

$$\begin{aligned} f_m &= \int_{-d/2}^{d/2} f(z) e^{-ig_m z} dz, \\ \mathcal{O}_{n,m} &= \int_{-d/2}^{d/2} e^{ig_n z} e^{-ig_m z} dz. \end{aligned} \quad (4.100)$$

The minimum is characterized by the condition of zero partial derivatives  $\partial\Delta(\{c_m\})/\partial c_m = 0$ , which leads to the following system of coupled linear equations:

$$f_m = \sum_n c_n \mathcal{O}_{n,m}. \quad (4.101)$$

The unique solution of these equations provides the expansion coefficients  $c_m$  corresponding to that transformation which is best in the sense of minimal deviation  $\Delta$ .

## 4.11 Computation of Surfaces within the embedding method

There are two ways to treat the vacuum in an embedding calculation of a surface. One way is to calculate the embedding potential of the vacuum and to embed the surface with two embedding potentials, one from the substrate and one from the vacuum. The second way is to include the vacuum into the surface and to embed the surface only by the substrate. We describe here the second way. The inclusion of the vacuum is done in the same way as in a standard FLAPW film calculation, the only difference being that only one vacuum is present in a surface calculation. Like in a film calculation, basis functions are introduced by which the wave function may be represented not only inside the interstitial and the MT-spheres (like in a bulk calculation) but also inside the vacuum region [36, 32]. Inside the vacuum region the APW basis function is a linear combination of the solutions of the Schrödinger equation for the vacuum region at an energy  $E_{\text{vac}}$  and of the energy derivatives of the Schrödinger equation. The coefficients of this linear combination are uniquely determined by the requirement that the APW basis function be continuous at the interstitial-vacuum boundary. The Kohn-Sham effective potential of the vacuum region is calculated from the charge density in the vacuum region. The embedding potential of the substrate is calculated from a principal layer of substrate material.

## 4.12 Flow chart: Non-Self-Consistent Embedding

In the following we summarize the steps needed to perform a non-self-consistent embedding calculation, which is the main topic of the present chapter. Self-consistent embedding will be discussed in chapter 5. In a non-self-consistent embedding calculation the Kohn-Sham effective potential from a standard FLAPW calculation is taken. Usually this effective potential is obtained self-consistently within standard FLAPW. Due to the different boundary conditions (e.g. periodic in standard FLAPW in contrast to embedded) this potential is not a selfconsistent one of the embedding calculation. A basis transformation has to be performed (see section 4.10) to obtain the effective Kohn-Sham potential in the basis set of the embedding method. The Kohn-Sham effective potential is not only needed for the embedded region, but also for the leads (or, in case of a surface calculation, the substrate). If the Kohn-Sham effective potential of the leads (or the substrate) is not taken from the same super-cell calculation as the effective potential of the embedded region, a shift of the potential zeros is needed in general to match the Fermi energy of the embedded region with the Fermi energy of the lead (or substrate). In order to compute the embedding potentials of the leads (or the substrate) from the transfer-matrix one calculates the Green function with von Neumann boundary conditions. Using the effective Kohn-Sham potential of the embedded region and the embedding potentials the Green function of the embedded region is calculated. In the case of an electronic transport calculation the conductance is computed from this Green function. In the case of a surface calculation the Bloch spectral function may be calculated.





# Chapter 5

## Self-Consistent Embedding

In chapter 4 we discussed the construction of the Green function for a given Kohn-Sham potential in the embedded region  $\Omega$  and explained how electronic transport properties may be evaluated from the Green function. If the scattering region  $\Omega$  is small, one may use the Kohn-Sham potential of a standard FLAPW calculation for this purpose. However, with increasing size of the scattering-region, the computational effort of standard FLAPW becomes prohibitively large. In chapter 7 we will describe an order-N scheme for the embedding method, which allows to keep the computational cost small even for relatively large transport junctions. Clearly, this order-N scheme requires the self-consistent computation of the charge density and the potential of the embedded region  $\Omega$ , which is the main topic of this chapter. A second application of self-consistent embedding concerns the description of *non-equilibrium*, e.g. the computation of the current beyond linear response in the presence of a finite bias. While within the standard FLAPW method the non-equilibrium charge density cannot be calculated, this is possible using the embedding method and requires a self-consistency scheme like the equilibrium charge density. The present chapter also discusses questions intimately related with self-consistency, namely the computation of *total energy* and *atomic forces*.

### 5.1 Generation of the charge density

The equilibrium charge density within the scattering volume  $\Omega$  may be calculated from the density matrix

$$\rho^{(\bar{\mathbf{k}})} = -\frac{1}{\pi} \Im \int_{-\infty}^{\infty} f(E) \mathbf{G}^{(\bar{\mathbf{k}})}(E + i0^+) dE, \quad (5.1)$$

where  $f(E)$  denotes the Fermi-Dirac distribution at given Fermi energy and temperature. Owing to the analyticity of  $\mathbf{G}^{(\bar{\mathbf{k}})}(E + i0^+)$  the energy integration may be performed using a contour in the upper half of the complex plane. As the Green function is much smoother deep in the complex plane than close to the real axis, the energy integration is facilitated this way. In practice, the energy integration is replaced by a summation over discrete

energy points with weights  $w_i$ :

$$\rho^{(\bar{\mathbf{k}})} = -\frac{1}{\pi} \Im \left[ \sum_i w_i \mathbf{G}^{(\bar{\mathbf{k}})}(E_i + i0^+) \right]. \quad (5.2)$$

If the integration is along a complex contour, both energies and weights are complex. How an efficient set of weights  $w_i$  may be constructed is discussed in Ref. [55].

In real space the density matrix is given by

$$\rho^{(\bar{\mathbf{k}})}(\mathbf{r}, \mathbf{r}') = \sum_{\mathbf{g}, \mathbf{g}'} \phi_{\mathbf{g}}^{(\bar{\mathbf{k}})}(\mathbf{r}) \rho_{\mathbf{g}, \mathbf{g}'}^{(\bar{\mathbf{k}})} (\phi_{\mathbf{g}'}^{(\bar{\mathbf{k}})}(\mathbf{r}'))^*, \quad (5.3)$$

where  $\phi_{\mathbf{g}}^{(\bar{\mathbf{k}})}(\mathbf{r})$  are the (L)APW-basis functions defined in Eq. (2.22,2.23). Within the interstitial the charge density is expanded in terms of symmetrized plane waves,

$$\Phi_s(\mathbf{r}) = \sum_{\mathbf{g} \in G_s} e^{i\mathbf{g} \cdot \mathbf{r}}, \quad (5.4)$$

the so-called stars [32], where each set of distinct reciprocal vectors  $G_s$  is generated by applying the 2D lattice space group operations on a representative  $\mathbf{g}_s \in G_s$  and keeping only distinct vectors. The stars are orthogonal:

$$\int_{\tilde{\Omega}} (\Phi_s(\mathbf{r}))^* \Phi_{s'}(\mathbf{r}) d^3 r = \delta_{s,s'} \tilde{\Omega} N_s, \quad (5.5)$$

where  $N_s$  is the number of members (i.e., the number of  $\mathbf{g}$ -vectors) in the star. The expansion of the interstitial charge density in terms of the stars is then

$$\rho(\mathbf{r}) = \sum_s \rho_s \Phi_s(\mathbf{r}), \quad (5.6)$$

where the coefficients  $\rho_s$  are given by

$$\begin{aligned} \rho_s &= \frac{1}{\tilde{\Omega}} \frac{1}{N_s} \sum_{\bar{\mathbf{k}}} w_{\bar{\mathbf{k}}} \int_{\tilde{\Omega}} \rho^{(\bar{\mathbf{k}})}(\mathbf{r}, \mathbf{r}) (\Phi_s(\mathbf{r}))^* d^3 r = \frac{1}{\tilde{\Omega}} \frac{1}{N_s} \sum_{\bar{\mathbf{k}}} w_{\bar{\mathbf{k}}} \sum_{\mathbf{g} \in G_s} \int_{\tilde{\Omega}} \rho^{(\bar{\mathbf{k}})}(\mathbf{r}, \mathbf{r}) e^{-i\mathbf{g} \cdot \mathbf{r}} d^3 r \\ &= \frac{1}{\tilde{\Omega}} \frac{1}{N_s} \sum_{\bar{\mathbf{k}}} w_{\bar{\mathbf{k}}} \sum_{\mathbf{g} \in G_s} \rho_{\mathbf{g}'', \mathbf{g}'}^{(\bar{\mathbf{k}})} \delta_{(\mathbf{g}'' - \mathbf{g}'), \mathbf{g}}. \end{aligned} \quad (5.7)$$

Within the MT-spheres symmetrized spherical harmonics (so called *lattice harmonics*) are used as basis set to express the charge density [32]. They are defined as follows:

$$K_{\nu}^{\alpha}(\hat{\mathbf{r}}) = \sum_{L \in H_{\nu, \alpha}} c_{\nu, L}^{\alpha} Y_L(\hat{\mathbf{r}}), \quad (5.8)$$

where  $\alpha$  is the index of the atom and  $\nu$  labels the lattice harmonics. The lattice harmonics  $K_{\nu}^{\alpha}(\hat{\mathbf{r}})$  are invariant with respect to the symmetry operations of the point group of atom

$\alpha$ . The coefficients  $c_{\nu,L}^\alpha$  are chosen such that the  $K_\nu^\alpha(\mathbf{r})$  form an orthonormal basis set of real-valued functions. Denoting the expansion coefficients of the charge density by  $\rho_\nu^\alpha(r)$  we may write the charge density within the MT-sphere of atom  $\alpha$  as

$$\rho^\alpha(\mathbf{r}) = \sum_\nu \rho_\nu^\alpha(|\mathbf{r}|) K_\nu^\alpha(\hat{\mathbf{r}}). \quad (5.9)$$

The expansion coefficients are given by

$$\rho_\nu^\alpha(r) = \sum_{\bar{\mathbf{k}}} w_{\bar{\mathbf{k}}} \int \rho^{(\bar{\mathbf{k}})}(\mathbf{r}, \mathbf{r}) K_\nu^\alpha(\hat{\mathbf{r}}) d\Omega. \quad (5.10)$$

Instead of computing the density directly from the density matrix as described above, it is also possible to diagonalize the density matrix and to use its eigenvectors as *effective states*. This latter procedure is computationally slower, but much easier to implement, as the existing implementation of a charge density generator from the standard FLAPW method may be taken over without any modifications: The only difference between standard FLAPW and the Green function based variant concerning charge generation is that instead of *physical* Bloch states the eigenstates of the density matrix are used. A detailed description of the calculation of the charge density from Bloch states is given in Ref. [36, 32]. The availability of both methods, the direct computation of the charge density from the density matrix and the use of effective states, is very helpful, when existing features, e.g. spin-orbit coupling, noncollinear magnetism, LDA+U, etc. are ported from standard FLAPW to the Green function based variant, because the results of both methods have to agree perfectly, which makes testing and debugging a simple matter.

## 5.2 Construction of the Coulomb Potential

In contrast to the exchange-correlation contribution to the Kohn-Sham potential the Coulomb potential is *highly non-local*: The electrostatic potential due to a unit charge measured at a distance  $r$  decays only like  $1/r$  with distance. As a consequence, there are several differences regarding its construction between the standard FLAPW method and the Green function based version used in this work. For a detailed discussion of the potential setup as implemented in standard FLAPW see eg. Refs. [36, 56, 32].

### 5.2.1 The Pseudocharge Method

Obviously, it is a simple matter to calculate the electrostatic potential if the charge density is provided as an expansion in terms of *plane waves*, i.e.,

$$\rho(\mathbf{r}) = \sum_{\mathbf{g}} \rho_{\mathbf{g}} e^{-i\mathbf{g}\cdot\mathbf{r}}, \quad (5.11)$$

since the Fourier components of the potential are then simply given by

$$V_g = \begin{cases} 0 & \mathbf{g} = 0 \\ \frac{4\pi\rho_{\mathbf{g}}}{g^2} & \mathbf{g} \neq 0 \end{cases} . \quad (5.12)$$

However, within FLAPW different representations for the charge (and likewise for the potential) are used inside the MT-spheres on the one hand and the interstitial region on the other hand. As it is numerically difficult to express the MT-charge density in terms of plane waves due to its *strong variation* close to the nuclei we use the pseudocharge method [57] instead. The concept of this approach is based on the observation that one cannot determine the MT-charge density uniquely from the potential it generates in the interstitial. This is pretty obvious: If we add any charge-neutral spherically symmetric charge-density to the *actual* charge density inside the MT-sphere, the potential outside the MT-sphere is not altered in any way. This ambiguity is now exploited as follows: Inside the MT-spheres the charge density is replaced by a pseudocharge, which has a rapidly converging Fourier expansion, Eq. (5.11), and the same *multipole moments* as the *actual* charge density. From this pseudocharge  $\rho^{\text{psq}}(\mathbf{r})$  we may now calculate the interstitial charge density. In the simplest case of a periodic crystal, the interstitial Coulomb potential is simply provided by Eq. (5.12). Once the electrostatic potential is known in the interstitial it can be constructed inside the MT-spheres from the boundary values on the MT-sphere surfaces and the *true* MT-sphere charge density. In summary, the construction of the Coulomb potential involves the following three steps:

- 1 Generate Fourier coefficients of the pseudocharge  $\rho_{\mathbf{g}}^{\text{pseu}}$ .
- 2 Calculate interstitial potential.
- 3 Obtain boundary values of the Coulomb potential on the MT-sphere boundaries.  
Calculate Coulomb potential inside the MT-spheres.

As both the generation of the pseudocharge (step 1) and the calculation of the Coulomb potential in the muffin-tin spheres (step 3) involve essentially only the MTs, there are no substantial differences between the standard FLAPW method and the Green function variant of FLAPW regarding the details of the pseudocharge method. The only modifications needed to adapt the scheme for the Green function variant concern the interstitial (step 2), which is the content of the next subsection.

### 5.2.2 Construction of the Coulomb Potential in the Interstitial

The construction of the interstitial Coulomb potential of the embedded region  $\Omega$  constitutes a boundary value problem for the Poisson equation. We proceed in two steps to find the Coulomb potential. First, we find some solution to the *inhomogeneous Poisson* equation. Second, we add a solution of the *homogeneous Poisson* equation such that the Coulomb

potential has the correct value on the boundary of  $\Omega$ . The solution of the inhomogeneous Poisson equation is given by

$$V_g^{\text{inhom}} = \begin{cases} 0 & \mathbf{g} = 0 \\ \frac{4\pi\tilde{\rho}_{\mathbf{g}}}{g^2} & \mathbf{g} \neq 0, \end{cases} \quad (5.13)$$

if the inhomogeneity  $\tilde{\rho}_{\mathbf{g}}$  satisfies  $\tilde{\rho}_0 = 0$ . As the length of  $\tilde{\Omega}$  in  $Z$ -direction is  $\tilde{d}$ , while the length of the actual physical region  $\Omega$  is  $d < \tilde{d}$ , the requirement  $\tilde{\rho}_0 = 0$  does not mean that the physical region is charge neutral. In the basis set used for the expansion of the interstitial charge density and potential we can expand any function, which is periodic in  $\tilde{\Omega}$ . Consequently, we have to determine  $\tilde{\rho}_{\mathbf{g}}$  in such a way that its Fourier transform satisfies  $\tilde{\rho}(\mathbf{r}) = \rho^{\text{psq}}(\mathbf{r})$  for  $\mathbf{r} \in \Omega$  and

$$\int_{\tilde{\Omega}} \tilde{\rho}(\mathbf{r}) d^3r = 0. \quad (5.14)$$

In order to achieve this one adds a smooth correction charge  $\rho^{\text{corr}}(\mathbf{r})$  to the pseudocharge. The correction charge has to be zero in  $\Omega$ , it has to be periodic in  $\tilde{\Omega}$  and it has to compensate the total charge of  $\rho^{\text{psq}}(\mathbf{r})$  to yield zero total charge in  $\tilde{\Omega}$ :

$$\begin{aligned} \rho^{\text{corr}}(\mathbf{r}) &= 0, \quad \mathbf{r} \in \Omega \\ \int_{\tilde{\Omega}} \rho^{\text{corr}}(\mathbf{r}) d^3r + \int_{\tilde{\Omega}} \rho^{\text{psq}}(\mathbf{r}) d^3r &= 0 \\ \tilde{\rho}(\mathbf{r}) &= \rho^{\text{psq}}(\mathbf{r}) + \rho^{\text{corr}}(\mathbf{r}). \end{aligned} \quad (5.15)$$

This correction affects only the Fourier components with  $\mathbf{g}_{\parallel} = 0$  and may be done conveniently in real space, after performing a one-dimensional FFT of the  $\mathbf{g}_{\parallel} = 0$  components of the pseudocharge. The boundary values of the solution  $V_{\mathbf{g}}^{\text{inhom}}$  to the inhomogeneous Poisson equation, Eq. (5.13), on the curvy planes  $S_L$  and  $S_R$  may be expressed elegantly in terms of the projection onto the curvy planes:

$$V_{\mathbf{g}}^{\text{inhom},S} = \sum_{\mathbf{g}} P_{S,\bar{\mathbf{g}},\mathbf{g}} V_{\mathbf{g}}^{\text{inhom}}, \quad S = S_L, S_R. \quad (5.16)$$

Likewise, the projections of the bulk Coulomb potentials of the left and right leads,  $V_{\mathbf{g}}^{\text{B,L}}$  and  $V_{\mathbf{g}}^{\text{B,R}}$ , are given by

$$\begin{aligned} V_{\mathbf{g}}^{\text{B},S_L} &= \sum_{\mathbf{g}} P_{S_L,\bar{\mathbf{g}},\mathbf{g}} V_{\mathbf{g}}^{\text{B,L}}, \\ V_{\mathbf{g}}^{\text{B},S_R} &= \sum_{\mathbf{g}} P_{S_R,\bar{\mathbf{g}},\mathbf{g}} V_{\mathbf{g}}^{\text{B,R}}. \end{aligned} \quad (5.17)$$

In the preparative step, in which the embedding potentials are calculated for the principal layers of the left and right leads, these boundary values,  $V_{\mathbf{g}}^{\text{B},S_L}$  and  $V_{\mathbf{g}}^{\text{B},S_R}$ , are also calculated. Ultimately, we have to find the solution of the Poisson equation, which has the same boundary values,  $V_{\mathbf{g}}^{\text{B},S_L}$  and  $V_{\mathbf{g}}^{\text{B},S_R}$ , on the embedding surfaces  $S_L$  and  $S_R$ . Thus, we have

to compute the solution of the homogeneous Poisson equation, which has the following projection on the curvy plane:

$$V_{\mathbf{g}}^{\text{hom},S} = V_{\mathbf{g}}^{\text{B},S} - V_{\mathbf{g}}^{\text{inhom},S}, \quad S = S_L, S_R. \quad (5.18)$$

A complete set of independent solutions of the homogeneous Poisson equation is provided by

$$V_{\mathbf{g}_{\parallel}}^{\text{hom},l}(\mathbf{r}) = \begin{cases} e^{i\mathbf{g}_{\parallel} \cdot \mathbf{r}}, & l = 1 \wedge \mathbf{g}_{\parallel} = 0 \\ e^{i\mathbf{g}_{\parallel} \cdot \mathbf{r}} e^{-|\mathbf{g}_{\parallel}|z}, & l = 1 \wedge \mathbf{g}_{\parallel} \neq 0 \\ e^{i\mathbf{g}_{\parallel} \cdot \mathbf{r}} z, & l = 2 \wedge \mathbf{g}_{\parallel} = 0 \\ e^{i\mathbf{g}_{\parallel} \cdot \mathbf{r}} e^{|\mathbf{g}_{\parallel}|z}, & l = 2 \wedge \mathbf{g}_{\parallel} \neq 0 \end{cases}. \quad (5.19)$$

Clearly, there are two independent solutions at each  $\mathbf{g}_{\parallel}$ . Obviously, we have to determine the coefficient vector  $c_{\mathbf{g}_{\parallel}}^l$  of the expansion

$$V^{\text{hom}}(\mathbf{r}) = \sum_{\mathbf{g}_{\parallel},l} c_{\mathbf{g}_{\parallel}}^l V_{\mathbf{g}_{\parallel}}^{\text{hom},l}(\mathbf{r}) \quad (5.20)$$

such that Eq. (5.18) is satisfied. The projections onto the curvy planes of the solutions  $V_{\mathbf{g}_{\parallel}}^{\text{hom},l}(\mathbf{r})$  to the homogeneous Poisson equation are given by

$$V_{\mathbf{g}_{\parallel},\mathbf{g}}^{\text{hom},S,l} = \sum_{\mathbf{g}} P_{S,\mathbf{g},\mathbf{g}} V_{\mathbf{g}_{\parallel},\mathbf{g}}^{\text{hom},l}, \quad S = S_L, S_R, \quad l = 1, 2, \quad (5.21)$$

where the coefficients  $V_{\mathbf{g}_{\parallel},\mathbf{g}}^{\text{hom},l}$  are the Fourier components of  $V_{\mathbf{g}_{\parallel}}^{\text{hom},l}(\mathbf{r})$  defined in Eq. (5.19). With  $N_{\parallel}$  denoting the number of in-plane modes, the size of the square matrix  $V_{\mathbf{g}_{\parallel},\mathbf{g}}^{\text{hom},S,l}$  is  $2N_{\parallel} \times 2N_{\parallel}$ . We are now able to rewrite Eq. (5.18, 5.20) as a coupled system of linear equations,

$$V_{\mathbf{g}}^{\text{hom},S} = \sum_{\mathbf{g}_{\parallel},l} c_{\mathbf{g}_{\parallel}}^l V_{\mathbf{g}_{\parallel},\mathbf{g}}^{\text{hom},S,l}, \quad (5.22)$$

which possesses a well-determined solution  $c_{\mathbf{g}_{\parallel}}^l$ . Finally, we may write the special solution of the inhomogeneous Poisson equation as follows:

$$V(\mathbf{r}) = V^{\text{inhom}}(\mathbf{r}) + \sum_{\mathbf{g}_{\parallel},l} c_{\mathbf{g}_{\parallel}}^l V_{\mathbf{g}_{\parallel}}^{\text{hom},l}(\mathbf{r}) \quad (5.23)$$

### 5.2.3 Construction of the Coulomb potential (Surface Calculations)

Regarding the construction of the Coulomb potential the case of a surface calculation is very similar to the case of a film calculation, the only difference being that only one vacuum region is present. Similar to a film calculation the Coulomb potential  $V(\mathbf{r})$  inside the vacuum region is first constructed in such a way that  $V(\mathbf{r}) \rightarrow 0$  in the limit  $z \rightarrow 0$ .

In a second step a solution of the homogeneous Poisson equation is added to match the Coulomb potential to the boundary condition on the left embedding surface. The set of solutions of the homogeneous Poisson equation is now restricted to those which are either constant or which decay in positive  $z$ -direction, i.e. only the set with  $l = 1$  in Eq. (5.19) is relevant in the case of a surface calculation. Thus, Eq. (5.19) is adapted to the case of a surface as follows:

$$V^{\text{hom}}(\mathbf{r}) = \sum_{\mathbf{g}_{\parallel}} c_{\mathbf{g}_{\parallel}} V_{\mathbf{g}_{\parallel}}^{\text{hom},1}(\mathbf{r}). \quad (5.24)$$

The coefficients  $c_{\mathbf{g}_{\parallel}}$  satisfy the coupled system of linear equations

$$V_{\mathbf{g}}^{\text{hom},S_L} = \sum_{\mathbf{g}_{\parallel}} c_{\mathbf{g}_{\parallel}} V_{\mathbf{g}_{\parallel},\mathbf{g}}^{\text{hom},S_L,1}, \quad (5.25)$$

where  $V_{\mathbf{g}}^{\text{hom},S_L}$  is the boundary value of the Coulomb potential on the left embedding plane. The matrix of the system of equations,  $V_{\mathbf{g}_{\parallel},\mathbf{g}}^{\text{hom},S_L,1}$ , is now a  $N_{\parallel} \times N_{\parallel}$  square matrix, where  $N_{\parallel}$  is the number of in-plane modes.

### 5.3 Self-Consistency scheme

In order to prepare a self-consistent calculation within the embedding method, the *embedding potentials* and the *boundary values of the Coulomb potential* on the embedding planes have to be evaluated and a *starting density* is needed. For this purpose, FLAPW bulk calculations are performed for the lead materials. The self-consistent Coulomb potential is then projected onto the curvy embedding planes, as prescribed by Eq. (5.17). Using the self-consistent Kohn-Sham potentials of the leads, the corresponding embedding potentials are computed according to Eq. (4.67). In analogy to the transformation Eq. (4.98) of the potentials from a standard FLAPW calculation into the geometry used in the Green function variant, the starting density of a standard FLAPW calculation may be transformed and used as starting density for the self-consistency within the embedding method.

After these preparative steps the self-consistent calculation of the charge density in the embedding region  $\Omega$  may be performed. One self-consistency iteration involves the following steps:

- Use the boundary values of the Coulomb potential and the *input charge density* in order to calculate the Coulomb potential as described in section 5.2. Add the exchange-correlation potential in order to obtain the complete Kohn-Sham effective potential.
- Use the Kohn-Sham effective potential and the embedding potentials to calculate the embedded Green function, as prescribed in Eq. (4.40).
- Obtain the *output charge density* as described in section 5.1.

## 5.4 Evaluation of total energy

In the total energy expression Eq. (2.13) all terms but the *eigenvalue sum* are given in terms of the density and the potentials. Within the Green function embedding method the analogue to the eigenvalue sum is the trace of the *energy density matrix*

$$\epsilon^{(\bar{\mathbf{k}})} = -\frac{1}{\pi} \Im \int_{-\infty}^{\infty} E f(E) \mathbf{G}^{(\bar{\mathbf{k}})}(E + i0^+) dE. \quad (5.26)$$

Consequently, we perform the replacement

$$\sum_i n_i \epsilon_i \rightarrow \text{Tr} [\epsilon^{(\bar{\mathbf{k}})}] \quad (5.27)$$

in Eq. (2.13) in order to adapt it for the use within our Green function scheme. Like the density matrix also the energy density matrix is computed most efficiently using a complex energy contour, which is possible as  $E \mathbf{G}^{(\bar{\mathbf{k}})}(E + i0^+)$  is analytical in the upper half of the complex plane.

## 5.5 Evaluation of atomic forces

### 5.5.1 Atomic Forces within standard FLAPW

The atomic force on atom  $\alpha$  may be obtained as the derivative of the total energy with respect to the position of this atom:

$$\mathbf{F}^\alpha = \frac{\partial E}{\partial \boldsymbol{\tau}_\alpha}. \quad (5.28)$$

In the context of the FLAPW method expressions for this derivative have been derived in several ways [58, 59, 60]. Various strategies for the evaluation of Eq. (5.28) are compared in Ref. [61]. We shortly sketch the derivation given by Yu, Singh and Krakauer in Ref. [59] for the standard *wave-function based* FLAPW-method. This will form the starting point for finding the expression for the atomic force within the *Green-function based* formulation of FLAPW used in this work. Differentiation of the total energy expression Eq. (2.13) yields

$$\mathbf{F}^\alpha = \mathbf{F}_{\text{HF}}^\alpha - \left[ \sum_{\mathbf{k}, i} n_{\mathbf{k}, i} \frac{\partial \epsilon_{\mathbf{k}, i}}{\partial \boldsymbol{\tau}_\alpha} - \int \rho(\mathbf{r}) \frac{\partial V_{\text{eff}}(\mathbf{r})}{\partial \boldsymbol{\tau}_\alpha} d^3 r \right], \quad (5.29)$$

where the *Hellman-Feynman force*, which is equal to the *electrostatic force on the nucleus* of atom  $\alpha$ , is given by

$$\mathbf{F}_{\text{HF}}^\alpha = Z_\alpha \frac{\partial}{\partial \boldsymbol{\tau}_\alpha} \left[ \int \frac{\rho(\mathbf{r})}{|\boldsymbol{\tau}_\alpha - \mathbf{r}|} d^3 r - \sum_{\beta \neq \alpha} \sum_{\mathbf{R}} \frac{Z_\beta}{|\boldsymbol{\tau}_\alpha - \boldsymbol{\tau}_\beta + \mathbf{R}|} \right]. \quad (5.30)$$



From the electrostatic potential  $V^{\text{es}}(\mathbf{r})$  and the charge density inside the muffin-tin the Hellman-Feynman force may be calculated as follows:

$$\mathbf{F}_{\text{HF}}^{\alpha} = Z_{\alpha} \sum_{m=-1}^1 \left\{ \frac{4\pi}{3} \int_0^{R_{\alpha}} \rho_{1m}(\mathbf{r}) \left[ 1 - \left( \frac{r}{R_{\alpha}} \right)^3 \right] dr + \frac{V_{1m}^{\text{es}}(R_{\alpha})}{R_{\alpha}} \right\} \nabla[rY_{1m}(\hat{\mathbf{r}})]. \quad (5.31)$$

Both core and valence states contribute to the term given in brackets in Eq. (5.29), which is a *correction to the Hellman-Feynman force*. Under the condition that the core states are well localized inside the muffin-tins, the core contribution to this correction is given by

$$\mathbf{F}_{\text{core}}^{\alpha} = - \int \rho_{\text{core}}^{\alpha}(\mathbf{r}) \nabla V_{\text{eff}}(\mathbf{r}) d^3 r, \quad (5.32)$$

where the integration region is the muffin-tin sphere of atom  $\alpha$ , and  $\rho_{\text{core}}^{\alpha}(\mathbf{r})$  the core-charge. Performing the angular integrations we obtain:

$$\mathbf{F}_{\text{core}}^{\alpha} = - \frac{8\pi}{3} \sum_{m=-1}^1 \nabla[rY_{1m}(\hat{\mathbf{r}})] \int_0^{R_{\alpha}} \rho_{\text{core}}^{\alpha}(r) \left[ rV_{1m}^{\text{eff}}(r) + \frac{1}{2}r^2 \frac{\partial V_{1m}^{\text{eff}}(r)}{\partial r} \right] dr. \quad (5.33)$$

As for the correction due to the valence states, we have to take into account that the LAPW-basis functions and consequently also the overlap and Hamiltonian matrices will change if the atoms' positions change. The variation of the  $i$ -th eigenvalue,  $\epsilon_{\mathbf{k},i}$ , is related to the variations of the Hamiltonian matrix  $H_{\mathbf{G},\mathbf{G}'}^{(\mathbf{k})}$  and the overlap matrix  $S_{\mathbf{G},\mathbf{G}'}^{(\mathbf{k})}$  like

$$\delta\epsilon_{\mathbf{k},i} = \sum_{\mathbf{G},\mathbf{G}'} (C_{\mathbf{k},i}(\mathbf{G}))^* [\delta H_{\mathbf{G},\mathbf{G}'}^{(\mathbf{k})} - \epsilon_{\mathbf{k},i} \delta S_{\mathbf{G},\mathbf{G}'}^{(\mathbf{k})}] C_{\mathbf{k},i}(\mathbf{G}'), \quad (5.34)$$

where the  $C_i(\mathbf{G})$  are the expansion coefficients of the  $i$ -th eigenstate,  $\Psi_{\mathbf{k},i}$ , in terms of the LAPW-basis functions  $\phi_{\mathbf{k},\mathbf{G}}(\mathbf{r})$ :

$$\Psi_{\mathbf{k},i}(\mathbf{r}) = \sum_{\mathbf{G}} C_{\mathbf{k},i}(\mathbf{G}) \phi_{\mathbf{k},\mathbf{G}}(\mathbf{r}). \quad (5.35)$$

Introducing the variation of the  $i$ -th eigenfunction due to a change of the LAPW-basis functions,

$$\delta\Psi_{\mathbf{k},i}(\mathbf{r}) = \sum_{\mathbf{G}} C_{\mathbf{k},i}(\mathbf{G}) \delta\phi_{\mathbf{k},\mathbf{G}}(\mathbf{r}), \quad (5.36)$$

we may cast Eq. (5.34) into the compact form

$$\delta\epsilon_{\mathbf{k},i} = \delta\langle\Psi_{\mathbf{k},i}|(\hat{H} - \epsilon_{\mathbf{k},i})|\Psi_{\mathbf{k},i}\rangle. \quad (5.37)$$

As the second derivatives of the basis-functions (within the APW+lo scheme also the first derivatives) are discontinuous at the muffin-tin boundaries, there is a finite change in

the kinetic energy of eigenstate  $i$  in the non-overlapping regions of the original and the displaced muffin-tin spheres of atom  $\alpha$ :

$$\delta T_{\mathbf{k},i} = \mathbf{D}_{\mathbf{k},i} \cdot \delta \boldsymbol{\tau}_\alpha, \quad (5.38)$$

where

$$\mathbf{D}_{\mathbf{k},i} = \int [(\Psi_{\mathbf{k},i}(\mathbf{r}))^* \hat{T} \Psi_{\mathbf{k},i}(\mathbf{r})|_{\text{MT}} - (\Psi_{\mathbf{k},i}(\mathbf{r}))^* \hat{T} \Psi_{\mathbf{k},i}(\mathbf{r})|_{\text{INT}}] d\mathbf{S}_\alpha \quad (5.39)$$

is a surface integral on the muffin-tin boundary of atom  $\alpha$  and  $\hat{T}$  is the operator of kinetic energy. The complete expression for the correction to the Hellman-Feynman force due to the valence states is then

$$\begin{aligned} \mathbf{F}_{\text{IBS}}^\alpha &= - \left[ \sum_{\mathbf{k},i} n_{\mathbf{k},i} \frac{\partial \epsilon_{\mathbf{k},i}}{\partial \boldsymbol{\tau}_\alpha} - \int \rho(\mathbf{r}) \frac{\partial V_{\text{eff}}(\mathbf{r})}{\partial \boldsymbol{\tau}_\alpha} d^3 r \right] \\ &= - \sum_{\mathbf{k},i} n_{\mathbf{k},i} \left[ \left\langle \frac{\partial \Psi_{\mathbf{k},i}}{\partial \boldsymbol{\tau}_\alpha} \right| (\hat{H} - \epsilon_{\mathbf{k},i}) | \Psi_{\mathbf{k},i} \right\rangle + \left\langle \Psi_{\mathbf{k},i} \right| (\hat{H} - \epsilon_{\mathbf{k},i}) \left| \frac{\partial \Psi_{\mathbf{k},i}}{\partial \boldsymbol{\tau}_\alpha} \right\rangle + \mathbf{D}_{\mathbf{k},i} \right], \end{aligned} \quad (5.40)$$

which is non-vanishing only because of the use of an *incomplete basis set* (IBS). The derivative of the basis functions with respect to the atomic displacement is given by

$$\frac{\partial \phi_{\mathbf{k},\mathbf{G}}(\mathbf{r})}{\partial \boldsymbol{\tau}_\alpha} = i(\mathbf{k} + \mathbf{G}) \phi_{\mathbf{k},\mathbf{G}}(\mathbf{r}) - \nabla \phi_{\mathbf{k},\mathbf{G}}(\mathbf{r}), \quad (5.41)$$

where variations in  $u_l$  and  $\dot{u}_l$  are neglected. It is non-vanishing only inside the MT-sphere of the displaced atom. Substitution into Eq. (5.40) yields

$$\begin{aligned} \mathbf{F}_{\text{IBS}}^\alpha &= - \sum_{\mathbf{k},i} n_{\mathbf{k},i} \left[ i \sum_{\mathbf{G},\mathbf{G}'} (\mathbf{G}' - \mathbf{G}) (C_{\mathbf{k},i}(\mathbf{G}))^* C_{\mathbf{k},i}(\mathbf{G}') \langle \phi_{\mathbf{k},\mathbf{G}} | (\hat{H} - \epsilon_{\mathbf{k},i}) | \phi_{\mathbf{k},\mathbf{G}'} \rangle_{\text{MT}} \right. \\ &\quad \left. - \langle \nabla \Psi_{\mathbf{k},i} | (\hat{H} - \epsilon_{\mathbf{k},i}) | \Psi_{\mathbf{k},i} \rangle_{\text{MT}} - \langle \Psi_{\mathbf{k},i} | (\hat{H} - \epsilon_{\mathbf{k},i}) | \nabla \Psi_{\mathbf{k},i} \rangle_{\text{MT}} + \mathbf{D}_i \right], \end{aligned} \quad (5.42)$$

where the integration is over the MT-sphere only, as indicated by the subscript MT. In order to evaluate the first term, it is convenient to separate the Hamiltonian into its spherical and its non-spherical parts,

$$\hat{H} = \hat{H}_{\text{sph}} + \hat{V}_{\text{eff}}^{NS}, \quad (5.43)$$

and to treat the spherical and non-spherical parts separately. For the spherical part we obtain

$$\begin{aligned} \mathbf{F}_{\text{IBS}}^{\alpha,\text{sph}} &= -i \sum_{\mathbf{k},i} n_{\mathbf{k},i} \sum_{\mathbf{G},\mathbf{G}'} (\mathbf{G}' - \mathbf{G}) (C_{\mathbf{k},i}(\mathbf{G}))^* C_{\mathbf{k},i}(\mathbf{G}') \langle \phi_{\mathbf{k},\mathbf{G}} | (\hat{H}_{\text{sph}} - \epsilon_{\mathbf{k},i}) | \phi_{\mathbf{k},\mathbf{G}'} \rangle_{\text{MT}} \\ &= \sum_{\mathbf{k},i} \sum_{l,m} \Im \{ \mathbf{A}_{lm}^i [2A_{lm}^i(\epsilon_l - \epsilon_{\mathbf{k},i}) + B_{lm}^i]^* + \mathbf{B}_{lm}^i [2B_{lm}^i(\epsilon_l - \epsilon_{\mathbf{k},i})N_l + A_{lm}^i]^* \}, \end{aligned} \quad (5.44)$$

where

$$\mathbf{A}_{lm}^i = \sum_{\mathbf{G}} \mathbf{G} C_{\mathbf{k},i}(\mathbf{G}) a_{lm}^\alpha(\mathbf{G}). \quad (5.45)$$

The contribution of the nonspherical potential is given by

$$\begin{aligned}
\mathbf{F}_{\text{IBS}}^{\alpha, \text{NS}} &= -i \sum_{\mathbf{k}, i} n_{\mathbf{k}, i} \sum_{\mathbf{G}, \mathbf{G}'} (\mathbf{G}' - \mathbf{G}) (C_{\mathbf{k}, i}(\mathbf{G}))^* C_{\mathbf{k}, i}(\mathbf{G}') \langle \phi_{\mathbf{k}, \mathbf{G}} | \hat{V}_{\text{eff}}^{\text{NS}} | \phi_{\mathbf{k}, \mathbf{G}'} \rangle_{\text{MT}} \\
&= 2 \sum_{\mathbf{k}, i} n_{\mathbf{k}, i} \sum_{l, m} \sum_{l', m'} \sum_{\nu, M} \Im [C_{L\nu, M}^{\nu} \int (Y_{l', m'}^*) Y_{L\nu, M} Y_{l, m} d\Omega \times \\
&\quad \times \int (A_{l', m'}^i u_{l'} + B_{l', m'}^i \dot{u}_{l'})^* V_{\nu} (A_{lm}^i u_l + B_{lm}^i \dot{u}_l) r^2 dr].
\end{aligned} \tag{5.46}$$

### 5.5.2 Atomic Forces within the Embedding Method

Clearly, the Hellman-Feynman force, as given in Eq. (5.31) depends only on the charge density and on the electrostatic potential, and consequently it may be used within the embedding method without any modifications. Likewise, we may simply take over the core correction to the force, Eq. (5.33), into the embedding method, as it depends only on the core charge and the effective potential. What cannot be taken over easily is the *incomplete basis set correction*, Eq. (5.40), because a formulation in terms of the Green function is needed. In the expression for the nonspherical contribution to the IBS, Eq. (5.46), we can easily identify the density matrix

$$\rho_{\mathbf{G}, \mathbf{G}'}^{\bar{\mathbf{k}}} = \sum_i n_{\bar{\mathbf{k}}, i} (C_{\bar{\mathbf{k}}, i}(\mathbf{G}))^* C_{\bar{\mathbf{k}}, i}(\mathbf{G}'), \tag{5.47}$$

so that Eq. (5.46) becomes

$$\mathbf{F}_{\text{IBS}}^{\alpha, \text{NS}} = -i \sum_{\bar{\mathbf{k}}} \sum_{\mathbf{G}, \mathbf{G}'} (\mathbf{G}' - \mathbf{G}) \rho_{\mathbf{G}, \mathbf{G}'}^{\bar{\mathbf{k}}} \langle \phi_{\mathbf{k}, \mathbf{G}} | \hat{V}_{\text{eff}}^{\text{NS}} | \phi_{\mathbf{k}, \mathbf{G}'} \rangle_{\text{MT}}. \tag{5.48}$$

Analogously, we may write Eq. (5.44) in terms of the density matrix  $\rho_{\mathbf{G}, \mathbf{G}'}^{\bar{\mathbf{k}}}$  and the *energy density matrix*

$$\epsilon_{\mathbf{G}, \mathbf{G}'}^{\bar{\mathbf{k}}} = \sum_i n_{\bar{\mathbf{k}}, i} \epsilon_{\bar{\mathbf{k}}, i} (C_{\bar{\mathbf{k}}, i}(\mathbf{G}))^* C_{\bar{\mathbf{k}}, i}(\mathbf{G}') \tag{5.49}$$

as follows:

$$\begin{aligned}
\mathbf{F}_{\text{IBS}}^{\alpha, \text{sph}} &= -i \sum_{\mathbf{k}, i} n_{\mathbf{k}, i} \sum_{\mathbf{G}, \mathbf{G}'} (\mathbf{G}' - \mathbf{G}) (C_{\mathbf{k}, i}(\mathbf{G}))^* C_{\mathbf{k}, i}(\mathbf{G}') \langle \phi_{\mathbf{k}, \mathbf{G}} | \hat{H}_{\text{sph}} | \phi_{\mathbf{k}, \mathbf{G}'} \rangle_{\text{MT}} + \\
&\quad + i \sum_{\mathbf{k}, i} n_{\mathbf{k}, i} \sum_{\mathbf{G}, \mathbf{G}'} (\mathbf{G}' - \mathbf{G}) (C_{\mathbf{k}, i}(\mathbf{G}))^* C_{\mathbf{k}, i}(\mathbf{G}') \langle \phi_{\mathbf{k}, \mathbf{G}} | \epsilon_{\mathbf{k}, i} | \phi_{\mathbf{k}, \mathbf{G}'} \rangle_{\text{MT}} \\
&= -i \sum_{\mathbf{k}} \sum_{\mathbf{G}, \mathbf{G}'} (\mathbf{G}' - \mathbf{G}) \rho_{\mathbf{G}, \mathbf{G}'}^{\bar{\mathbf{k}}} \langle \phi_{\mathbf{k}, \mathbf{G}} | \hat{H}_{\text{sph}} | \phi_{\mathbf{k}, \mathbf{G}'} \rangle_{\text{MT}} + \\
&\quad + i \sum_{\mathbf{k}} \sum_{\mathbf{G}, \mathbf{G}'} (\mathbf{G}' - \mathbf{G}) \epsilon_{\mathbf{G}, \mathbf{G}'}^{\bar{\mathbf{k}}} \langle \phi_{\mathbf{k}, \mathbf{G}} | \phi_{\mathbf{k}, \mathbf{G}'} \rangle_{\text{MT}}.
\end{aligned} \tag{5.50}$$

Clearly, two ways are possible to implement the IBS correction force within the embedding method. The obvious way is to calculate the density and energy density matrices and to obtain the IBS correction by evaluating Eq. (5.48) and Eq. (5.50) directly. Alternatively, one may also diagonalize the density and energy density matrices in order to obtain *effective* eigenstates  $C_{\mathbf{k},i}(\mathbf{G})$ , which one may then use to evaluate Eq. (5.44) and Eq. (5.46) directly. The latter approach has the advantage, that only minor modifications are needed with respect to the existing wave-function based implementation of the IBS correction. However, in the former approach no diagonalization and no summation over eigenstates are needed, what saves computational time. We note that two different sets of eigenstates  $C_{\mathbf{k},i}(\mathbf{G})$  are needed for the latter approach: The set of eigenstates of the density matrix and the set of eigenstates of the energy density matrix. All terms in Eq. (5.44) which involve the Bloch eigenvalue  $\epsilon_{\mathbf{k},i}$  have to be evaluated using the eigenstates of the energy density matrix, while the remaining terms are evaluated from the eigenstates of the density matrix.

# Chapter 6

## Efficient Embedding

In the present chapter we discuss how the efficiency of the embedding method may be optimized by exploiting the fact that the embedding potential is a *surface potential* defined on the embedding planes. While it is possible to obtain the Green function from a matrix inversion as prescribed by Eq. (4.40), this is usually not the most efficient way to do it, especially if not the *full* Green function is needed, but only its *surface projections* Eq. (4.60). The surface projections are matrices of the size  $N_{2D} \times N_{2D}$ , while the Green function has the dimension of the LAPW basis set, which we denote  $N_{LAPW}$ . What is the most efficient way to do the computations depends on the quantities that are supposed to be calculated. Various schemes are presented in the following.

### 6.1 Solution of a linear system of equations

For the calculation of the *complex band structure* or the *conductance*, only the surface projections of the Green function are needed. In case of the complex band structure we need the Green function with von Neumann boundary conditions, while the physical Green function is needed for the conductance. Both Green functions are given by Eq. (4.40). Multiplying Eq. (4.40) by  $[\mathbf{P}_{S_L}, \mathbf{P}_{S_R}]^\dagger$  from the right we see that the incomplete surface projection of the Green function  $\mathbf{G}^{(\bar{\mathbf{k}})}(E)$ , which is given by

$$\mathbf{Y} := \mathbf{G}^{(\bar{\mathbf{k}})}(E)[\mathbf{P}_{S_L}, \mathbf{P}_{S_R}]^\dagger, \quad (6.1)$$

is a solution of

$$[E\mathbf{S}^{(\bar{\mathbf{k}})} - \mathbf{H}^{(\bar{\mathbf{k}})} - \mathbf{\Sigma}^{(\bar{\mathbf{k}})}(E)]\mathbf{Y} = [\mathbf{P}_{S_L}, \mathbf{P}_{S_R}]^\dagger. \quad (6.2)$$

The fully surface-projected Green function is obtained in a subsequent step as

$$\begin{pmatrix} \overline{\mathbf{G}}_{S_L, S_L}^{(\bar{\mathbf{k}})}(E) & \overline{\mathbf{G}}_{S_L, S_R}^{(\bar{\mathbf{k}})}(E) \\ \overline{\mathbf{G}}_{S_R, S_L}^{(\bar{\mathbf{k}})}(E) & \overline{\mathbf{G}}_{S_R, S_R}^{(\bar{\mathbf{k}})}(E) \end{pmatrix} = [\mathbf{P}_{S_L}, \mathbf{P}_{S_R}]\mathbf{Y}. \quad (6.3)$$

Clearly, solving the linear system of equations, Eq. (6.2), for  $\mathbf{Y}$  is more efficient than calculating first the  $N_{LAPW} \times N_{LAPW}$  matrix  $\mathbf{G}^{(\bar{\mathbf{k}})}(E)$  by matrix inversion according to

Eq. (4.40) and then performing the surface projection Eq. (4.60) to obtain the  $N_{2D} \times N_{2D}$  matrices  $\overline{\mathbf{G}}_{S,S'}^{(\bar{\mathbf{k}})}(E)$ . This scheme is the most efficient one, whenever the number of energy points for which the surface-projected Green function is needed at each  $k$ -point is small. However, if the number of energy points is large one may benefit from the spectral representation and solving a linear system of equations as described here is no longer the method of choice. How to profit from the spectral representation is discussed in the following sections.

## 6.2 Spectral representation of the Green function

For the calculation of the complex band structure following the procedure described after Eq. (4.64) or the embedding potential according to Eq. (4.67) the transfer matrix Eq. (4.64) is needed, which is calculated from the Green function with von Neumann's boundary conditions. For the calculation of the Green function satisfying von Neumann's boundary conditions, the embedding potentials are set to zero, and Eq. (4.40) simplifies:

$$\mathbf{G}^{0(\bar{\mathbf{k}})}(E) = [E\mathbf{S}^{(\bar{\mathbf{k}})} - \mathbf{H}^{(\bar{\mathbf{k}})}]^{-1}. \quad (6.4)$$

Due to this simple energy dependence, it is efficient to calculate the Green function from the spectral representation of the Hamiltonian: The spectral representation has to be calculated only once for a given  $\bar{\mathbf{k}}$  point, while the inversion would have to be performed at each energy. Denoting the eigenvectors and eigenvalues of the generalized eigenvalue problem by  $\mathbf{v}_j$  and  $\epsilon_j$ , respectively, we have

$$\mathbf{H}^{(\bar{\mathbf{k}})}\mathbf{v}_j = \epsilon_j\mathbf{S}^{(\bar{\mathbf{k}})}\mathbf{v}_j. \quad (6.5)$$

Introducing the matrix of eigenvectors

$$\mathbf{V} := [\mathbf{v}_1, \dots, \mathbf{v}_{N_{LAPW}}] \quad (6.6)$$

and the diagonal matrix of eigenvalues

$$\mathcal{E}_{ij} = \epsilon_i\delta_{ij}, \quad (6.7)$$

and making use of the identities

$$\mathbf{V}^\dagger\mathbf{S}^{(\bar{\mathbf{k}})}\mathbf{V} = \mathbf{1} \quad (6.8)$$

and

$$\mathbf{V}^\dagger\mathbf{H}^{(\bar{\mathbf{k}})}\mathbf{V} = \mathcal{E} \quad (6.9)$$

we obtain

$$\mathbf{G}^{0(\bar{\mathbf{k}})}(E) = [E\mathbf{S}^{(\bar{\mathbf{k}})} - \mathbf{H}^{(\bar{\mathbf{k}})}]^{-1} = \mathbf{V}[E - \mathcal{E}]^{-1}\mathbf{V}^\dagger. \quad (6.10)$$

Hence, the calculation of the Green function has been reduced to the inversion of a diagonal matrix and matrix multiplications. According to Eq. (4.64), only the surface projections

of the Green function, Eq. (4.60), are needed. Thus, the size of the matrices that have to be multiplied at each energy point and consequently the computational burden may be further reduced by introducing the projected matrix of eigenvectors

$$\bar{\mathbf{V}} = [\mathbf{P}_{S_L}, \mathbf{P}_{S_R}] \mathbf{V} \quad (6.11)$$

in terms of which the surface projected Green function runs

$$\begin{pmatrix} \bar{\mathbf{G}}_{S_L, S_L}^{0(\bar{\mathbf{k}})}(E) & \bar{\mathbf{G}}_{S_L, S_R}^{0(\bar{\mathbf{k}})}(E) \\ \bar{\mathbf{G}}_{S_R, S_L}^{0(\bar{\mathbf{k}})}(E) & \bar{\mathbf{G}}_{S_R, S_R}^{0(\bar{\mathbf{k}})}(E) \end{pmatrix} = \bar{\mathbf{V}}[E - \boldsymbol{\varepsilon}]^{-1} \bar{\mathbf{V}}^\dagger. \quad (6.12)$$

### 6.3 Dyson equation

The calculation of the surface projected Green function in the presence of an embedding potential is more complicated due to the *energy dependence* of the embedding potential. Consequently, one can no longer straightforwardly profit from the spectral representation, as in the previous section. However, combining the spectral representation of the Green function with von Neumann boundary conditions with the *Dyson equation* and the surface projector, it becomes possible to devise an efficient computational scheme. From the Green function with von Neumann boundary conditions, the Green function in the presence of an embedding potential may be obtained by iterating the corresponding Dyson equation:

$$\begin{aligned} \mathbf{G}^{(\bar{\mathbf{k}})}(E) &= \mathbf{G}^{0(\bar{\mathbf{k}})}(E) + \mathbf{G}^{0(\bar{\mathbf{k}})}(E) \boldsymbol{\Sigma}^{(\bar{\mathbf{k}})}(E) \mathbf{G}^{0(\bar{\mathbf{k}})}(E) + \\ &+ \mathbf{G}^{0(\bar{\mathbf{k}})}(E) \boldsymbol{\Sigma}^{(\bar{\mathbf{k}})}(E) \mathbf{G}^{0(\bar{\mathbf{k}})}(E) \boldsymbol{\Sigma}^{(\bar{\mathbf{k}})}(E) \mathbf{G}^{0(\bar{\mathbf{k}})}(E) + \dots, \end{aligned} \quad (6.13)$$

where  $\boldsymbol{\Sigma}^{(\bar{\mathbf{k}})}(E)$  is the sum of the left and right embedding potentials,  $\boldsymbol{\Sigma}_{S_L}^{(\bar{\mathbf{k}})}(E)$  and  $\boldsymbol{\Sigma}_{S_R}^{(\bar{\mathbf{k}})}(E)$ , respectively. Inserting Eq. (4.49) for  $\boldsymbol{\Sigma}^{(\bar{\mathbf{k}})}(E)$  into the previous equation and calculating its surface projection, Eq. (4.60), the surface projectors may be rearranged to yield a Dyson equation formulated entirely in terms of surface quantities:

$$\begin{aligned} \bar{\mathbf{G}}^{(\bar{\mathbf{k}})}(E) &= \mathbf{P} \mathbf{G}^{0(\bar{\mathbf{k}})}(E) \mathbf{P}^\dagger + \mathbf{P} \mathbf{G}^{0(\bar{\mathbf{k}})}(E) \mathbf{P}^\dagger \bar{\boldsymbol{\Sigma}}^{(\bar{\mathbf{k}})}(E) \mathbf{P} \mathbf{G}^{0(\bar{\mathbf{k}})}(E) \mathbf{P}^\dagger + \dots \\ &= \bar{\mathbf{G}}^{0(\bar{\mathbf{k}})}(E) + \bar{\mathbf{G}}^{0(\bar{\mathbf{k}})}(E) \bar{\boldsymbol{\Sigma}}^{(\bar{\mathbf{k}})}(E) \bar{\mathbf{G}}^{0(\bar{\mathbf{k}})}(E) + \dots \\ &= [1 - \bar{\mathbf{G}}^{0(\bar{\mathbf{k}})}(E) \bar{\boldsymbol{\Sigma}}^{(\bar{\mathbf{k}})}(E)]^{-1} \bar{\mathbf{G}}^{0(\bar{\mathbf{k}})}(E), \end{aligned} \quad (6.14)$$

where we introduced the notation

$$\bar{\mathbf{G}}^{(\bar{\mathbf{k}})}(E) = \begin{pmatrix} \bar{\mathbf{G}}_{S_L, S_L}^{(\bar{\mathbf{k}})}(E) & \bar{\mathbf{G}}_{S_L, S_R}^{(\bar{\mathbf{k}})}(E) \\ \bar{\mathbf{G}}_{S_R, S_L}^{(\bar{\mathbf{k}})}(E) & \bar{\mathbf{G}}_{S_R, S_R}^{(\bar{\mathbf{k}})}(E) \end{pmatrix}, \quad (6.15)$$

$$\bar{\boldsymbol{\Sigma}}^{(\bar{\mathbf{k}})}(E) = \begin{pmatrix} \bar{\boldsymbol{\Sigma}}_{S_L}^{(\bar{\mathbf{k}})}(E) & \mathbf{0} \\ \mathbf{0} & \bar{\boldsymbol{\Sigma}}_{S_R}^{(\bar{\mathbf{k}})}(E) \end{pmatrix}, \quad (6.16)$$

and

$$\mathbf{P} = [\mathbf{P}_{S_L}, \mathbf{P}_{S_R}]. \quad (6.17)$$

Writing the last equation in Eq. (6.14) in a more familiar form of the Dyson equation, we finally obtain

$$\overline{\mathbf{G}}^{(\bar{\mathbf{k}})}(E) = \overline{\mathbf{G}}^{0(\bar{\mathbf{k}})}(E) + \overline{\mathbf{G}}^{0(\bar{\mathbf{k}})}(E) \overline{\Sigma}^{(\bar{\mathbf{k}})}(E) \overline{\mathbf{G}}^{(\bar{\mathbf{k}})}(E). \quad (6.18)$$

This result is of great usefulness both for practical calculations and for theoretical investigations. Where numerical applications are concerned, it shows that inverting a large  $N_{\text{LAPW}} \times N_{\text{LAPW}}$  matrix according to Eq. (4.40) and performing the surface projections Eq. (4.60) afterwards, is essentially equivalent to inverting a small matrix of size  $N_{2\text{D}} \times N_{2\text{D}}$ , namely  $[1 - \overline{\mathbf{G}}^{0(\bar{\mathbf{k}})}(E) \overline{\Sigma}^{(\bar{\mathbf{k}})}(E)]$ , which is a much smaller computational burden. Furthermore, we will use this result, Eq. (6.18), to prove the equivalence between several computational schemes for the embedding potential in the next section.

We formulated the Dyson equation for the complete surface projected Green function in Eq. (6.18), which involves matrices of size  $2N_{2\text{D}} \times 2N_{2\text{D}}$ . However, according to Eq. (4.61), only the projection  $\mathbf{G}_{S_L, S_R}^{(\bar{\mathbf{k}})}(E)$  is needed for the calculation of the conductance. Using Equations (6.15) and (6.16), the compact formulation of the Dyson equation given in Eq. (6.15) may be recast as a coupled set of four equations involving matrices of size  $N_{2\text{D}} \times N_{2\text{D}}$ . Solving this set of coupled equations for  $\overline{\mathbf{G}}_{S_L, S_R}^{(\bar{\mathbf{k}})}(E)$ , one obtains an efficient formula for the computation of  $\overline{\mathbf{G}}_{S_L, S_R}^{(\bar{\mathbf{k}})}(E)$ :

$$\begin{aligned} \mathbf{G}_{S_L, S_R}^{(\bar{\mathbf{k}})}(E) &= \\ &= \left[ \mathbf{1} - \left( \overline{\mathbf{G}}_{S_L S_L}^{0(\bar{\mathbf{k}})}(E) + \mathbf{A} \overline{\mathbf{G}}_{S_R S_L}^{0(\bar{\mathbf{k}})}(E) \right) \overline{\Sigma}_{S_L}^{(\bar{\mathbf{k}})}(E) \right]^{-1} \left( \overline{\mathbf{G}}_{S_L S_R}^{0(\bar{\mathbf{k}})}(E) + \mathbf{A} \overline{\mathbf{G}}_{S_R S_R}^{0(\bar{\mathbf{k}})}(E) \right), \end{aligned} \quad (6.19)$$

where the matrix  $\mathbf{A}$  is defined as follows:

$$\mathbf{A} = \overline{\mathbf{G}}_{S_L S_R}^{0(\bar{\mathbf{k}})}(E) \overline{\Sigma}_{S_R}^{(\bar{\mathbf{k}})}(E) \left( \mathbf{1} - \overline{\mathbf{G}}_{S_R S_R}^{0(\bar{\mathbf{k}})}(E) \overline{\Sigma}_{S_R}^{(\bar{\mathbf{k}})}(E) \right)^{-1} \quad (6.20)$$

### 6.3.1 Propagation of the embedding potential

There exist several applications of the embedding method, where it is of interest to know how the embedding potential evolves, when the embedding surface is moved. Besides the use for the development of computational schemes exhibiting an order-N scaling behavior, which has been sketched in section 4.6 and will be discussed in detail in chapter 7, an iterative method for the determination of the embedding potential has been proposed [25]:

Considering a principal layer of a bulk system, the left embedding potential  $\overline{\Sigma}_{S_L}^{(\bar{\mathbf{k}})}(E)$  on the left embedding surface  $S_L$  of the principal layer is propagated to the right embedding surface  $S'_L$ , where it is given by  $\overline{\Sigma}_{S'_L}^{(\bar{\mathbf{k}})}(E)$ . Apart from a phase factor, the propagated embedding potential  $\overline{\Sigma}_{S'_L}^{(\bar{\mathbf{k}})}(E)$  has to coincide with the left embedding potential  $\overline{\Sigma}_{S_L}^{(\bar{\mathbf{k}})}(E)$ ,



which leads to the equation

$$\overline{\Sigma}_{S_L}^{(\bar{\mathbf{k}})}(E) = \mathbf{U}_{\parallel}^{(\bar{\mathbf{k}})} \overline{\Sigma}_{S'_L}^{(\bar{\mathbf{k}})}(E) (\mathbf{U}_{\parallel}^{(\bar{\mathbf{k}})})^{-1}. \quad (6.21)$$

Consequently, the embedding potential may be identified as a fix point of the propagation operation from the left to the right side of a principal layer. The fix point of Eq. (6.21) may be determined iteratively. In the following, we prove, that this scheme for the calculation of the embedding potential is mathematically equivalent to Eq. (4.67). Decomposing the eigenvalue Eq. (4.65) into its components, we obtain

$$\begin{aligned} \Psi \lambda &= \tilde{\mathbf{T}}_{11}^{(\bar{\mathbf{k}})}(E) \Psi - \tilde{\mathbf{T}}_{12}^{(\bar{\mathbf{k}})} \overline{\mathbf{S}}_{S_L} \Psi', \\ -\overline{\mathbf{S}}_{S_L} \Psi' \lambda &= \tilde{\mathbf{T}}_{21}^{(\bar{\mathbf{k}})} \Psi - \tilde{\mathbf{T}}_{22}^{(\bar{\mathbf{k}})} \overline{\mathbf{S}}_{S_L} \Psi', \end{aligned} \quad (6.22)$$

where  $\Psi$  and  $\Psi'$  are the eigenvector matrices defined in Eq. (4.68) and  $\lambda$  is the corresponding diagonal matrix of eigenvalues. Using Eq. (6.22), we may evaluate Eq. (4.67) for the embedding potential:

$$\begin{aligned} \overline{\Sigma}_{S_L}^{(\bar{\mathbf{k}})}(E) &= -\frac{1}{2}(\overline{\mathbf{S}}_{S_L} \Psi')(\Psi)^{-1} = -\frac{1}{2}(\overline{\mathbf{S}}_{S_L} \Psi' \lambda)(\Psi \lambda)^{-1} = \\ &= \frac{1}{2} \left( \tilde{\mathbf{T}}_{21}^{(\bar{\mathbf{k}})}(E) \Psi - \tilde{\mathbf{T}}_{22}^{(\bar{\mathbf{k}})}(E) \overline{\mathbf{S}}_{S_L} \Psi' \right) \left( \tilde{\mathbf{T}}_{11}^{(\bar{\mathbf{k}})}(E) \Psi - \tilde{\mathbf{T}}_{12}^{(\bar{\mathbf{k}})}(E) \overline{\mathbf{S}}_{S_L} \Psi' \right)^{-1} = \\ &= \frac{1}{2} (\tilde{\mathbf{T}}_{21}^{(\bar{\mathbf{k}})}(E) + 2\tilde{\mathbf{T}}_{22}^{(\bar{\mathbf{k}})}(E) \overline{\Sigma}_{S_L}^{(\bar{\mathbf{k}})}(E)) (\tilde{\mathbf{T}}_{11}^{(\bar{\mathbf{k}})}(E) + 2\tilde{\mathbf{T}}_{12}^{(\bar{\mathbf{k}})}(E) \overline{\Sigma}_{S_L}^{(\bar{\mathbf{k}})}(E))^{-1} \\ &= \frac{1}{2} \mathbf{U}^{(\bar{\mathbf{k}})}(\mathbf{b}_{\parallel}) (\mathbf{T}_{21}^{(\bar{\mathbf{k}})}(E) + 2\mathbf{T}_{22}^{(\bar{\mathbf{k}})}(E) \overline{\Sigma}_{S_L}^{(\bar{\mathbf{k}})}(E)) \times \\ &\quad \times (\mathbf{T}_{11}^{(\bar{\mathbf{k}})}(E) + 2\mathbf{T}_{12}^{(\bar{\mathbf{k}})}(E) \overline{\Sigma}_{S_L}^{(\bar{\mathbf{k}})}(E))^{-1} (\mathbf{U}^{(\bar{\mathbf{k}})}(\mathbf{b}_{\parallel}))^{-1}. \end{aligned} \quad (6.23)$$

Thus, the embedding potential  $\overline{\Sigma}_{S_L}^{(\bar{\mathbf{k}})}(E)$  calculated according to Eq. (4.67) satisfies Eq. (6.21). Obviously, any combination of  $N_{2D}$  eigenvectors of Eq. (4.65) used to construct an embedding potential according to Eq. (4.67) leads to a solution of Eq. (6.21).

We derived the Eq. (4.70) for the propagation of the embedding potential based on the transfer-matrix technique. An alternative formula for the propagation of the embedding potential may be obtained directly from Green's theorem [25]: On the left embedding surface  $S_L$  of the propagation volume  $A$  boundary conditions are imposed via the left embedding potential, while on the right embedding surface  $S'_L$ , von Neumann boundary conditions are imposed. Denoting the corresponding Green function of the propagation volume  $A$  by  $\mathbf{G}^{t(\bar{\mathbf{k}})}(E)$ , the propagated embedding potential on the right embedding surface  $S'_L$  is given by the surface inverse of the surface projection  $\overline{\mathbf{G}}_{S'_L, S'_L}^{t(\bar{\mathbf{k}})}(E)$ :

$$\overline{\Sigma}_{S'_L}^{(\bar{\mathbf{k}})}(E) = -(\overline{\mathbf{G}}_{S'_L, S'_L}^{t(\bar{\mathbf{k}})}(E))^{-1}. \quad (6.24)$$

We now use the Dyson equation for the surface projected Green function, Eq. (6.14), to cast Eq. (6.24) into a form that can be evaluated numerically efficiently. As we impose von

Neumann boundary conditions, Eq. (6.14) simplifies:

$$\overline{\mathbf{G}}^{t(\bar{\mathbf{k}})}(E) = \mathbf{D}^{-1} \overline{\mathbf{G}}^{0(\bar{\mathbf{k}})}(E), \quad (6.25)$$

where we defined the matrix  $\mathbf{D}$  as follows:

$$\mathbf{D} = \begin{pmatrix} \left( \mathbf{1} - \overline{\mathbf{G}}_{S_L, S_L}^{0(\bar{\mathbf{k}})}(E) \overline{\Sigma}_{S_L}^{(\bar{\mathbf{k}})}(E) \right) & \mathbf{0} \\ -\overline{\mathbf{G}}_{S_R, S_L}^{0(\bar{\mathbf{k}})}(E) \overline{\Sigma}_{S_L}^{(\bar{\mathbf{k}})}(E) & \mathbf{1} \end{pmatrix}. \quad (6.26)$$

Using the expression

$$\mathbf{D}^{-1} = \begin{pmatrix} (\mathbf{D}_{11})^{-1} & \mathbf{0} \\ -(\mathbf{D}_{22})^{-1} \mathbf{D}_{12} (\mathbf{D}_{11})^{-1} & (\mathbf{D}_{22})^{-1} \end{pmatrix} \quad (6.27)$$

for the inverse of a lower triangular  $2 \times 2$ -matrix with square-matrix valued entries, we obtain the formula

$$\overline{\Sigma}_{S'_L}^{(\bar{\mathbf{k}})}(E) = -(\overline{\mathbf{G}}_{S'_L, S'_L}^{0(\bar{\mathbf{k}})}(E) + \overline{\mathbf{G}}_{S'_L, S_L}^{0(\bar{\mathbf{k}})}(E) \mathbf{F} \overline{\mathbf{G}}_{S_L, S'_L}^{0(\bar{\mathbf{k}})}(E))^{-1} \quad (6.28)$$

for the propagated embedding potential  $\Sigma$ , where we used the abbreviation  $\mathbf{F}$  for the following matrix:

$$\mathbf{F} = \overline{\Sigma}_{S_L}^{(\bar{\mathbf{k}})}(E) (\mathbf{1} - \overline{\mathbf{G}}_{S_L, S_L}^{0(\bar{\mathbf{k}})}(E) \overline{\Sigma}_{S_L}^{(\bar{\mathbf{k}})}(E))^{-1}. \quad (6.29)$$

Compared to Eq. (4.70), the Eq. (6.28) for the propagation of the embedding potential allows for a faster numerical evaluation, because the transfer matrix does not have to be computed. Inserting the Eq. (4.64) into Eq. (4.70), it is straightforward to prove that Eq. (6.28) is equivalent to Eq. (4.70).

### 6.3.2 Calculation of the full Green function

When the full Green function (and not only its surface projection) is needed, one can still benefit from the spectral representation if the Green function has to be calculated for many energies. In this case one calculates the series Eq. (6.13) as follows:

$$\begin{aligned} \mathbf{G}^{(\bar{\mathbf{k}})}(E) &= \mathbf{G}^{0(\bar{\mathbf{k}})}(E) + \mathbf{G}^{0(\bar{\mathbf{k}})}(E) \Sigma^{(\bar{\mathbf{k}})}(E) \mathbf{G}^{0(\bar{\mathbf{k}})}(E) + \dots = \\ &= \mathbf{G}^{0(\bar{\mathbf{k}})}(E) + \mathbf{G}^{0(\bar{\mathbf{k}})}(E) \mathbf{P}^\dagger \overline{\Sigma}^{(\bar{\mathbf{k}})}(E) \mathbf{P} \mathbf{G}^{0(\bar{\mathbf{k}})}(E) + \dots = \\ &= \mathbf{G}^{0(\bar{\mathbf{k}})}(E) + \mathbf{G}^{0(\bar{\mathbf{k}})}(E) \mathbf{P}^\dagger \overline{\mathbf{H}}^{(\bar{\mathbf{k}})}(E) \mathbf{P} \mathbf{G}^{0(\bar{\mathbf{k}})}(E), \end{aligned} \quad (6.30)$$

where we introduced the matrix  $\overline{\mathbf{H}}^{(\bar{\mathbf{k}})}(E)$ :

$$\begin{aligned} \overline{\mathbf{H}}^{(\bar{\mathbf{k}})}(E) &= \overline{\Sigma}^{(\bar{\mathbf{k}})}(E) + \overline{\Sigma}^{(\bar{\mathbf{k}})}(E) \overline{\mathbf{G}}^{0(\bar{\mathbf{k}})}(E) \overline{\Sigma}^{(\bar{\mathbf{k}})}(E) + \dots = \\ &= \overline{\Sigma}^{(\bar{\mathbf{k}})}(E) \left[ \mathbf{1} - \overline{\mathbf{G}}^{0(\bar{\mathbf{k}})}(E) \overline{\Sigma}^{(\bar{\mathbf{k}})}(E) \right]^{-1}. \end{aligned} \quad (6.31)$$

The first term in Eq. (6.30), which is the Green function without embedding potential,  $\mathbf{G}^{0(\bar{\mathbf{k}})}(E)$ , may be efficiently computed according to Eq. (6.10), which involves a matrix-matrix product with matrices of size  $N_{\text{LAPW}} \times N_{\text{LAPW}}$ . The numerical effort for this scales with the third power of  $N_{\text{LAPW}}$ , but is cheaper than the inversion needed for the evaluation of Eq. (4.40). The second term in Eq. (6.30) is less expensive to evaluate than the first term. Its numerical effort is roughly proportional to  $(N_{\text{LAPW}})^2 N_{2\text{D}}$ .

### 6.3.3 Charge density (Equilibrium case)

For the calculation of the equilibrium density matrix, Eq. (4.42), the energy integration is performed in the complex plane, where the Green function is smoother than on the real axis. The integration is approximated by a sum of Green functions at appropriate energy points  $E_i$ :

$$\rho = -\frac{1}{N} \frac{1}{\pi} \sum_{\bar{\mathbf{k}}} \Im \sum_i w_i \mathbf{G}^{(\bar{\mathbf{k}})}(E_i), \quad (6.32)$$

where  $w_i$  is an integration weight. Inserting Eq. (6.10) into Eq. (6.30), one obtains

$$\begin{aligned} \sum_i w_i^{(\bar{\mathbf{k}})} \mathbf{G}^{(\bar{\mathbf{k}})}(E_i) = \\ \mathbf{v}^{(\bar{\mathbf{k}})} \sum_i w_i^{(\bar{\mathbf{k}})} \left( E_i - \boldsymbol{\varepsilon}^{(\bar{\mathbf{k}})} \right)^{-1} \left[ \mathbf{1} + \left( \bar{\mathbf{v}}^{(\bar{\mathbf{k}})} \right)^\dagger \bar{\mathbf{H}}^{(\bar{\mathbf{k}})}(E) \bar{\mathbf{v}}^{(\bar{\mathbf{k}})} \left( E_i - \boldsymbol{\varepsilon}^{(\bar{\mathbf{k}})} \right)^{-1} \right] \left( \mathbf{v}^{(\bar{\mathbf{k}})} \right)^\dagger. \end{aligned} \quad (6.33)$$

An efficient way to calculate this is to first evaluate the sum

$$\mathbf{Z}^{(\bar{\mathbf{k}})} = \sum_i w_i^{(\bar{\mathbf{k}})} \left( E_i - \boldsymbol{\varepsilon}^{(\bar{\mathbf{k}})} \right)^{-1} \left[ \mathbf{1} + \left( \bar{\mathbf{v}}^{(\bar{\mathbf{k}})} \right)^\dagger \bar{\mathbf{H}}^{(\bar{\mathbf{k}})}(E) \bar{\mathbf{v}}^{(\bar{\mathbf{k}})} \left( E_i - \boldsymbol{\varepsilon}^{(\bar{\mathbf{k}})} \right)^{-1} \right] \quad (6.34)$$

and then to perform the final matrix multiplications:

$$\sum_i w_i^{(\bar{\mathbf{k}})} \mathbf{G}^{(\bar{\mathbf{k}})}(E_i) = \mathbf{v}^{(\bar{\mathbf{k}})} \mathbf{Z}^{(\bar{\mathbf{k}})} \left( \mathbf{v}^{(\bar{\mathbf{k}})} \right)^\dagger. \quad (6.35)$$

At each energy point, the computational cost to evaluate the contribution to the sum in Eq. (6.34) scales like  $(N_{\text{LAPW}})^2 N_{2\text{D}}$ .

### 6.3.4 Charge density (Nonequilibrium case)

In the present section we discuss the issue of calculating the density matrix of the scattering region of a transport setup as shown in Fig. 4.2, when a finite bias is applied. It has been shown that the imaginary part of the embedding potential is a negative semi-definite operator [51]. Its eigenstates constitute the lead channel states. Negative eigenvalues correspond to open channels and zero eigenvalues to closed channels. The scattering state due to an open channel state with energy  $E$  incident from the left is given by [51]

$$\Psi_j^{(\bar{\mathbf{k}})}(E) = 2i\alpha_j^{(\bar{\mathbf{k}})}(E) \mathbf{G}^{(\bar{\mathbf{k}})}(E) \mathbf{P}_{S_L}^\dagger \mathbf{v}_j^{(\bar{\mathbf{k}})}(E), \quad (6.36)$$

where the index  $j$  numerates the open channels at given energy  $E$ ,  $\alpha_j^{(\bar{\mathbf{k}})}(E)$  is the corresponding eigenvalue of the embedding potential and  $\mathbf{v}_j^{(\bar{\mathbf{k}})}(E)$  the normalized eigenvector. If a bias is applied to the tunneling setup of Fig. 4.2, this gives rise to a nonequilibrium situation. If the right Fermi energy  $E_{F,R}$  is higher than the left Fermi energy  $E_{F,L}$ , the density matrix due to the unoccupied channels of the left lead in the energy window between  $E_{F,L}$  and  $E_{F,R}$  has to be subtracted from the equilibrium density matrix calculated for an occupation of the system up to the energy  $E_{F,R}$ . The density matrix due to the channels of the left lead may be calculated from Eq. (6.36) as follows:

$$\rho = \frac{1}{N} \sum_{\bar{\mathbf{k}}} \int_{E_{F,L}}^{E_{F,R}} dE \sum_j D_j^{(\bar{\mathbf{k}})}(E) \Psi_j^{(\bar{\mathbf{k}})}(E) (\Psi_j^{(\bar{\mathbf{k}})}(E))^\dagger, \quad (6.37)$$

where the density of states of the  $j$ -th channel,  $D_j(E)$ , is given by

$$D_j(E) = \frac{1}{4\pi|\alpha_j(E)|}, \quad (6.38)$$

which follows from the requirement, that each open channel gives rise to one conductance quantum  $e^2/h = 1/(2\pi)$ . Inserting Eq. (6.36) into Eq. (6.37) and approximating the energy integration by a summation, one obtains

$$\rho_{S_L}^{(\bar{\mathbf{k}})} = -\frac{1}{\pi} \sum_i w_i \mathbf{G}^{(\bar{\mathbf{k}})}(E_i) \mathbf{P}_{S_L}^\dagger \Im \bar{\Sigma}_{S_L}^{(\bar{\mathbf{k}})}(E_i) \mathbf{P}_{S_L} (\mathbf{G}^{(\bar{\mathbf{k}})}(E_i))^\dagger, \quad (6.39)$$

as contribution of point  $\bar{\mathbf{k}}$ , where  $w_i$  is a weight connected to the energy integration. Compared to the equilibrium case discussed in section 6.3.3, the energy integration in Eq. (6.37) is performed on the real axis. Consequently, the weights  $w_i$  are real-valued. Due to the fact that  $\Im \bar{\Sigma}_{S_L}^{(\bar{\mathbf{k}})}(E)$  and  $(\mathbf{G}^{(\bar{\mathbf{k}})}(E))^\dagger$  are non-analytic functions, it is not possible to replace the integration along the real axis by an integration along a contour in the complex plane. It is straightforward to show that the sum of  $\rho_{S_L}^{(\bar{\mathbf{k}})}$  and the analogous expression for the density matrix due to states incident from the right,  $\rho_{S_R}^{(\bar{\mathbf{k}})}$ , reduces to the expression for the equilibrium density:

$$\rho_{S_L}^{(\bar{\mathbf{k}})} + \rho_{S_R}^{(\bar{\mathbf{k}})} = -\frac{1}{\pi} \Im \sum_i w_i \mathbf{G}^{(\bar{\mathbf{k}})}(E_i). \quad (6.40)$$

We note that the expression for the density matrix due to channels in the left lead, Eq. (6.39), is of the same formal structure as the analogous expressions within transport theories formulated for tight-binding approaches and approaches based on a localized basis set [62], where the imaginary part of the so-called lead self-energy plays the role of the term  $\mathbf{P}_{S_L}^\dagger \Im \bar{\Sigma}_{S_L}^{(\bar{\mathbf{k}})}(E_i) \mathbf{P}_{S_L}$  of our embedding-based formulation. Defining the rectangular matrix

$$\mathbf{A}^{(\bar{\mathbf{k}})}(E) = [\mathbf{v}_1^{(\bar{\mathbf{k}})}(E) \sqrt{|\alpha_1^{(\bar{\mathbf{k}})}(E)|}, \mathbf{v}_2^{(\bar{\mathbf{k}})}(E) \sqrt{|\alpha_2^{(\bar{\mathbf{k}})}(E)|}, \dots], \quad (6.41)$$

which is composed of the open channel states scaled with their eigenvalues, we can write

$$\Im \overline{\Sigma}_{S_L}^{(\bar{\mathbf{k}})}(E) = -\mathbf{A}^{(\bar{\mathbf{k}})}(E) \mathbf{A}^{(\bar{\mathbf{k}})}(E)^\dagger \quad (6.42)$$

for the imaginary part of the embedding potential. Employing this factorization of the imaginary part of the embedding potential and Eq. (6.30) for the Green function we may write

$$\rho_{S_L}^{(\bar{\mathbf{k}})} = \frac{1}{\pi} \boldsymbol{\nu}^{(\bar{\mathbf{k}})} \mathbf{Z}^{(\bar{\mathbf{k}})} \left( \boldsymbol{\nu}^{(\bar{\mathbf{k}})} \right)^\dagger, \quad (6.43)$$

where

$$\mathbf{Z}^{(\bar{\mathbf{k}})} = \sum_i w_i \mathbf{X}^{(\bar{\mathbf{k}})}(E_i) \left( \mathbf{X}^{(\bar{\mathbf{k}})}(E_i) \right)^\dagger \quad (6.44)$$

and

$$\mathbf{X}^{(\bar{\mathbf{k}})}(E) = \left( E_i - \boldsymbol{\varepsilon}^{(\bar{\mathbf{k}})} \right)^{-1} \boldsymbol{\nu}^\dagger \left[ \mathbf{1} + \overline{\mathbf{H}}^{(\bar{\mathbf{k}})}(E) \overline{\mathbf{G}}^{0(\bar{\mathbf{k}})}(E) \right] \mathbf{A}^{(\bar{\mathbf{k}})}(E). \quad (6.45)$$



# Chapter 7

## Order-N Embedding

Density functional theory codes based on the Full-potential Linearized Augmented-Plane-Wave method have been highly successful due to their generality and wide applicability. In particular, in the field of surfaces, open structures and complex magnetic materials with many chemical elements, the FLAPW method sets the standard for precision among the *ab initio* methods. On the other hand, the computational effort of the FLAPW method is relatively high, obeying a cubic scaling law with system size, making the applicability to larger systems increasingly more difficult. In section 4.6 we have already introduced basic concepts of an order-N implementation of the embedding method: Given the Kohn-Sham potential of the embedding region  $\Omega$  the conductance may be calculated with a linear dependence of the computational time on the length of  $\Omega$ . In the present chapter we give a detailed description of an order-N implementation of the embedding method, which is particularly suitable for the calculation of transport properties and the self-consistent charge density in and out of equilibrium. Additionally, the method may also be applied to films and surfaces. In the case of the film geometry the order-N Green-function implementation of the FLAPW method is able to fully replace the standard implementation of the FLAPW method, which is based on the calculation of the Bloch-functions of the entire system.

### 7.1 Order-N Self-Consistency Scheme

Usually, the MTJs and spin-valves calculated by first-principles DFT methods exhibit a layered structure. For example, the famous Fe/MgO/Fe MTJ is often modeled assuming in-plane translational invariance, with only one Fe-atom per Fe-layer and only one Mg- and one O-atom per MgO-layer. In order to calculate such layered systems, the scattering region  $\Omega$  may be divided into  $M$  layers, labeled  $\Omega_1, \dots, \Omega_M$ , as illustrated in Fig. 7.1. In order to calculate the charge density of all layers for a given Kohn-Sham potential, we need the Green functions with correct boundary conditions in all layers. Thus, for each layer  $l$  the two embedding potentials  $\Sigma_{L,l}$  and  $\Sigma_{R,l}$  are needed. The two embedding potentials  $\Sigma_{L,1}$  and  $\Sigma_{R,M}$  are obtained from bulk calculations of the left and right leads, respectively. The unknown left embedding potentials are calculated by propagating the

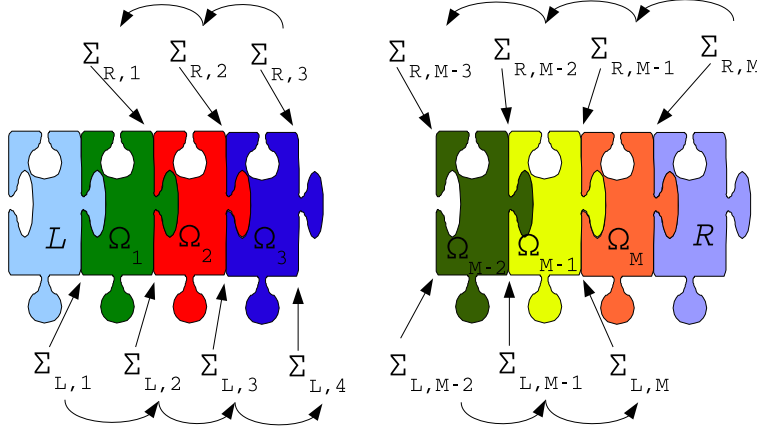


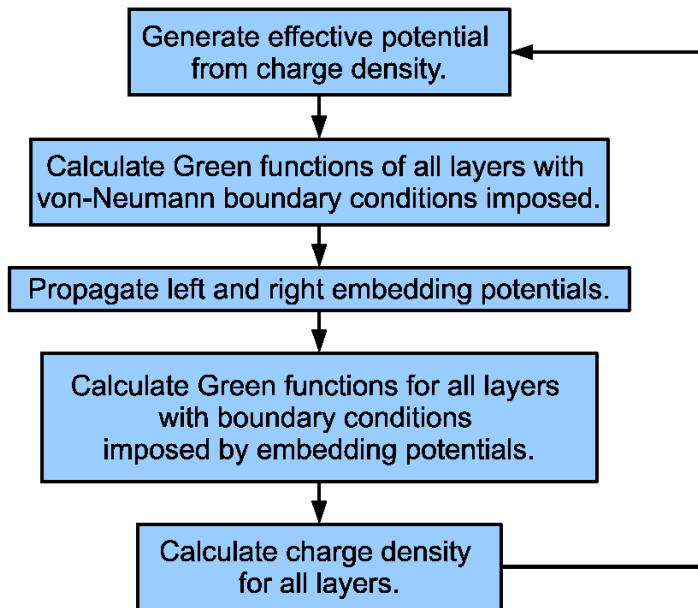
Figure 7.1: The scattering region  $\Omega$  is divided into  $M$  sub-regions,  $\Omega_1$  to  $\Omega_M$ . For each sub-region  $\Omega_l$  two embedding potentials are needed:  $\Sigma_{L,l}$  and  $\Sigma_{R,l}$ . The left embedding potentials  $\Sigma_{L,l}$  are obtained by propagating  $\Sigma_{L,1}$  layer by layer to the right. Likewise, the right embedding potentials  $\Sigma_{R,l}$  are obtained by propagating  $\Sigma_{R,M}$  to the left.

first left embedding potential  $\Sigma_{L,1}$  layer by layer to the right side, as discussed already in section 4.6. In section 6.3.1 we described an efficient method based on the Dyson equation for this propagation of the embedding potential. Analogously, the unknown right embedding potentials  $\Sigma_{R,l}$  are obtained by propagating  $\Sigma_{L,M}$  to the left. For the propagation of the embedding potentials the surface projected Green functions with von-Neumann boundary conditions are needed. In order to compute them, one sets up the Hamiltonian and overlap matrices for all layers and uses the spectral representation as described in section 6.2. After computing the left and right embedding potentials for all layers the physical Green functions satisfying out-going boundary conditions may be calculated for all layers by employing the efficient scheme given in Eq. (6.3.3). As the next step, following the description given in section 5.1, the charge densities in all layers are calculated from the Green functions. The final step needed to complete the self-consistency cycle is the generation of the effective potential from the charge density. In Fig. 7.2 we show the flow-chart of the order- $N$  self-consistency.

## 7.2 Order- $N$ for films and surfaces

In the case of a surface calculation, the first left embedding potential is obtained from a bulk calculation of a principal layer of substrate material. However, a right embedding potential of layer  $N$  does not exist, because the vacuum region is included explicitly in the last layer. Nevertheless, for all other layers right embedding potentials are needed. The right embedding potential for layer  $N - 1$  is obtained as surface inverse of the Green function of the last layer calculated with von Neumann boundary conditions on the embedding surface between layers  $N - 1$  and  $N$ . The left embedding potential for layer  $N$  is obtained as usual by propagating the left embedding potential of layer 1 to the right side.



Figure 7.2: Flow-Chart of the Order- $N$  Self-Consistency Scheme.

### 7.2.1 An order- $N$ implementation for the film geometry

Definitely, calculating a film with the Green-function formulation of FLAPW is not profitable, because there is no need for embedding surfaces: The Green function is simply the inverse of  $ES - H$ , where  $S$  and  $H$  are the overlap and Hamiltonian matrices, which are identical to the ones of the standard implementation of FLAPW in this case. This Green function has poles at all eigenvalues of the Bloch states of the film. However, in order to treat thick films computationally efficiently, one may modify the order- $N$  implementation for surfaces by including a second vacuum on the left side. In the case of a film calculation, the first left embedding potential does not exist. Likewise, the last right embedding potential does not exist. The left embedding potential of the second layer is obtained as surface inverse of the Green function of the first layer calculated with von Neumann boundary conditions on the embedding surface between layers 1 and 2. Like for the surface calculation, the right embedding potential for layer  $N - 1$  is obtained as surface inverse of the Green function of the last layer calculated with von Neumann boundary conditions on the embedding surface between layers  $N - 1$  and  $N$ .

In contrast to the other geometries discussed so far in this work in the context of the embedding method, which are the transport geometry and the surface geometry, the treatment of a film within the embedding method requires to calculate also the Fermi energy self-consistently. Two ways to do this are thinkable: One may either obtain the Fermi energy self-consistently for each self-consistency cycle or determine it on the fly. One may expect, that the latter option helps to save computational time. It is crucial that the output charge of each self-consistency iteration is neutral. Moreover, the requirement of

charge neutrality may be exploited to refine the Fermi energy for the next cycle. In order to do this one divides the total charge (for a charge neutral system the total charge is zero) by the density of states at the Fermi energy. This ratio may be interpreted as an approximation for the deviation from the true Fermi energy in the present self-consistency cycle. Hence, one adds this ratio to the Fermi energy to obtain a new Fermi energy for the next self-consistency cycle. If one multiplies the spectral function at the Fermi energy with this ratio and adds the result to the charge determined in the present self-consistency run, one obtains an output charge, which is neutral. In this way one may obtain the refinement of the Fermi energy and the neutral output charge from one common calculation. In practice, we found that this scheme usually converges only if a mixing scheme is used to update the Fermi energy. For example, one may calculate the correction of the Fermi energy as described above, add it to the Fermi energy to obtain a new Fermi energy, and then mix this new Fermi energy with the old Fermi energy. This way, strong fluctuations of the Fermi energy are avoided, which stabilizes the self-consistency.

### 7.3 Parallelization

Within the FLAPW method the largest share of computational effort within a self-consistency cycle is devoted to the construction and the subsequent diagonalization of the Hamiltonian matrix. As both the construction and the diagonalization of the Hamiltonian have to be performed for each  $k$ -point, *k-point parallelization* is a very natural concept for parallelizing the FLAPW method. However, with increasing system size the computational burden at a given  $k$ -point may easily attain a level, where it becomes desirable to have additional options of parallelization besides the one over  $k$ -points. Apart from the  $k$ -points the only additional natural parallelization option is given by the spin-loop. However, *parallelizing the spin-loop* only increases the number of processors by which a given calculation may be tackled by a factor of two and is not straightforward if the two spin-channels are coupled, like in calculations of non-collinear magnetism and calculations including spin-orbit coupling. Using a group of processors to speed up the computations performed for a given spin and  $k$ -point is possible and is usually called *eigenvector parallelization*, as the parallelization of the computation of eigenvalues and eigenvectors is the most difficult part at this level of parallelization. However, the diagonalization of a general Hermitian matrix cannot be split up into independent computations of equal computational cost and consequently eigenvector parallelization has poor scaling properties.

However, within the order- $N$  Green function embedding method, a *parallelization over layers* becomes possible. If parallelization is done over layers and  $k$ -points, it becomes attractive to parallelize also such parts of the program as the setup of the potential. *Parallelization over the energies* is an additional option within our Green function based method.

We implemented the various parallelization strategies in such a way that either a single parallelization strategy (e.g. only  $k$ -point parallelization) may be used or that various parallelization strategies may be combined. If only a small number of processors is available to parallelize the calculation, then  $k$ -point parallelization exhibits the best scaling properties.

However, without parallelization over the layers, the data of all layers has to be kept in memory or written to disk, because the propagation of the embedding potential and the calculation of the Coulomb potential require the data of all layers. Keeping the data of all layers in memory is generally not possible for the systems of our interest. For example, the supercomputer Jülicher Blue Gene/P (JUGENE), has a memory limitation of 2GB per node (1 node has 4 cores) and 256MB per core (see App. D). Consequently, a parallelization over layers is usually necessary in calculations on the JUGENE supercomputer. This is why the following sections on the details of the parallelization of the order-N embedding method are written from a perspective that assumes that parallelization over the layers is always present as a basis parallelization, which may be supplemented by e.g.  $k$ -point parallelization. Also, in order to keep the following sections readable, a focus is made on the parallelization of the self-consistency mode, and in particular the self-consistent calculation of the charge density.

For a given layer  $l$  we denote the group of processors that do the computations pertinent to it by  $P_l$ . We use the letter  $Q$  as a symbol for all parallelization strategies that are used besides parallelization over layers, e.g.  $k$ -points, spin, energies.

### 7.3.1 Parallelization of the Potential Generation

The charge density and the potential of layer  $l$  are available to the group  $P_l$  of processes. To construct the Coulomb potential we proceed similarly as in section 5.2, i.e. we first construct the *pseudocharge*. For each layer the pseudocharge is calculated as explained in section 5.2.1 and expressed in terms of the stars of the corresponding layer. For a given layer  $l$  the pseudocharge is calculated by the group  $P_l$  of processes, leading to a parallelization in terms of layers and  $Q$ .

As discussed in section 5.2 the calculation of the Coulomb potential from the charge density constitutes a non-local problem, i.e. it is not possible to construct the Coulomb potential for a given layer without using information about the other layers. Consequently, we have to expand the pseudocharge in an appropriate basis set of the *composed system*. By putting together the pseudocharge densities of the individual layers in *real space*, the pseudocharge density of the composed system is constructed on a *real space grid*. For this purpose a mapping function is set up which maps each grid point of the real space grid of the composed system – called the *global grid* from now on – onto a layer and a point in it. Using this mapping the pseudocharge on the global grid is obtained by collecting the pseudocharge from the individual layers. From the mapping function it is known for which points of each layer the pseudocharge is needed. For this set of points the pseudocharge is explicitly obtained in each layer by evaluating the stars, Eq. (5.4), analytically.

In order to obtain the pseudocharge density  $\rho_{\mathbf{g}}^{\text{pseu}}$  in reciprocal space, as needed to evaluate Eq. (5.15), one 3D-FFT could be performed after collecting the pseudocharge data from the layers. However, due to the *linearity of the FFT transformation*, a simple layer parallelization of the 3D-FFT may be implemented by performing 2D-FFTs in all layers for all those planes perpendicular to the stacking direction which contain points for which the pseudocharge is needed. After gathering the pseudocharge data on the global

grid, only 1D-FFTs have to be performed on the large grid to obtain  $\rho_{\mathbf{g}}^{\text{pseu}}$ . Using  $\tilde{\rho}_{\mathbf{g}}$  from Eq. (5.15) the solution to the *inhomogeneous* Poisson equation,  $V_{\mathbf{g}}^{\text{inhom}}$ , is constructed according to Eq. 5.13.

In the next step we add a solution of the *homogeneous* Poisson equation to the solution of the inhomogeneous one in order to satisfy the correct *boundary conditions* of the Coulomb potential on the embedding planes.

Ultimately, the Coulomb potential is needed expressed in terms of the stars of the individual layers. In order to achieve this, the  $z$ -dependent factor of the stars of the composed system is evaluated at the grid points  $z_i^l$  of a given layer. Alternatively, one may replace the analytic evaluation of the  $z$ -dependent part of the potential by a 1D-FFT. As the grid points of the global grid and the grid points of the local grid of a given layer do not match in general, an interpolation from the global grid to the local grid is needed. Both methods lead to an expression of the potential, where the spatial dependence in the stacking direction is given in terms of values on a real space grid, while the in-plane spatial dependence is given in terms of Fourier coefficients. Performing in all layers 1D-FFTs of this potential  $V_{\mathbf{g}_{\parallel}}^l(z_i^l)$  completes the transformation.

The next step after the calculation of the Coulomb potential inside the interstitial region is the calculation of the Coulomb potential inside the MT spheres. This is done as described in section 5.2.1. For each layer the group  $P_l$  of processors performs this job, i.e. a Q-parallelization of the computationally expensive parts of the potential generation is performed.

In order to obtain the Kohn-Sham potential, we have to add the exchange-correlation potential to the Coulomb potential. As the exchange correlation potential is *local* in the charge (and the gradient of the charge) for LDA (GGA), no communication between the layers is needed: Using the charge density of layer  $l$ , the group  $P_l$  computes the exchange-correlation potential of layer  $l$ . Q-parallelization of the computation of the exchange correlation potential pays out especially if the GGA is used. Concerning the muffin-tin part, we parallelized the loop over radial grid points.

The final operation that has to be performed on the interstitial potential before it can be used in the Hamiltonian setup is the convolution with the step function. For each layer the processes  $P_l$  are used to perform this convolution.

### 7.3.2 Parallelization of the Embedding potential propagation

After the group  $P_l$  of processes has set up and diagonalized the Hamiltonian matrix, the transfer matrix  $T_l(E)$  is calculated according to Eq. (4.64) and the efficient scheme described in section 6.2. In order to obtain the left embedding potentials  $\Sigma_{2,L}(E), \Sigma_{3,L}(E), \dots, \Sigma_{N,L}(E)$  for layers  $2, 3, \dots, N$ , one has to propagate the left embedding potential  $\Sigma_{1,L}(E)$  layer by layer to the right side of the system. Likewise, the rightmost right embedding potential  $\Sigma_{N,R}(E)$  is propagated to the left side of the system to obtain the embedding potentials  $\Sigma_{N-1,R}(E), \Sigma_{N-2,R}(E), \dots, \Sigma_{1,R}(E)$ . The propagation steps are not independent of each other, e.g. for the left embedding potential, the propagation step from layer  $l$  to layer  $l+1$  is dependent on the previous propagation steps involving layers  $1, 2, \dots, l-1$  and

their transfer matrices  $T_1(E), T_2(E), \dots, T_{l-1}(E)$ . Consequently, all propagation steps at a given energy  $E$ , k-point  $k$  and spin  $\sigma$  are done by the group  $R_{l(E),k,\sigma}$  of processes, where we introduced a mapping  $l(E)$  of energies onto layers. As the number of layers is usually different from the number of energy points, an outer energy-loop is introduced to save memory in the case where the number of energy points is larger than the number of layers: The outer energy loop is used to form  $[N_E/N_L] + \Theta(N_E - [N_E/N_L]N_L)$  groups of energy points, each of which contains maximally  $N_L$  energy points. The mapping  $l(E)$  is then given by  $l(E) = \text{mod}(E - 1, N_L) + 1$ . For each group  $R_{l(E),k,\sigma}$  of processes storage for  $N_L$  transfer matrices is allocated. At a given point  $E_2$  of the outer energy loop, the transfer matrices  $T_l((E_2 - 1) * [N_E/N_L] + 1), \dots, T_l((E_2 - 1) * [N_E/N_L] + N_L)$  are computed. Then the transfer matrices of all layers at energy  $E = (E_2 - 1) * [N_E/N_L] + l$  are communicated to the group  $R_{l(E),k,\sigma}$  of processes. The collective communication mpi subroutine `mpi_alltoall` is designed exactly for this purpose (see App. C) and its use allows for a highly efficient communication when compared with alternative solutions based on point to point communication. Now, the propagation of the embedding potential at energy  $E = (E_2 - 1) * [N_E/N_L] + l$  may be performed by the group  $R_{l(E),k,\sigma}$  of processes. For the calculation of the embedded Green function at the energy points  $(E_2 - 1) * [N_E/N_L] + 1, \dots, \max((E_2 - 1) * [N_E/N_L] + 1, E_N)$ , the group  $R_{l,k,\sigma}$  of processors needs the embedding potentials of layer  $l$  for this set of energies, which need to be communicated from the processors which calculated them. Again, the collective communication mpi subroutine `mpi_alltoall` fits exactly to this communication problem (see App. C).

## 7.4 A simple test case: Cu/Vacuum/Cu

As a simple test case to verify the implementation we calculated the conductance at  $\bar{\Gamma}$  through a Cu/Vacuum/Cu junction. We used 6.82 a.u. as lattice constant of fcc Cu. In order to obtain a vacuum layer in the system, we left out one layer of Cu. The scattering region is embedded on both sides with the embedding potential of semi-infinite Cu. The number of Copper layers that are explicitly included into the scattering region was varied: Four calculations with 6, 20, 30 and 50 layers of Cu in the scattering region were performed. To perform the order-N calculations we chose the layers such that each layer contains only one Cu atom. Hence, the system was divided into 6, 20, 30 and 50 layers. The charge density was calculated self-consistently for the four systems and the conductance was computed for this self-consistent charge density. As the perturbation due to the vacuum layer is expected to affect only the copper layers that are very close it is reasonable to predict that the four results for the conductance should be very similar. Indeed this is the case, as seen in Fig. 7.3.

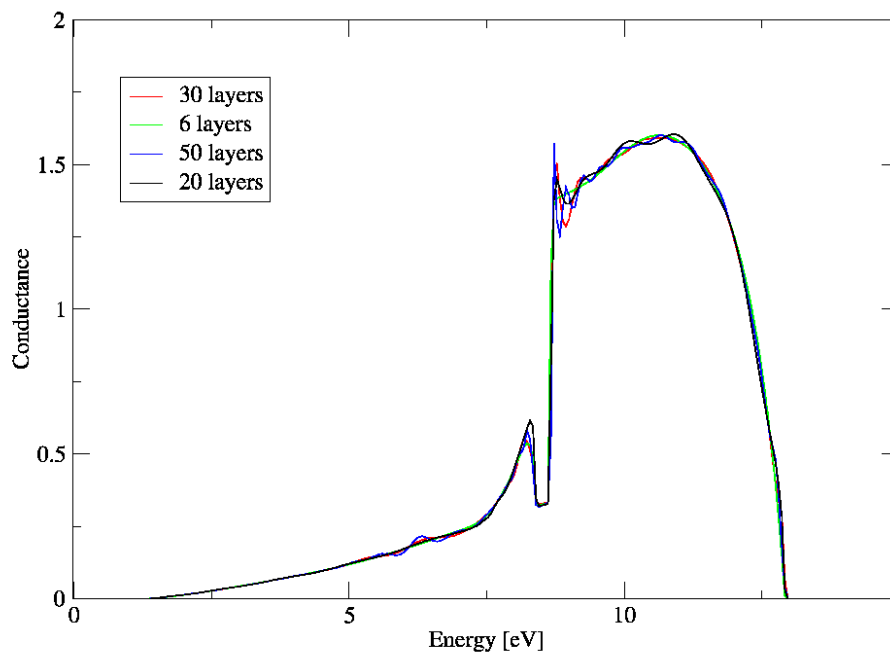


Figure 7.3: Conductance (in units of  $e^2/h$ ) of the Copper/Vacuum/Copper junction at  $\bar{\Gamma}$  for different numbers of copper layers in the scattering region.

# Chapter 8

## Applications of the Embedding Method

The purpose of the present chapter is to give illustrative examples of applications of the order-N embedding method described in chapters 4-7. Additionally, in order to investigate how well the order-N embedding method compares to standard FLAPW regarding the reliability of force and total energy calculations, comparisons are made for a set of test cases.

### 8.1 (001) Surface of bct Cobalt

Under ambient conditions, cobalt crystallizes into a ferromagnetic hcp structure. It has been shown experimentally [63] that thin films of bct Co may be grown on Fe up to a critical thickness of 10 monolayers of Co. The spectral properties of thin films of Co grown on Fe are interesting, e.g. in the context of using Co-interlayers in MgO-based tunnel junctions. If bulk bct Co is constrained to have the Fe (2.867 Å) in-plane lattice constant, the interlayer distance in cobalt is given by  $c/2 = 1.333$  Å, corresponding to a  $c/a$ -ratio of 0.93, as determined from the energy minimum of a bulk FLAPW calculation using GGA [64]. We used a MT-radius of 1.11 Å for cobalt and a plane-wave cutoff of  $7.6 \text{ Å}^{-1}$ . In order to determine the surface relaxations of the (001) surface of ferromagnetic bct Co we embedded 11 layers of cobalt, terminated by vacuum on the top, with a semi-infinite cobalt substrate from below. The embedding potential of the cobalt substrate was obtained from the transfer-matrix of a principal layer of bulk bct cobalt. For the geometry optimization we used the pbe [64] exchange correlation potential and supplemented the FLAPW basis set with local orbitals for the 3p-states of cobalt. We calculated the charge density within the embedded region self-consistently and determined the relaxed positions of the atoms with the help of the atomic forces calculated as described in section 5.5.2. The system was decomposed into 11 layers and treated with the order-N method. In Fig. 8.1 we show the structure of the relaxed cobalt surface. The surface relaxations affect mainly the top two layers, where the topmost layer is torn towards the second layer, while the second



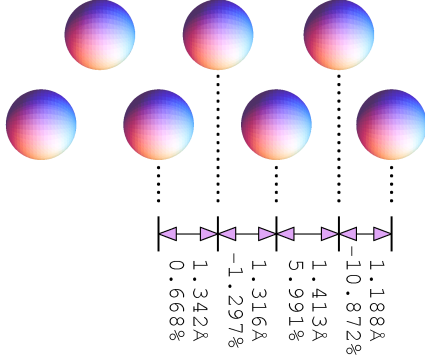


Figure 8.1: Relaxed bct Co surface. The in-plane lattice constant is constrained to be  $a = 2.867 \text{ \AA}$ . Under this constraint the bulk interlayer distance in Cobalt is given by  $c/2 = 1.333 \text{ \AA}$ , corresponding to the  $c/a$ -ratio of 0.93. For the topmost layers we list the interlayer distances and their deviations from the bulk interlayer distance.

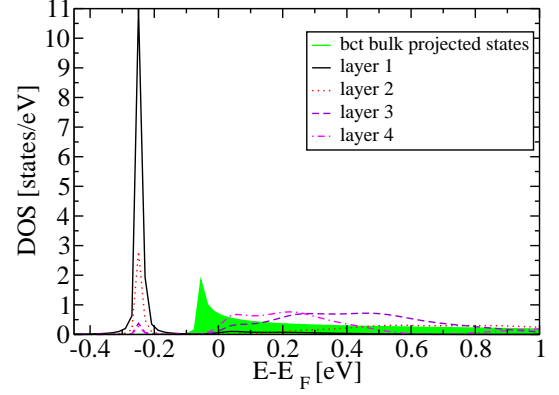


Figure 8.2: Minority DOS of layers 1 to 4 of the Cobalt surface at  $\bar{\Gamma}$ . Layer 1 is at the surface. The shaded area illustrates the projected bulk density of states of  $\Delta_1$  symmetry for bct Co ( $a = 2.867 \text{ \AA}$  and  $c/a = 0.93$ ).

layer is pushed away from the third layer. The surface relaxations as calculated with the embedding method agree very well with the surface relaxations found in a corresponding film calculation. Within GGA we find enhanced magnetic moments for the cobalt atoms at the surface of  $1.93 \mu_B$  for the topmost layer and  $1.83 \mu_B$  for the second layer, which are larger than the bulk value of the magnetic moment of bct cobalt of  $1.78 \mu_B$  by  $0.15 \mu_B$  and  $0.04 \mu_B$ , respectively.

In Fig. 8.3 we show the minority DOS of  $\Delta_1$  symmetry of the surface layer, as obtained within LDA [65]. We identify the region of high spectral intensity close to the  $\bar{\Gamma}$  point as a surface state. At  $\bar{\Gamma}$  it is located at a binding energy of  $-0.25 \text{ eV}$ . The minority DOS of  $\Delta_1$  symmetry at  $\bar{\Gamma}$  for layers 1 (at surface) to 4 is shown in Fig. 8.2. The spectral intensity due to the surface state decreases rapidly with increasing distance from the surface.

In Fig. 8.4 we plot the minority DOS of  $\Delta_1$  symmetry of layer number four (counting starts at the surface layer). In comparison with Fig. 8.3, which shows the surface layer, we find that the weight of the surface state is reduced in the fourth layer and additionally to the surface state the bulk state has become visible. While the dispersion of the  $\Delta_1$  surface state is concave, it is convex for the  $\Delta_1$  bulk state, which might allow a clear distinction between bulk and surface  $\Delta_1$  states in experiments using angular resolved photo emission.



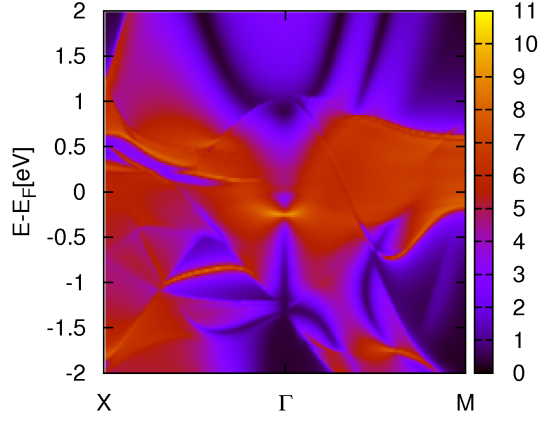


Figure 8.3: Minority DOS of the surface layer of the Cobalt(001) surface.

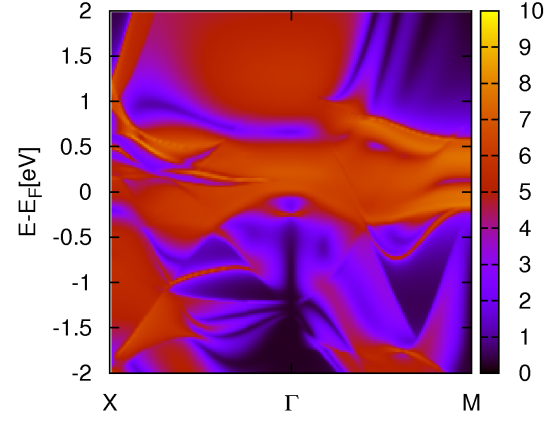


Figure 8.4: Minority DOS of layer number 4 of the Cobalt(001) surface.

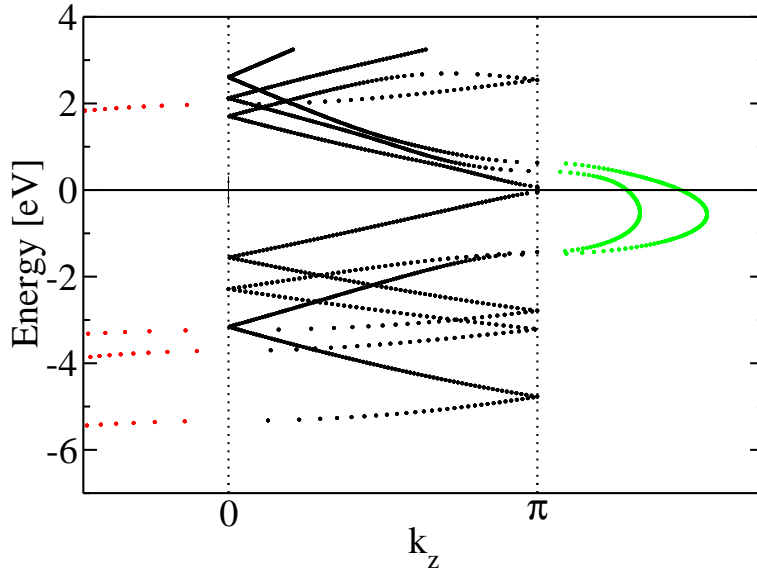


Figure 8.5: Complex band structure of Sb(111) at the  $\bar{M}$ -point. A very slowly decaying evanescent state is located slightly below the Fermi energy between  $-0.303\text{eV}$  and  $-0.168\text{eV}$ .

## 8.2 Surface State of Antimony

Experimentally, the band dispersion and the Fermi surface of Sb(111) have been measured [66]. The Sb(111) surface is found to be metallic. The existence of two spin-split surface bands is attributed to spin-orbit coupling and the broken space-inversion symmetry at the surface. The surface states of Sb are interesting in the context of the prediction that the alloy  $\text{Bi}_{1-x}\text{Sb}_x$  is a strong topological insulator [67].

We performed bulk and surface calculations of Sb. A MT-radius of 2.5 a.u. and a plane-wave cutoff of 3.8 a.u. were used. Exchange and correlation were treated within LDA using the parameterization of Moruzzi, Janak and Williams [65]. A principal layer of bulk Sb with the normal in (111)-direction corresponds to 6 atoms in a hexagonal unit cell. The complex band structure of bulk Sb at the  $\bar{M}$ -point is shown in Fig. 8.5. Bulk Sb is a semimetal. At  $k_z = \pi$  there is a small gap, 0.14 eV in size. Interestingly, there is a very slowly decaying evanescent state at  $k_z = \pi$ , which connects the Bloch bands between which the gap is located. The imaginary part of the complex wave vector is  $\kappa_z \leq 0.006$  a.u.. Experimentally, at the  $\bar{M}$ -point a surface state is observed, which extends far into the bulk. We attribute the observed slow decay of the surface state to this slowly decaying evanescent state.

A self consistent calculation of the (111)-surface of Sb was performed within the embedding method including spin-orbit coupling. In Fig. 8.6 we show the spin-split surface bands along the line  $\bar{\Gamma}$  to  $\bar{M}$ . These surface bands are obtained as positions of the maxima of the Bloch-spectral function. The calculated spin-split surface band is in good agreement to experiment [66].

In Fig. 8.7 we show the spin-split surface bands for the  $\text{Bi}_{0.4}\text{Sb}_{0.6}$  alloy. The alloy is modeled by tuning the spin-orbit coupling parameters between the values for Sb and Bi. The spin-split bands cross at  $\bar{\Gamma}$  and on the line  $\bar{\Gamma}$ - $\bar{M}$ . The position of the crossing depends on the doping. Close to the  $\bar{M}$  point one of the surface bands runs into the upper bulk continuum and the other surface band into the lower bulk continuum. As a consequence the number of bands that cross the Fermi level is odd. One of the bands crosses the Fermi level by an odd number of times. This situation cannot be destroyed by the presence of impurities. The circulating edge states are said to be topologically protected.  $\text{Bi}_{1-x}\text{Sb}_x$  is said to be a topological insulator [67]. It is insulating in the bulk, but metallic at the surface and in contrast to ordinary insulators with surface metallicity the surface metallicity is robust.

## 8.3 Electronic Transport in Fe/MgO/Fe

The lattice constants of bcc-Fe and MgO are 2.867 Å and 4.21 Å, respectively. Rotated by 45° the MgO lattice matches on to the Fe lattice:  $4.21 \text{ Å}/\sqrt{2} \approx 2.98 \text{ Å}$ . Due to the nearly perfect lattice match Fe/MgO/Fe junctions may be grown fully epitaxially. Based on first-principles theories an extremely high MR ratio of over 1000% has been predicted [68] for fully epitaxial Fe(001)/MgO(001)/Fe(001) MTJs. This giant TMR effect originates

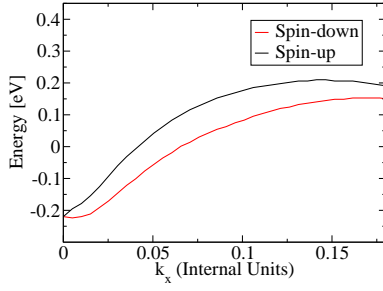
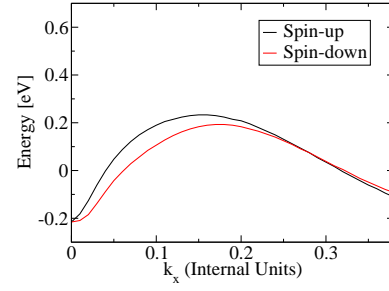


Figure 8.6: Spin-split surface bands of Sb.

Figure 8.7: Spin-split surface bands of the Bi-Sb alloy  $\text{Bi}_{0.4}\text{Sb}_{0.6}$ .

from the coherent spin-dependent tunneling of highly spin-polarized  $\Delta_1$  Bloch states of Fe at  $\bar{\Gamma}$ . The  $\Delta_1$  states in MgO are characterized by a slow decay when compared to the  $\Delta_2$ ,  $\Delta'_2$  and  $\Delta_5$  states. This leads to a strong suppression of the tunneling current for the antiparallel alignment of magnetizations of the electrodes, as  $\Delta_1$  states are not available at the Fermi energy in the minority band. Indeed, very large MR ratios of about 200% at room temperature have been observed experimentally in fully epitaxial Fe(001)/MgO(001)/Fe(001) MTJs [69, 70].

The geometry of the relaxed Fe/MgO interface has been discussed in Ref. [29]. Using the order-N method we calculated the transport properties of the Fe/MgO/Fe MTJ for 3 and 5 layers of MgO. 7 layers of Fe are included in the scattering region on both sides of the barrier. Exchange and correlation were treated within LDA [65]. In Fig. 8.8 we show the  $k$ -resolved conductance for majority spin and in Fig. 8.9 for minority spin for a barrier thickness of 3 layers of MgO. In agreement with the discussion above the conductance of the majority spin channel is characterized by a maximum around  $\bar{\Gamma}$ , which is due to the slow decay of the  $\Delta_1$  states in MgO. In contrast, the conductance of the minority spin channel is strongly suppressed around  $\bar{\Gamma}$  due to the absence of minority  $\Delta_1$  states at the Fermi level. Figures 8.10 and 8.11 show the corresponding plots for a barrier thickness of 5 layers of MgO. The maximum at  $\bar{\Gamma}$  decreases by roughly a factor of 15 due to the increase of the barrier thickness of 2 layers. For the majority spin the integrated conductances are  $1.17 \cdot 10^{-2} e^2/h$  (3 layers of MgO) and  $3.97 \cdot 10^{-4} e^2/h$  (5 layers of MgO), resulting in a decrease of the conductance by roughly a factor of 30. As the area of the peak around  $\bar{\Gamma}$  shrinks, the integrated conductance is reduced stronger than the peak height, when increasing the barrier thickness.

## 8.4 Electronic Transport in Co/MgO/Co

It has been theoretically predicted [71], that a higher TMR than the one measured in Fe/MgO/Fe MTJs may be realized by using bcc cobalt instead of bcc iron as lead material. The reason for the higher TMR value is the absence of states of  $\Delta_1$  symmetry at the Fermi level in the minority density of states of bcc cobalt accompanied by the fact that in the majority channel only states of  $\Delta_1$  symmetry are present at the Fermi level. This leads to

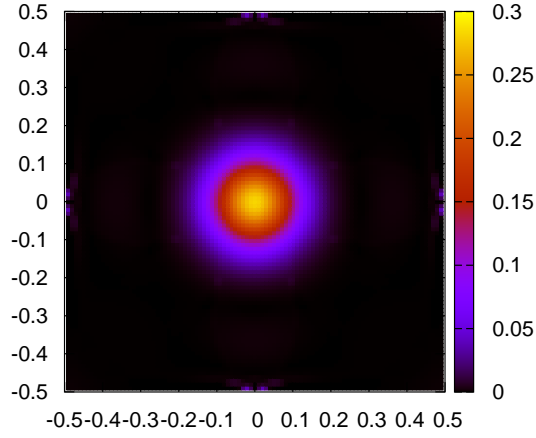


Figure 8.8:  $k$ -resolved conductance of the majority spin channel (in units of  $e^2/h$ ) for a Fe/MgO/Fe MTJ with a barrier thickness of 3 layers.

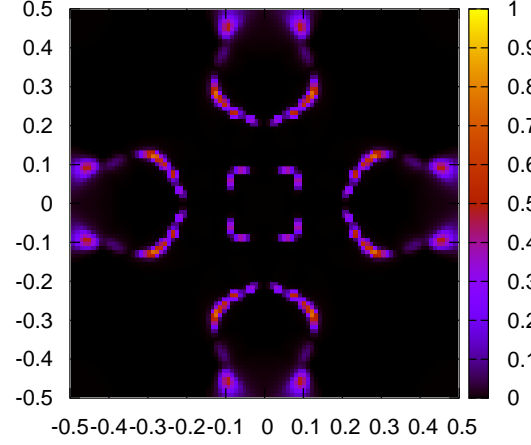


Figure 8.9:  $k$ -resolved conductance of the minority spin channel (in units of  $e^2/h$ ) for a Fe/MgO/Fe MTJ with a barrier thickness of 3 layers.

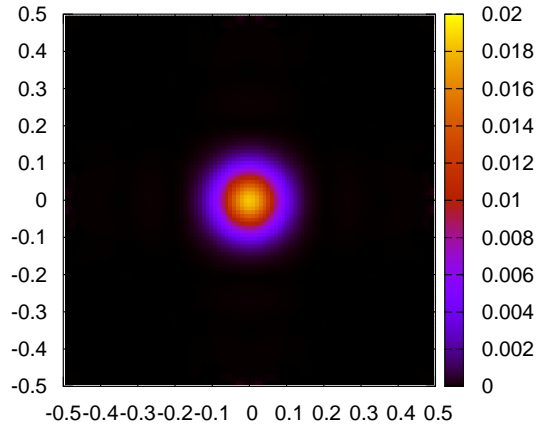


Figure 8.10:  $k$ -resolved conductance of the majority spin channel (in units of  $e^2/h$ ) for a Fe/MgO/Fe MTJ with a barrier thickness of 5 layers.

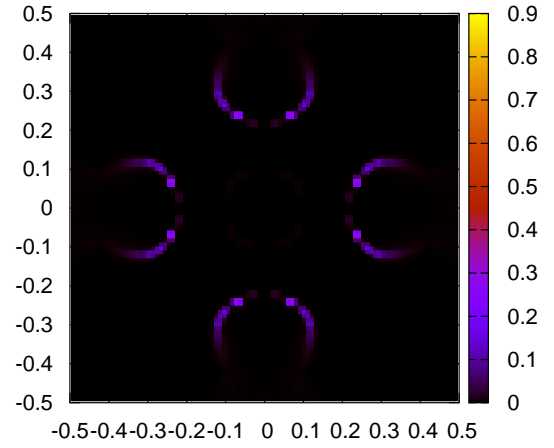


Figure 8.11:  $k$ -resolved conductance of the minority spin channel (in units of  $e^2/h$ ) for a Fe/MgO/Fe MTJ with a barrier thickness of 5 layers.

Table 8.1: Geometry of the relaxed Co/MgO/Co interface (atomic units).  $d_{\text{Co}}$ : Out-of-plane interlayer distance of Co.  $d_{\text{Co(I)}}$ : Interplanar distance of first layer close to MgO.  $d_{\text{Co-O}}$ : First Co-O distance.  $d_{\text{corr}}$ : First Mg-O distance.  $d_{\text{O-O(I)}}$ : First O-O distance.  $d_{\text{MgO}}$ : Out-of-plane interlayer distance of MgO.

$d_{\text{Co}}$	$d_{\text{Co(I)}}$	$d_{\text{Co-O}}$	$d_{\text{corr}}$	$d_{\text{O-O(I)}}$	$d_{\text{MgO}}$
2.52	2.42	4.19	0.12	4.34	4.38

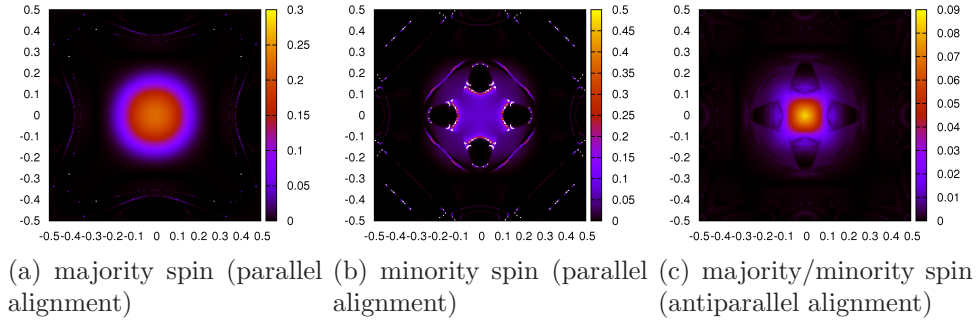


Figure 8.12: 2BZ plot of the conductance  $\Gamma$  per unit cell (in units of  $e^2/h$ ) for the Co/MgO/Co MTJ with 3 layers of MgO as barrier.

a stronger attenuation of the conductance for the antiparallel alignment of the magnetic leads of the MTJ than in the case of iron, where the minority and majority densities of states overlap at the Fermi energy for states with  $\Delta_2$  and  $\Delta_5$  symmetry. Unfortunately, bcc cobalt is unstable. However, it may be grown on an appropriate substrate. In the experiment of Ref. [72] bcc iron was used as substrate to stabilize bcc cobalt. Strictly speaking, due to the lattice mismatch between iron and cobalt, thin films of cobalt on iron are tetragonally distorted and do not exhibit a perfect bcc structure. Because of this tetragonal distortion the  $\Delta_1$  minority state is pulled below the Fermi energy, which is expected to reduce the TMR dramatically. In the present section we investigate the electronic transport properties of Co/MgO/Co MTJs assuming a bcc structure of Co. For the calculation of the electronic transport properties of the Co/MgO/Co magnetic tunnel junction we embedded a stack of 7 Co-layers, 3 MgO-layers and again 7 Co-layers between semi-infinite Co-leads. Geometry optimization has been performed within GGA, using the pbe [64] exchange-correlation functional. The relaxed interface is described in Table 8.1. Transport properties of the Co/MgO/Co interface were calculated using the LDA exchange correlation potential [65]. The charge density of the embedded region was calculated self-consistently using the embedding method once for the parallel and once for the antiparallel alignment of the magnetization of the semi-infinite Co-leads. In Fig. 8.12(a) we show the  $k$ -resolved conductance of the majority spin at the Fermi energy for the parallel alignment of the magnetizations of the two Co leads. Like in the Fe/MgO/Fe MTJ, a broad peak around  $\bar{\Gamma}$  characterizes the conductance of the majority spin channel. For the corresponding conductance of the minority spin, shown in Fig. 8.12(b), the magnitude of the conductance at  $\bar{\Gamma}$  is comparable in size to the conductance of the majority spin channel. This is in marked difference to the Fe/MgO/Fe MTJ, where the conductance at  $\bar{\Gamma}$  is strongly attenuated due to the absence of  $\Delta_1$  minority states at the Fermi energy. We show the  $k$ -resolved conductance of one spin-channel (the conductances of the two spin-channels are identical) for the antiparallel alignment in Fig. 8.12(c). As expected, there is an appreciable conductance in the antiparallel configuration, which is due to the coupling between  $\Delta_1$  majority states of one lead with  $\Delta_1$  minority states of the other lead.

For the present setup we calculated  $\frac{\Gamma_P}{\Gamma_{AP}} = 4.7$ .

Table 8.2: Conductances and TMR-values of the Fe/Co/MgO/Co/Fe MTJ for three different thicknesses ( $\Delta = 3, 5$ , and 7) of the barrier.

$\Delta$	$\Gamma_{P\uparrow}[e^2/h]$	$\Gamma_{P\downarrow}[e^2/h]$	$\Gamma_P[e^2/h]$	$\Gamma_{AP}[e^2/h]$	TMR
3	$2.06 \cdot 10^{-2}$	$6.10 \cdot 10^{-3}$	$2.67 \cdot 10^{-2}$	$3.63 \cdot 10^{-3}$	6.36
5	$7.51 \cdot 10^{-4}$	$9.29 \cdot 10^{-4}$	$1.67 \cdot 10^{-3}$	$1.55 \cdot 10^{-4}$	9.81
7	$4.19 \cdot 10^{-5}$	$4.38 \cdot 10^{-4}$	$4.80 \cdot 10^{-4}$	$1.36 \cdot 10^{-5}$	34.31

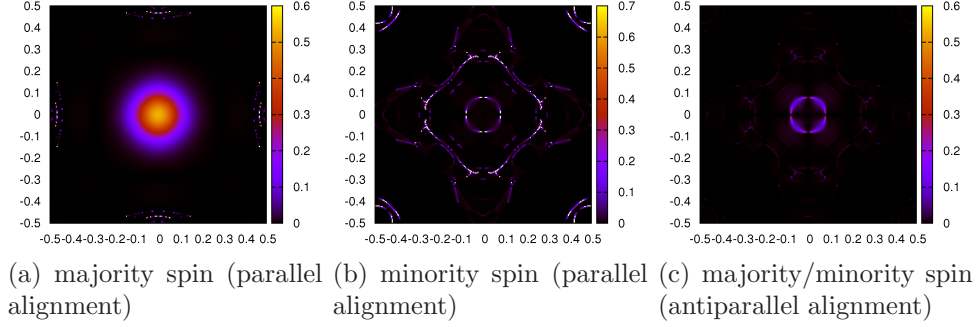


Figure 8.13: 2BZ plot of the conductance for the Fe/Co/MgO/Co/Fe tunnel junction with 3 layers of MgO.

## 8.5 Electronic Transport in Fe/Co/MgO/Co/Fe

At first glance, the results of the previous section might let one expect that MTJs based on bct Cobalt as lead material are not competitive with Fe/MgO/Fe MTJs due to the reduction of the TMR by the presence of minority  $\Delta_1$  states at the Fermi energy. However, by introducing a few interlayers of Co between Fe and the MgO barrier one may in fact achieve a higher TMR ratio than without the Co interlayers: As only  $\Delta_1$  states are available in Cobalt at the Fermi energy in the majority channel, the  $\Delta_2$  and  $\Delta_5$  majority bands of Fe decay as soon as they enter Cobalt. Consequently, for the antiparallel alignment of the electrodes, the conductance is reduced when compared to the Fe/MgO/Fe junction. In figures 8.13, 8.14 and 8.15 the spin and  $k$ -resolved conductances are shown for three different thicknesses of the barrier: 3 layers, 5 layers and 7 layers. In contrast to the Co/MgO/Co junction, at  $\bar{\Gamma}$  the conductance is strongly reduced for the Fe/Co/MgO/Co/Fe junction in the case of antiparallel alignment of the two magnetizations. Consequently the achieved TMR-values are higher. Table 8.2 lists the conductances and TMR-values.

## 8.6 Anisotropy of a surface layer of EuO

As an example for total energy calculations within the embedding method we consider a surface layer of EuO (composed of two atomic layers) on a BaO substrate. The substrate (deep in the bulk of the substrate) is assumed to exhibit cubic in-plane symmetry. The cubic in-plane configuration is not a stable one for the EuO surface layers [73]. The oxygen

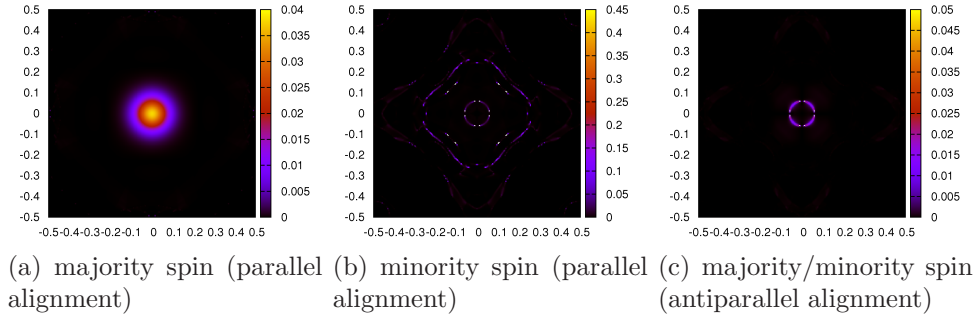


Figure 8.14: 2BZ plot of the conductance for the Fe/Co/MgO/Co/Fe tunnel junction with 5 layers of MgO.

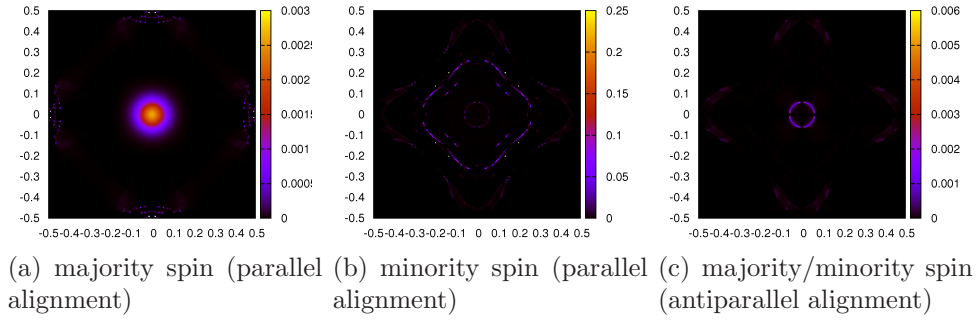


Figure 8.15: 2BZ plot of the conductance for the Fe/Co/MgO/Co/Fe tunnel junction with 7 layers of MgO.

is displaced from the symmetric position. Due to the broken symmetry at the surface the symmetry is also broken in the first few layers of the BaO substrate. We label the direction of the displacement  $x$ , the direction of the surface normal  $z$  and the remaining direction  $y$ . The EuO surface layers are magnetic. We calculate the anisotropy (only the contribution due to spin-orbit coupling) within the embedding method. The calculation is performed using GGA+U. The value of U was chosen to be 8.3 eV and the value of J to be 0.77 eV. All atomic coordinates are relaxed. Due to spin-orbit coupling the total energy depends on the orientation of the magnetization of the EuO surface layer. 8 layers of BaO are explicitly included in the surface calculation, which is embedded with the embedding potential of the semi-infinite BaO substrate. As the system is insulating, a  $7 \times 7$   $k$ -mesh is found to be sufficient to obtain converged results for the anisotropy. With the magnetization pointing in  $x$ -direction the total energy is lower by  $8.94 \mu\text{eV}$  than the configuration with magnetization pointing in  $y$ -direction. Our order-N implementation allows to compute a layer-decomposition of the total energy. From this layer-decomposition we find that the anisotropy energy is strongly concentrated in the EuO surface layers.



## Chapter 9

# Spin-Transfer Torque

*Magnetization control* of magnetic nanoparticles is a highly important issue in the fields of *spintronics* and *magnetic data storage technology*. Using the conventional approach of switching the magnetization of nano-sized objects via application of magnetic fields has several drawbacks. First, the potential for *down-scaling* of devices is rather limited in this approach, as magnetic fields are long-ranged due to their dipolar nature and hence difficult to focus on the nano-scale. Second, regarding the aspect of *power consumption*, it turns out that the manipulation of magnetic nanoparticles by application of magnetic fields is not the most efficient way, as the electric currents needed for the generation of the magnetic fields are relatively high.

One promising alternative to the use of magnetic fields to induce magnetization dynamics is the *current induced switching of the magnetization*, which has been proposed by Slonczewski [8] and Berger [7]. The mechanism behind the current induced magnetization switching is the so called *spin-transfer torque*, which arises in FM1/NM/FM2 and FM1/NI/FM2 trilayer structures traversed by an electric current, where a non-magnetic metal (NM) or a non-magnetic insulator (NI) is sandwiched between two ferromagnetic metals (FM1 and FM2), as shown in Fig. 9.1. This effect occurs both for a current flowing *perpendicular to the planes* (*CPP-geometry*) and for a current flowing *in-plane* (*CIP-geometry*). Only the CPP-geometry will be discussed in the following.

Electrons entering NM via the FM1/NM interface are spin-polarized according to the magnetization in FM1. We assume that the magnetization direction of the *polarizer* FM1 is *pinned*. Denoting the angle between the total spin moments of FM1 and FM2 by  $\theta$  and choosing the spin-quantization axis to be given by the direction of the total spin in FM2, the wave function of the electrons impinging on the NM/FM2 interface is given by

$$\Psi_{\text{in}}(x) = \begin{pmatrix} \cos\left(\frac{\theta}{2}\right) \\ i \sin\left(\frac{\theta}{2}\right) \end{pmatrix} e^{ik_x x}, \quad (9.1)$$

where  $k_x > 0$  is the component of the wave vector in  $x$ -direction. At the NM/FM2 interface a spin-dependent scattering takes place. In the idealized case that FM2 reflects the minority component of the spinor  $\Psi_{\text{in}}$  while transmitting the majority component, the

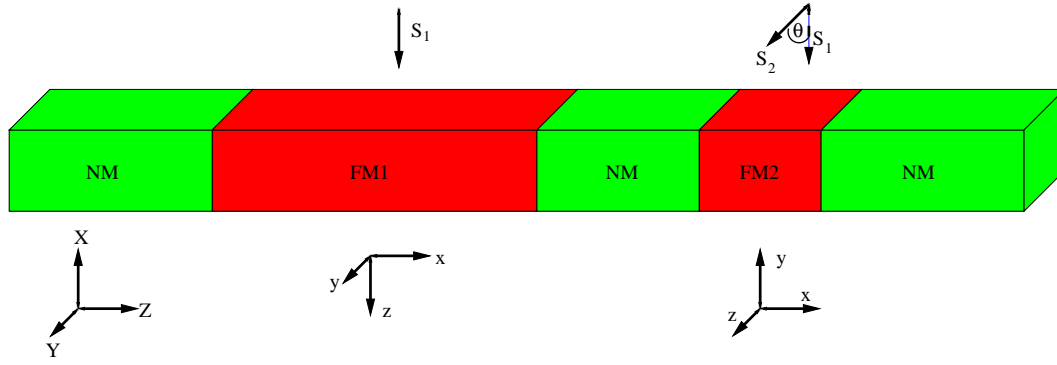


Figure 9.1: Schematic of a CPP-GMR/STT device. The heart of the device is the trilayer system FM1/NM/FM2 composed of two ferromagnetic metals (FM1 and FM2) and a non-magnetic metal (NM). The device is terminated by two buffer layers of a non-magnetic metal. The axes ( $XYZ$ ) define the global coordinate frame. Within the MT-spheres a local coordinate frame ( $xyz$ ) is used, with the local  $z$ -axis parallel to the local spin moment. The local frames are obtained from the global frame by two rotations around the Euler angles  $\alpha$  and  $\beta$ . For FM1 the Euler angles are  $\alpha_1 = 0^\circ$  and  $\beta_1 = 90^\circ$ . For FM2 they are  $\alpha_2 = \theta$  and  $\beta_2 = 90^\circ$ . See Appendix B for the definition of Euler angles. With this choice of axes, the  $XY$ -plane is parallel to the  $yz$ -planes and the  $x$ -axes of the local frames are parallel. The magnetization of FM1 is pinned while the magnetization of FM2 is free. The relative angle between the total spin moments  $S_1$  and  $S_2$  of FM1 and FM2 is  $\theta$ . A current flowing perpendicular to the planes exerts a torque on  $S_2$ , which can be used to switch the magnetization of FM2 between the parallel and antiparallel alignment with respect to the magnetization of FM1.

reflected wave function is

$$\Psi_r(x) = \begin{pmatrix} 0 \\ -i \sin\left(\frac{\theta}{2}\right) \end{pmatrix} e^{-ik_x x} \quad (9.2)$$

while the transmitted wave function is

$$\Psi_t(x) = \begin{pmatrix} \cos\left(\frac{\theta}{2}\right) \\ 0 \end{pmatrix} e^{ik_x x}, \quad (9.3)$$

where we assumed the NM/FM2 interface to be located at  $x = 0$ . Within the region NM the charge current density  $J$  and the spin current density  $(J_x^S, J_y^S, J_z^S)$  are given by

$$\begin{aligned} J &= k_x \cos^2\left(\frac{\theta}{2}\right) \\ J_x^S &= 0 \\ J_y^S &= \frac{1}{2} k_x \sin(\theta) \\ J_z^S &= \frac{1}{2} k_x \cos^2\left(\frac{\theta}{2}\right). \end{aligned} \quad (9.4)$$

The current density of the electron spin in  $y$ -direction,  $J_y^S$ , is discontinuous at the NM/FM2 interface, while the remaining current densities are continuous. In FM2 we have  $J_y^S = 0$  as the *transverse spin component* is completely *absorbed* at the NM/FM2 interface. This discontinuity in the transverse component of the spin current density corresponds to a *net flow of angular momentum* into the NM/FM2 interface, which is given by  $\frac{1}{2} k_x \sin(\theta)$  per unit area. Assuming conservation of total angular momentum one concludes that the flow of angular momentum into the NM/FM2 interface due to the electron current is accompanied by a corresponding change of the magnetization of the analyzing ferromagnetic metal FM2. Interpreting the discontinuity in  $J_y^S$  as the *effect of a torque* which the ferromagnetic metal FM2 exerts on the current, the accompanying change of the magnetization of FM2 may be seen as the effect of an equal but opposite torque which the current exerts on the ferromagnetic metal FM2 due to the principle of *actio equals reactio*. The torque on FM2 may be used to induce magnetization dynamics in FM2, especially it may be used to *switch the magnetization* in FM2 into the configuration where it is aligned *parallel* to the magnetization in FM1. When the reflected wave  $\Psi_r(x)$  hits the NM/FM1 interface spin-dependent scattering takes place again, giving rise to a *torque on the polarizer* FM1. However, as we assume the magnetization of the polarizer to be pinned, no magnetization dynamics is induced in FM1.

We now consider the situation of reversed current, where the electrons flow in negative  $Z$ -direction. In this case the electrons enter NM via the FM2/NM interface. The wave *back-scattered* from the FM1/NM interface exerts then a torque on FM2, which may be used to switch the magnetization into the *antiparallel* alignment.

Besides the simple *switching* there is a second way how the magnetization in the free-layer may react to an applied DC current: It may undergo a *steady state precession*, which

might be interesting for high-frequency applications such as nanometer-scale microwave sources, detectors and mixers. Additionally, spin-transfer torque driven *domain wall motion* is investigated for potential memory and logic applications [74, 75].

Our introductory *toy-model* discussion of the spin torque given above includes only one source of *net spin-current flow*, namely the *spin-dependent transmission*. Additional sources are *spin precession* and *rotation* of reflected and transmitted spins [76]. In section 9.2.1 we will extend our toy-model to include the effect of spin-precession. In the above toy-model discussion we calculated the net spin-current flow into the free layer and exploited the equivalence between the *torque* exerted on a volume and the *net spin-current flow* into that volume. In the following section we will discuss how the torque may be calculated directly.

## 9.1 Calculation of the spin-transfer torque from first principles

We consider the free magnetic layer FM2, as sketched in Fig. 9.1. As the current traverses the free layer, its magnetization direction may change unless the *exchange field*  $\mathbf{B}^{\text{xc}}(\mathbf{r}, t)$  is parallel to the magnetization direction of the current. This change of the magnetization  $\mathbf{m}^{\text{curr}}(\mathbf{r}, t)$  of the current is due to the torque  $\mathbf{N}^{\text{curr}}(t)$  which the slab exerts on the current and which is given by

$$\mathbf{N}^{\text{curr}}(t) = \int_{V_{\text{FL}}} d^3r \mathbf{m}^{\text{curr}}(\mathbf{r}, t) \times \mathbf{B}^{\text{xc}}(\mathbf{r}, t), \quad (9.5)$$

where the integration volume  $V_{\text{FL}}$  is the free layer. Conversely, as a consequence of the law *actio equals reactio* the current exerts an equal but opposite torque  $\mathbf{N}^{\text{FL}}(t)$  on the free layer:

$$\mathbf{N}^{\text{FL}}(t) = - \int_{V_{\text{FL}}} d^3r \mathbf{m}^{\text{curr}}(\mathbf{r}, t) \times \mathbf{B}^{\text{xc}}(\mathbf{r}, t). \quad (9.6)$$

This torque may change and ultimately switch the magnetization of the free layer. However, in a realistic system, the magnetization within the slab may not change freely due to anisotropies. Consequently, part of the torque or even the complete torque might be transferred to the lattice, e.g. if a given torque is too small to switch the magnetization because of large anisotropies. The equation governing the *magnetization dynamics* induced by the torque is the subject of section 9.2.3.

As the exchange field of the slab exerts a torque on the spins of the electrons composing the current which traverses the slab the spins change their orientations and the associated spin current acquires a dependence on the position within the slab. In the following we derive the *relation between the torque acting on the magnetization of the current and the accompanying change of spin current*. The rate of change of the magnetization density  $\mathbf{m}^{\text{curr}}(\mathbf{r}, t)$  contributed by an electron with the wave function  $\Psi(\mathbf{r}, t)$  is given by

$$\dot{\mathbf{m}}^{\text{curr}}(\mathbf{r}, t) = \frac{\partial}{\partial t} [(\Psi(\mathbf{r}, t))^* \boldsymbol{\sigma} \Psi(\mathbf{r}, t)]. \quad (9.7)$$

Using the Schrödinger equation for noncollinear systems without spin-orbit coupling (the time-dependent generalization of Eq. (2.16))

$$i\frac{\partial}{\partial t}\Psi(\mathbf{r}, t) = [-\frac{1}{2}\Delta + V_{\text{eff}}(\mathbf{r}, t) + \boldsymbol{\sigma} \cdot \mathbf{B}^{\text{xc}}(\mathbf{r}, t)]\Psi(\mathbf{r}, t) \quad (9.8)$$

to express the time derivative of the wave function, we obtain for the  $i$ -th component of the magnetization

$$\dot{m}_i^{\text{curr}}(\mathbf{r}, t) = -\nabla \cdot \Im[(\Psi(\mathbf{r}, t))^* \sigma_i \nabla \Psi(\mathbf{r}, t)] - i(\Psi(\mathbf{r}, t))^* \sum_j B_j^{\text{xc}}(\mathbf{r}, t) [\sigma_i, \sigma_j] \Psi(\mathbf{r}, t). \quad (9.9)$$

Defining the spin-current density  $\mathbf{J}_i^S$  for the  $i$ -th component of the spin as

$$\begin{aligned} \mathbf{J}_i^S(\mathbf{x}, t) &= \frac{1}{2i} [(\Psi(\mathbf{x}, t))^* \frac{\sigma_i}{2} \nabla \Psi(\mathbf{x}, t) - (\nabla \Psi(\mathbf{x}, t))^* \frac{\sigma_i}{2} \Psi(\mathbf{x}, t)] \\ &= \Im[\Psi(\mathbf{x}, t))^* \frac{\sigma_i}{2} \nabla \Psi(\mathbf{x}, t)] \end{aligned} \quad (9.10)$$

and making use of the identity

$$[\sigma_i, \sigma_j] = 2i\epsilon_{ijk}\sigma_k \quad (9.11)$$

we finally obtain

$$\dot{m}_i^{\text{curr}}(\mathbf{r}, t) + 2\nabla \cdot \mathbf{J}_i^S(\mathbf{x}, t) = -2[\mathbf{m}^{\text{curr}}(\mathbf{r}, t) \times \mathbf{B}^{\text{xc}}(\mathbf{r}, t)]_i. \quad (9.12)$$

In the case of  $\mathbf{B}^{\text{xc}}(\mathbf{r}, t) = 0$  Eq. (9.12) turns into the continuity equation for the magnetization density: Any change of the magnetization density  $\mathbf{m}^{\text{curr}}(\mathbf{r}, t)$  at the point  $\mathbf{r}$  is due to a net flow of magnetic moment into or out of that point  $\mathbf{r}$ . However, for  $\mathbf{B}^{\text{xc}}(\mathbf{r}, t) \neq 0$  the continuity equation is modified by the right hand side of Eq. (9.12), which describes the change of the magnetization density due to the torque exerted on it. Assuming that the magnetization of the free layer changes slowly compared to the time needed by the electrons to traverse the free layer, we are dealing with a *quasi-stationary situation* when we try to describe the current propagating through the free layer. For such a quasi-stationary system we have approximately  $\dot{\mathbf{m}}^{\text{curr}}(\mathbf{r}, t) = 0$ , and consequently Eq. (9.12) may be used to relate spin-current density and torque:

$$\nabla \cdot \mathbf{J}_i^S(\mathbf{r}) = -[\mathbf{m}^{\text{curr}}(\mathbf{r}) \times \mathbf{B}^{\text{xc}}(\mathbf{r})]_i. \quad (9.13)$$

Thus, as an alternative to Eq. (9.6), the torque on the free layer may also be calculated from the equation

$$N_i^{\text{FL}} = \int_{V_{\text{FL}}} d^3r \nabla \cdot \mathbf{J}_i^S(\mathbf{r}) = \hat{\mathbf{n}} \cdot [\int_{S_R} d^2r \mathbf{J}_i^S(\mathbf{r}) - \int_{S_L} d^2r \mathbf{J}_i^S(\mathbf{r})], \quad (9.14)$$

where  $S_R$  and  $S_L$  are the right and left boundary surfaces of the free layer, respectively, and the surface normal vector  $\hat{\mathbf{n}}$  points to the right. The second equality holds due to Gauss's theorem.

A realistic *simulation of the magnetization dynamics* of the free layer during the current-induced magnetization switching process requires to solve *two coupled problems*: First, the *evaluation of the torque* for a given magnetic configuration of the free layer. Second, the *time evolution of the magnetic configuration* of the free layer in the presence of a given torque. The problem of the time evolution of the magnetization of the free layer may be solved in several ways, differing in the level of approximation involved. An accurate treatment requires the solution of the *Heisenberg-model*, which treats magnetism on the atomic scale. In the *micromagnetic approximation* magnetism is resolved on the scale of a few nanometers. A rather crude approximation is given by the *macrospin model* (see section 9.2.3), where all magnetic moments of the free layer are assumed to be aligned in parallel and the direction of the magnetization is the only degree of freedom of the free layer. The calculation of the total torque exerted on the free layer, according to Eq. (9.6) or Eq. (9.14), is sufficient for the treatment of the magnetization dynamics within the macrospin model. However, for the refined approaches of the Heisenberg-model or the micromagnetic approximation a *spatially resolved torque* is desirable as input. In order to modify Eq. (9.14) for this purpose the free layer is divided into several slabs confined by boundary surfaces  $S_l$  and the torque  $\mathbf{N}^l$  on slab  $l$  is calculated from the net flow of spin angular momentum into the slab through its boundaries  $S_l$  and  $S_{l+1}$ :

$$N_i^l = \hat{\mathbf{n}} \cdot \left[ \int_{S_{l+1}} d^2r \mathbf{J}_i^S(\mathbf{r}) - \int_{S_l} d^2r \mathbf{J}_i^S(\mathbf{r}) \right]. \quad (9.15)$$

Expressed in terms of the current of spin angular momentum per unit cell through boundary  $S_l$ ,

$$I_{l,i}^S = \hat{\mathbf{n}} \cdot \int_{S_l} d^2r \mathbf{J}_i^S(\mathbf{r}), \quad (9.16)$$

Eq. (9.15) becomes

$$N_i^l = (I_{l,i}^S - I_{l+1,i}^S). \quad (9.17)$$

Conceptionally, the *layer-wise evaluation of the torque* fits nicely into the framework of the *embedding-based order- $N$  Green function method*, which is applied in this work.

The formulation of the torque given in Eq. (9.6) lends itself to a generalization leading to a slightly different definition of a local torque: As interstitial and MT-spheres are treated separately within the FLAPW framework, and the contribution of the interstitial to the torque is expected to be small, it is convenient to define the torque  $\mathbf{N}^\mu$  on the MT-sphere of atom  $\mu$  as:

$$\mathbf{N}^\mu = - \int_{MT^\mu} d^3r \mathbf{m}^{\text{curr}}(\mathbf{r}) \times \mathbf{B}^{\text{xc}}(\mathbf{r}), \quad (9.18)$$

where the integration volume is given by the MT-sphere of atom  $\mu$ . Obviously, this latter picture of local torques acting on local magnetic moments corresponds well to the treatment of magnetization dynamics within the Heisenberg model. Making use of Eq. (9.13) we may again express the torque in terms of the accompanying spin current flow out of the volume of the MT-sphere of atom  $\mu$ :

$$N_i^\mu = \int_{MT^\mu} \mathbf{J}_i^S \cdot d\mathbf{S}. \quad (9.19)$$

Especially in the limit of zero bias it is convenient to consider the *torkance*  $\mathbf{T}^\mu(E)$  instead of the torque  $\mathbf{N}^\mu$ , which may be obtained from the *energy resolved magnetization*  $\mathbf{m}^{\text{curr}}(\mathbf{r}, E)$  as follows:

$$\mathbf{T}^\mu(E) = -|e| \int_{MT^\mu} d^3r \mathbf{m}^{\text{curr}}(\mathbf{r}, E) \times \mathbf{B}^{\text{xc}}(\mathbf{r}). \quad (9.20)$$

The torkance  $\mathbf{T}^\mu(E)$  describes how much the scattering states at energy  $E$  contribute to the torque  $\mathbf{N}^\mu$ . Consequently, the torque is the bias-voltage window integral of the torkance and the torkance is the differential torque per voltage.

### 9.1.1 Current induced torques in the presence of spin orbit coupling

In Eq. (9.6,9.18) we gave a general formulation of the torque, which may also be applied in the presence of spin-orbit coupling [77, 78]. In justifying Eq. (9.6,9.18) we called in Newton's law of *actio equals reactio*, which allowed us to calculate the torque on the free magnetic layer from the torque exerted on the electrons as they traverse the free magnetic layer. At this point it is reassuring to verify that invoking Newton's law leads to the same result as a thorough investigation of the very *mechanism* behind the torque on the free magnetic layer. The presence of a stationary current due to the infinitesimal bias  $\delta U = \delta E/e$  modifies the equilibrium magnetization  $\mathbf{m}(\mathbf{r})$  by  $\delta \mathbf{m}(\mathbf{r}) = \partial \mathbf{m}^{\text{curr}}(\mathbf{r}) / \partial E \delta E$  and the equilibrium exchange field  $\mathbf{B}^{\text{xc}}(\mathbf{r})$  by  $\delta \mathbf{B}^{\text{xc}}(\mathbf{r}) = \partial \mathbf{B}^{\text{xc}}(\mathbf{r}) / \partial \mathbf{m}(\mathbf{r}) \delta \mathbf{m}(\mathbf{r})$ . Due to the change of the exchange field the free layer experiences a local torkance, which is given by

$$\begin{aligned} \mathbf{T}(\mathbf{r}, E) &= |e| \mathbf{m}(\mathbf{r}) \times \frac{\delta \mathbf{B}^{\text{xc}}(\mathbf{r})}{\delta E} = |e| \mathbf{m}(\mathbf{r}) \times \left[ \frac{1}{m(\mathbf{r})} \frac{\partial \mathbf{m}^{\text{curr}}(\mathbf{r})}{\partial E} B^{\text{xc}}(n(\mathbf{r}), m(\mathbf{r})) \right] = \\ &= -|e| \frac{\partial \mathbf{m}^{\text{curr}}(\mathbf{r})}{\partial E} \times \mathbf{B}^{\text{xc}}(\mathbf{r}) = -|e| \mathbf{m}^{\text{curr}}(\mathbf{r}, E) \times \mathbf{B}^{\text{xc}}(\mathbf{r}), \end{aligned} \quad (9.21)$$

where we made use of Eq. (2.21) for the exchange field:

$$\mathbf{B}^{\text{xc}}(\mathbf{r}) = \mathbf{B}^{\text{xc}}(n(\mathbf{r}), m(\mathbf{r})) \hat{\mathbf{m}}(\mathbf{r}). \quad (9.22)$$

Obviously, Eq. (9.21) justifies Eq. (9.20).

The equivalence of Eq. (9.6) to Eq. (9.14) and of Eq. (9.18) to Eq. (9.19) follows from Eq. (9.13). As Eq. (9.13) does not hold in the presence of spin-orbit coupling, we cannot use Eq. (9.14,9.19) in this case.

According to our introductory discussion, Eq. (9.4), the requirements for the occurrence of a spin-torque are that two ferromagnets (a polarizer and an analyzer, FM1 and FM2 in Fig. 9.1) have to be present and that the magnetizations in FM1 and FM2 have to enclose the angle  $0^\circ \neq \theta \neq 180^\circ$ . However, that discussion did not take spin-orbit coupling into account. In fact, in the presence of spin-orbit coupling, the torques are not zero for perfect parallel or antiparallel alignment of the magnetizations, i.e., for the configurations

characterized by angles  $\theta = 0^\circ$  or  $\theta = 180^\circ$ . It can also be shown that the magnetization of a uniformly magnetized single domain experiences a torque in the presence of a current due to spin-orbit coupling [79, 80, 81], i.e., theoretically there is no need for the typical trilayer structure involving both a polarizer and an analyzer if spin-orbit coupling is sufficiently strong. However, the *spin-orbit induced torque* is a *field-like torque* and consequently a steady state magnetization precession cannot be sustained only based on this torque (see also section 9.2.3).

## 9.2 Current induced Torques and magnetization Dynamics in Model systems

### 9.2.1 The interface between a normal metal and a ferromagnetic metal

Our introductory discussion of the spin transfer torque, Eq. (9.1-9.4), was based on the assumption that the magnetic layers completely reflect impinging electrons and that the Fermi wave vector within the nonmagnetic spacer is identical to the Fermi wave vector of the majority channel in the magnetic layers. A more realistic description of the behavior of electrons close to interfaces between nonmagnetic metals and ferromagnetic metals has been given by Berger [82, 7]. A similar analysis has been performed by Slonczewski [83] for ferromagnets separated by a tunneling barrier. Our following simplified discussion is similar to the one of Ref. [7]. While the wave function of the electrons impinging on the NM/FM2 interface is still given by Eq. (9.1) with respect to the reference frame of FM2 (see Fig. 9.1), the reflected wave is now assumed to be

$$\Psi_r(x) = \begin{pmatrix} A \\ B \end{pmatrix} e^{-ik_x x} \quad (9.23)$$

instead of Eq. (9.2). Analogously, the transmitted wave is

$$\Psi_t(x) = \begin{pmatrix} C e^{ik_x^\uparrow x} \\ D e^{ik_x^\downarrow x} \end{pmatrix}, \quad (9.24)$$

where we introduced Fermi wave vectors  $k_x^\uparrow$  and  $k_x^\downarrow$  for majority and minority, respectively. The coefficients  $A$ ,  $B$ ,  $C$ , and  $D$  are determined from the boundary conditions for continuity of the wave function and its derivative at the N/FM2 interface:

$$\begin{aligned} A &= \frac{k_x - k_x^\uparrow}{k_x + k_x^\uparrow} \cos\left(\frac{\theta}{2}\right) \\ B &= i \frac{k_x - k_x^\downarrow}{k_x + k_x^\downarrow} \sin\left(\frac{\theta}{2}\right) \\ C &= 2 \frac{k_x}{k_x + k_x^\uparrow} \cos\left(\frac{\theta}{2}\right) \\ D &= 2i \frac{k_x}{k_x + k_x^\downarrow} \sin\left(\frac{\theta}{2}\right). \end{aligned} \quad (9.25)$$



From the transmitted wave, Eq. (9.24), we obtain the following components of the magnetization:

$$\begin{aligned} m_x(x) &= -4 \frac{\sin(\theta)}{(1 + k_x^\uparrow/k_x)(1 + k_x^\downarrow/k_x)} \sin((k_x^\uparrow - k_x^\downarrow)x) \\ m_y(x) &= 4 \frac{\sin(\theta)}{(1 + k_x^\uparrow/k_x)(1 + k_x^\downarrow/k_x)} \cos((k_x^\uparrow - k_x^\downarrow)x) \\ m_z(x) &= 2k_x^2 \left( \frac{-1 + \cos(\theta)}{(k_x + k_x^\downarrow)^2} + \frac{1 + \cos(\theta)}{(k_x + k_x^\uparrow)^2} \right). \end{aligned} \quad (9.26)$$

Obviously, Eq. (9.26) describes a precession of the magnetic moment around the  $z$ -axis with the wave-vector  $(k_x^\uparrow - k_x^\downarrow)$ . One expects that the precessional motion decays as the electron moves through the free magnetic layer due to scattering with impurities and phonons and due to dephasing effects not present in this simple model. In Ref. [7] these effects are included phenomenologically through a damping factor  $\exp(-\alpha x)$  by which the components of the magnetization,  $m_x(x)$  and  $m_y(x)$ , are multiplied. This damping factor ensures that the magnetization of the current will ultimately align with the magnetization of the free layer for a sufficiently thick free layer. Due to  $m_x(0) = 0$  the magnetization of the electron lies in the  $yz$ -plane when it enters the free magnetic layer and forms an angle  $\theta_m = \arctan(m_y(0)/m_z(0))$  with its magnetization. If the free magnetic layer is sufficiently thick, the combined net effect of the precessional motion and the damping is that the magnetization of the current is rotated by the angle  $\theta_m$  in the  $yz$ -plane. The corresponding torque, which the free layer experiences, points in  $y$ -direction, and is given by

$$N_y(\theta) = \int_0^\infty dx m_x(x) B_z(x) = -\frac{4B_z}{(1 + k_x^\uparrow/k_x)(1 + k_x^\downarrow/k_x)(k_x^\uparrow - k_x^\downarrow)}, \quad (9.27)$$

where we made use of

$$\lim_{\alpha \rightarrow 0} \int_0^\infty e^{-\alpha x} \sin(\beta x) dx = \lim_{\alpha \rightarrow 0} \frac{\beta}{\beta^2 + \alpha^2} = \frac{1}{\beta}, \quad (9.28)$$

which holds for real-valued  $\alpha$  and  $\beta$  and  $\alpha > 0$ . As this torque lies *in the plane* defined by the magnetizations of the free and fixed layers, we denote it *in-plane torque* in the following. Very often *spin-transfer torque* and *in-plane torque* are used synonymous. Due to the relation

$$\lim_{\alpha \rightarrow 0} \int_0^\infty e^{-\alpha x} \cos(\beta x) dx = \lim_{\alpha \rightarrow 0} \frac{\alpha}{\beta^2 + \alpha^2} = 0 \quad (9.29)$$

we find  $N_x(\theta) = 0$ , as expected on the basis of the preceding discussion. However, for thin free layers the model predicts a finite value for  $N_x(\theta)$ , because the magnetic moment of the electron has not yet aligned its magnetic moment with the magnetic moment of the free layer. In the following we will refer to  $N_x(\theta)$  as *out-of-plane torque*. Since the out-of-plane torque is perpendicular to the magnetization direction of the free magnetic layer as if its origin were the reaction of the magnetization to a magnetic field, it is often called *field-like torque*. There are several reasons why the *field-like torque* can be much smaller

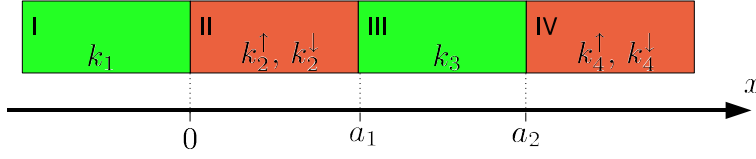


Figure 9.2: Four-layer structure: Two non-magnetic regions I and III (green) and two magnetic regions II and IV (red). The wave vectors in the non-magnetic regions are  $k_1$  and  $k_3$ . The wave vectors in the magnetic regions are  $k_2^\uparrow$ ,  $k_2^\downarrow$  (region II) and  $k_4^\uparrow$ ,  $k_4^\downarrow$  (region IV).

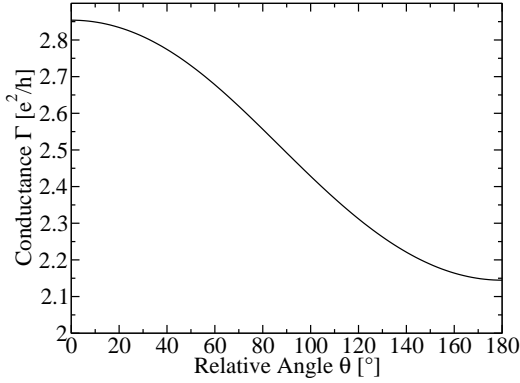


Figure 9.3: Conductance  $\Gamma(\theta)$  of the model of a four-layer structure as a function of the relative angle  $\theta$ .

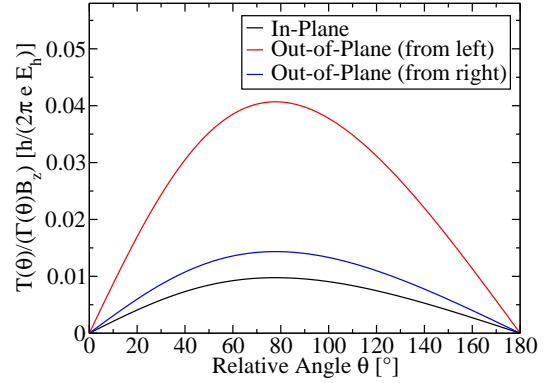


Figure 9.4: Torque per current and exchange bias  $T(\theta)/(\Gamma(\theta)B_z^{xc})$  of the model of a four-layer structure as a function of the relative angle  $\theta$ .

than the *spin-transfer torque*. One reason already mentioned concerns those cases where the free magnetic layer is so *thick* that the magnetic moment of the electron traversing it is parallel to the magnetization of the free magnetic layer when the electron leaves it. A second reason is related to the oscillatory dependence of the magnetization and hence the torque on  $(k_x^\uparrow - k_x^\downarrow)$  in Eq. (9.26): In the *Fermi-surface integral* of the  $k$ -dependent torque contributions of different sign compensate one another. A third reason concerns the question of how ideal a realistic spin-valve can be manufactured: The out-of-plane torque is an oscillating function of layer-thickness and due to *thickness variations* of the free magnetic layer over the cross section of the sample the local torques may differ in sign and compensate each other.

### 9.2.2 Modeling a complete four-layer structure

The discussion of the simple model on the interface between a normal metal and a magnetic metal in the previous section 9.2.1 helped us to understand the origin of the spin-transfer-torque, but was missing aspects such as multiple scattering. In the following we discuss the extension of the model of section 9.2.1 to a structure containing three normal-metal magnetic-metal interfaces, as sketched in Fig. 9.2. Regions I and III constitute normal metals with wave vectors  $k_1$  and  $k_3$ , respectively. Regions II and IV represent the magnetic

metals. Region two is described by wave vectors  $k_2^\uparrow$  and  $k_2^\downarrow$  for majority and minority, respectively. Analogously, wave vectors  $k_4^\uparrow$  and  $k_4^\downarrow$  characterize region four. For states incident from the left and due to the spin-up channel the wave functions are given by

$$\psi_l^\uparrow(x) = \begin{cases} \begin{pmatrix} e^{ik_1x} + a_{11}^\uparrow e^{-ik_1x} \\ a_{21}^\uparrow e^{-ik_1x} \end{pmatrix} & x \leq 0 \\ \begin{pmatrix} a_{12}^\uparrow e^{-ik_2^\uparrow x} + b_{12}^\uparrow e^{ik_2^\uparrow x} \\ a_{22}^\uparrow e^{-ik_2^\downarrow x} + b_{22}^\uparrow e^{ik_2^\downarrow x} \end{pmatrix} & 0 \leq x \leq a_1 \\ \begin{pmatrix} a_{13}^\uparrow e^{-ik_3x} + b_{13}^\uparrow e^{ik_3x} \\ a_{23}^\uparrow e^{-ik_3x} + b_{23}^\uparrow e^{ik_3x} \end{pmatrix} & a_1 \leq x \leq a_2 \\ \begin{pmatrix} b_{14}^\uparrow \cos\left(\frac{\theta}{2}\right) e^{ik_4^\uparrow x} + ib_{24}^\uparrow \sin\left(\frac{\theta}{2}\right) e^{ik_4^\downarrow x} \\ ib_{14}^\uparrow \sin\left(\frac{\theta}{2}\right) e^{ik_4^\uparrow x} + b_{24}^\uparrow \cos\left(\frac{\theta}{2}\right) e^{ik_4^\downarrow x} \end{pmatrix} & a_2 \leq x \end{cases} \quad (9.30)$$

while those due to the spin-down channel are

$$\psi_l^\downarrow(x) = \begin{cases} \begin{pmatrix} a_{11}^\downarrow e^{-ik_1x} \\ e^{ik_1x} + a_{21}^\downarrow e^{-ik_1x} \end{pmatrix} & x \leq 0 \\ \begin{pmatrix} a_{12}^\downarrow e^{-ik_2^\uparrow x} + b_{12}^\downarrow e^{ik_2^\uparrow x} \\ a_{22}^\downarrow e^{-ik_2^\downarrow x} + b_{22}^\downarrow e^{ik_2^\downarrow x} \end{pmatrix} & 0 \leq x \leq a_1 \\ \begin{pmatrix} a_{13}^\downarrow e^{-ik_3x} + b_{13}^\downarrow e^{ik_3x} \\ a_{23}^\downarrow e^{-ik_3x} + b_{23}^\downarrow e^{ik_3x} \end{pmatrix} & a_1 \leq x \leq a_2 \\ \begin{pmatrix} b_{14}^\downarrow \cos\left(\frac{\theta}{2}\right) e^{ik_4^\uparrow x} + ib_{24}^\downarrow \sin\left(\frac{\theta}{2}\right) e^{ik_4^\downarrow x} \\ ib_{14}^\downarrow \sin\left(\frac{\theta}{2}\right) e^{ik_4^\uparrow x} + b_{24}^\downarrow \cos\left(\frac{\theta}{2}\right) e^{ik_4^\downarrow x} \end{pmatrix} & a_2 \leq x. \end{cases} \quad (9.31)$$

Analogously, scattering states incident from the right due to the spin-up channel are given by

$$\psi_r^\uparrow(x) = \begin{cases} \begin{pmatrix} a_{11}^\uparrow e^{-ik_1x} \\ a_{21}^\uparrow e^{-ik_1x} \end{pmatrix} & x \leq 0 \\ \begin{pmatrix} a_{12}^\uparrow e^{-ik_2^\uparrow x} + b_{12}^\uparrow e^{ik_2^\uparrow x} \\ a_{22}^\uparrow e^{-ik_2^\downarrow x} + b_{22}^\uparrow e^{ik_2^\downarrow x} \end{pmatrix} & 0 \leq x \leq a_1 \\ \begin{pmatrix} a_{13}^\uparrow e^{-ik_3x} + b_{13}^\uparrow e^{ik_3x} \\ a_{23}^\uparrow e^{-ik_3x} + b_{23}^\uparrow e^{ik_3x} \end{pmatrix} & a_1 \leq x \leq a_2 \\ \begin{pmatrix} b_{14}^\uparrow \cos\left(\frac{\theta}{2}\right) e^{ik_4^\uparrow x} + ib_{24}^\uparrow \sin\left(\frac{\theta}{2}\right) e^{ik_4^\downarrow x} + \cos\left(\frac{\theta}{2}\right) e^{-ik_4^\uparrow x} \\ ib_{14}^\uparrow \sin\left(\frac{\theta}{2}\right) e^{ik_4^\uparrow x} + b_{24}^\uparrow \cos\left(\frac{\theta}{2}\right) e^{ik_4^\downarrow x} + i \sin\left(\frac{\theta}{2}\right) e^{-ik_4^\uparrow x} \end{pmatrix} & a_2 \leq x \end{cases} \quad (9.32)$$

while those due to the spin-down channel are:

$$\psi_r^\downarrow(x) = \begin{cases} \begin{pmatrix} a_{11}^\downarrow e^{-ik_1 x} \\ a_{21}^\downarrow e^{-ik_1 x} \end{pmatrix} & x \leq 0 \\ \begin{pmatrix} a_{12}^\downarrow e^{-ik_2^\uparrow x} + b_{12}^\downarrow e^{ik_2^\uparrow x} \\ a_{22}^\downarrow e^{-ik_2^\uparrow x} + b_{22}^\downarrow e^{ik_2^\uparrow x} \end{pmatrix} & 0 \leq x \leq a_1 \\ \begin{pmatrix} a_{13}^\downarrow e^{-ik_3 x} + b_{13}^\downarrow e^{ik_3 x} \\ a_{23}^\downarrow e^{-ik_3 x} + b_{23}^\downarrow e^{ik_3 x} \end{pmatrix} & a_1 \leq x \leq a_2 \\ \begin{pmatrix} b_{14}^\downarrow \cos\left(\frac{\theta}{2}\right) e^{ik_4^\uparrow x} + ib_{24}^\downarrow \sin\left(\frac{\theta}{2}\right) e^{ik_4^\uparrow x} + i \sin\left(\frac{\theta}{2}\right) e^{-ik_4^\uparrow x} \\ ib_{14}^\downarrow \sin\left(\frac{\theta}{2}\right) e^{ik_4^\uparrow x} + b_{24}^\downarrow \cos\left(\frac{\theta}{2}\right) e^{ik_4^\uparrow x} + \cos\left(\frac{\theta}{2}\right) e^{-ik_4^\uparrow x} \end{pmatrix} & a_2 \leq x. \end{cases} \quad (9.33)$$

Requiring continuity of the wave function and its first derivative at  $x = 0$ ,  $x = a_1$ , and  $x = a_2$  one obtains two sets of linear equations for the unknown coefficients  $a_{ij}^s$  and  $b_{ij}^s$ , one set characterizing  $\psi_l^s(x)$  and a second set characterizing  $\psi_r^s(x)$ . As the expressions which one obtains for  $a_{ij}^s$  and  $b_{ij}^s$  as solution to this system of linear equations are rather lengthy, we do not explicitly write them here. From the coefficients  $a_{ij}^s$  and  $b_{ij}^s$  one obtains the conductance as follows:

$$\Gamma_l = \frac{1}{2\pi} \left( \frac{k_4^\uparrow}{k_1} |b_{14}^\uparrow|^2 + \frac{k_4^\downarrow}{k_1} |b_{24}^\uparrow|^2 + \frac{k_4^\uparrow}{k_1} |b_{14}^\downarrow|^2 + \frac{k_4^\downarrow}{k_1} |b_{24}^\downarrow|^2 \right) \quad (9.34)$$

for states incident from the left and

$$\Gamma_r = \frac{1}{2\pi} \left( \frac{k_1}{k_4^\uparrow} |a_{11}^\uparrow|^2 + \frac{k_1}{k_4^\downarrow} |a_{21}^\uparrow|^2 + \frac{k_1}{k_4^\uparrow} |a_{11}^\downarrow|^2 + \frac{k_1}{k_4^\downarrow} |a_{21}^\downarrow|^2 \right) \quad (9.35)$$

for states incident from the right. Of course, the conductance exhibits the symmetry property

$$\Gamma_l = \Gamma_r. \quad (9.36)$$

The in-plane torkance  $T_\parallel$  and the out-of-plane torkance  $T_\perp$  on the free layer, i.e., the region  $0 \leq x \leq a_1$ , are given by

$$\begin{aligned} T_{l,\parallel} &= T_{l,y} = \frac{2}{k_1} \int_0^{a_1} m_{l,x}(x) B_z^{\text{xc}}(x) dx = \frac{4}{k_1} \int_0^{a_1} \Re[(\psi_l^\uparrow(x))^* \psi_l^\downarrow(x)] B_z^{\text{xc}}(x) dx, \\ T_{l,\perp} &= T_{l,x} = -\frac{2}{k_1} \int_0^{a_1} m_{l,y}(x) B_z^{\text{xc}}(x) dx = \frac{4}{k_1} \int_0^{a_1} \Im[(\psi_l^\uparrow(x))^* \psi_l^\downarrow(x)] B_z^{\text{xc}}(x) dx \end{aligned} \quad (9.37)$$

in the case of states incident from the left and by analogous expressions for the states incident from the right.

It is straightforward to solve the system of linear equations mentioned above numerically. In Fig. 9.3 and Fig. 9.4 we show the results which one obtains for the following parameters:  $k_1 = 4$ ,  $k_2^\uparrow = 4$ ,  $k_2^\downarrow = 1$ ,  $k_3 = 4$ ,  $k_4^\uparrow = 4$ ,  $k_4^\downarrow = 10$ ,  $a_1 = 2$ ,  $a_2 = 4$ . The conductance of the model is shown in Fig. 9.3. In Fig. 9.4 we compare the torkances due to states incident from the left to the torkances due to states incident from the right. We adjusted the signs of the torkances so that all of them are positive in order to make

comparison easier. Generally, we find that while the in-plane torque is antisymmetric with respect to inversion of the direction of current-flow, the out-of-plane torque exhibits neither symmetry nor antisymmetry with respect to inversion of current-flow:

$$\begin{aligned} T_{l,\parallel} &= -T_{r,\parallel}, \\ |T_{l,\perp}| &\neq |T_{r,\perp}|, \end{aligned} \quad (9.38)$$

which is a remarkable difference to the relation Eq. 9.36 for the conductance.

### 9.2.3 Macrospin model of current induced magnetization switching

We assume the total spin moment  $\mathbf{S}_1$  of the fixed magnetic layer (FM1; see Fig. 9.1) to be constant and to point in the direction  $\hat{\mathbf{S}}_1$ , and consider only the dynamics of the free magnetic layer (FM2). Within the macrospin model [84] the magnetization of the free magnetic layer is assumed to be spatially uniform. Consequently, the macrospin model is not able to describe magnetic excitations within the free layer (e.g. spin-wave excitations); only the collective motion of all magnetic moments in parallel is considered. The dynamics of the direction of the free-layer spin moment  $\hat{\mathbf{S}}_2(t)$  is described by the *generalized Landau-Lifshitz-Gilbert equation*:

$$\frac{d\hat{\mathbf{S}}_2(t)}{dt} = -|\gamma|\hat{\mathbf{S}}_2(t) \times H_{\text{eff}} + \alpha_G \hat{\mathbf{S}}_2(t) \times \frac{d\hat{\mathbf{S}}_2(t)}{dt} + \frac{|\gamma|}{M}(\mathbf{N}_{\parallel} + \mathbf{N}_{\perp}), \quad (9.39)$$

where  $\gamma$  is the *gyromagnetic ratio*, the *effective field*  $H_{\text{eff}}$  is related to the total energy of the free layer,  $E_{\text{FL}}$ , by

$$\mathbf{H}_{\text{eff}} = -\frac{1}{V_{\text{FL}}} \frac{\partial E_{\text{FL}}}{\partial \mathbf{m}}, \quad (9.40)$$

the *Gilbert damping* term  $\alpha_G \hat{\mathbf{S}}_2 \times \dot{\hat{\mathbf{S}}}_2$  describes the energy dissipation, e.g. through lattice vibrations and spin-flip scattering, in a phenomenological way, the *spin-transfer term* is given by

$$\mathbf{N}_{\parallel} = g(\theta) I \hat{\mathbf{S}}_2 \times [\hat{\mathbf{S}}_1 \times \hat{\mathbf{S}}_2], \quad (9.41)$$

where the *spin-transfer efficiency*  $g(\theta)$  describes both the deviation of the angular dependence of  $\mathbf{N}_{\parallel}$  from sine-behavior and the size of the spin-transfer torque. For transition-metal ferromagnets  $\gamma$  lies typically in the range from -2.1 to -2.2, where the small orbital moment due to spin-orbit coupling explains the deviation of  $\gamma$  from the  $g_e$ -factor of the electron,

$$g_e = -2\left(1 + \frac{\alpha}{2\pi} + \dots\right) \approx -2.0023. \quad (9.42)$$

In general the *effective field*  $H_{\text{eff}}$  is the sum of the external magnetic field (associated with the *Zeeman energy*), the magnetostatic field (leading e.g. to the *shape anisotropy energy*), and the field associated with the *magnetocrystalline anisotropy energy*. If the current-induced torques are absent the *Gilbert damping* term aligns the magnetization of the free

layer with the effective magnetic field. Consequently, steady magnetization precessions are only possible if a torque is present which can compete with the damping, which is the case for the *in-plane torque*,  $\mathbf{N}_{\parallel}$ , but not for the *out-of-plane torque*,  $\mathbf{N}_{\perp}$ . If the in-plane torque is zero, any magnetization precession will be extinguished by the damping and the out-of-plane torque will simply contribute to the effective field, i.e., rotate the magnetization direction away from the direction it would take for zero out-of-plane torque.

The precession of the magnetization of a ferromagnet may influence the spin current in an adjacent nonmagnet, which is not surprising when viewing it as the inverse effect to the current-induced magnetization dynamics. This so called *spin pumping* may be included as an additional damping term in Eq. (9.39) [84].

### 9.2.4 Slonczewski's model

Slonczewski proposed a model for GMR and STT in the CPP-geometry, which relies on effective-circuit theory and an approximate form of the statistical operator in the non-magnetic interlayer (NM). As the involved approximations turn out to be rather good for many systems and as the model requires only a small set of well-known material properties, Slonczewski's model is widely used for the unified description of GMR and STT. We shortly describe the model here. Following Slonczewski [85] we denote the eigenstates of  $S_z$  as  $|L, \sigma\rangle$  for the polarizer (FM1) and  $|R, \sigma\rangle$  for the analyzer (FM2). The spin rotation transformation  $\langle L, \sigma | R, \sigma' \rangle = U_{\sigma, \sigma'}$  is given by

$$\mathbf{U} = \begin{pmatrix} \cos\left(\frac{\theta}{2}\right) & i \sin\left(\frac{\theta}{2}\right) \\ i \sin\left(\frac{\theta}{2}\right) & \cos\left(\frac{\theta}{2}\right) \end{pmatrix}, \quad (9.43)$$

where we defined the coordinate frames in (FM1) and (FM2) and the angle  $\theta$  like in Fig. 9.1. If (FM1) and (FM2) have the property that they nearly perfectly transmit incident majority spin electrons any reflected left-moving electron in NM has polarization  $|R, -\rangle$  and any reflected right-moving electron in NM has polarization  $|L, -\rangle$ . In this case one may use the approximation that electrons in NM which move rightward ( $v > 0$ ) have either the spin-polarization  $|L, +\rangle$  or  $|L, -\rangle$  and that electrons in NM which move leftward ( $v < 0$ ) have either the spin-polarization  $|R, +\rangle$  or  $|R, -\rangle$ , which leads to the following density matrix in NM:

$$\begin{aligned} \rho_{\text{NM}} = & \sum_{\sigma=\pm 1} |L, \sigma\rangle \sum_{\mathbf{k}} |\mathbf{k}\rangle f_{\sigma}^{\rightarrow}(\mathbf{k}) \langle \mathbf{k}| \langle L, \sigma| + \\ & + \sum_{\sigma=\pm 1} |R, \sigma\rangle \sum_{\mathbf{k}} |\mathbf{k}\rangle f_{\sigma}^{\leftarrow}(\mathbf{k}) \langle \mathbf{k}| \langle R, \sigma|, \end{aligned} \quad (9.44)$$

where we introduced two Fermi-distribution functions  $f_{\sigma}^{\rightarrow}(\mathbf{k})$  for right-moving electrons and likewise two Fermi-distribution functions  $f_{\sigma}^{\leftarrow}(\mathbf{k})$  for left-moving electrons. Approximating the Fermi distribution functions, the following expressions are obtained from the density

matrix Eq. (9.44) for the densities and currents:

$$\begin{aligned} n_{i,\sigma} &= \frac{1}{4} \frac{\partial n}{\partial E} \bigg|_{E_F} \sum_{\sigma'} \{ \mu_{\sigma'}^{\rightarrow} |\langle i, \sigma | L, \sigma' \rangle|^2 + \mu_{\sigma'}^{\leftarrow} |\langle i, \sigma | R, \sigma' \rangle|^2 \} + \frac{n_0}{2} \\ J_{i,\sigma} &= \frac{v_F}{4} \frac{\partial n}{\partial E} \bigg|_{E_F} \sum_{\sigma'} \{ -\mu_{\sigma'}^{\rightarrow} |\langle i, \sigma | L, \sigma' \rangle|^2 + \mu_{\sigma'}^{\leftarrow} |\langle i, \sigma | R, \sigma' \rangle|^2 \} \end{aligned} \quad (9.45)$$

Eliminating the four chemical potentials, one gets the set of relations

$$\begin{aligned} \Delta J_R &= \frac{\Delta J_L (1 + \cos^2(\theta)) - G \Delta W_L \sin^2(\theta)}{2 \cos(\theta)} \\ \Delta W_R &= \frac{-G^{-1} \Delta J_L \sin^2(\theta) + \Delta W_L (1 + \cos^2(\theta))}{2 \cos(\theta)}, \end{aligned} \quad (9.46)$$

where

$$G = e^2 n_F v_0 / 2 \quad (9.47)$$

is a parameter of the interlayer,  $\Delta J_i$  are spin-currents, and  $\Delta W_i = \frac{2}{en_F} (n_{i,-} - n_{i,+})$ . Applying effective-circuit theory one obtains the following expression for the areal resistivity of a symmetric trilayer:

$$R(\theta) = \frac{(R_+ + R_-) \sin^2(\frac{\theta}{2}) + 2AGR_+R_- \cos^2(\frac{\theta}{2})}{2 \sin^2(\frac{\theta}{2}) + AG(R_+ + R_-) \cos^2(\frac{\theta}{2})}, \quad (9.48)$$

where  $R_+$  and  $R_-$  are the interface resistances of majority and minority, respectively. For a symmetric NM/FM/NM/FM/NM five-layer structure, the interface resistances  $R_+$  and  $R_-$  are two times the respective interface resistances of NM/FM. Resistances of FM due to bulk scattering, e.g. caused by impurities, have to be added to  $R_+$  and  $R_-$ , respectively. Clearly, the areal resistivities of the parallel and the antiparallel alignments are given by

$$\begin{aligned} R_{\uparrow} &= \frac{2R_-R_+}{R_- + R_+}, \\ R_{\downarrow} &= R(180^\circ) = (R_+ + R_-)/2. \end{aligned} \quad (9.49)$$

For the torque per current one obtains

$$\frac{N}{I} = \frac{R_- - R_+}{R_+ + R_-} \frac{\Lambda \hbar}{4 e \Lambda \cos^2(\theta/2) + \Lambda^{-1} \sin^2(\theta/2)} \sin(\theta), \quad (9.50)$$

with  $\Lambda = [AG(R_+ + R_-)/2]^{1/2}$ .

### 9.2.5 Interpretation of GMR and STT data

Experimental data on the angular variation of the GMR signal are usually reduced to the normalized resistance

$$r(\theta) = \frac{R(\theta) - R(0^\circ)}{R(180^\circ) - R(0^\circ)}. \quad (9.51)$$

Expressing the resistance  $R(\theta)$  in terms of the conductance  $\Gamma(\theta)$  we obtain for the normalized resistance:

$$r(\theta) = \frac{\Gamma(0^\circ) - \Gamma(\theta)}{\Gamma(0^\circ) - \Gamma(180^\circ)} \frac{\Gamma(180^\circ)}{\Gamma(\theta)}. \quad (9.52)$$

Typically, the resistance of a GMR-junction shows the following angular dependency:

$$R(\theta) = c \sin^2 \left( \frac{\theta}{2} \right) + R(0). \quad (9.53)$$

The normalized resistance of such a system is then symmetric with respect to the relative angle  $\theta = 90^\circ$  and given by

$$r(\theta) = \sin^2 \left( \frac{\theta}{2} \right) = 1 - \cos^2 \left( \frac{\theta}{2} \right). \quad (9.54)$$

A measure of the deviation of a realistic GMR device from this idealized behavior is provided by the parameter  $\chi_{\text{GMR}}$ , which may be obtained by fitting the GMR data with the expression

$$r(\theta) = \frac{1 - \cos^2 \left( \frac{\theta}{2} \right)}{1 + \chi_{\text{GMR}} \cos^2 \left( \frac{\theta}{2} \right)}. \quad (9.55)$$

Within the model of Slonczewski the parameter  $\chi_{\text{GMR}}$  is given by:

$$\chi_{\text{GMR}} = \frac{1}{2} AG(R_+ + R_-) - 1. \quad (9.56)$$

From Eq. (9.4) we saw that for an ideal spin filtering system the torque has the following angular dependence:

$$N(\theta) = N_0 \sin(\theta). \quad (9.57)$$

Deviations from this ideal behavior are expressed in terms of the asymmetry parameter  $\Lambda_{\text{STT}}$  within the expression

$$\frac{N(\theta)}{I(\theta)} = a \frac{\sin(\theta)}{\Lambda_{\text{STT}} \cos^2 \left( \frac{\theta}{2} \right) + \Lambda_{\text{STT}}^{-1} \sin^2 \left( \frac{\theta}{2} \right)} \quad (9.58)$$

From the model of Slonczewski the following result for the asymmetry parameter  $\Lambda_{\text{STT}}$  can be obtained:

$$\Lambda_{\text{STT}} = \sqrt{1 + \chi_{\text{STT}}}, \quad (9.59)$$

where we have  $\chi_{\text{STT}} = \chi_{\text{GMR}}$  within Slonczewski's model. An ideal spin filtering system is characterized by an asymmetry parameter  $\Lambda_{\text{STT}} = 1$ . Consequently, the spin-torque efficiency  $g(\theta)$  discussed in Eq. (9.41) is given by

$$g(\theta) = \frac{1}{\Lambda_{\text{STT}} \cos^2 \left( \frac{\theta}{2} \right) + \Lambda_{\text{STT}}^{-1} \sin^2 \left( \frac{\theta}{2} \right)} \quad (9.60)$$

for the Slonczewski model.



### 9.3 Calculation of the spin-transfer torque within the Embedding method

In order to evaluate the spin transfer torque acting on the magnetic moment of atom  $\mu$  according to Eq. (9.18) we need to evaluate the magnetization density associated with the non-equilibrium current for noncollinear systems. According to our discussion of scattering states given in section 6.3.4, a noncollinear scattering state incident from the left at energy  $E$  is given by

$$\Psi_{j,s}^{(\mathbf{k})}(E) = 2i\alpha_j^{(\mathbf{k})}(E) \sum_{s'} \mathbf{G}_{s,s'}^{(\mathbf{k})}(E) \mathbf{P}_{S_L}^\dagger \mathbf{v}_{j,s'}^{(\mathbf{k})}(E), \quad (9.61)$$

and the corresponding expression for the spectral function due to states incident from the left at energy  $E$  is

$$\mathbf{A}_{s,s'}(E) = \sum_{\mathbf{k}} w_{\mathbf{k}} \sum_j D_j^{(\mathbf{k})}(E) \Psi_{j,s}^{(\mathbf{k})}(E) (\Psi_{j,s'}^{(\mathbf{k})}(E))^\dagger, \quad (9.62)$$

where  $D_j^{(\mathbf{k})}(E)$  is the density of states of the  $j$ -th channel, Eq. (6.38), and  $\Psi_{j,s}^{(\mathbf{k})}(E)$  is the spinor component  $s$  of the state incident from the left associated with channel  $j$  at energy  $E$ , as given in Eq. (6.36). After insertion of  $D_j^{(\mathbf{k})}(E)$  and  $\Psi_{j,s}^{(\mathbf{k})}(E)$  into Eq. (9.62) we obtain the generalization of Eq. (6.39) for the noncollinear case:

$$\mathbf{A}_{s,s'}(E) = -\frac{1}{\pi} \sum_{\mathbf{k}, s'', s'''} w_{\mathbf{k}} \mathbf{G}_{s,s''}^{(\mathbf{k})}(E) [\mathbf{P}_{S_L}^\dagger \Im \bar{\Sigma}_{S_L}^{(\mathbf{k})}(E) \mathbf{P}_{S_L}]_{s'', s'''} (\mathbf{G}^{(\mathbf{k})}(E))_{s''', s'}^\dagger, \quad (9.63)$$

where  $w_{\mathbf{k}}$  is a weight associated with the integration over  $k$ -points. Expanding the LAPW-basis functions inside the MT-sphere of atom  $\mu$  according to Eq. (2.23), we obtain for the coefficient of the lattice harmonic  $\lambda$  of the nonequilibrium spectral function of atom  $\mu$  at radial grid point  $r$ :

$$A_{s,s'}^\mu(r, \lambda, E) = \sum_{L'', L', L, i, j} c_{\lambda, L} G(L'', L', L) R_{i,s}^\mu(r, L') A_{s,s'}(i, j, E) (R_{j,s'}^\mu(r, L''))^*. \quad (9.64)$$

In section 9.1 we discussed the torque  $\mathbf{N}^\mu$  given by Eq. (9.18), which arises due to the action of the exchange field  $\mathbf{B}^{\text{xc}}(\mathbf{r})$  on the magnetization  $\mathbf{m}^{\text{curr}}(\mathbf{r})$  of the current. At finite bias this magnetization  $\mathbf{m}^{\text{curr}}(\mathbf{r})$  may be obtained from the energy integral of the spectral function over the interval  $[\mu_R, \mu_L]$ , where  $\mu_R$  and  $\mu_L$  are the Fermi energies of the right and left leads, respectively. In the local frame of atom  $\mu$  the magnetization density is given by

$$\begin{aligned} m_x^{\text{curr}, \mu}(\mathbf{r}, E) &= \sum_{\lambda} 2\Re A_{2,1}^\mu(r, \lambda, E), \\ m_y^{\text{curr}, \mu}(\mathbf{r}, E) &= \sum_{\lambda} 2\Im A_{2,1}^\mu(r, \lambda, E), \\ m_z^{\text{curr}, \mu}(\mathbf{r}, E) &= \sum_{\lambda} (A_{1,1}^\mu(r, \lambda, E) - A_{2,2}^\mu(r, \lambda, E)). \end{aligned} \quad (9.65)$$

Using the analog expansion of the exchange field  $B^{\text{xc}}(\mathbf{r})$  inside the MT-sphere of atom  $\mu$  in terms of lattice harmonics

$$B^{\text{xc}}(\mathbf{r})|_{MT^\mu} = \sum_{\lambda,L} B_\mu^{\text{xc}}(r, \lambda) c_{\lambda,L} Y_L(\hat{\mathbf{r}}) \quad (9.66)$$

we define the radial integrals  $n^\mu(\lambda, s, s', E)$  of the exchange field with the nonequilibrium spectral function:

$$n^\mu(\lambda, s, s', E) = \int r^2 A_{s,s'}^\mu(r, \lambda, E) B_\mu^{\text{xc}}(r, \lambda) dr. \quad (9.67)$$

As outlined in section 2.1.7 the implementation of noncollinear magnetism used in the present work assumes the exchange field to be collinear in each MT-sphere: The non-collinearity is present solely in the freedom that the exchange fields in different MT-spheres may point into different directions and in the noncollinear exchange field used in the interstitial region. Consequently, the exchange field inside the MT-sphere of atom  $\mu$  points in the  $z$ -direction of the local coordinate frame. Thus, the components of the torkance in the local frame of atom  $\mu$  are given by

$$\begin{aligned} \tilde{T}_x^\mu(E) &= - \int_{MT^\mu} m_y^{\text{curr}}(\mathbf{r}, E) B^{\text{xc}}(\mathbf{r}) d^3r = - \sum_\lambda 2\Im n^\mu(\lambda, 2, 1, E), \\ \tilde{T}_y^\mu(E) &= \int_{MT^\mu} m_x^{\text{curr}}(\mathbf{r}, E) B^{\text{xc}}(\mathbf{r}) d^3r = \sum_\lambda 2\Re n^\mu(\lambda, 2, 1, E), \\ \tilde{T}_z^\mu(E) &= 0. \end{aligned} \quad (9.68)$$

The matrix  $\mathbf{R}(\hat{\mathbf{m}}^\mu)$  that provides the transformation of the torkance  $\tilde{\mathbf{T}}^\mu(E)$  from the local frame to the global frame according to

$$\mathbf{T}^\mu(E) = \mathbf{R}(\hat{\mathbf{m}}^\mu) \tilde{\mathbf{T}}^\mu(E) \quad (9.69)$$

is given in Appendix B. An alternative expression for the torkance acting on the magnetic moment within a given MT-sphere may be obtained by using Eq. (9.19) as a starting point instead of Eq. (9.18). In order to evaluate the spin-current through the MT-boundary the spinor component  $\Psi_{j,s}^{(\mathbf{k})}(E)$  of the scattering state incident from the left associated with channel  $j$  at energy  $E$ , as given in Eq. (6.36), is evaluated on the MT-sphere boundary of atom  $\mu$  in terms of spherical harmonics. Likewise the radial derivative is evaluated on the MT-sphere boundary in terms of spherical harmonics. Denoting the coefficients of the expansion in terms of spherical harmonics  $F_\mu^{(\mathbf{k})}(j, E, L, s)$  in case of the scattering state and  $G_\mu^{(\mathbf{k})}(j, E, L, s)$  in case of its radial derivative the torkance at energy  $E$  on atom  $\mu$  is given by

$$\tilde{T}_k^\mu(E) = \sum_{\mathbf{k}} w_{\mathbf{k}} \sum_{s,s',j,L} \Im[(F_\mu^{(\mathbf{k})}(j, E, L, s))^* \sigma_{k,s,s'} G_\mu^{(\mathbf{k})}(j, E, L, s')] D_j^{(\mathbf{k})}(E). \quad (9.70)$$

In order to evaluate the current of spin angular momentum  $I_{l,i}^S$ , Eq. (9.16), through plane  $S_l$ , which is needed for the evaluation of the torque according to Eq. (9.17), we sum the contributions of all scattering states associated with channels incident from the left:

$$I_{l,i}^S = \frac{1}{2} \int dE \sum_{\mathbf{k}} w_{\mathbf{k}} \sum_j D_j^{\mathbf{k}}(E) \int_{S_l} \Im[(\Psi_j^{(\mathbf{k})}(\mathbf{r}, E))^* \sigma_i \nabla \Psi_j^{(\mathbf{k})}(\mathbf{r}, E)] d^2r. \quad (9.71)$$

The corresponding spin conductance is given by

$$\Gamma_{l,i}^S(E) = \frac{1}{2} \sum_{\mathbf{k}} w_{\mathbf{k}} \sum_j D_j^{\mathbf{k}}(E) (\Psi_j^{(\mathbf{k})}(E))^\dagger \Im[\sigma_i \Sigma_{R,l}^{(\mathbf{k})}(E)] \Psi_j^{(\mathbf{k})}(E), \quad (9.72)$$

where we made use of Eq. (4.37) to express the normal derivative of the wave function in terms of the embedding potential and the wave function. Using Eq. (9.61) for the scattering states we finally obtain

$$\Gamma_{l,i}^S(E) = \frac{1}{2} \sum_{\mathbf{k}} w_{\mathbf{k}} \text{Tr}[(G_{R,L}^{(\mathbf{k})}(E))^\dagger \Im[\sigma_i \Sigma_{R,l}^{(\mathbf{k})}(E)] G_{R,L}^{(\mathbf{k})}(E) \Im[\Sigma_{L,l}^{(\mathbf{k})}(E)]]. \quad (9.73)$$

The torque on layer  $l$  is calculated from the spin conductances as follows:

$$T_{l,i}(E) = \Gamma_{l,i}^S(E) - \Gamma_{l+1,i}^S(E). \quad (9.74)$$

## 9.4 Computational procedure

In the following we describe the computational procedure which we employed for the calculation of the GMR and STT in the Cu-Co-Cu and Ag-Fe-Ag nanopillars to be discussed in the following sections. We performed the calculations using the order-N embedding technique described in chapter 7 choosing the layers such that each layer contains one atom. We calculated the charge density self-consistently within the non-collinear mode of the program using a  $14 \times 14$   $k$ -point grid and a complex energy contour of 45 energy-points with a Fermi smearing corresponding to a temperature of 315 K. In order to calculate the charge density in a computationally efficient way we used the formulation based on the Dyson equation, Eq. (6.35). Defining the  $z$ -axis to point in the direction of stacking, we chose all magnetization directions to lie in the  $xy$ -plane. While the magnetization direction of the free iron layer was varied in 18 steps of  $10^\circ$  from  $0^\circ$  (parallel to the  $x$ -axis) to  $180^\circ$  (parallel to the  $y$ -axis) the magnetization directions of all remaining layers were chosen to point in  $x$ -direction. For each of these 18 magnetic configurations the charge density was calculated self-consistently. In order to minimize the number of self-consistency steps required for the calculation of the configuration with the relative angle  $n \times 10^\circ$  between the magnetization directions we generated the starting density from the converged spin density of the configuration with the relative angle  $(n - 1) \times 10^\circ$  by rotating the magnetization direction within all layers corresponding to the free magnetic layer.

In order to ensure convergence of the  $k$ -point integration with respect to the number of  $k$ -points in the calculations of the GMR and STT we used two  $k$ -point sets, the first one a  $98 \times 98$   $k$ -point mesh corresponding to 9604 (1225)  $k$ -points in the full (irreducible part of the) 2BZ, the second one a  $296 \times 296$   $k$ -point mesh corresponding to 87616 (11026)  $k$ -points in the full (irreducible part of the) 2BZ.

## 9.5 GMR and STT in Co-Cu-Co nanopillars

The GMR effect and current induced switching of the magnetization in Co-Cu-Co trilayer systems have been studied intensively in several experiments [86, 11, 87].

One major aspect of our following *ab initio* calculation of the GMR and STT in Co-Cu-Co trilayer systems is to benchmark our computational method, which we described in section 9.4, against existing *ab-initio* calculations of this system [78, 88]. Consequently, we chose the setup used in Ref. [78] for our calculation: Between a semi-infinite left Co-lead and a semi-infinite right Cu-lead we sandwich 9 monolayers of Cu acting as interlayer and 15 monolayers of Co acting as free magnetic layer. Both Co and Cu are treated as fcc materials with a lattice constant of 3.54 Å. The stacking direction is the (001) direction of Co and Cu. Viewing the fcc structure as a bct structure with a  $c/a$ -ratio of  $\sqrt{2}$ , one realizes that the optimal in-plane unit cell for the present system is obtained by rotating the cubic fcc unit cell by  $45^\circ$  about the (001) direction and identifying the bct unit cell with lattice parameter  $a = 2.50$  Å. Accordingly, everywhere in the system the distance of adjacent atomic planes is set to 1.77 Å. The semi-infinite left lead we model by 9 monolayers of Co, which are embedded from the left with an embedding potential of bulk Co and analogously we model the semi-infinite right lead by 9 monolayers of Cu, which are embedded from the right with an embedding potential of bulk Cu. Thus, the embedded region contains 42 atoms in total per in-plane unit cell.

In agreement with the description of the computational procedure given in section 9.4 we decompose the system into 42 layers, where each layer contains one atom per in-plane unit cell. We set the Cu and Co MT-radii to 1.22 Å, and used a planewave cutoff of  $7.4 \text{ Å}^{-1}$ . Our calculations were performed within LDA, using the parameterization of Moruzzi, Janak and Williams [65] for the exchange correlation potential. For the self-consistent calculation of the charge density we used a  $14 \times 14$   $k$ -point mesh. Defining the  $x$ - and  $y$ -axes to be rotated by  $45^\circ$  with respect to the axes of the cubic fcc lattice of Co and Cu about the (001) direction, the magnetization directions of both the free and the fixed magnetic layer are parallel to the  $x$ -axis for the configuration with zero relative angle in our calculation. We varied the relative angle between the magnetization directions in 18 steps of  $10^\circ$  from  $0^\circ$  to  $180^\circ$ . For the relative angles of  $0^\circ$  and  $180^\circ$  we show the  $k$ -dependent conductances in Fig. 9.5 and 9.6.

In Fig. 9.7 we show the integrated conductance of the Co-Cu-Co trilayer system as a function of the relative angle between the magnetization directions. For the 2BZ integration meshes of  $96 \times 96$  and  $296 \times 296$   $k$ -points were used. It is seen from the figure that already  $96 \times 96$   $k$ -points suffice to give accurate results for the integrated conductance.

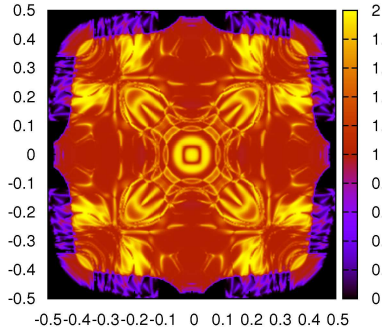


Figure 9.5:  $k$ -dependent conductance per unit cell (in units of  $e^2/h$ ) of the Co-Cu-Co nanopillar in the 2BZ at a relative angle of  $0^\circ$  between the magnetization directions.

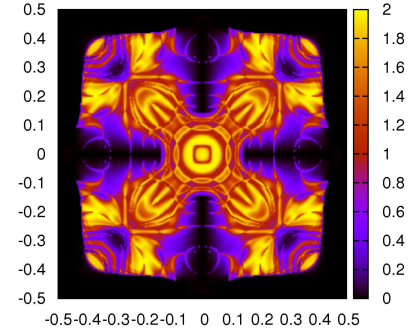


Figure 9.6:  $k$ -dependent conductance per unit cell (in units of  $e^2/h$ ) of the Co-Cu-Co nanopillar in the 2BZ at a relative angle of  $180^\circ$  between the magnetization directions.

From the integrated conductance at  $0^\circ$  and  $180^\circ$  relative angle we obtain a GMR ratio  $\text{GMR} = (\Gamma_P - \Gamma_{AP})/\Gamma_{AP}$  of 49.7% in very good agreement with the theoretical result of Ref. [78], which is 48%. Experimentally, much smaller values for the GMR of Co-Cu-Co trilayers are reported. The conductances per unit cell are  $\Gamma_P = 0.995e^2/h$  and  $\Gamma_{AP} = 0.665e^2/h$ , corresponding to areal conductivities of  $6.2 \cdot 10^{14} \text{S/m}^2$  and  $4.1 \cdot 10^{14} \text{S/m}^2$  in good agreement with Ref. [78]. The respective areal resistivities are  $R_P = 1.62 \text{f}\Omega\text{m}^2$  and  $R_{AP} = 2.43 \text{f}\Omega\text{m}^2$ . Using similar expressions like those given in Eq. (9.49) we may compare our results to those of circuit theory. According to Ref. [89] the interface resistances of the Cu/Co(100) interface are given by  $R_\uparrow = 0.31 \text{f}\Omega\text{m}^2$  for the majority spin and  $R_\downarrow = 2.31 \text{f}\Omega\text{m}^2$  for the minority spin. The corresponding areal resistances of the spin valve are then  $R_P = 3R_-R_+/(R_- + R_+) = 0.82 \text{f}\Omega\text{m}^2$  and  $R_{AP} = 3.68 \text{f}\Omega\text{m}^2$ , corresponding to an even higher GMR ratio. The differences to our results are probably due to the neglect of coherent multiple interface scattering within circuit theory.

At  $90^\circ$  relative angle, the integrated conductance is 0.438, which is slightly larger than the value expected for a symmetric GMR. In order to quantify this asymmetry of the angular variation of the GMR we calculated the asymmetry parameter  $\chi_{\text{GMR}}$  by fitting Eq. (9.51) to the normalized resistance obtained from our conductance data. We show the normalized resistance in Fig. 9.8. At  $90^\circ$  relative angle we find a normalized resistance of 0.277, which is smaller than the value of 0.5 which one would obtain for a system with symmetric angular dependency of the GMR ratio by roughly a factor of two. For the asymmetry  $\chi_{\text{GMR}}$  we extract a value of 1.92 from the fit of our GMR curve to Eq. (9.55). While our GMR data agree rather well ( $\chi^2 = 0.0023$ ) with the fit to Slonczewski's model, small deviations are clearly visible in Fig. 9.8.

We show the  $k$ -dependent in-plane and out-of-plane torques due to states incident from the left in Fig. 9.9 and Fig. 9.10, respectively, for the entire 2BZ. One can differentiate

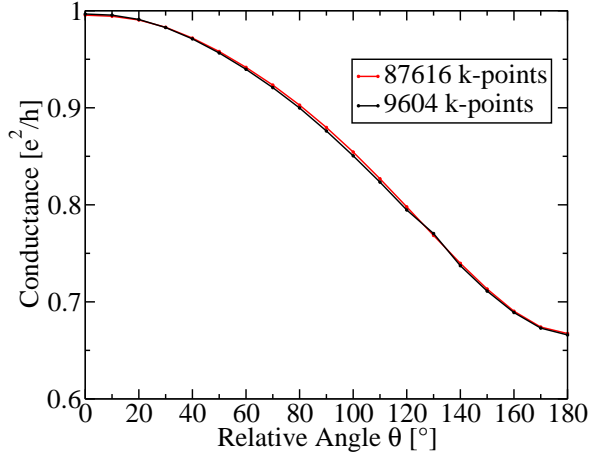


Figure 9.7: Integrated conductance as a function of the relative angle between the magnetization directions for the Co-Cu-Co nanopillar using two different  $k$ -meshes for the 2BZ integration.

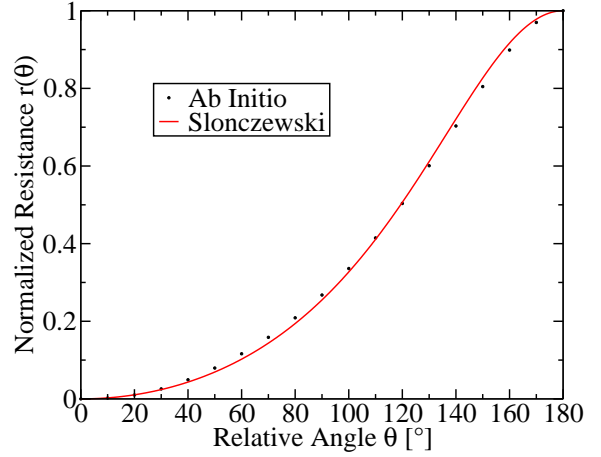


Figure 9.8: Values of the normalized resistance (black dots) for the Co-Cu-Co trilayer system and fit (red curve) with Slonczewski's model. A  $296 \times 296$   $k$ -point mesh was used for the 2BZ integration.

between areas in the 2BZ where the  $k$ -dependent torkance is negative and areas where it is positive. The distributions of positive and negative areas in the 2BZ for the in-plane and out-of-plane torkances are similar, though not equal. When compared to the out-of-plane torkance, the in-plane torkance exhibits a smoother variation in the 2BZ.

In Fig. 9.11 we show the angular dependence of the in-plane and out-of-plane torkance due to states incident from the left calculated at the Fermi energy for a mesh of  $296 \times 296$   $k$ -points. For the calculation of the torkance we applied various formulations, Eq. (9.68, 9.70, 9.73), and summed all torkance contributions from the atoms constituting the free magnetic layer. Obviously, the results obtained from the different torkance-formulas, Eq. (9.68, 9.70, 9.73), are in good agreement. In particular, the agreement between the torkance evaluated from the difference between spin-current conductivities through adjacent embedding planes, Eq. (9.73), which is labeled EPSCT (embedding plane spin current torque) in the figure, and the torkance evaluated from the surface integral of the spin-current density over the muffin-tin boundary, Eq. (9.70), denoted MTSCCT (muffin tin spin current torque) in the figure, is very good. One may conclude from this that the contribution of the interstitial region to the torkance is negligible for the system at hand. The fact that slightly different results are produced by Eq. (9.70), which computes the torkance from the surface integral of the spin-current density over the muffin-tin boundary, and Eq. (9.68), which formulates the torkance as a cross product of magnetization and exchange field, is interesting. In Eq. (9.13) we have proven the equivalence of Eq. (9.70) and Eq. (9.68) in the absence of spin-orbit coupling. However, we assumed a non-relativistic Hamilton operator in our proof, which is at variance with the use of a scalar relativistic Hamiltonian in the ab-initio calculation. Consequently, we attribute the differences to relativistic effects not considered in the derivation of Eq. (9.13). We conclude that the evaluation of the cross



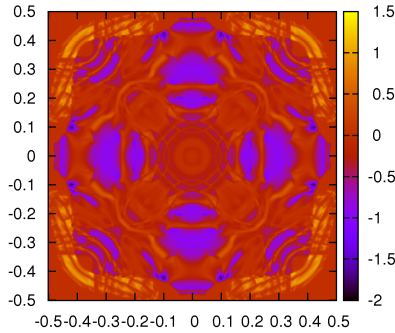


Figure 9.9:  $k$ -dependent in-plane torkance at the Fermi energy due to states incident from the left for the Co-Cu-Co nanopillar at a relative angle of  $90^\circ$  between the magnetization directions.

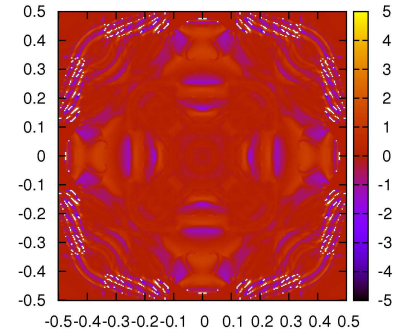


Figure 9.10:  $k$ -dependent out-of-plane torkance at the Fermi energy due to states incident from the left for the Co-Cu-Co nanopillar at a relative angle of  $90^\circ$  between the magnetization directions.

product of magnetization and exchange field provides slightly more accurate results for the torkance.

For metallic trilayer systems in general, the out of plane torkance is not expected to contribute strongly to the total torkance [90, 76]. While we find the out-of-plane torque to be smaller than the in-plane torque for most relative angles, its contribution to the total torque is not negligible. One may speculate at this point that the analyzing free magnetic layer does not fully polarize the current for the present setup with 15 layers as analyzer and that the out-of-plane torkance would be smaller for a thicker free layer.

A comparison of results obtained for the torkance for two different  $k$ -point meshes, a  $98 \times 98$  and a  $296 \times 296$  mesh, is shown in Fig. 9.12. For the calculation of the torkance we applied Eq. (9.70). Like in Fig. 9.11 we summed all torkance contributions from the atoms constituting the free magnetic layer, evaluated the torkance at the Fermi energy, and considered only states incident from the left. The figure shows that the convergence of the in-plane torkance with respect to the  $k$ -point set chosen for the 2BZ integration is significantly faster than the convergence of the out-of-plane torque, which has also been reported in Ref. [78].

While we find the in-plane torkances to be equal but opposite for states incident from the left and states incident from the right we obtain different out-of-plane torkances for the right-going and the left-going states. In Fig. (9.13) we compare the out-of-plane torkances for these two cases. In section 9.2.2 it was shown for a simple model that in general the out-of-plane torque does not exhibit any symmetry with respect to inversion of the direction of current flow and that the out-of-plane torques for incidence from left and right can differ substantially. In this respect, our ab-initio results for the out-of-plane torkance lead to the same conclusion.

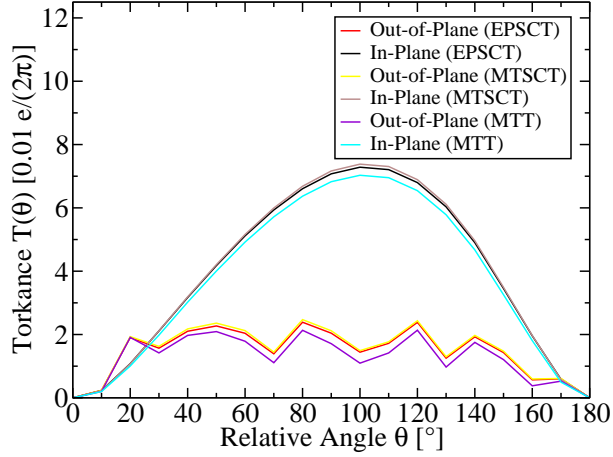


Figure 9.11: Torkance  $T(\theta)$  at the Fermi energy vs. relative angle  $\theta$  for the Co-Cu-Co nanopillar. Three different formulations of the torkance are compared: Spin current difference along the free magnetic layer (EP-SCT), spin current flow into the muffin-tins (MTSCT), and cross product of magnetization and exchange field (MTT).

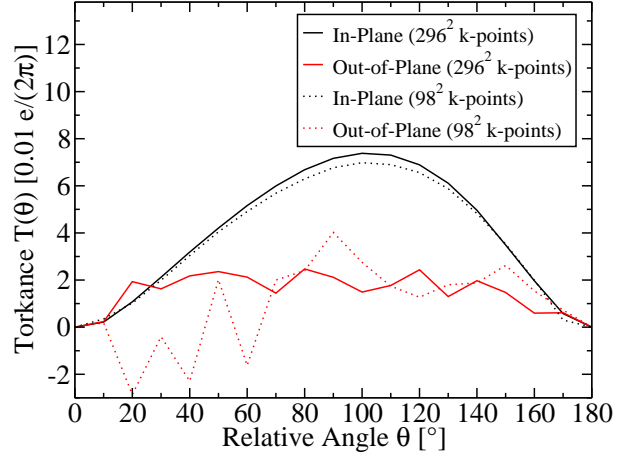


Figure 9.12: Torkance  $T(\theta)$  at the Fermi energy vs. relative angle  $\theta$  for the Co-Cu-Co nanopillar. Red lines: Out-of-plane torkance. Black lines: In-plane torkance. Solid lines: A  $296 \times 296$   $k$ -mesh was used for the 2BZ integration. Dotted lines: A  $98 \times 98$   $k$ -mesh was used.

The angular dependence of the in-plane and out-of plane torque per current is shown in Fig. 9.14. We find the in-plane torque per current to be in good agreement with the theoretical results found in the literature [88, 78]. The maximal in-plane torque per current is assumed at roughly  $110^\circ$ , while the in-plane torkance assumes a maximum at roughly  $100^\circ$ . Due to the decrease of the conductance with increasing relative angle the maximum at  $100^\circ$  of the torkance is shifted to  $110^\circ$ . For the present system, a very dense  $k$ -mesh is required to obtain the out of plane torque with a high accuracy. Consequently, we attribute the discrepancy between our result for the out of plane torque and the results presented in the literature [88, 78] to the use of different  $k$ -point meshes. Fitting the in-plane torque to Eq. (9.58) we obtain an asymmetry of  $\Lambda_{\text{STT}} = 1.43$  and the prefactor  $a_{\text{STT}} = 0.165$ . While our STT data are reasonably well described by the fit to Slonczewski's result, interesting deviations occur at angles of  $0^\circ$  and  $180^\circ$ : Slonczewski's model predicts the ratio of the spin transfer torque efficiencies at  $180^\circ$  and  $0^\circ$  to be given by  $\Lambda^2$ , which is 2.1 in the present case. Our calculations predict smaller spin transfer torque efficiencies both at  $0^\circ$  and  $180^\circ$  relative angle and also a smaller difference between the two values for the two orientations when compared to the results of Slonczewski. While the spin transfer torque efficiencies extracted from the experiments are larger than both theoretical results based on Slonczewski's model and theoretical results obtained from ab-initio calculations, neither experiment nor ab-initio calculation confirm the large difference between the efficiencies at  $0^\circ$  and  $180^\circ$  predicted by Slonczewski's model. Our calculation predicts slightly different asymmetry parameters  $\Lambda$  for the GMR ( $\Lambda_{\text{GMR}} = \sqrt{1 + \chi_{\text{GMR}}} = 1.69$ ) and for the STT



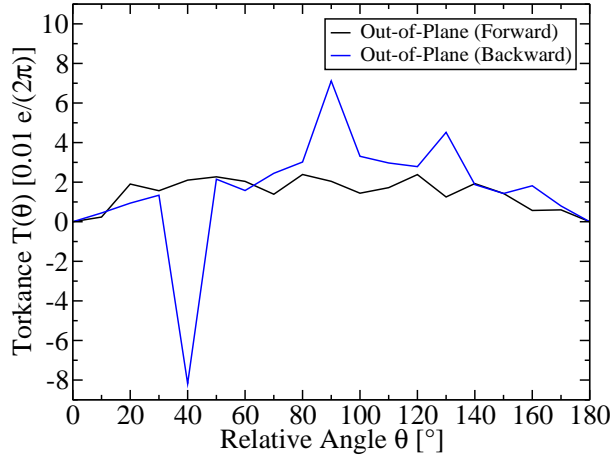


Figure 9.13: Out-of-plane torkances  $T(\theta)$  for the Co-Cu-Co nanopillar vs. relative angle  $\theta$  for states incident from the left (black line) and states incident from the right (blue line).

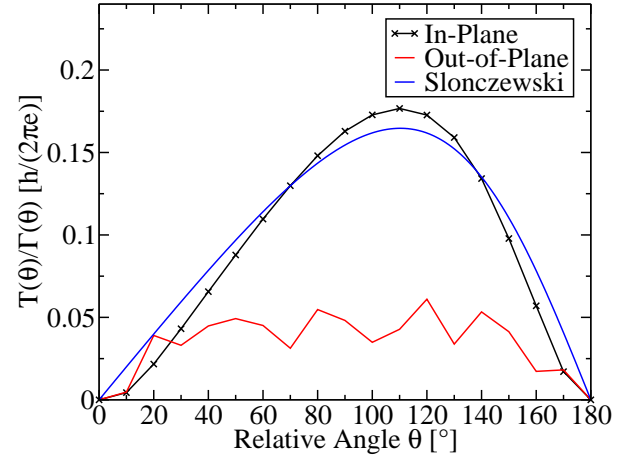


Figure 9.14: Torque per current  $T(\theta)/\Gamma(\theta)$  due to states incident from the left for the Co-Cu-Co nanopillar vs. relative angle  $\theta$ . Red line: Out-of-plane torque. Black crosses: In-plane torque. Blue line: Fit with the Slonczewski model.

( $\Lambda_{\text{STT}} = 1.45$ ). While Slonczewski's model predicts the two asymmetries to be exactly equal, the deviation we find is quite small.

In Fig. 9.15 we show the layer-resolved torkances for relative angles of  $10^\circ$ ,  $170^\circ$ ,  $50^\circ$ , and  $100^\circ$ . Layers 19 to 33 constitute the free magnetic layer, while layers 1 to 9 are part of the fixed magnetic layer, which is semi-infinite in the present case. Within the interlayer and the buffer layers the layer resolved torkances are very small when compared to the layer resolved torkances in the magnetic layers. The layer resolved torkance exhibits a decaying oscillatory behavior within the magnetic layers. The oscillations decay more slowly for the out-of-plane torque, and hence the total out of plane torque acting on the free magnetic layer is smaller compared to the total in plane torque. The in-plane torque on the free magnetic layer originates mainly from the first three Co-layers.

## 9.6 GMR and STT in Fe-Ag-Fe nanopillars

Experimentally, single-crystalline Fe-Ag-Fe nanopillars have been discovered as promising spintronics devices which can be used for current-induced magnetization switching [91, 92] and realization of spin-transfer oscillators [93]. Fe-Ag-Fe nanopillars are interesting in several respects. For example, the magnetocrystalline anisotropy of bcc-Fe in Fe-Ag-Fe nanopillars causes an effective field with four-fold in-plane symmetry, which allows to switch the magnetization in two steps of  $90^\circ$  [93]. Three resistance levels correspond to the three configurations of parallel, perpendicular and antiparallel alignment of the magnetizations. The configuration with perpendicularly aligned magnetizations

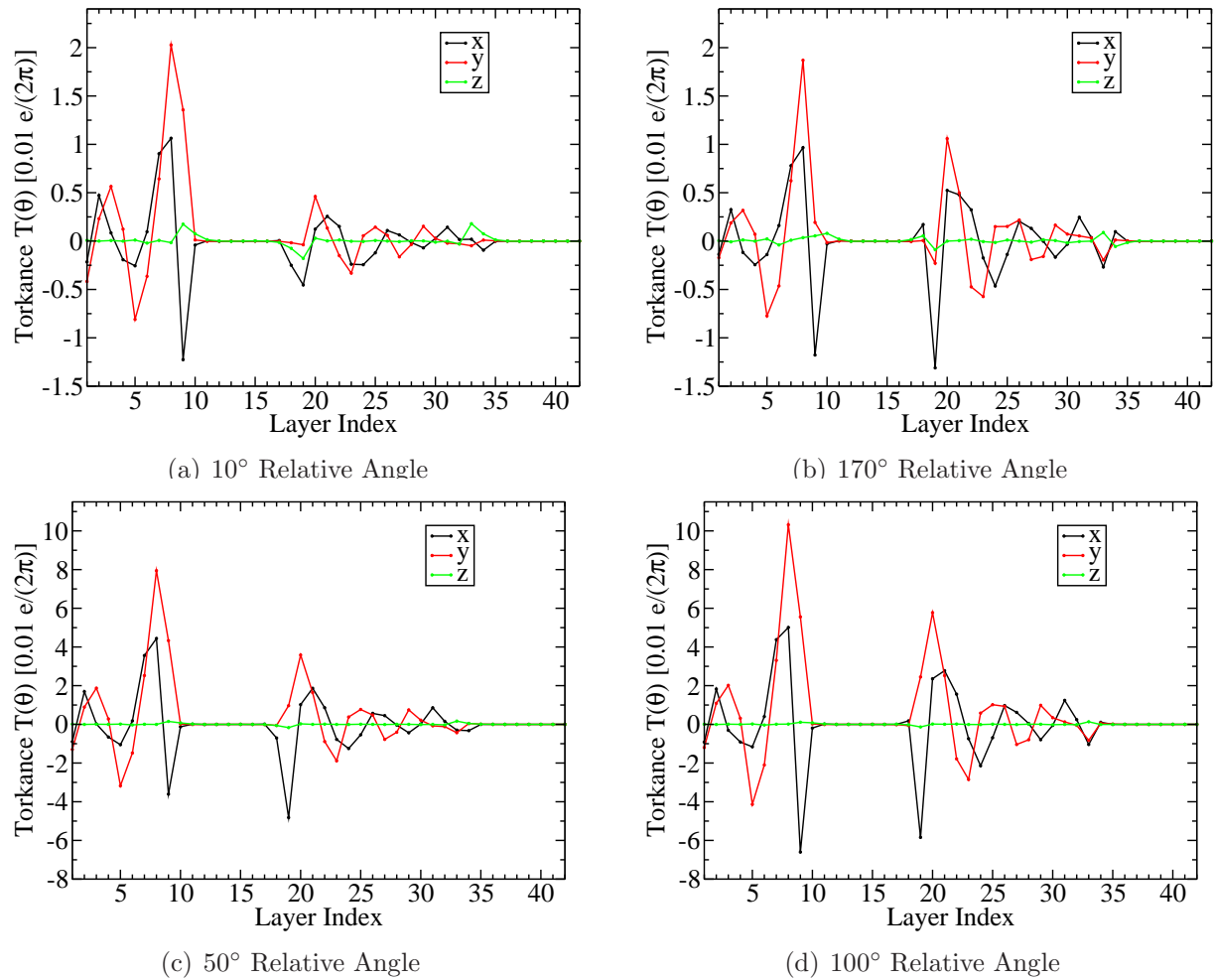


Figure 9.15: Layer resolved torkances for relative angles of 10°, 170°, 50°, and 100° for the Co-Cu-Co spin valve.

provides an alternative to the use of external magnetic fields for the stabilization of the steady-state precessional motion, which constitutes a major difficulty for the design of spin-transfer oscillators. While external magnetic fields may be used for this purpose, they are difficult to realize in applications. Furthermore, experimental data on GMR and STT in Fe-Ag-Fe exhibit strong asymmetries, corresponding to a large spin-accumulation at the Fe-Ag interface. A third interesting aspect concerns the influence of spin-orbit coupling on the GMR. As Ag and Au have very similar lattice constants, one may interchange Ag by Au. In fact, in the experimental setup of Ref. [92] the stacking is Fe-Ag-Fe-Ag-Fe-Au. With atomic numbers of 47 and 79 Ag and especially Au exhibit signatures of spin-orbit coupling in their electronic structures. The effect of spin-orbit coupling on the GMR is a twofold one. First, the electronic band structure is modified by relativistic effects, which can either increase or decrease the GMR depending on the system under study. Second, as spin-orbit coupling causes transitions between electronic states characterized by different spin quantum numbers, one expects the GMR to be reduced due this spin scattering. Due to a large difference in the spin-dependent interface resistances of the Fe-Ag interface for spin up and spin down Slonczewski's model is expected to give a good and unified description of GMR and STT in Fe-Ag-Fe nanopillars. Nevertheless, there are differences between experimental data and the properties expected on the basis of Slonczewski's model. Consequently, it is also interesting to investigate how well theoretical predictions based on Slonczewski's model reproduce ab-initio calculations on Fe-Ag-Fe nanopillars, and whether and to which degree ab-initio calculations may improve the description given by Slonczewski's model.

In order to calculate the spin transfer torque in Fe-Ag-Fe nanopillars we studied a system composed of a semi-infinite Ag lead, a fixed layer of Fe (19 atomic planes), a Ag spacer layer (15 atomic planes), a Fe free layer (7 atomic planes), and a semi-infinite Ag lead. The dimensions of the Ag spacer layer (roughly 6 nm) and the Fe free layer (roughly 2 nm) of our setup are then in agreement with those of the experimental setup of Ref. [92], where a layer stack of 1nm Fe (seed layer), 150 nm Ag (buffer layer), 20 nm Fe (fixed layer), 6 nm Ag (interlayer), 2 nm Fe (free layer), and 50 nm Au (capping layer) is grown on an annealed GaAs(100) substrate by molecular beam epitaxy. While the actual experimental stacking is Ag-Fe-Ag-Fe-Au, we first perform calculations on Ag-Fe-Ag-Fe-Ag, to understand the influence of interchanging Ag by Au on GMR and STT in a second calculation. However, as the interchange of Ag by Au concerns only one of the buffer layers and not the interlayer in the experiment, we capture all main features of the experiment with our slightly modified setup. The experimental lattice constants of bcc-Fe and fcc-Ag are given by 2.867 Å and 4.085 Å, respectively. The ratio of these lattice constants roughly amounts to  $\sqrt{2}$ . Consequently, the structures match when the cubic axes of the bcc-Fe and the fcc-Ag are rotated with respect to each other by 45° in the sample plane. This becomes clear when the fcc structure is viewed as a bct structure with a  $c/a$ -ratio of  $\sqrt{2}$ . Experimentally, Fe and Ag are reported to exhibit good epitaxial match. To determine the geometry of the Ag-Fe interface we relaxed the atomic coordinates of a symmetric film composed of 6 layers Ag, 5 layers Fe, and again 6 layers Ag within GGA using the exchange correlation potential of Perdew, Burke and Ernzerhof [64]. The in-plane lattice constant was fixed to the experimental lattice constant of Fe (2.867 Å) and all atoms of the film

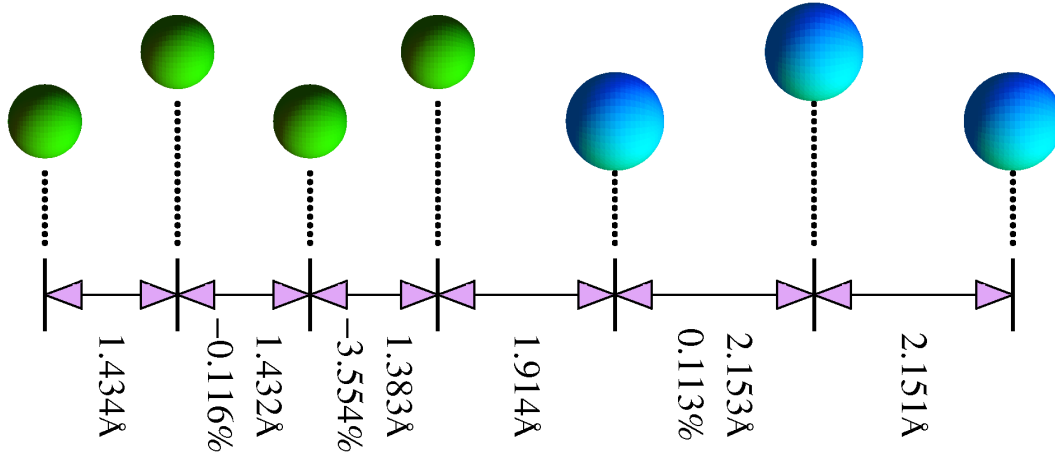


Figure 9.16: Structure of the relaxed Fe-Ag interface: Interplanar spacings and their deviations from the respective bulk values for Fe (green) and Ag (blue).

were allowed to relax during the geometry optimization. We set the Fe and Ag MT-radii to 1.17 Å and 1.32 Å, respectively. A planewave cutoff of 7.4 Å<sup>-1</sup> and a 16 × 16 *k*-point mesh were used in the calculation.

In Fig. 9.16 we illustrate the resulting geometry of the Ag-Fe interface. The deviation of the Ag-Ag interplanar distance from its bulk value close to the Ag-Fe interface is very small. We calculated that the total energy minimum of bulk Ag constrained to the Fe in-plane lattice constant is assumed at a *c/a*-ratio of 1.498 corresponding to a Ag-Ag interplanar distance of 2.151 Å. On the Fe-side of the interface the relaxations affect mainly the first Fe-layer, which is drawn towards the second Fe-layer by 3.6%.

For the calculation of the transport properties of the Fe-Ag-Fe nanopillar we used the LDA exchange correlation potential of Moruzzi, Janak and Williams [65]. In order to model the left and right Ag-leads we explicitly included 8 layers of Ag in the calculation, which were terminated by embedding potentials of a principal layer of Ag on the left and right sides, respectively. Consequently, the embedded region is composed of 57 atomic planes. Following the description of the computational procedure given in section 9.4 the total number of layers into which the system is decomposed is likewise 57. Defining the *x*- and *y*-axes to be parallel to the cubic axes of bcc-Fe, the magnetization directions of both the free and the fixed magnetic layer are parallel to the *x*-axis for the configuration with zero relative angle in our calculation. We varied the relative angle between the magnetization directions in 18 steps of 10° from 0° to 180°. The *k*-dependent conductances in the 2BZ are shown for relative angles of 0° and 180° in Fig. 9.17 and Fig. 9.18, respectively.

In Fig. 9.19 we show the integrated conductance of the Fe-Ag-Fe nanopillar as a function of the relative angle between the magnetization directions.

Obviously, the curves for the integrated conductance for the 96 × 96 and the 296 × 296 *k*-point meshes are almost identical, meaning that the 96 × 96 *k*-point mesh yields well-converged values for the integrated conductance for the Fe-Ag-Fe system. From the integrated conductance at 0° and 180° relative angle we obtain values of 205% (98 × 98 *k*-

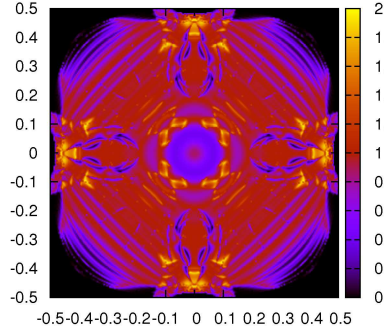


Figure 9.17:  $k$ -dependent conductance of the Fe-Ag-Fe nanopillar in the 2BZ at a relative angle of  $0^\circ$  between the magnetization directions.

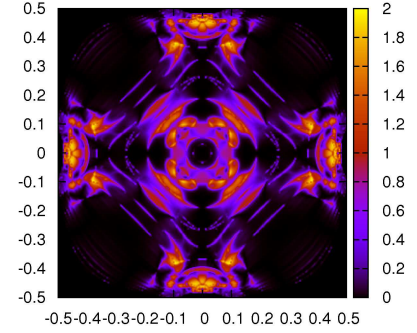


Figure 9.18:  $k$ -dependent conductance of the Fe-Ag-Fe nanopillar in the 2BZ at a relative angle of  $180^\circ$  between the magnetization directions.

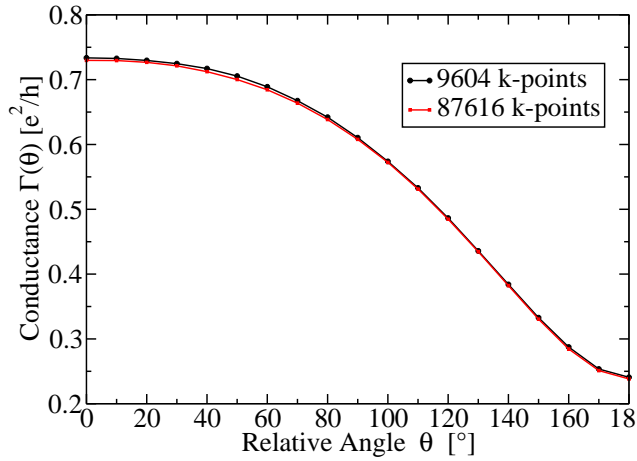


Figure 9.19: Integrated conductance as a function of the relative angle between the magnetization directions for the Fe-Ag-Fe nanopillar using a  $98 \times 98$  (black curve) and a  $296 \times 296$  (red curve)  $k$ -mesh for the 2BZ integration.

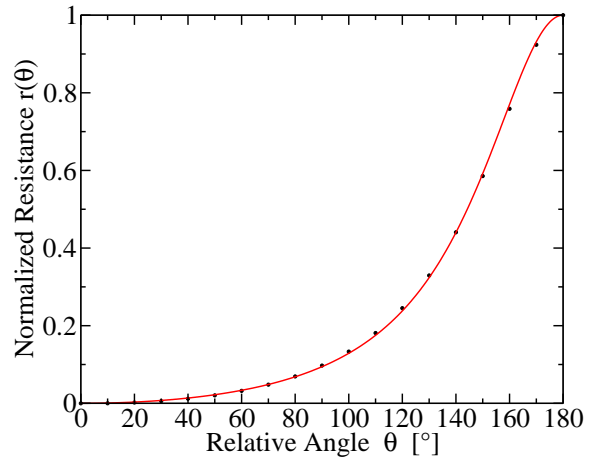


Figure 9.20: Values of the normalized resistance (black dots) for the Fe-Ag-Fe nanopillar and fit (red curve) with Slonczewski model.

Table 9.1: Comparison of the conductances for parallel ( $\Gamma_P$ ) and antiparallel ( $\Gamma_{AP}$ ) alignment of magnetizations and of the resulting GMR ratios of the Fe-Ag-Fe nanopillar for two calculations: With spin-orbit coupling (SOC) and without spin-orbit coupling (NOSOC).

	$\Gamma_P [e^2/h]$	$\Gamma_{AP} [e^2/h]$	GMR [%]
SOC	0.718	0.225	219
NOSOC	0.734	0.241	205

point mesh) and 206% ( $296 \times 296$   $k$ -point mesh) for the GMR ratio  $\text{GMR} = (\Gamma_P - \Gamma_{AP}) / \Gamma_{AP}$ . The GMR ratio found experimentally [92] for Fe-Ag-Fe nanopillars is almost two orders of magnitude smaller than our theoretical result and amounts to only 3.3%.

In order to visualize the asymmetry of the angular variation of the GMR and to make the comparison with the experiment easier we calculated the normalized resistance according to Eq. (9.51) from our conductance data obtained for the  $296 \times 296$   $k$ -point mesh. We show the normalized resistance in Fig. 9.20. At  $90^\circ$  relative angle we find a normalized resistance of 0.0972, which is much smaller than the value of 0.5 which one would obtain for a system with symmetric angular dependency of the GMR ratio. Based on the model of Slonczewski and interface resistances calculated theoretically [89] one obtains [94] an asymmetry parameter of  $\chi \approx 15$  leading to  $r(\theta) \approx 0.059$ . Experimentally [92] a smaller asymmetry of  $\chi = 1.56$  is found, which corresponds to  $r(90^\circ) = 0.28$ . For the asymmetry  $\chi$  we extract a value of 8.6 from a fit of our GMR curve to Eq. (9.55).

In order to investigate the influence of spin-orbit coupling on the GMR of Fe-Ag-Fe nanopillars we performed a second calculation of the GMR-ratio including spin-orbit coupling. Using a  $98 \times 98$   $k$ -point mesh for the 2BZ integration we found a GMR ratio of 219%, which is slightly larger than the value without spin-orbit coupling by roughly 7%. The values of the conductance and the GMR ratio for the two calculations with and without spin-orbit coupling are summarized in table 9.1. Interestingly, spin-orbit coupling reduces the integrated conductance in both the parallel and the antiparallel configuration by roughly the same amount of  $\Gamma_{P/AP}^{\text{NOSOC}} - \Gamma_{P/AP}^{\text{SOC}} = 0.016$ . The  $k$ -resolved in-plane and out-of-plane torkances are shown in Fig. 9.21 and Fig. 9.22, respectively. For the Fe-Ag-Fe trilayer structure we can make the same qualitative statements about the  $k$ -resolved torkances as in the case of the Co-Cu-Co trilayer system: The pattern of alternating sign of the torkance is very similar for the in-plane and the out-of-plane torkance and related to the variation of the conductance. The variations of the out-of-plane torkance are stronger than those of the in-plane torkance.

In Fig. 9.23 and Fig. 9.24 we show the in-plane and the out-of-plane torkances and torques per current calculated in the limit of zero bias for a  $98 \times 98$   $k$ -point mesh. For the calculation of the torque we applied Eq. (9.70) and summed all torque contributions from the atoms constituting the free magnetic layer. When comparing the asymmetries of the in-plane torkance and the in-plane torque per current one notices that the asymmetry in the torque per current is partially due to the asymmetry of the conductance: The maximum of the in-plane torkance at roughly  $120^\circ$  is shifted to roughly  $150^\circ$  due to the division by the conductance. We find that the out-of-plane torque is smaller than the in-plane torque

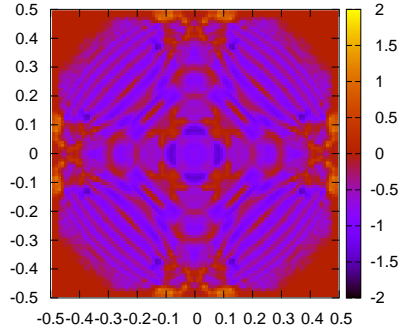


Figure 9.21:  $k$ -resolved in-plane torkance at a relative angle of  $90^\circ$  for the Fe-Ag-Fe trilayer structure.

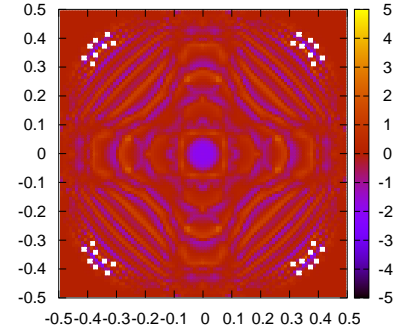


Figure 9.22:  $k$ -resolved out-of-plane torkance at a relative angle of  $90^\circ$  for the Fe-Ag-Fe trilayer structure.

Table 9.2: Comparison of the asymmetry parameters  $\Lambda$  of GMR and STT as obtained experimentally, within Slonczewski's model and within the present work

	Exp.	Slonc.	present work
GMR	1.6	4.0	3.1
STT	3.4	4.0	3.86

by at least an order of magnitude and consequently does not contribute significantly to the total torque. The in-plane torque is found to be almost perfectly perpendicular to the magnetization direction of the free layer. Fitting the in-plane torque to Eq. (9.58) we obtain an asymmetry of  $\Lambda_{\text{STT}} = 3.86$  and the prefactor  $a_{\text{STT}} = 1.4$ . From the experimental data on the STT, one extracts an asymmetry of  $\Lambda_{\text{STT}} = 3.4$ , which is in reasonable agreement with the result of our calculation. Based on Slonczewski's model an asymmetry of 4.0 is expected. [92, 94] Interestingly, our calculation predicts a smaller anisotropy parameter  $\Lambda$  for the GMR ( $\Lambda_{\text{GMR}} = \sqrt{1 + \chi_{\text{GMR}}} = 3.1$ ) than for the STT ( $\Lambda_{\text{STT}} = 3.86$ ), which is in better agreement with the experimental observation than the result of Slonczewski's model that both asymmetries,  $\Lambda_{\text{GMR}}$  and  $\Lambda_{\text{STT}}$ , agree. In Table 9.2 we list the asymmetry parameters as obtained from experiment, Slonczewski's model and the present calculation for comparison.

In Fig. 9.25 we show the layer-resolved torkance for the configuration with a relative angle of  $90^\circ$ . Layers 43 to 49 constitute the free magnetic layer, while layers 9 to 27 form the fixed magnetic layer. The layer resolved torkances within the interlayer and the buffer layers are very small when compared to those in the magnetic layers. Within the magnetic layers the layer resolved torkance exhibits a decaying oscillatory behavior. In case of the out-of-plane torque the oscillations decay more slowly, which is the reason why the total out of plane torkance acting on the free magnetic layer is much smaller compared to the



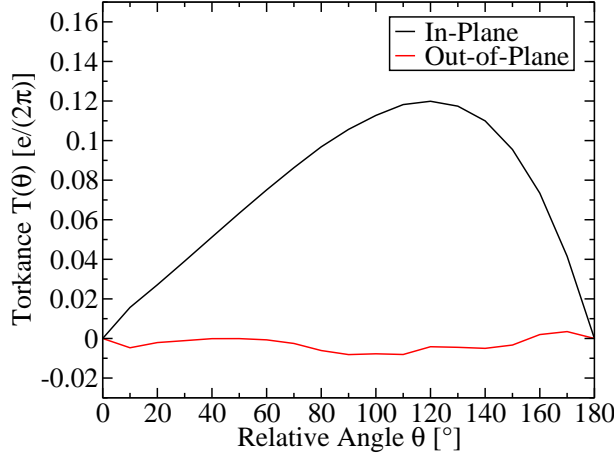


Figure 9.23: Torkance  $T(\theta)$  as a function of the relative angle  $\theta$  for the Fe-Ag-Fe trilayer structure.

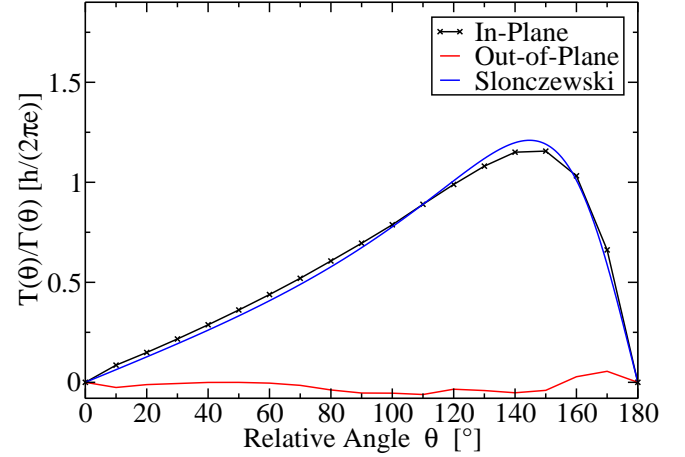


Figure 9.24: Torque per current for the Fe-Ag-Fe nanopillar as a function of the relative angle  $\theta$ . Red line: Out-of-plane torque. Black crosses: In-plane torque. Blue line: Fit of the in-plane torque with the Slonczewski model.

Table 9.3: Spin-resolved conductances for parallel and antiparallel alignment of the magnetizations of the Ag-Fe-Ag-Fe-Au junction.

	$\Gamma_P[\frac{e^2}{h}]$	$\Gamma_{AP}[\frac{e^2}{h}]$
↑	0.57	0.0873
↓	0.0289	0.079

total in-plane torkance. The total in-plane torque of the free magnetic layer stems mainly from the torque on the first two Fe-layers.

In order to estimate how much the results of this section would change if Au instead of Ag was used as capping layer like in the experiment, we calculated the conductance for the Ag-Fe-Ag-Fe-Au stacking. The geometry of the Fe-Au interface is discussed in the next section. For the stacking Ag-Fe-Ag-Fe-Au we obtain a GMR of 260%, which is higher than the GMR of the stacking Ag-Fe-Ag-Fe-Ag by roughly 50%. In table 9.3 we list the spin-resolved conductances for parallel and antiparallel alignment of the magnetizations of the Ag-Fe-Ag-Fe-Au junction. As the junction does not possess inversion or z-reflection symmetry, the conductances of minority and majority differ for the antiparallel alignment. From an additional noncollinear calculation at a relative angle of  $90^\circ$  we obtain a value of 0.0906 for the normalized resistance  $r(90^\circ)$ , which is very close to the value of 0.0972 found previously for the Ag-Fe-Ag-Fe-Ag stacking. This suggests that the normalized resistances of the Ag-Fe-Ag-Fe-Au and the Ag-Fe-Ag-Fe-Ag stackings are characterized by very similar asymmetries, which is in agreement with the expectation that the shape of the GMR signal should not depend strongly on the details of the system outside the Fe-Ag-Fe trilayer, which



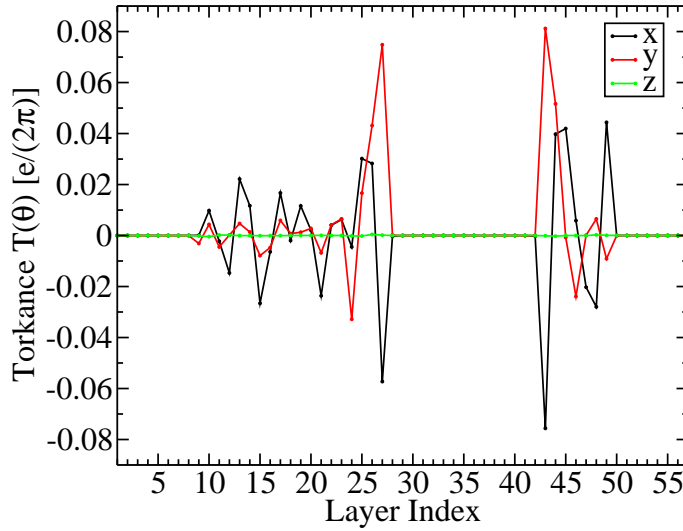


Figure 9.25: Layer resolved torkance for a relative angle of  $90^\circ$  for the Fe-Ag-Fe nanopillar. Directions with respect to local coordinate frame.

is the heart of the junction.

## 9.7 GMR and STT in Fe-Au-Fe nanopillars

In the following we study the influence of spin-orbit coupling on GMR and STT for the Fe-Au-Fe trilayer system. In comparison with the Fe-Ag-Fe spin-valve of the previous section we expect a stronger influence of spin-orbit coupling for the present system due to the replacement of Ag by Au. The setup used for our calculation is very similar to the one of the previous section: Instead of 15 layers of Ag acting as spacer layer we now use 15 layers of Au, while choosing leads, free layer, and fixed layer to have the same composition as in the previous section. Thus, the system we study in this section is composed of a semi-infinite Ag lead, a fixed layer of Fe (19 atomic planes), a Au spacer layer (15 atomic planes), a Fe free layer (7 atomic planes), and a semi-infinite Ag lead, where we modeled the left and right Ag-leads by explicitly including 8 layers of Ag in the calculation, which were terminated by embedding potentials of a principal layer of Ag on the left and right sides, respectively. In total, the embedded region is composed of 57 atomic planes.

We relaxed the atomic coordinates of a symmetric film composed of 6 layers Au, 5 layers Fe, and again 6 layers Au within GGA (parameterization of Perdew, Burke and Ernzerhof [64]) in order to determine the geometry of the Au-Fe interface. For the Fe and Au MT-radii we chose values of  $1.17 \text{ \AA}$  and  $1.40 \text{ \AA}$ , respectively, and for the planewave cutoff  $7.4 \text{ \AA}^{-1}$ . A  $16 \times 16$   $k$ -point mesh was employed in the calculation. We fixed the in-plane lattice constant to the experimental lattice constant of Fe ( $2.867 \text{ \AA}$ ) and allowed all atoms of the film to relax during the geometry optimization, which was done neglecting spin-orbit coupling. The resulting geometry of the Fe-Au interface is illustrated in Fig. 9.26.

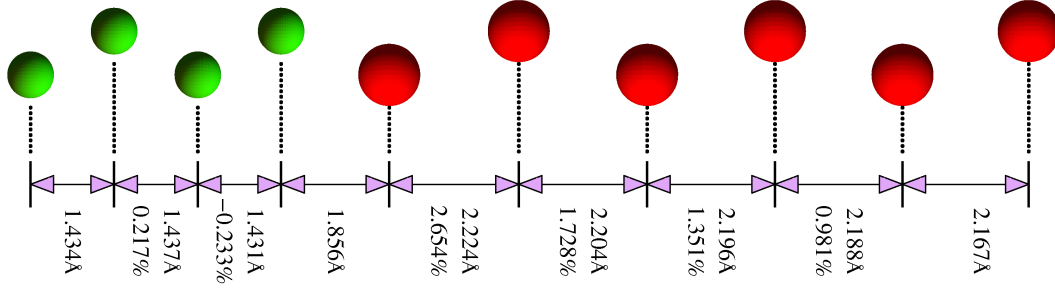


Figure 9.26: Structure of the relaxed Fe-Au interface: Interplanar spacings and their deviations from the respective bulk values for Fe (green) and Au (red).

Table 9.4: Comparison of results for calculations with spin-orbit coupling (SOC) and without spin-orbit coupling (NOSOC).

	$\Gamma_P[\frac{e^2}{h}]$	$\Gamma_{AP}[\frac{e^2}{h}]$	$\Gamma_{90^\circ}[\frac{e^2}{h}]$	GMR [%]	$r(90^\circ)$
SOC	0.744	0.224	0.554	232	0.148
NOSOC	0.755	0.224	0.596	237	0.113

The presence of the interface does not cause the interplanar spacings in Fe to deviate from their bulk value by more than 0.25%. In Au the maximal deviation of the interplanar spacing from its bulk value amounts to 2.7% and the interplanar spacing increases as the interface is approached.

For the calculation of STT and GMR we used the same parameters as in the previous section on the Fe-Ag-Fe spin-valve. In table 9.4 we compare the integrated conductance for the parallel, antiparallel and  $90^\circ$  configurations as well as the resulting GMR-ratios and GMR-asymmetries for calculations with spin-orbit coupling and without.

In Figs. 9.27 and 9.28 we show the plots of the integrated conductance and the normalized resistance of the Fe-Au-Fe spin-valve, where spin-orbit coupling has been included in the calculation. The integration of the conductance has been performed using a  $96 \times 96$   $k$ -point mesh.

Fitting our data for the normalized resistance with Eq. (9.55), we obtain a value of 5.2 for the asymmetry parameter  $\chi_{\text{GMR}}$ .

## 9.8 TMR and STT in Fe-MgO-Fe

The first experimental demonstrations of spin-transfer induced switching have been performed for all-metallic structures. Due to their low resistance ( $R \sim 10\Omega$ ) and magnetoresistance ( $\Delta R/R \sim 5\% - 50\%$ ) they are not well suited for MRAM circuits. Using magnetic tunnel junctions allows to realize magnetoresistances suitable for application in MRAM devices. Experimentally, it has been shown for  $\text{Al}_2\text{O}_3$ -based MTJs [95, 96] and later for MgO-based MTJs [97, 98, 99] that spin-polarized tunnel currents can switch the magnetic state via the spin-transfer torque. Besides the prospect of boosting the MRAM technol-

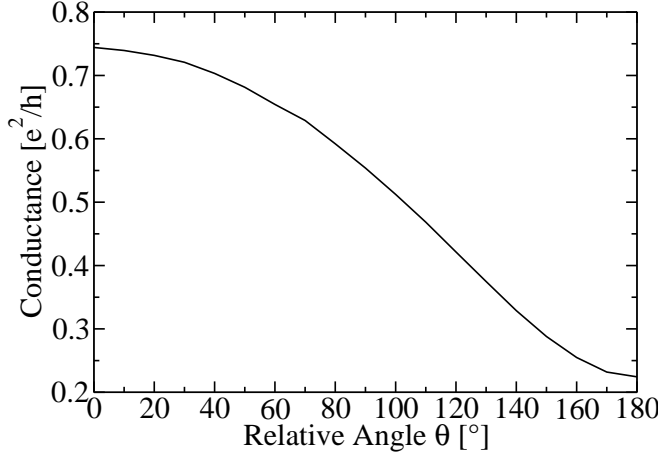


Figure 9.27: Integrated conductance as a function of the relative angle between the magnetization directions for the Fe-Au-Fe nanopillar using a  $98 \times 98$   $k$ -mesh for the 2BZ integration.

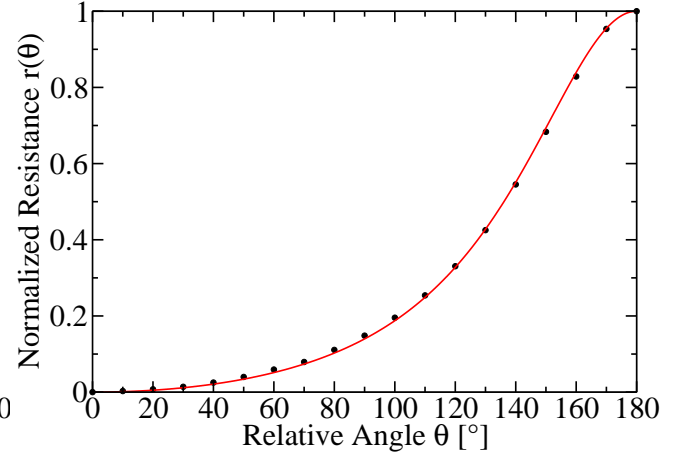


Figure 9.28: Normalized resistance as a function of the relative angle between the magnetization directions for the Fe-Au-Fe nanopillar using a  $98 \times 98$   $k$ -mesh for the 2BZ integration.

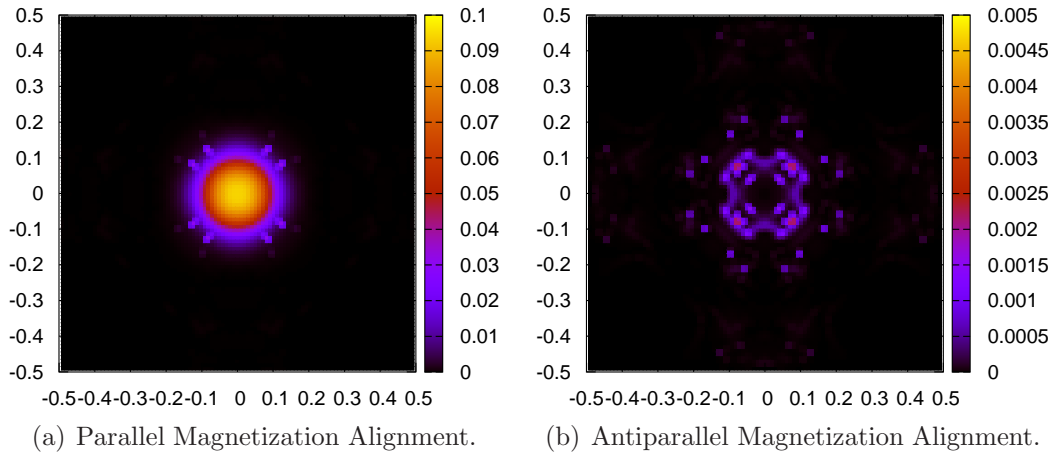


Figure 9.29: 2BZ plot of the  $k$ -dependent conductance (in units of  $e^2/h$ ) per unit cell of the Ag-Fe-MgO-Fe-Ag MTJ at the Fermi level.

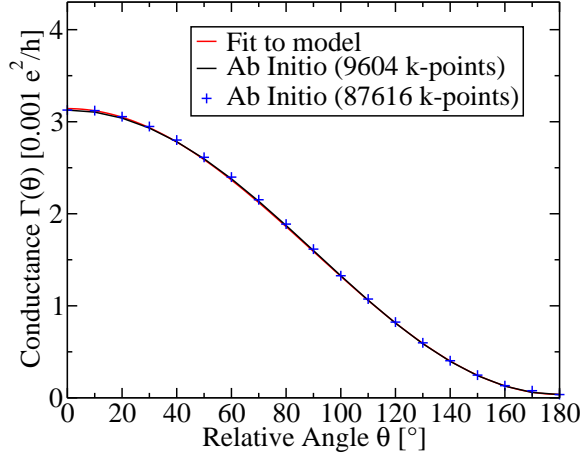


Figure 9.30: Conductance  $\Gamma(\theta)$  per unit cell at the Fermi level as a function of the relative angle  $\theta$  for the Ag-Fe-MgO-Fe-Ag MTJ.

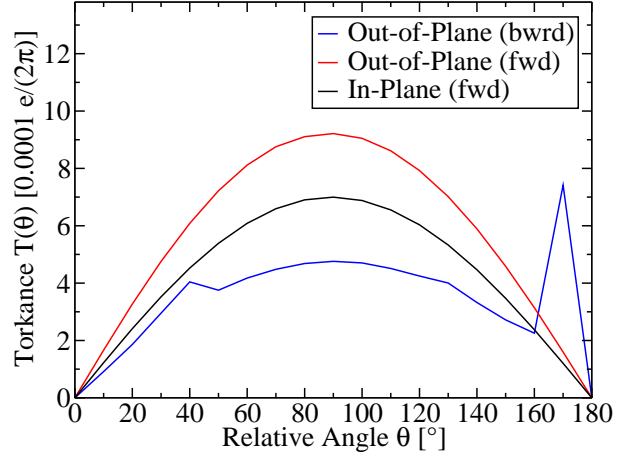


Figure 9.31: Torkance  $T(\theta)$  on the free layer of a Ag-Fe-MgO-Fe-Ag tunnel junction due to states incident from the left (“fwd”) and right (“bwr”) at the Fermi energy.

ogy the investigation of current induced torques in MTJs might lead to better microwave oscillators [100] and novel radio-frequency detectors [98] based on the spin-torque diode effect [101].

In the present section, we study a magnetic tunnel junction composed of 8 layers of Ag (left lead), 19 layers of Fe (fixed layer), 5 layers of MgO (tunnel barrier), 7 layers of Fe (free layer), and 8 layers of Ag (right lead). The experimental lattice constant of Fe (2.867 Å) is used as in-plane lattice constant. The structure of the relaxed interfaces of Fe/Ag and Fe/MgO have been discussed already in section 9.6 and chapter 8.3, respectively. Ab-initio calculations of current induced torques in a comparable MgO-based tunnel-junction are discussed in Ref. [102]. The MTJ of Ref. [102] consists of an MgO barrier (6 monolayers), a Fe fixed layer (20 monolayers), and a Fe free layer (variable thickness between 1 and 20 monolayers) embedded between semi-infinite Cu in bcc-Fe structure. Consequently, the heart of the MTJ investigated in Ref. [102] is similar to the one of our setup, which allows us to compare our results.

The  $k$ -dependent conductance at the Fermi energy is shown in Fig. 9.29 for relative angles of  $0^\circ$  and  $180^\circ$ . In agreement with our discussion of spin-dependent tunneling in Fe/MgO/Fe MTJs in section 8.3 the conductance in the parallel alignment is dominated by a broad peak around  $\bar{\Gamma}$ , while the conductance at  $\bar{\Gamma}$  is strongly reduced for the antiparallel alignment: At  $\bar{\Gamma}$  Fe is a half-metal (only majority states) at the Fermi level for states with  $\Delta_1$  symmetry, which decay most slowly in MgO and hence contribute strongest to the tunneling. In contrast to the all-metallic junctions discussed in the previous sections, the current is carried only by a small fraction of the Fermi surface. This is expected to reduce dephasing, which controls the decay of the torque in all-metallic spin-valves.

In Fig. 9.30 we show the integrated conductance per unit cell at the Fermi level as a function of the angle between the magnetization directions. The angular dependence of

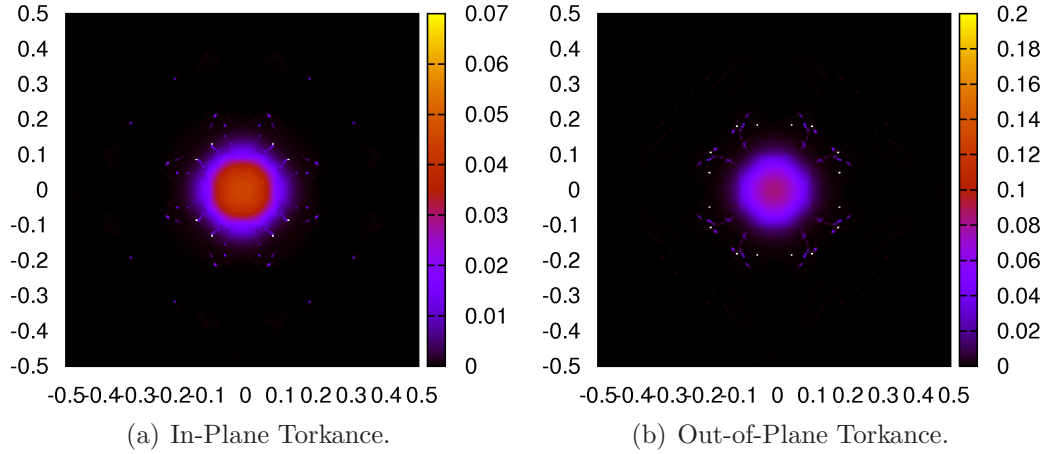


Figure 9.32: 2BZ plot of the  $k$ -dependent torkance (in units of  $e/(2\pi)$ ) per unit cell of the Ag-Fe-MgO-Fe-Ag MTJ at the Fermi level.

the conductance is very well captured by the model

$$\Gamma(\theta) = a_0 + a_1 \cos(\theta). \quad (9.75)$$

Fitting this model to our ab-initio results we obtain  $a_0 = 1.59 \times 10^{-3} e^2/h$  and  $a_1 = 1.55 \times 10^{-3} e^2/h$ . The proportionality of the conductance to  $\cos(\theta)$ , which is typical [103, 83, 104, 105, 106] for tunnel junctions, is a direct consequence of Eq. (9.4). In table 9.5 we list conductivities and resistivities at  $0^\circ$  and  $180^\circ$ . The corresponding TMR-value is given by  $(R_{AP} - R_P)/R_P = 8800\%$ .

In Fig. 9.32 the  $k$ -resolved in-plane and out-of-plane torkances are shown for states incident from the left at the Fermi energy for the configuration with  $90^\circ$  relative angle between the magnetization directions. As expected on the basis of the  $k$ -resolved conductance shown in Fig. 9.29 basically only a small area around  $\bar{\Gamma}$  contributes to the total torkance. This is in marked contrast to what we found for all-metallic junctions in the previous sections. Furthermore, while we found the  $k$ -resolved torkance of all-metallic junctions to exhibit strong variations in the 2BZ, it is relatively smooth for the MTJ studied here.

The angular dependence of the torkance on the free layer at the Fermi energy is shown in Fig. 9.31. We show only the in-plane torkance due to electrons incident from the left as the one due to electrons incident from the right is equal but opposite. The out-of-plane torkances due to states incident from left and right differ. As expected on the basis of Eq. (9.4) and in agreement with theoretical predictions [103, 83, 106, 107, 108] for the torkance due to ballistic electrons the model

$$T_{\parallel}(\theta) = b \sin \theta \quad (9.76)$$

gives a very good description of the in-plane component of the torque. From the fit to our ab-initio results we obtain the parameter  $b = 6.95 \times 10^{-4} e/(2\pi)$ . According to the theory

of Slonczewski [103], the in-plane torkance  $T_{\parallel}(\theta)$  is predicted to be related to the resistance in parallel configuration,  $(dV/dI)_P$ , and the polarization  $P$  as follows:

$$\frac{T_{\parallel}(\theta)}{\sin(\theta)} \left( \frac{dV}{dI} \right)_P = \frac{\hbar}{4e} \frac{2P}{1+P^2}. \quad (9.77)$$

Thus, we assume that this product of in-plane torkance and resistance does not depend strongly on the device geometry and allows a comparison of our results to the experiment. Note, that this quantity is similar to the *torque per current*. However, at variance with the definition of the torque per current, effectively the torkance at  $90^\circ$  is divided by the conductance at  $0^\circ$  in Eq. (9.77). In the experiment of Ref. [97] (1.25nm MgO barrier between  $\text{Co}_{60}\text{Fe}_{20}\text{B}_{20}$  leads of 2.5nm and 3nm) the resistance in the parallel configuration is 3.19 k $\Omega$  and the in-plane torkance was measured to be  $T_{\parallel}(\theta)/\sin(\theta) = (0.13 \pm 0.02)\hbar/(2ek\Omega)$ , i.e., the value of the left-hand side of Eq. (9.77) is  $(0.21 \pm 0.03)\hbar/e$ . From the fits of the models, Eq. (9.76) and Eq. (9.75), to our data we obtain

$$\frac{T_{\parallel}(\theta)}{\sin(\theta)} \left( \frac{dV}{dI} \right)_P = \frac{b}{a_0 + a_1} = \frac{6.95 \cdot 10^{-4}e/(2\pi)}{1.59 \cdot 10^{-3}e^2/h + 1.55 \cdot 10^{-3}e^2/h} = 0.22 \frac{\hbar}{e}, \quad (9.78)$$

which is in excellent agreement with the experiment of Ref. [97]. One may also estimate this value as follows: As the conductance in the antiparallel configuration is smaller than the conductance in the parallel configuration by roughly two orders of magnitude, the conductance at  $90^\circ$  is approximately half of the conductance at  $0^\circ$ . Thus, Eq. (9.77) amounts to roughly half of the torque per current at  $90^\circ$ . If the angle between the magnetizations is  $90^\circ$  it is expected that per electron an angular momentum of  $\hbar/2$  is transferred to the free magnetic layer and likewise to the fixed magnetic layer, resulting in a value of  $0.25 \frac{\hbar}{e}$  for Eq. (9.77). The deviation of the *ab initio* result ( $0.22 \frac{\hbar}{e}$ ) and the experimental result  $((0.21 \pm 0.03)\hbar/e)$  from this ideal value are quite small. In Ref. [102] an even better agreement with this simple model description is reported: At  $90^\circ$  relative angle the torque per current is found to be almost exactly  $0.5 \frac{\hbar}{e}$ . In agreement with Ref. [102] we find also the out-of-plane torkance due to states incident from the left to be almost perfectly sinusoidal. However, in contrast to Ref. [102] the out-of-plane torkance due to states incident from the left is larger than the in-plane torkance in our case and the out-of-plane torkance due to states incident from the right is not sinusoidal. Generally, when compared to the in-plane torque the out-of-plane torque depends stronger on the geometry of the system, which might explain the discrepancy between our results and those of Ref. [102]. Experimentally, it was found that in MgO-based MTJs the out-of-plane torque can be sizable (10-30% of the size of the in-plane torque) and substantially affect the magnetization dynamics [97, 99, 109]. While the out-of-plane torque measured in experiments is smaller than the in-plane torque, one has to take into account that it exhibits a strong dependence on the geometry: Due to fluctuations of the thicknesses of the magnetic layers or the barrier the out-of-plane torque may be strongly reduced due to averaging [102]. Consequently, the finding of a small out-of-plane torque in the experiment is not necessarily significant for an *ideal* junction. Considerable attention has been devoted to the bias-dependence of

Table 9.5: Conductivities and resistivities of the Ag-Fe-MgO-Fe-Ag junction.

$\Gamma_P/\text{u.c.} [e^2/h]$	$\Gamma_P/A [\text{S/m}^2]$	$R_P A [\Omega\text{m}^2]$	$\Gamma_{AP}/\text{u.c.} [e^2/h]$	$\Gamma_{AP}/A [\text{S/m}^2]$	$R_{AP} A [\Omega\text{m}^2]$
$3.13 \cdot 10^{-3}$	$1.48 \cdot 10^{12}$	$6.78 \cdot 10^{-13}$	$3.53 \cdot 10^{-5}$	$1.66 \cdot 10^{10}$	$6.01 \cdot 10^{-11}$

the out-of-plane torque [110, 97, 111, 112] and the question whether it follows a linear or a quadratic dependence on the bias. According to Ref. [113] a symmetric bias dependence is expected only in symmetric MTJs. Clearly, our setup is not perfectly symmetric as the free and fixed layer thicknesses differ.

The in-plane components of the layer-resolved torkance at a relative angle of  $90^\circ$  are shown in Fig. 9.33. Since the layer-resolved in-plane torkance due to states incident from the left is equal but opposite to the in-plane torkance due to states incident from the right, we show only one case. Layers 33-39 constitute the free magnetic layer, layers 9-27 the fixed magnetic layer, and layers 28-32 the MgO-barrier. As the total spin of the fixed magnetic layer is parallel to the  $x$ -axis, while the total spin of the free magnetic layer is parallel to the  $y$ -axis, the in-plane torque on the free layer points in  $x$ -direction and the in-plane torque on the fixed layer points in  $y$ -direction. Clearly, the torques on both the free and the fixed layer are exerted almost entirely on the one layer which touches the barrier. Thus, the decay of the layer-resolved in-plane torque is faster than for the metallic spin-valves we had studied in the preceding sections. The torques within the barrier and the Ag-layers are very small when compared to the torques on the magnetic layers.

A plot of the layer-resolved out-of-plane torkances for the two cases of states incident from the left and states incident from the right is depicted in Fig. 9.34. There are several qualitative differences between the torkances for the two directions of incidence. While the out-of-plane torque on the free layer due to states coming from the left is strongly localized in the first layer of the free magnetic layer, this is not true for states coming from the right. However, the out-of-plane torque associated with left-moving electrons on the fixed layer is relatively well localized in the first layers of the fixed magnetic layer, while this is not the case for the right-moving electrons. Interestingly, there are substantial out-of-plane torques on those MgO and Ag-layers which are close to the magnetic layers if the electrons are left-moving. This is why we included these torques into the total torque on the free magnetic layer as shown in Fig. 9.31. The inclusion of these torques in the summation has a large effect. To show this, we plot in Fig. 9.35 the torkance due to states incident from the right, but summing only the torkances of the magnetic atoms of the free layer. The out-of-plane torkance exhibits now an interesting angular dependence, namely it is roughly proportional to  $\sin(2\theta)$ . Additionally, its values are very large when compared to the in-plane torkance.

The torque per current for the case of right-moving electrons is shown in Fig. 9.36. Clearly, the strong asymmetry is due to the strong variation of the conductance as a function of the relative angle, which is typical of MTJs.



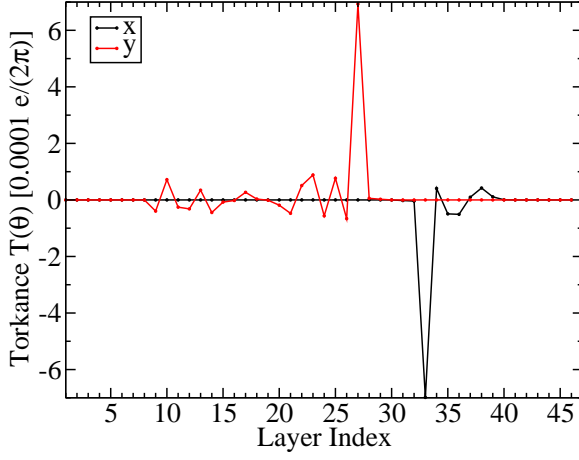


Figure 9.33: Layer-resolved in-plane torkance  $T(\theta)$  per unit cell at the Fermi level due to states incident from the left and at a relative angle of  $90^\circ$  for the Ag-Fe-MgO-Fe-Ag MTJ. Directions refer to the global frame. In-plane torkances due to states incident from the right are equal but opposite and not shown.

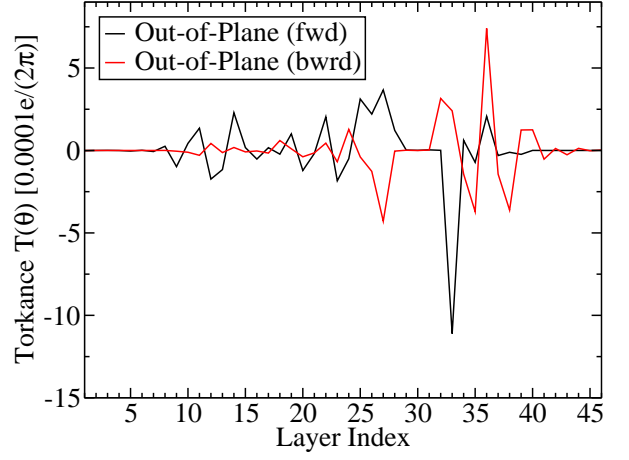


Figure 9.34: Layer-resolved out-of-plane torkance  $T(\theta)$  per unit cell at the Fermi level and at a relative angle of  $90^\circ$  for the Ag-Fe-MgO-Fe-Ag tunnel junction due to states incident from the left (“fwd”) and right (“bwr”).

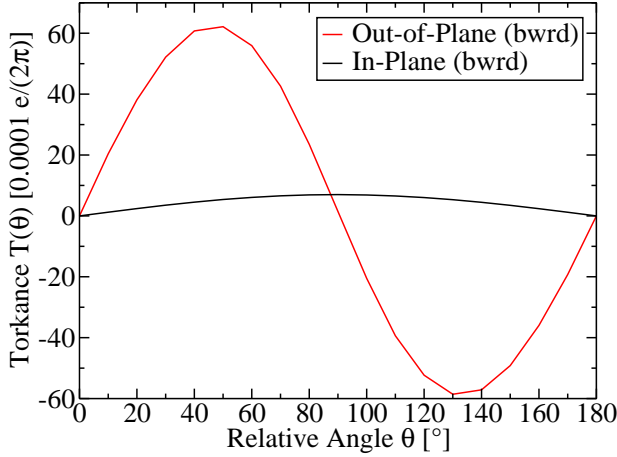


Figure 9.35: Torkance  $T(\theta)$  on the free layer of a Ag-Fe-MgO-Fe-Ag tunnel junction due to states incident from the right at the Fermi energy.

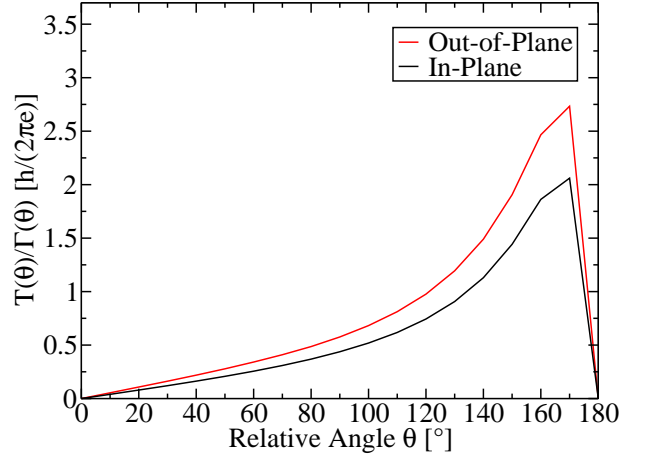


Figure 9.36: Torque per current  $T(\theta)/\Gamma(\theta)$  on the free layer of a Ag-Fe-MgO-Fe-Ag tunnel junction due to states incident from the left at the Fermi energy.



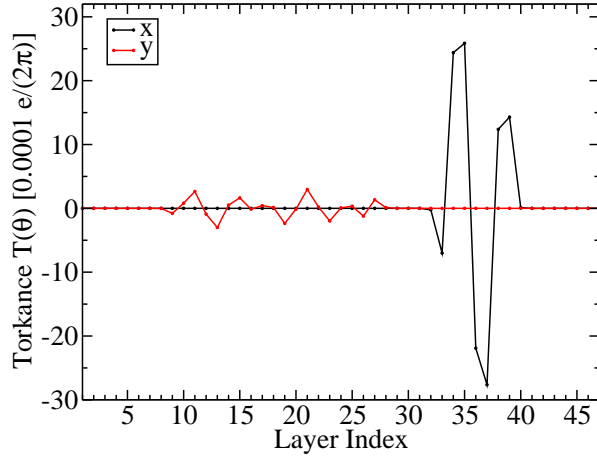


Figure 9.37: Layer-resolved in-plane torkance  $T(\theta)$  per unit cell at the Fermi level due to states incident from the left and at a relative angle of  $90^\circ$  for the Ag-Co-MgO-Co-Ag MTJ. Directions refer to the global frame. In-plane torkances due to states incident from the right are equal but opposite and not shown.

### 9.8.1 Co instead of Fe in the magnetic layers

In order to investigate the dependency of the torque on the material of the magnetic layers in MgO-based MTJs, we performed calculations of a magnetic tunnel junction composed of 8 layers of Ag (left lead), 19 layers of Co (fixed layer), 5 layers of MgO (tunnel barrier), 7 layers of Co (free layer) and 8 layers of Ag (right lead). This is the same stacking as in the Fe/MgO/Fe MTJ discussed above, but with Fe replaced by Co. The Fe/Co and Co/MgO interfaces have been discussed already in section 8.4. Due to Eq. (9.75,9.76) it is sufficient to compute the conductance and the in-plane torkance at a relative angle of  $90^\circ$  to capture the main properties of the MTJ. The conductance at  $90^\circ$  is  $4.25 \cdot 10^{-3} e^2/h$ . The torkance at  $90^\circ$  is  $2.04 \cdot 10^{-3} e/(2\pi)$ . Thus, the value of Eq. (9.77) amounts to  $0.24\hbar/e$ . Like in the case of the Fe/MgO/Fe junction discussed above, this is in very good agreement with  $0.25\hbar/e$ , which is expected from the simple model of a MTJ between two half-metals, which we discussed in the context of Eq. (9.77). However, in contrast to the Fe/MgO/Fe junction, the layer-resolved in-plane torkance decays much more slowly: All atomic layers of the free magnetic layer experience a significant share of the total in-plane torque. This is shown in Fig. 9.37.



# Chapter 10

## Wannier Functions

Commonly, the electronic structure of periodic solids is described in terms of Bloch functions (BFs), which are eigenfunctions of both the Hamiltonian and lattice translation operators. Due to their delocalized nature BFs are difficult to visualize and hence do not offer a very intuitive picture of the underlying physics. For the same reason, BFs do not provide a very efficient framework for the study of local correlations. An alternative approach to electronic structure that does not exhibit these weaknesses is provided by maximally localized Wannier functions (MLWFs). Related to the BFs via a unitary transformation, MLWFs constitute a mathematically equivalent concept for the study of electronic structure. They are well localized in real space and in contrast to the complex BFs purely real<sup>1</sup>, at least for collinear systems without spin-orbit coupling. Therefore, it is easy to visualize them and to gain physical insight e.g. into the bonding properties of the system under study by extracting characteristic parameters such as the MLWFs' centers, spreads, and hopping integrals as well as by analyzing their shapes.

Wannier functions (WFs) were first introduced by Wannier in 1937 [114] as the Fourier transforms of BFs. Similar to a  $\delta$ -function, which is the Fourier transform of a plane wave, WFs are localized in real space while the BFs are not. However, BFs are only determined up to an arbitrary phase factor, and hence the definition of WFs as Fourier transforms of BFs does not specify the WFs uniquely. As the localization properties of the WFs depend strongly on the phase factors of the BFs, the Wannier function approach experienced little enthusiasm until very recently, after methods for the calculation of WFs with optimal localization properties had been developed. One of these new techniques for the construction of localized WFs is based on the N-th order muffin-tin-orbital (NMTO) method [115, 116, 117]. Another method performs at each  $k$ -point a unitary transformation among the BFs belonging to different bands yielding a new set of functions, the Fourier transforms of which are the MLWFs [19]. Only the latter technique is considered in this work.

Shedding new light on otherwise hard to calculate properties of materials, nowadays

---

<sup>1</sup>In the presence of spin-orbit coupling the requirement of real-valuedness of the Wannier function cannot be fulfilled in general. Similarly, the Wannier functions of non-collinear structures are generally complex-valued.

MLWFs have almost reached the popularity of BFs, and using both allows to achieve a rich diversity in understanding, originating from revealing both itinerant and localized aspects of electrons in periodic potentials. For example, a modern theory of polarization [118, 119, 120, 24, 121] is based on the displacements of the centers of the MLWFs. The orbital polarization may be expressed in terms of MLWFs [122, 123]. Studying the MLWFs for disordered systems yields a transparent description of bonding properties [124]. MLWFs provide a minimal basis set that allows for efficient computations of the quantum transport of electrons through nanostructures and molecules [125, 126]. Within the research area of strongly correlated electrons MLWFs are becoming the preferred basis for studying the local correlations [21, 22, 23].

## 10.1 Maximally localized Wannier functions

For an isolated band, i.e., a band that does not become degenerate with other bands at any  $k$ -point, with corresponding BFs  $|\psi_{\mathbf{k}}\rangle$ , the definition of WFs as Fourier transforms of BFs leads to the following expression:

$$|W_{\mathbf{R}}\rangle = \frac{1}{N} \sum_{\mathbf{k}} e^{-i\mathbf{k}\cdot\mathbf{R}} |\psi_{\mathbf{k}}\rangle, \quad (10.1)$$

where  $\mathbf{R}$  is a direct lattice vector, which specifies the unit cell the WF belongs to, and the Brillouin zone is represented by a uniform mesh of  $N$   $k$ -points. The  $|\psi_{\mathbf{k}}\rangle$  are normalized with respect to the unit cell, while the  $|W_{\mathbf{R}}\rangle$  constitute an orthonormal basis set with respect to the volume of  $N$  unit cells:

$$\begin{aligned} \langle \psi_{\mathbf{k}} | \psi_{\mathbf{k}'} \rangle &= N \delta_{\mathbf{k}, \mathbf{k}'}, \\ \langle W_{\mathbf{R}} | W_{\mathbf{R}'} \rangle &= \delta_{\mathbf{R}, \mathbf{R}'}, \end{aligned} \quad (10.2)$$

where the integration is over  $N$  unit cells. However, Eq. (10.1) does not define the WFs uniquely: The BFs are determined only up to a phase factor – hence, for a given set of BFs and a general  $k$ -point dependent phase  $\phi(\mathbf{k})$ ,

$$|W_{\mathbf{R}}\rangle' = \frac{1}{N} \sum_{\mathbf{k}} e^{-i\mathbf{k}\cdot\mathbf{R}} e^{i\phi(\mathbf{k})} |\psi_{\mathbf{k}}\rangle \quad (10.3)$$

equally constitute a set of WFs.

### 10.1.1 One dimensional example

In the following we illustrate some basic properties of Wannier functions using the one-dimensional model potential

$$V(x) = -\cos(2\pi x). \quad (10.4)$$

Clearly, the periodicity of this potential is simply 1. We construct Wannier functions corresponding to the first band from the Bloch functions at the 5  $k$ -points  $-0.8\pi$ ,  $-0.4\pi$ ,  $0.0$ ,  $0.4\pi$ ,  $0.8\pi$ . According to the discussion above, we consider the set of Wannier functions

$$|W\rangle = \frac{1}{5} [e^{i\phi_1}|k = -0.8\pi\rangle + e^{i\phi_2}|k = -0.4\pi\rangle + e^{i\phi_3}|k = 0.0\rangle + e^{i\phi_4}|k = 0.4\pi\rangle + e^{i\phi_5}|k = 0.8\pi\rangle], \quad (10.5)$$

which still has a gauge freedom due to the arbitrariness of the phases  $\phi_1$ ,  $\phi_2$ ,  $\phi_3$ ,  $\phi_4$  and  $\phi_5$ . In Fig. 10.1 we show the resulting Wannier functions for four different choices of phases. The phases of the Wannier function in Fig. 10.1(a) have been chosen such that the localization is maximal, i.e., the spread

$$\langle W|x^2|W\rangle = \int |W(x)|^2 x^2 dx \quad (10.6)$$

is minimal. Redefining the Bloch functions in such a way that the phases are all zero for this *maximally localized* Wannier function, the phases of the remaining Wannier functions in Fig. 10.1 are:

b  $(\pi, 0, 0, 0, \pi)$

c  $(0, \pi, 0, \pi, 0)$

d  $(\pi, \pi, 0, \pi, \pi)$ .

All four Wannier functions are real-valued, but they are very different regarding their localization. In the next section we will discuss how well-localized Wannier functions may be generated in general.

We constructed the Wannier functions from 5 equidistant  $k$ -points. This has the consequence, that the resulting Wannier functions have a period of 5 unit cells, which can clearly be seen in Fig. 10.1. In general the Wannier functions exhibit a periodicity of  $N$  unit cells, if they are constructed from  $N$   $k$ -points. This may be understood as follows: We assume the number  $N$  of  $k$ -points to be odd. The set of  $k$ -points is then given by

$$k_n = \frac{2n\pi}{LN}, \quad n = -\frac{N-1}{2}, \dots, \frac{N-1}{2}, \quad (10.7)$$

where  $L$  is the length of the unit cell. In general, Bloch functions may be written as a product of a lattice periodic part and the phase factor  $e^{ikx}$  (see also Eq. (10.10) below). Clearly, the Bloch functions are then periodic in  $NL$  for the set of  $k$ -points specified in Eq. (10.7). Consequently, the resulting Wannier functions are also periodic in  $NL$ .

Usually, the local maxima of  $|W(x)|$  are located either in the minima of the potential or at least close to them. The Wannier function in Fig. 10.1(a), which possesses optimal localization properties with respect to the criterion Eq. (10.6), exhibits one well pronounced maximum at zero, in a minimum of the potential. However, even for this maximally localized Wannier function, there exist local maxima of  $|W(x)|$ . They are due to the *hybridization* between neighboring sites. If we increase the depth of the potential the hybridization will decrease and the satellite peaks of  $|W(x)|$  will get smaller and smaller.

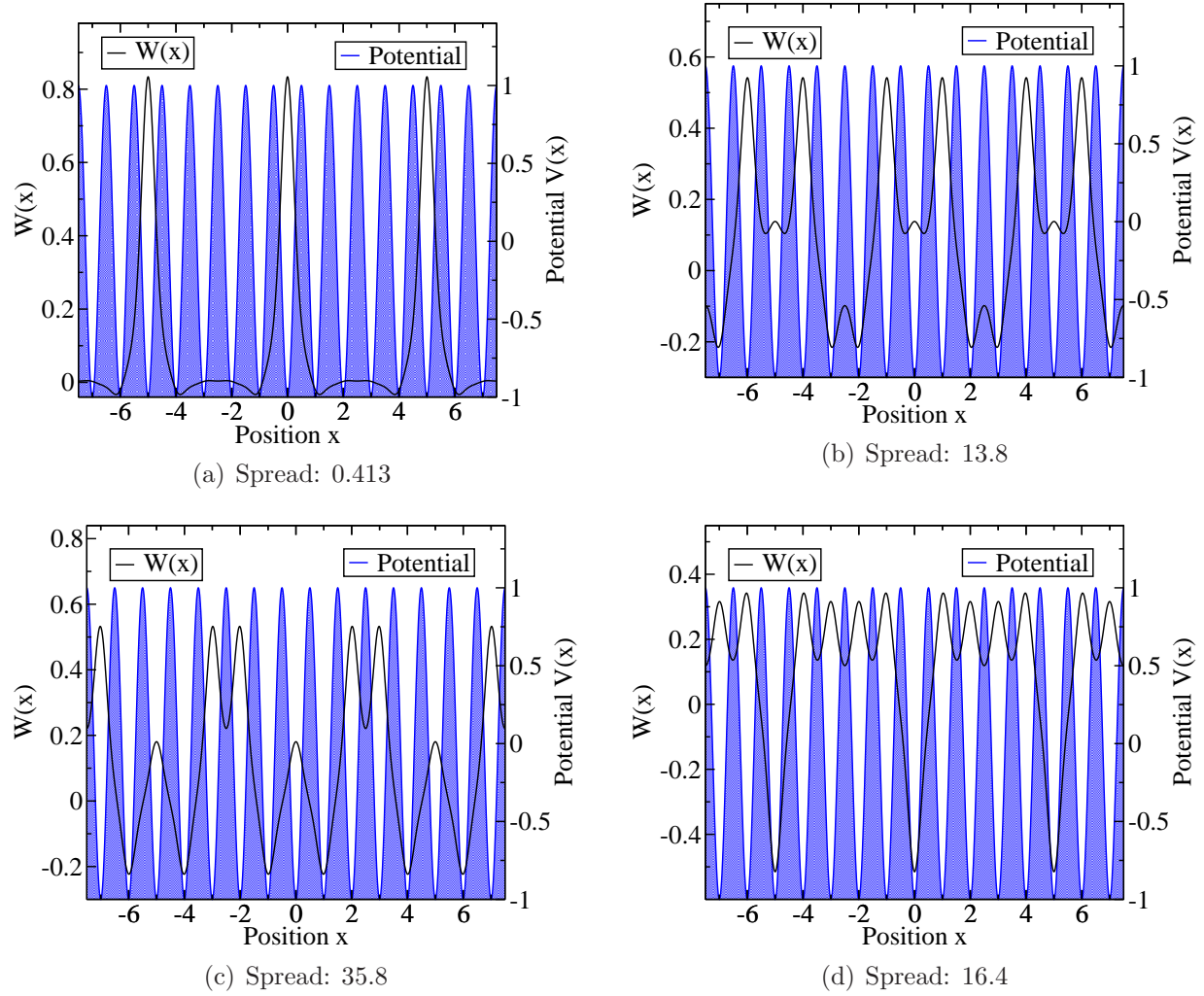


Figure 10.1: Wannier functions of a one-dimensional model potential. (a) Maximally localized Wannier function. (b),(c),(d) The Wannier functions are constructed from the same Bloch functions as (a), but the phases of the Bloch functions differ from the choice in (a). The localization property depends very strongly on the phases of the Bloch functions.

### 10.1.2 Maximal localization procedure

For their use in practice, it is desirable to have WFs that decay exponentially in real space, exhibit the symmetry properties of the system studied, and are real- rather than complex-valued<sup>1</sup> functions. For the one-dimensional Schrödinger equation and an isolated single energy band, Kohn [127] has shown that there exists only one WF which is real<sup>1</sup>, falls off exponentially with distance and has maximal symmetry. WFs with maximal spatial localization [19] (MLWFs) fulfill these requirements of real-valuedness<sup>1</sup>, optimal decay properties and maximal symmetry. The constraint of maximal localization eliminates the nonuniqueness of WFs and determines  $\phi(\mathbf{k})$  up to a constant.

In the general case, energy bands cross or are degenerate at certain  $k$ -points, making it necessary to consider a group of bands. This increases the freedom in defining WFs further, as now bands may be mixed at each  $k$ -point via the transformation  $U_{mn}^{(\mathbf{k})}$ :

$$|W_{\mathbf{R}n}\rangle = \frac{1}{N} \sum_{\mathbf{k}} e^{-i\mathbf{k}\cdot\mathbf{R}} \sum_m U_{mn}^{(\mathbf{k})} |\psi_{\mathbf{k}m}\rangle, \quad (10.8)$$

where the BF has a band index  $m$ , the WF an orbital index  $n$ , and the number of bands – which may depend on the  $k$ -point – has to be larger than or equal to the number of WFs that are supposed to be extracted. Imposing the constraint of maximal spatial localization on the WFs determines the set of  $U_{mn}^{(\mathbf{k})}$ -matrices up to a common global phase [19, 20]. In case the number of bands is equal to the number of WFs, the  $U_{mn}^{(\mathbf{k})}$  matrices are unitary. This situation usually occurs when an isolated group of bands may efficiently be chosen for the system under study. In the more general case of entangled energy bands [20], however, the number of bands is  $k$ -point dependent and  $U_{mn}^{(\mathbf{k})}$  no longer unitary.

Requiring the spread of the WFs to be minimal imposes the constraint of maximal spatial localization. The spread of the WFs is defined as the sum of the second moments,

$$\Omega = \sum_n [\langle \mathbf{r}^2 \rangle_n - (\langle \mathbf{r} \rangle_n)^2], \quad (10.9)$$

where  $\langle \rangle_n$  denotes the expectation value with respect to the Wannier orbital  $|W_{0n}\rangle$  and the sum includes all WFs formed from the composite group of bands. Minimization of the spread yields the set of optimal  $U_{mn}^{(\mathbf{k})}$ -matrices.

An efficient algorithm for the minimization of the spread Eq. (10.9) has been given by Marzari and Vanderbilt first for isolated groups of bands [19], and later on generalized for the case of entangled energy bands [20]. The corresponding computer code is publicly available [128] and was used in this work. Two quantities are required as input by this computational method and have to be provided by the first-principles calculation: First, the projections  $A_{mn}^{(\mathbf{k})} = \langle \psi_{\mathbf{k}m} | g_n \rangle$  of localized orbitals  $|g_n\rangle$  onto the BFs are needed to construct a starting point for the iterative optimization of the MLWFs. Second, the overlaps between the lattice periodic parts

$$u_{\mathbf{k}m}(\mathbf{r}) = e^{-i\mathbf{k}\cdot\mathbf{r}} \psi_{\mathbf{k}m}(\mathbf{r}) \quad (10.10)$$

of the BF's at nearest-neighbor  $k$ -points  $\mathbf{k}$  and  $\mathbf{k} + \mathbf{b}$ ,

$$M_{mn}^{(\mathbf{k}, \mathbf{b})} = \langle u_{\mathbf{k}m} | u_{\mathbf{k}+\mathbf{b},n} \rangle, \quad (10.11)$$

are necessary to evaluate the relevant observables [19]:

$$\langle \mathbf{r} \rangle_n = -\frac{1}{N} \sum_{\mathbf{k}, \mathbf{b}} w_{\mathbf{b}} \mathbf{b} \Im \ln \tilde{M}_{nn}^{(\mathbf{k}, \mathbf{b})} \quad (10.12)$$

and

$$\langle \mathbf{r}^2 \rangle_n = \frac{1}{N} \sum_{\mathbf{k}, \mathbf{b}} w_{\mathbf{b}} \left[ 1 - |\tilde{M}_{nn}^{(\mathbf{k}, \mathbf{b})}|^2 + (\Im \ln \tilde{M}_{nn}^{(\mathbf{k}, \mathbf{b})})^2 \right], \quad (10.13)$$

where  $w_{\mathbf{b}}$  is a weight associated with  $\mathbf{b}$ , and

$$\tilde{M}_{mn}^{(\mathbf{k}, \mathbf{b})} = \sum_{m_1} \sum_{m_2} (U_{m_1 m}^{(\mathbf{k})})^* U_{m_2 n}^{(\mathbf{k}+\mathbf{b})} M_{m_1 m_2}^{(\mathbf{k}, \mathbf{b})} \quad (10.14)$$

evolves during the minimization process due to the iterative refinement of the  $U_{mn}^{(\mathbf{k})}$ . The relations Eqns. (10.12, 10.13) are valid for uniform  $k$ -point grids, while in the continuum-limit the  $k$ -space expressions for the matrix elements of the position operator are given by [19]

$$\langle W_{\mathbf{R}n} | \mathbf{r} | W_{\mathbf{0}m} \rangle = i \frac{V}{(2\pi)^3} \int d^3 k e^{i\mathbf{k} \cdot \mathbf{R}} \langle \tilde{u}_{\mathbf{k}n} | \nabla_{\mathbf{k}} | \tilde{u}_{\mathbf{k}m} \rangle \quad (10.15)$$

and

$$\langle W_{\mathbf{R}n} | \mathbf{r}^2 | W_{\mathbf{0}m} \rangle = -\frac{V}{(2\pi)^3} \int d^3 k e^{i\mathbf{k} \cdot \mathbf{R}} \langle \tilde{u}_{\mathbf{k}n} | \nabla_{\mathbf{k}}^2 | \tilde{u}_{\mathbf{k}m} \rangle. \quad (10.16)$$

Replacing the gradient  $\nabla_{\mathbf{k}}$  by finite-difference expressions valid on a uniform  $k$ -point mesh, one obtains the weights  $w_{\mathbf{b}}$  in Eqns. (10.12, 10.13). Through Eqns. (10.12, 10.13, 10.14) the spread  $\Omega$  in Eq. (10.9) may be expressed in terms of and be minimized with respect to the  $U_{mn}^{(\mathbf{k})}$ -matrices.

Interestingly, for a composite isolated group of bands the sum of the centers of the Wannier functions,

$$\sum_n \langle \mathbf{r} \rangle_n = \text{constant}, \quad (10.17)$$

does not depend on the unitary transformation  $U_{mn}^{(\mathbf{k})}$ . More precisely, it can only change by a lattice translation vector. Hence, it is gauge invariant modulo a lattice translation vector. This will become clear in section 10.6 on the Berry phase. Clearly, our one-dimensional example shown in Fig. 10.1 exhibits this property: The center of mass of the Wannier function does not change when the phases of the Bloch functions are changed, only the spread changes.



### 10.1.3 First-guess Wannier functions

The iterative optimization process requires as a starting point first guesses for the MLWFs. In order to construct these, one projects localized orbitals  $|g_n\rangle$  onto the BF-subspace:

$$|\phi_{\mathbf{k}n}\rangle = \sum_m |\psi_{\mathbf{k}m}\rangle \langle \psi_{\mathbf{k}m} | g_n \rangle = \sum_m A_{mn}^{(\mathbf{k})} |\psi_{\mathbf{k}m}\rangle. \quad (10.18)$$

As the first-guess WFs are supposed to constitute an orthonormal basis set, the  $|\phi_{\mathbf{k}n}\rangle$  are orthonormalized via the overlap matrix  $S_{mn}^{(\mathbf{k})} = \langle \phi_{\mathbf{k}m} | \phi_{\mathbf{k}n} \rangle$

$$|\tilde{\psi}_{\mathbf{k}n}\rangle = \sum_m ((S^{(\mathbf{k})})^{-\frac{1}{2}})_{mn} |\phi_{\mathbf{k}m}\rangle, \quad (10.19)$$

before the WFs are calculated from them according to

$$|W_{\mathbf{R}n}\rangle = \frac{1}{N} \sum_{\mathbf{k}} e^{-i\mathbf{k}\cdot\mathbf{R}} |\tilde{\psi}_{\mathbf{k}n}\rangle. \quad (10.20)$$

While the first-guess WFs are dependent on the choice of localized orbitals  $|g_n\rangle$  they converge in the ideal case to the one and only one set of MLWFs in the course of the minimization procedure. However, the spread functional  $\Omega$ , Eq. (10.9), may possess local minima besides the global minimum, i.e., when the iterative minimization of the spread has converged into a minimum, it is not clear that the corresponding WFs are MLWFs since there might exist a smaller minimum of the spread. In section 10.8.1 we will present an example, where the minimization of the spread leads to a local minimum if the first-guess Wannier functions are not chosen optimally. Thus, even though the gauge degrees of freedom that remain on the level of the first-guess Wannier functions are eliminated by the minimization of the spread functional, it is important in practice to start from good first-guess Wannier functions, i.e., the localized orbitals  $|g_n\rangle$  should be chosen such that they resemble the MLWFs as closely as possible. In fact, choosing the  $|g_n\rangle$  arbitrarily increases the effort to find the minimum of the spread considerably, i.e., far more iterations are needed.

Although the first-guess WFs of Eq. (10.20) are not unique they agree well with the MLWFs in many cases. Examples where there is substantial difference between first-guess WFs and MLWFs include systems where the centers of the Wannier orbitals do not coincide with the centers of the atoms. If for the system under study the first-guess WFs are already satisfactory, one may skip the localization procedure and take Eq. (10.20) as the final result. Computing WFs in this way requires much less time, as the  $M_{mn}^{(\mathbf{k},\mathbf{b})}$  matrix elements do not have to be calculated and the minimization of the spread functional is not performed. First-guess WFs have been successfully applied to describe  $\text{SrVO}_3$  [22],  $\text{V}_2\text{O}_3$  [22] and  $\text{NiO}$  [129], for example.

## 10.2 Implementation within the FLAPW method

### 10.2.1 Calculation of $M_{mn}^{(\mathbf{k}, \mathbf{b})}$ within the FLAPW formalism

For the calculation of MLWFs the most important quantity is the  $M_{mn}^{(\mathbf{k}, \mathbf{b})}$  matrix, which – according to Eqns. (10.12, 10.13) – contains all information needed to determine spreads and centers. With the lattice periodic part  $u_{\mathbf{k}m}(\mathbf{r})$  being related to its BF by  $u_{\mathbf{k}m}(\mathbf{r}) = e^{-i\mathbf{k}\cdot\mathbf{r}}\psi_{\mathbf{k}m}(\mathbf{r})$ , the  $M_{mn}^{(\mathbf{k}, \mathbf{b})}$  matrix elements assume the form

$$M_{mn}^{(\mathbf{k}, \mathbf{b})} = \int e^{-i\mathbf{b}\cdot\mathbf{r}} (\psi_{\mathbf{k}m}(\mathbf{r}))^* \psi_{[\mathbf{k}+\mathbf{b}]_{\text{BZ}}, n}(\mathbf{r}) d^3r. \quad (10.21)$$

By  $[\mathbf{k}]_{\text{BZ}}$  we denote the wave vector obtained from  $\mathbf{k}$  by subtracting the reciprocal lattice vector that moves  $\mathbf{k}$  into the first Brillouin zone, according to  $[\mathbf{k}]_{\text{BZ}} = \mathbf{k} - \mathbf{G}(\mathbf{k})$ .

Within FLAPW [130, 17], space is partitioned into the muffin-tin (MT) spheres centered around atoms  $\mu$  and the interstitial (INT) region. Consequently,  $M_{mn}^{(\mathbf{k}, \mathbf{b})}$  has contributions from both,

$$M_{mn}^{(\mathbf{k}, \mathbf{b})} = M_{mn}^{(\mathbf{k}, \mathbf{b})}|_{\text{INT}} + \sum_{\mu} M_{mn}^{(\mathbf{k}, \mathbf{b})}|_{\text{MT}^{\mu}}, \quad (10.22)$$

which will be discussed separately in the following. The treatment of the vacuum regions occurring in film and one-dimensional setups is discussed in the sections 10.2.4 and 10.2.5, respectively.

Inside the muffin-tin, the BF is expanded into spherical harmonics, radial basis functions  $u_l$ , which are solutions of the scalar relativistic equation at band-averaged energies, and the energy derivatives  $\dot{u}_l$  of the  $u_l$ :

$$\psi_{\mathbf{k}m}(\mathbf{r})|_{\text{MT}^{\mu}} = \sum_L [A_{L,m}^{\mu}(\mathbf{k})u_l^{\mu}(r') + B_{L,m}^{\mu}(\mathbf{k})\dot{u}_l^{\mu}(r')] Y_L(\hat{\mathbf{r}}'), \quad (10.23)$$

where atom  $\mu$  is located at  $\boldsymbol{\tau}_{\mu}$  and  $\mathbf{r}' = \mathbf{r} - \boldsymbol{\tau}_{\mu}$ . Here,  $m$  is the band-index and  $L = (l, l_z)$  stands for the angular momentum quantum numbers  $l$  and  $l_z$ . The case where the LAPW basis is supplemented with local orbitals is treated in section 10.2.2. Using the Rayleigh plane wave expansion

$$e^{-i\mathbf{b}\cdot\mathbf{r}} = 4\pi e^{-i\mathbf{b}\cdot\boldsymbol{\tau}_{\mu}} \sum_L (-1)^l i^l j_l(r'b) Y_L(\hat{\mathbf{b}}) Y_L^*(\hat{\mathbf{r}}'), \quad (10.24)$$

the contribution  $M_{mn}^{(\mathbf{k}, \mathbf{b})}|_{\text{MT}^{\mu}}$  of the muffin-tin region of atom  $\mu$  to the  $M_{mn}^{(\mathbf{k}, \mathbf{b})}$  matrix reads:

$$\begin{aligned} M_{mn}^{(\mathbf{k}, \mathbf{b})}|_{\text{MT}^{\mu}} = 4\pi e^{-i\mathbf{b}\cdot\boldsymbol{\tau}_{\mu}} \sum_{L, L'} [ & (A_{L,m}^{\mu}(\mathbf{k}))^* A_{L',n}^{\mu}([\mathbf{k} + \mathbf{b}]_{\text{BZ}}) t_{11}^{\mu}(\mathbf{b}, L, L') + \\ & + (A_{L,m}^{\mu}(\mathbf{k}))^* B_{L',n}^{\mu}([\mathbf{k} + \mathbf{b}]_{\text{BZ}}) t_{12}^{\mu}(\mathbf{b}, L, L') + \\ & + (B_{L,m}^{\mu}(\mathbf{k}))^* A_{L',n}^{\mu}([\mathbf{k} + \mathbf{b}]_{\text{BZ}}) t_{21}^{\mu}(\mathbf{b}, L, L') + \\ & + (B_{L,m}^{\mu}(\mathbf{k}))^* B_{L',n}^{\mu}([\mathbf{k} + \mathbf{b}]_{\text{BZ}}) t_{22}^{\mu}(\mathbf{b}, L, L') ]. \end{aligned} \quad (10.25)$$

The matrix elements  $t_{11}^\mu(\mathbf{b}, L'', L)$  and  $t_{12}^\mu(\mathbf{b}, L'', L)$  are given by the sums over radial integrals

$$\begin{aligned} t_{11}^\mu(\mathbf{b}, L'', L) &= \sum_{L'} G_{ll'l''}^{mm'm''}(\hat{\mathbf{b}}) \int r^2 j_{l'}(rb) u_l^\mu(r) u_{l''}^\mu(r) dr, \\ t_{12}^\mu(\mathbf{b}, L'', L) &= \sum_{L'} G_{ll'l''}^{mm'm''}(\hat{\mathbf{b}}) \int r^2 j_{l'}(rb) \dot{u}_l^\mu(r) u_{l''}^\mu(r) dr, \end{aligned} \quad (10.26)$$

and analogously for  $t_{21}^\mu$  and  $t_{22}^\mu$ , where

$$G_{ll'l''}^{mm'm''}(\hat{\mathbf{b}}) = G_{ll'l''}^{mm'm''} i^{l'} (-1)^{l'} Y_{L'}(\hat{\mathbf{b}}), \quad (10.27)$$

with the Gaunt coefficients

$$G_{ll'l''}^{mm'm''} = \int Y_{lm}(\hat{\mathbf{r}}) Y_{l'm'}^*(\hat{\mathbf{r}}) Y_{l''m''}^*(\hat{\mathbf{r}}) d\Omega. \quad (10.28)$$

The properties of the Gaunt coefficients are discussed in appendix A.

The quantities defined in Eq. (10.26) depend on the vectors  $\mathbf{b}$  joining a given  $k$ -point to its nearest neighbors. As a uniform  $k$ -mesh is used the set of  $\mathbf{b}$  vectors and hence also the integrals defined in Eq. (10.26) are independent of the  $k$ -point. Thus, the quantities Eq. (10.26) have to be calculated only once.

Employing the expansion of the BF in the interstitial region

$$\psi_{\mathbf{k}m}(\mathbf{r}) = \frac{1}{\sqrt{V}} \sum_{\mathbf{G}} c_{\mathbf{k}m}(\mathbf{G}) e^{i(\mathbf{k}+\mathbf{G})\cdot\mathbf{r}}, \quad (10.29)$$

the INT contribution to the  $M_{mn}^{(\mathbf{k},\mathbf{b})}$  matrix is deduced:

$$M_{mn}^{(\mathbf{k},\mathbf{b})}|_{\text{INT}} = \frac{1}{V} \sum_{\mathbf{G},\mathbf{G}'} (c_{\mathbf{k},m}(\mathbf{G}))^* c_{[\mathbf{k}+\mathbf{b}]_{\text{BZ}},n}(\mathbf{G}') \int_{\text{INT}} e^{i([\mathbf{k}+\mathbf{b}]_{\text{BZ},n}+\mathbf{G}')\cdot\mathbf{r}} e^{-i(\mathbf{k}+\mathbf{G})\cdot\mathbf{r}} e^{-i\mathbf{b}\cdot\mathbf{r}} d^3x, \quad (10.30)$$

where the integration stretches over the interstitial only. Introducing the step function  $\Theta(\mathbf{r})$  that cuts out the muffin tins and its Fourier transform  $\Theta_{\mathbf{G}}$ , Eq. (10.30) can be cast into the final form

$$M_{mn}^{(\mathbf{k},\mathbf{b})}|_{\text{INT}} = \sum_{\mathbf{G},\mathbf{G}'} (c_{\mathbf{k},m}(\mathbf{G}))^* c_{[\mathbf{k}+\mathbf{b}]_{\text{BZ}},n}(\mathbf{G}') \Theta_{\mathbf{G}(\mathbf{k}+\mathbf{b})+\mathbf{G}-\mathbf{G}'}, \quad (10.31)$$

where  $\mathbf{G}(\mathbf{k}+\mathbf{b})$  denotes the reciprocal space vector that moves  $(\mathbf{k}+\mathbf{b})$  into the first Brillouin zone,  $[\mathbf{k}+\mathbf{b}]_{\text{BZ}} = \mathbf{k}+\mathbf{b} - \mathbf{G}(\mathbf{k}+\mathbf{b})$ .

### 10.2.2 Local orbital contributions to the $M_{mn}^{(\mathbf{k},\mathbf{b})}$ matrix

In order to increase the variational freedom of the FLAPW-basis or to describe semicore levels adequately, it may be supplemented by local orbitals [33]. In this case the expressions for the BFs in the spheres are modified:

$$\psi_{\mathbf{k}m}(\mathbf{r})|_{\text{MT}^\mu} = \sum_L (A_{L,m}^\mu(\mathbf{k}) u_l^\mu(r) + B_{L,m}^\mu(\mathbf{k}) \dot{u}_l^\mu(r)) Y_L(\hat{\mathbf{r}}) + \sum_{Lo} C_{Lo,m}^\mu(\mathbf{k}) u_{lo}^\mu(r) Y_{Lo}(\hat{\mathbf{r}}), \quad (10.32)$$

where  $Lo = (lo, mo)$  stands for the corresponding values of the angular quantum numbers  $(l, m)$  assigned to each local orbital. Due to the local orbitals, additional terms arise in the expression Eq. 10.25 for the  $M_{mn}^{(\mathbf{k}, \mathbf{b})}|_{\text{MT}^\mu}$  matrix:

$$\begin{aligned}
M_{mn}^{(\mathbf{k}, \mathbf{b})}|_{\text{MT}^\mu}^{Lo} &= 4\pi e^{-i\mathbf{b} \cdot \boldsymbol{\tau}_\mu} \times \\
&\times \left( \sum_{L, Lo'} (A_{L,m}^\mu(\mathbf{k}))^* C_{Lo',m}^\mu([\mathbf{k} + \mathbf{b}]) t_{11}^\mu(\mathbf{b}, L, Lo') + \right. \\
&+ \sum_{L, Lo'} (B_{L,m}^\mu(\mathbf{k}))^* C_{Lo',m}^\mu([\mathbf{k} + \mathbf{b}]) t_{21}^\mu(\mathbf{b}, L, Lo') + \\
&+ \sum_{Lo, L'} (C_{Lo,m}^\mu(\mathbf{k}))^* A_{L',m}^\mu([\mathbf{k} + \mathbf{b}]) t_{11}^\mu(\mathbf{b}, Lo, L') + \\
&+ \sum_{Lo, L'} (C_{Lo,m}^\mu(\mathbf{k}))^* B_{L',m}^\mu([\mathbf{k} + \mathbf{b}]) t_{12}^\mu(\mathbf{b}, Lo, L') + \\
&\left. + \sum_{Lo, Lo'} (C_{Lo,m}^\mu(\mathbf{k}))^* C_{Lo',m}^\mu([\mathbf{k} + \mathbf{b}]) t_{11}^\mu(\mathbf{b}, Lo, Lo') \right), \tag{10.33}
\end{aligned}$$

where the corresponding radial function for the local orbital is taken in the  $t_{ij}^\mu$ -integrals, whenever a radial function  $u$  has an index  $lo$ .

### 10.2.3 Calculation of $A_{mn}^{(\mathbf{k})}$ within the FLAPW formalism

For the localized orbitals  $|g_n\rangle$  required to determine the first-guess WFs, we mostly use functions that are zero everywhere in space except in the muffin-tin sphere of that atom, to which the resulting WF is attributed in this sense. In practice, this works not only for WFs that are atom-centered but also for bond-centered ones. Thus,  $g_n(\mathbf{r})$  is given by

$$g_n(\mathbf{r}) = \sum_L c_{n,L} \tilde{u}_l(r') Y_L(\hat{\mathbf{r}}'), \tag{10.34}$$

where  $\mathbf{r}' = \mathbf{r} - \boldsymbol{\tau}_\mu$  is the position relative to the center of the atom, to which the first-guess WF is attributed, and the coefficients  $c_{n,L}$  control the angular distribution of  $g_n(\mathbf{r})$ . For the radial part  $\tilde{u}_l(r)$  of the localized orbital we use the solution  $u_l^\mu(r)$  of the radial scalar relativistic equation for the actual potential obtained from the first-principles calculation at an energy corresponding to the bands from which the WF is constructed. It is also possible to use Gaussians [19], or the radial parts of hydrogenic wave functions for  $\tilde{u}_l(r)$ . Where angular momentum is concerned in Eq. (10.34), contributions of different angular momenta have to be summed in the general case to allow the definition of hybrids such as  $sp^3$  orbitals, while there is only an  $l = 2$  contribution for WFs corresponding to  $d$  orbitals, for example.

For a general radial part  $\tilde{u}_l(r)$  the projection of the localized orbital  $|g_n\rangle$  onto the BF is given by

$$A_{mn}^{(\mathbf{k})} = \sum_L c_{n,L} [(a_{L,m}^\mu(\mathbf{k}))^* \int u_l^\mu(r) \tilde{u}_l(r) r^2 dr + (b_{L,m}^\mu(\mathbf{k}))^* \int \dot{u}_l^\mu(r) \tilde{u}_l(r) r^2 dr], \tag{10.35}$$

where the expansion of the BF given in Eq. (10.23) was used. Choosing  $\tilde{u}_l(r) = u_l^\mu(r)$  Eq. (10.35) simplifies as follows:

$$A_{mn}^{(\mathbf{k})} = \langle \psi_{\mathbf{k}m} | g_n \rangle = \sum_L c_{n,L} (a_{L,m}^\mu(\mathbf{k}))^*. \quad (10.36)$$

In order to construct better first guesses for bond-centered WFs  $|g_n\rangle$  may also be constructed as a linear combination of two localized orbitals - one orbital for each atom participating in the bond. An example for this will be given in section 10.8.3 on graphene.

#### 10.2.4 The $M_{mn}^{(\mathbf{k},\mathbf{b})}$ matrix in case of film calculations

In case of the film implementation of the FLAPW method, an additional semi-infinite vacuum region is present, which results in an additional contribution to the wave function overlaps  $M_{mn}^{(\mathbf{k},\mathbf{b})}|_{\text{VAC}}$ . In the following we give explicit expressions for the vacuum contributions to the  $M_{mn}^{(\mathbf{k},\mathbf{b})}$  matrix elements.

In the film geometry, the interstitial region stretches in  $z$ -direction from  $-D/2$  to  $D/2$ , which is chosen to be the direction orthogonal to the film. Thus, one of the two vacua extends from  $-\infty$  to  $-D/2$  while the second vacuum extends from  $D/2$  to  $+\infty$ . The two vacua are treated analogously and we will restrict the discussion to the vacuum between  $D/2$  and  $+\infty$ . According to the topology of the vacuum region, the Bloch wave functions are represented there in the following way:

$$\psi_{\mathbf{k}m}(\mathbf{r})|_{\text{VAC}} = \sum_{\mathbf{G}_\parallel} \Psi_{\mathbf{G}_\parallel}^m(\mathbf{k}_\parallel, z) e^{i(\mathbf{G}_\parallel + \mathbf{k}_\parallel) \cdot \mathbf{r}_\parallel}, \quad (10.37)$$

with

$$\Psi_{\mathbf{G}_\parallel}^m(\mathbf{k}_\parallel, z) = A_{\mathbf{G}_\parallel}^m(\mathbf{k}_\parallel) u_{\mathbf{G}_\parallel}^{\mathbf{k}_\parallel}(z) + B_{\mathbf{G}_\parallel}^m(\mathbf{k}_\parallel) \dot{u}_{\mathbf{G}_\parallel}^{\mathbf{k}_\parallel}(z), \quad (10.38)$$

where  $\mathbf{G} = (\mathbf{G}_\parallel, G_z)$  and  $\mathbf{r} = (\mathbf{r}_\parallel, z)$  have been used, with  $\mathbf{G}_\parallel$  and  $\mathbf{r}_\parallel$  the in-plane components. The  $k$ -point  $\mathbf{k}_\parallel$  belongs to the two-dimensional BZ.  $u_{\mathbf{G}_\parallel}^{\mathbf{k}_\parallel}(z)$  and  $\dot{u}_{\mathbf{G}_\parallel}^{\mathbf{k}_\parallel}(z)$  are the solution of the one-dimensional Schrödinger equation in the vacuum and its energy derivative, respectively. Substituting Eq. 10.37 into Eq. 10.21 yields:

$$M_{mn}^{(\mathbf{k}_\parallel, \mathbf{b})} = \sum_{\mathbf{G}_\parallel} \sum_{\mathbf{G}'_\parallel} \int_{\text{VAC}} e^{i\mathbf{G} \cdot \mathbf{x}} (\Psi_{\mathbf{G}_\parallel}^m(\mathbf{k}_\parallel, z))^* \Psi_{\mathbf{G}'_\parallel}^n([\mathbf{k}_\parallel + \mathbf{b}], z) d^3r \quad (10.39)$$

with  $\mathbf{G} = \mathbf{G}'_\parallel - \mathbf{G}_\parallel - \mathbf{G}(\mathbf{k}_\parallel + \mathbf{b})$ . While vectors  $\mathbf{k}_\parallel$  and  $[\mathbf{k}_\parallel + \mathbf{b}]$  always lie in the two-dimensional Brillouin zone, the  $\mathbf{b}$  and  $\mathbf{G}(\mathbf{k}_\parallel + \mathbf{b})$  vectors have a  $z$ -component in general, which leads to the following expression for the  $M_{mn}^{(\mathbf{k}_\parallel, \mathbf{b})}$  matrix elements:

$$M_{mn}^{(\mathbf{k}_\parallel, \mathbf{b})} = \sum_{\mathbf{G}_\parallel, \mathbf{G}'_\parallel} S_{\parallel} \delta_{\mathbf{G}_\parallel} \int_{D/2}^{\infty} e^{-iG_z(\mathbf{k}_\parallel + \mathbf{b})z} (\Psi_{\mathbf{G}_\parallel}^m(\mathbf{k}_\parallel, z))^* \Psi_{\mathbf{G}'_\parallel}^n([\mathbf{k}_\parallel + \mathbf{b}], z) dz, \quad (10.40)$$

where  $S_{\parallel}$  is the in-plane unit-cell area and the last integral is a linear combination of one-dimensional integrals of the form

$$\begin{aligned} & \int_{D/2}^{\infty} e^{-i G_z(\mathbf{k}_{\parallel} + \mathbf{b})z} u_{\mathbf{G}_{\parallel}}^{\mathbf{k}_{\parallel}}(z) u_{\mathbf{G}'_{\parallel}}^{[\mathbf{k}_{\parallel} + \mathbf{b}]}(z) dz, \\ & \int_{D/2}^{\infty} e^{-i G_z(\mathbf{k}_{\parallel} + \mathbf{b})z} u_{\mathbf{G}_{\parallel}}^{\mathbf{k}_{\parallel}}(z) \dot{u}_{\mathbf{G}'_{\parallel}}^{[\mathbf{k}_{\parallel} + \mathbf{b}]}(z) dz, \end{aligned} \quad (10.41)$$

which are easily computed numerically for every pair of  $(\mathbf{G}_{\parallel}, \mathbf{G}'_{\parallel})$ .

### 10.2.5 The $M_{mn}^{(\mathbf{k}, \mathbf{b})}$ matrix in case of one dimensional calculations

In the case of the one-dimensional setup the vacuum region surrounds a cylinder with the symmetry axis along the  $z$ -direction and radius  $R_{\text{vac}}$ . The wave function in the vacuum is represented in the following form (in the 1D case the Bloch vector is  $\mathbf{k} = (0, 0, k_z)$ ):

$$\psi_{k_z m}(\mathbf{r}) = \sum_{G_z, p} (A_{p, G_z}^{m, k_z} u_p^{G_z}(k_z, r) + B_{p, G_z}^{m, k_z} \dot{u}_p^{G_z}(k_z, r)) e^{ip\varphi} e^{i(G_z + k_z)z}, \quad (10.42)$$

where  $\mathbf{r} = (z, r, \varphi)$  in cylindrical coordinates,  $G_z$  is the  $z$ -component of the reciprocal vector  $\mathbf{G}$ , and  $p$  is an integer number labeling a cylindrical angular harmonic. The exponentially decaying functions  $u$  and  $\dot{u}$  are the solutions of the radial equation for the vacuum and its energy derivative, respectively. Taking into account the expansion of a plane wave in cylindrical coordinates

$$e^{i\mathbf{G}\mathbf{r}} = e^{iG_z z} \sum_p i^p e^{ip(\varphi - \varphi_{\mathbf{G}})} J_p(G_r r), \quad (10.43)$$

with  $\varphi_{\mathbf{G}}$  and  $G_r$  being cylindrical angular and radial coordinates, respectively, of the vector  $\mathbf{G} = (G_z, G_r, \varphi_{\mathbf{G}})$  in reciprocal space, and  $J_p$  standing for the cylindrical Bessel function of order  $p$ , the 1D-vacuum contribution to the  $M_{mn}^{(k_z, \mathbf{b})}$  matrix reads:

$$\begin{aligned} M_{mn}^{(k_z, \mathbf{b})}|_{\text{VAC}} &= \int_{\text{VAC}} e^{-i\mathbf{b}\cdot\mathbf{r}} (\psi_{k_z m}(\mathbf{r}))^* \psi_{[k_z + \mathbf{b}], n}(\mathbf{r}) d^3r \\ &= \sum_{G_z, G'_z} \sum_{p, p'} \int_{\text{VAC}} e^{i(G'_z - G_z - G_z(k_z + \mathbf{b}))z} \times \\ &\times e^{-i\mathbf{G}_{\parallel}(k_z + \mathbf{b})\cdot\mathbf{r}_{\parallel}} e^{i(p' - p)\varphi} \Psi_{p, p', G'_z}^{m, n, G_z}(k_z, [k_z + \mathbf{b}], r) d^3x, \end{aligned} \quad (10.44)$$

where in analogy to the case of the film geometry, vectors  $\mathbf{b}$  and  $\mathbf{G}(k_z + \mathbf{b})$  may have a non-zero component in the plane normal to the  $z$ -axis, and the function  $\Psi$  is constructed from the products of the  $u$ - and  $\dot{u}$ -functions with corresponding  $A$ - and  $B$ -coefficients at  $k$ -points  $k_z$  and  $[k_z + \mathbf{b}]$ . Introducing the vector  $\mathcal{G} = G'_z - G_z - G_z(k_z + \mathbf{b})$  the expression

for the  $M_{mn}^{(k_z, \mathbf{b})}$  can be reduced to

$$M_{mn}^{(k_z, \mathbf{b})}|_{\text{VAC}} = \sum_{G_z, G'_z} \sum_{p, p'} \mathcal{S} \cdot \delta_{\mathcal{G}} \cdot i^{p-p'} e^{-i(p-p')\varphi_{\mathbf{G}}(k_z + \mathbf{b})} \times \\ \times \int_{R_{\text{vac}}}^{\infty} r J_{p'-p}(G_r(k_z + \mathbf{b})r) \Psi_{p, p', G'_z}^{m, n, G_z}(k_z, [k_z + \mathbf{b}], r) dr, \quad (10.45)$$

with  $\mathcal{S} = 2\pi T$ , and  $T$  standing for the lattice constant of the system under consideration along the  $z$ -axis.

## 10.3 Wannier Representation of the Hamiltonian

Formulating the Hamiltonian in terms of WFs is a particularly useful starting point when effects of correlation [23, 129, 22] are studied within DMFT. Furthermore, the hopping integrals – along with the MLWFs' spreads, centers and shapes – provide intuitive insight into the electronic structure.

Written in terms of BFs the Hamiltonian  $\hat{H}$  assumes the diagonal form

$$\hat{H} = \frac{1}{N} \sum_{\mathbf{k}, n} \epsilon_n(\mathbf{k}) |\psi_{\mathbf{k}n}\rangle \langle \psi_{\mathbf{k}n}|, \quad (10.46)$$

where  $\epsilon_n(\mathbf{k})$  stands for the eigenvalues of  $\hat{H}$ . If the number of bands is equal to the number of MLWFs extracted the  $U_{mn}^{(\mathbf{k})}$ -matrices in Eq. (10.8) are unitary. In this case we arrive at the equivalent form of the Hamiltonian

$$\hat{H} = \sum_{\mathbf{R}_1 m} \sum_{\mathbf{R}_2 m'} H_{m, m'}(\mathbf{R}_1 - \mathbf{R}_2) |W_{\mathbf{R}_1 m}\rangle \langle W_{\mathbf{R}_2 m'}|, \quad (10.47)$$

where

$$H_{m, m'}(\mathbf{R}_1 - \mathbf{R}_2) = \frac{1}{N} \sum_{\mathbf{k}n} \epsilon_n(\mathbf{k}) \langle W_{\mathbf{R}_1 m} | \psi_{\mathbf{k}n} \rangle \langle \psi_{\mathbf{k}n} | W_{\mathbf{R}_2 m'} \rangle \\ = \frac{1}{N} \sum_{\mathbf{k}n} \epsilon_n(\mathbf{k}) e^{i\mathbf{k} \cdot (\mathbf{R}_1 - \mathbf{R}_2)} (U_{nm}^{(\mathbf{k})})^* U_{nm'}^{(\mathbf{k})}. \quad (10.48)$$

The hopping integrals  $H_{m, m'}(\mathbf{R}_1 - \mathbf{R}_2)$  quantify the hopping of electrons from Wannier orbital  $|W_{\mathbf{R}_2 m'}\rangle$  into Wannier orbital  $|W_{\mathbf{R}_1 m}\rangle$ .

Using Eq. (10.47) we may obtain interpolated Kohn-Sham eigenvalues  $\epsilon_n(\mathbf{k})$  at  $k$ -points not included in the set of  $k$ -points used for the construction of the Wannier functions. For this purpose we define the Bloch-like functions

$$|\tilde{\psi}_{\mathbf{k}n}\rangle = \frac{1}{\sqrt{N}} \sum_{\mathbf{R}} e^{i\mathbf{R} \cdot \mathbf{k}} |W_{\mathbf{R}, n}\rangle. \quad (10.49)$$

The matrix elements of the Hamiltonian operator with respect to the Bloch-like functions at  $k$ -point  $\mathbf{k}$  are:

$$H_{m,m'}^{\mathbf{k}} = \frac{1}{N} \sum_{\mathbf{R}_1, \mathbf{R}_2} H_{m,m'}(\mathbf{R}_1 - \mathbf{R}_2) e^{-i(\mathbf{R}_1 - \mathbf{R}_2) \cdot \mathbf{k}} = \sum_{\mathbf{R}} H_{m,m'}(\mathbf{R}) e^{-i\mathbf{R} \cdot \mathbf{k}}. \quad (10.50)$$

Diagonalization of  $H_{m,m'}^{\mathbf{k}}$  yields the sought interpolated eigenvalues  $\epsilon_n(\mathbf{k})$ . If the original  $k$ -mesh used for the construction of Wannier functions is fine enough, e.g. an  $8 \times 8 \times 8$  mesh, the interpolation is very precise. At the same time, the interpolation is very efficient, because the size of the square matrix  $\mathbf{H}^{\mathbf{k}}$  is small compared to the size of the full FLAPW-Hamiltonian at that  $k$ -point. Thus, the Fermi surface may be interpolated very efficiently using this Wannier-interpolation scheme. Similar interpolation schemes may be set up also for operators other than the Hamiltonian [131, 132, 133].

## 10.4 Spin-orbit coupling

In the case of spin-orbit coupling Eq. (10.21) assumes the form

$$M_{mn}^{\mathbf{k}, \mathbf{b}} = \sum_{\sigma} \int e^{-i\mathbf{b} \cdot \mathbf{r}} (\psi_{\mathbf{k}m\sigma}(\mathbf{r}))^* \psi_{[\mathbf{k}+\mathbf{b}],n\sigma}(\mathbf{r}) d^3r, \quad (10.51)$$

where  $\psi_{\mathbf{k}m\sigma}(\mathbf{r})$  is the BF with lattice vector  $\mathbf{k}$ , band index  $n$ , and spin index  $\sigma$ . The spin index  $\sigma$  refers to the eigenstates of the projection of the spin-operator onto the spin-quantization axis. Likewise Eq. (10.35) has to be changed into

$$\begin{aligned} A_{mn}^{(\mathbf{k})} = & \sum_L \sum_{\sigma} c_{nL\sigma} [(a_{Lm\sigma}^{\mu}(\mathbf{k}))^* \int u_{l,\sigma}^{\mu}(r) \tilde{u}_{l,\sigma}(r) r^2 dr \\ & + (b_{Lm\sigma}^{\mu}(\mathbf{k}))^* \int \dot{u}_{l,\sigma}^{\mu}(r) \tilde{u}_{l,\sigma}(r) r^2 dr]. \end{aligned} \quad (10.52)$$

In the regime from weak to modest spin-orbit coupling it is reasonable to choose the localized orbitals  $|g_n\rangle$  to be eigenstates of the projection of the spin-operator onto the spin-quantization axis. This means that for given  $n$   $c_{nL\sigma}$  may differ from zero only for one spin component  $\sigma$ .

Eq. (10.47) remains valid in the case of spin-orbit coupling, but the matrix elements  $H_{m,m'}(\mathbf{R}_1 - \mathbf{R}_2)$  in Eq. (10.47) correspond to hopping between spinor-valued Wannier orbitals then, where the two spin-components are given by

$$|W_{\mathbf{R}m\sigma}\rangle = |\sigma\rangle \langle \sigma | W_{\mathbf{R}m}\rangle, \quad \sigma = \uparrow, \downarrow. \quad (10.53)$$

Alternatively, the hopping matrix elements may be decomposed according to the spin-channels:

$$\begin{aligned} H_{mm'}^{\sigma\sigma'}(\mathbf{R}_1 - \mathbf{R}_2) &= \frac{1}{N} \sum_{\mathbf{k}n} \epsilon_n(\mathbf{k}) \langle W_{\mathbf{R}_1m\sigma} | \Psi_{\mathbf{k}n} \rangle \langle \Psi_{\mathbf{k}n} | W_{\mathbf{R}_2m'\sigma'} \rangle \\ &= \frac{1}{N} \sum_{\mathbf{k}n} \sum_{n'n''} \epsilon_n(\mathbf{k}) e^{i\mathbf{k} \cdot (\mathbf{R}_1 - \mathbf{R}_2)} (U_{n''m}^{(\mathbf{k})})^* O_{n''n\sigma}^{(\mathbf{k})} O_{nn'\sigma'}^{(\mathbf{k})} U_{n'm'}^{(\mathbf{k})}, \end{aligned} \quad (10.54)$$



where the overlap  $\langle \Psi_{\mathbf{k}n\sigma} | \Psi_{\mathbf{k}n'\sigma} \rangle$  is denoted  $O_{nn'\sigma}^{(\mathbf{k})}$ . The corresponding real-space representation of the Hamiltonian is given by

$$\hat{H} = \sum_{\mathbf{R}_1 m} \sum_{\mathbf{R}_2 m'} \sum_{\sigma, \sigma'} H_{m, m'}^{\sigma, \sigma'}(\mathbf{R}_1 - \mathbf{R}_2) |W_{\mathbf{R}_1 m \sigma}\rangle \langle W_{\mathbf{R}_2 m' \sigma'}|. \quad (10.55)$$

Compared with Eq. (10.48) the decomposition Eq. (10.54) of the hopping matrix elements into spin-channels gives further insight into how the spin-channels are coupled.

The angular characters of the spin-orbit induced corrections can be understood easily, by applying the  $\hat{\mathbf{L}} \cdot \hat{\mathbf{S}}$  operator on the MLWFs that one would obtain in a calculation without spin-orbit coupling. It is convenient to make use of the identity

$$\hat{\mathbf{L}} \cdot \hat{\mathbf{S}} = \hat{L}_z \hat{S}_z + \frac{1}{2} [\hat{L}_+ \hat{S}_- + \hat{L}_- \hat{S}_+]. \quad (10.56)$$

As a detailed example we consider the effect of  $\hat{\mathbf{L}} \cdot \hat{\mathbf{S}}$  on  $|d_{xy}\rangle | \uparrow \rangle$ :

$$\begin{aligned} \hat{L}_z \hat{S}_z |d_{xy}\rangle | \uparrow \rangle &= -i |d_{x^2-y^2}\rangle | \uparrow \rangle \\ \frac{1}{2} \hat{L}_+ \hat{S}_- |d_{xy}\rangle | \uparrow \rangle &= \frac{i}{\sqrt{2}} |Y_{2,-1}\rangle | \downarrow \rangle \\ &= -\frac{i}{2} |d_{xz}\rangle | \downarrow \rangle - \frac{1}{2} |d_{yz}\rangle | \downarrow \rangle \end{aligned} \quad (10.57)$$

Hence, the resulting idealized MLWF has an up-component the real part of which is  $d_{xy}$  and the imaginary part of which is  $-d_{x^2-y^2}$ . The real part of the down-component is  $-\frac{1}{2}d_{yz}$  while the imaginary part of the down-component is given by  $-\frac{1}{2}d_{xz}$ . In Table 10.1 we list the results for various angular functions for later reference in the results section. By

$$d_{3y^2-r^2} = -\frac{1}{2}d_{3z^2-r^2} - \frac{1}{2}\sqrt{3}d_{x^2-y^2} \quad (10.58)$$

and

$$d_{x^2-z^2} = \frac{1}{2}d_{x^2-y^2} - \frac{1}{2}\sqrt{3}d_{3z^2-r^2} \quad (10.59)$$

we denote the angular functions obtained by rotating  $d_{3z^2-r^2}$  and  $d_{x^2-y^2}$  around the  $x$ -axis by an angle of  $\frac{\pi}{2}$ , respectively.

For later reference we consider the example of the Wannier orbital  $d_{xy} | \uparrow \rangle_{\text{sqa}}$ , which is an eigenstate of the projection of the spin operator onto the spin-quantization axis. If the spin-quantization axis does not coincide with the  $z$ -direction, a transformation from the states  $|\sigma\rangle_{\text{sqa}}$  to the basis of eigenstates of the  $z$ -component of the spin-operator is required before Eq. (10.56) can be applied. For a general spin-quantization axis specified in terms of angles  $\theta$  and  $\phi$  the transformation matrix is given by:

$$\begin{pmatrix} \cos\left(\frac{\theta}{2}\right) e^{-i\frac{\phi}{2}} & \sin\left(\frac{\theta}{2}\right) e^{-i\frac{\phi}{2}} \\ \sin\left(\frac{\theta}{2}\right) e^{i\frac{\phi}{2}} & -\cos\left(\frac{\theta}{2}\right) e^{i\frac{\phi}{2}} \end{pmatrix} \quad (10.60)$$

Table 10.1: Angular part of idealized spin-orbit coupled MLWFs. Columns 2,3 and 4: Components of the angular function obtained by applying  $\hat{\mathbf{L}} \cdot \hat{\mathbf{S}}$  to the angular function in column 1.

$\uparrow$ , real part	$\uparrow$ , imaginary part	$\downarrow$ , real part	$\downarrow$ , imaginary part
$d_{xy}$	$-d_{x^2-y^2}$	$-\frac{1}{2}d_{yz}$	$-\frac{1}{2}d_{xz}$
$d_{xz}$	$\frac{1}{2}d_{yz}$	$d_{x^2-z^2}$	$\frac{1}{2}d_{xy}$
$d_{3y^2-r^2}$	$-\frac{1}{2}\sqrt{3}d_{xy}$	0.0	$-\frac{1}{2}\sqrt{3}d_{yz}$
$p_z$	0.0	$\frac{1}{2}p_x$	$\frac{1}{2}p_y$

After application of Eq. (10.56) the states are transformed back to the original basis. We give the result for the spin-quantization axis pointing in  $[111]$ -direction:

$$\begin{aligned}
& \hat{L}_z \hat{S}_z d_{xy} | \uparrow \rangle_{\text{sqa}} \\
&= -\frac{i}{\sqrt{3}} d_{x^2-y^2} | \uparrow \rangle_{\text{sqa}} - i \sqrt{\frac{2}{3}} d_{x^2-y^2} | \downarrow \rangle_{\text{sqa}} \\
& \frac{1}{2} [\hat{L}_+ \hat{S}_- + \hat{L}_- \hat{S}_+] d_{xy} | \uparrow \rangle_{\text{sqa}} \\
&= \frac{i}{2} \sqrt{\frac{1}{3}} [d_{yz} - d_{xz}] | \uparrow \rangle_{\text{sqa}} + \frac{\sqrt{2}}{4} [d_{yz} + d_{xz}] | \downarrow \rangle_{\text{sqa}} \\
&+ i \frac{\sqrt{6}}{12} [d_{xz} - d_{yz}] | \downarrow \rangle_{\text{sqa}}.
\end{aligned} \tag{10.61}$$

## 10.5 Use of symmetry in Wannier function calculations

In order to construct Wannier functions from a given set of Bloch functions according to the prescription Eq. (10.8) the Bloch functions of the entire Brillouin zone are needed. This applies to the maximally localized Wannier functions, for which both the  $A_{mn}^{(\mathbf{k})}$  and the  $M_{mn}^{(\mathbf{k}, \mathbf{b})}$  matrices are required, as well as to the first-guess Wannier functions, for which only  $A_{mn}^{(\mathbf{k})}$  has to be computed. To increase computational efficiency, one may first calculate the Bloch functions only for the irreducible part of the Brillouin zone and obtain the remaining Bloch functions by applying the symmetry transformations. By definition the symmetry operations leave the Kohn-Sham potential  $V(\mathbf{r})$  and the Hamilton operator  $\hat{H}$  unchanged:

$$V(\mathbf{R}_i \mathbf{r} + \mathbf{t}_i) = V(\mathbf{r}), \tag{10.62}$$

where  $i$  labels the symmetry operations,  $\mathbf{R}_i$  is the rotation matrix of symmetry operation  $i$  and  $\mathbf{t}_i$  is the shift vector needed to describe non-symmorphic symmetry operations. The transformed wave function  $\tilde{\psi}(\mathbf{r})$  obtained from the Bloch function  $\psi_{\mathbf{k}m}(\mathbf{r})$  by application of the  $i$ -th symmetry,

$$\tilde{\psi}(\mathbf{r}) = \psi_{\mathbf{k}m}(\mathbf{R}_i \mathbf{r} + \mathbf{t}_i), \tag{10.63}$$

is a solution of the Kohn-Sham equations. Writing  $\psi_{\mathbf{k}m}(\mathbf{r})$  as an expansion in terms of plane-waves,

$$\psi_{\mathbf{k}m}(\mathbf{r}) = \sum_{\mathbf{G}} c_{\mathbf{k},m}(\mathbf{G}) e^{i(\mathbf{k}+\mathbf{G})\cdot\mathbf{r}}, \quad (10.64)$$

we identify  $\tilde{\psi}(\mathbf{r})$  as a Bloch function at  $k$ -point  $\mathbf{k}' = \mathbf{R}_i^T \mathbf{k}$ :

$$\begin{aligned} \psi_{\mathbf{k}m}(\mathbf{R}_i \mathbf{r} + \mathbf{t}_i) &= \sum_{\mathbf{G}} c_{\mathbf{k},m}(\mathbf{G}) e^{i(\mathbf{k}+\mathbf{G})\cdot(\mathbf{R}_i \mathbf{r} + \mathbf{t}_i)} \\ &= \sum_{\mathbf{G}} c_{\mathbf{k},m}(\mathbf{G}) e^{i(\mathbf{R}_i^T (\mathbf{k}+\mathbf{G}))\cdot(\mathbf{r} + \mathbf{R}_i^{-1} \mathbf{t}_i)}. \end{aligned} \quad (10.65)$$

For collinear systems in the absence of spin-orbit coupling one more symmetry that may be exploited is time-inversion symmetry. In this case the Kohn-Sham potential  $V(\mathbf{r})$  is scalar and real-valued. Consequently, the wave function

$$\tilde{\psi}(\mathbf{r}) = (\psi_{\mathbf{k},m}(\mathbf{r}))^* \quad (10.66)$$

is a solution of the Kohn-Sham equations, which one identifies as a Bloch function at  $k$ -point  $-\mathbf{k}$ :

$$(\psi_{\mathbf{k}m}(\mathbf{r}))^* = \sum_{\mathbf{G}} (c_{\mathbf{k},m}(\mathbf{G}))^* e^{-i(\mathbf{k}+\mathbf{G})\cdot\mathbf{r}}. \quad (10.67)$$

In practice, in order to obtain the Bloch functions at the  $k$ -point  $\mathbf{k}' = \mathbf{R}_i^T \mathbf{k}$ , we rotate the set  $\{\mathbf{G}\}_{\mathbf{k}}$  of reciprocal lattice vectors at  $k$ -point  $\mathbf{k}$  and incorporate the phase factors into the eigenvectors:

$$\begin{aligned} \mathbf{G} &\rightarrow \mathbf{R}_i^T \mathbf{G}, \\ c_{\mathbf{k},m}(\mathbf{G}) &\rightarrow c_{\mathbf{k},m}(\mathbf{G}) e^{i[\mathbf{R}_i^T (\mathbf{k}+\mathbf{G})]\cdot\mathbf{R}_i^{-1} \mathbf{t}_i}. \end{aligned} \quad (10.68)$$

As a consequence of Eq. (10.67), one may obtain the Bloch functions at  $k$ -point  $\mathbf{k}' = -\mathbf{R}_i^T \mathbf{k}$  from the Bloch functions at  $k$ -point  $\mathbf{k}$  in the case of a collinear calculation without spin-orbit coupling. However, if the system is inversion symmetric, the operation  $-\mathbf{R}_i$  is also a space-group symmetry and exploiting time-inversion does not lead to an additional reduction of the number of  $k$ -points in the irreducible part of the Brillouin zone. If the system is not inversion symmetric, the irreducible part of the Brillouin zone is given by the smallest set of  $k$ -points, from which the  $k$ -points of the entire Brillouin zone may be generated by applying the rotation matrices  $\mathbf{R}_i$  and  $-\mathbf{R}_i$ . If  $-\mathbf{R}_i^T$  is a symmetry operation which is composed of a spatial rotation and time inversion Eq. (10.68) needs to be modified:

$$\begin{aligned} \mathbf{G} &\rightarrow -\mathbf{R}_i^T \mathbf{G}, \\ c_{\mathbf{k},m}(\mathbf{G}) &\rightarrow (c_{\mathbf{k},m}(\mathbf{G}))^* e^{i[\mathbf{R}_i^T (\mathbf{k}+\mathbf{G})]\cdot\mathbf{R}_i^{-1} \mathbf{t}_i}. \end{aligned} \quad (10.69)$$

Clearly, the  $A_{mn}^{(\mathbf{k})}$  and the  $M_{mn}^{(\mathbf{k},\mathbf{b})}$  matrices themselves satisfy symmetry relations and consequently it is not necessary to generate all Bloch functions for the  $k$ -points outside the irreducible part of the Brillouin zone by applying the symmetry transformations to

the Bloch functions of the irreducible part. However, the calculation of  $A_{mn}^{(\mathbf{k})}$  is not computationally expensive and hence we generate the Bloch functions for all  $k$ -points in the Brillouin zone and compute  $A_{mn}^{(\mathbf{k})}$  at each  $k$ -point. As the calculation of the  $M_{m,n}^{(\mathbf{k},\mathbf{b})}$  matrix is time-demanding, we exploit its symmetry and calculate only the minimum number of matrix elements needed. We determine the minimal set of  $k$ -point pairs  $(\mathbf{k}, \mathbf{k} + \mathbf{b})$  from which all required  $k$ -point pairs may be generated by application of the transformation

$$(\mathbf{k}, \mathbf{k} + \mathbf{b}) \rightarrow (\mathbf{R}_i^T \mathbf{k}, \mathbf{R}_i^T (\mathbf{k} + \mathbf{b})). \quad (10.70)$$

The matrix element  $M_{m,n}^{(\mathbf{R}_i^T \mathbf{k}, \mathbf{R}_i^T \mathbf{b})}$  is then obtained from the matrix element  $M_{m,n}^{(\mathbf{k}, \mathbf{b})}$ :

$$\begin{aligned} M_{m,n}^{(\mathbf{R}_i^T \mathbf{k}, \mathbf{R}_i^T \mathbf{b})} &= \int e^{-i\mathbf{R}_i^T \mathbf{b} \cdot \mathbf{r}} (\psi_{\mathbf{R}_i^T \mathbf{k}m}(\mathbf{r}))^* \psi_{[\mathbf{R}_i^T \mathbf{k} + \mathbf{R}_i^T \mathbf{b}],n}(\mathbf{r}) d^3r \\ &= \int e^{-i\mathbf{b} \cdot (\mathbf{R}_i \mathbf{r} + \mathbf{t}_i)} (\psi_{\mathbf{k}m}(\mathbf{R}_i \mathbf{r} + \mathbf{t}_i))^* \psi_{[\mathbf{k} + \mathbf{b}],n}(\mathbf{R}_i \mathbf{r} + \mathbf{t}_i) d^3r \\ &= \int e^{-i\mathbf{b} \cdot \mathbf{r}} (\psi_{\mathbf{k}m}(\mathbf{r}))^* \psi_{[\mathbf{k} + \mathbf{b}],n}(\mathbf{r}) d^3r \\ &= M_{m,n}^{(\mathbf{k}, \mathbf{b})}. \end{aligned} \quad (10.71)$$

Another symmetry of the  $M_{mn}^{(\mathbf{k}, \mathbf{b})}$  matrix relates its complex conjugate elements at the  $k$ -point pair  $(\mathbf{k}, \mathbf{k} + \mathbf{b})$  to its elements at the  $k$ -point pair  $(\mathbf{k} + \mathbf{b}, \mathbf{k})$ :

$$(M_{mn}^{(\mathbf{k}, \mathbf{b})})^* = \int e^{i\mathbf{b} \cdot \mathbf{r}} (\psi_{\mathbf{k}m}(\mathbf{r})) (\psi_{[\mathbf{k} + \mathbf{b}],n}(\mathbf{r}))^* d^3r = M_{nm}^{([\mathbf{k} + \mathbf{b}], -\mathbf{b})}. \quad (10.72)$$

## 10.6 The Berry Phase

We consider a quantum mechanical Hamiltonian operator  $\hat{H}(\boldsymbol{\xi})$ , which depends on some parameters  $\boldsymbol{\xi}$ , and its  $\boldsymbol{\xi}$ -dependent ground-state  $|\psi(\boldsymbol{\xi})\rangle$ , which satisfies the Schrödinger-equation

$$\hat{H}(\boldsymbol{\xi})|\psi(\boldsymbol{\xi})\rangle = E(\boldsymbol{\xi})|\psi(\boldsymbol{\xi})\rangle, \quad (10.73)$$

where  $E(\boldsymbol{\xi})$  is the corresponding ground-state eigenvalue. Let  $\mathcal{C}$  be a closed contour in  $\boldsymbol{\xi}$ -space and  $\{\boldsymbol{\xi}_i\}$  a discretization of this contour  $\mathcal{C}$  consisting of  $N$  points. We may define the phase difference between neighboring points  $i$  and  $i + 1$  as

$$e^{-i\varphi_{i,i+1}} = \frac{\langle \psi(\boldsymbol{\xi}_i) | \psi(\boldsymbol{\xi}_{i+1}) \rangle}{|\langle \psi(\boldsymbol{\xi}_i) | \psi(\boldsymbol{\xi}_{i+1}) \rangle|} \quad (10.74)$$

or explicitly as

$$\varphi_{i,i+1} = -\Im \log \langle \psi(\boldsymbol{\xi}_i) | \psi(\boldsymbol{\xi}_{i+1}) \rangle. \quad (10.75)$$

Clearly, the phase difference  $\varphi_{i,i+1}$  cannot have any physical meaning, because the phases of the wave function at  $\boldsymbol{\xi}_i$  and  $\boldsymbol{\xi}_{i+1}$  can be chosen at random. Interestingly, the phase

difference which accumulates along the complete contour  $\mathcal{C}$  is independent of the gauge because the arbitrary phase factors cancel pairwise:

$$\begin{aligned}\varphi_{1,1} &= \sum_{i=1}^N \varphi_{i,i+1} = \\ &= -\Im \log \{ \langle \psi(\boldsymbol{\xi}_1) | \psi(\boldsymbol{\xi}_2) \rangle \langle \psi(\boldsymbol{\xi}_2) | \psi(\boldsymbol{\xi}_3) \rangle \cdots \langle \psi(\boldsymbol{\xi}_{N-1}) | \psi(\boldsymbol{\xi}_N) \rangle \langle \psi(\boldsymbol{\xi}_N) | \psi(\boldsymbol{\xi}_1) \rangle \}.\end{aligned}\quad (10.76)$$

Typically, physical observables correspond to Hermitian operators and their eigenvalues in quantum mechanics. However, any *gauge-invariant* quantity has the potential to be *observable*. In section 10.7 it will be shown that the ferroelectric polarization may be obtained indeed from a gauge-invariant phase of the type Eq. (10.76). We will see then that the ferroelectric polarization of a periodic crystal cannot be expressed simply as an expectation value of a quantum mechanical operator.

Generalizing the above definition of the phase difference between neighboring points  $i$  and  $i + 1$  given in Eq. (10.75) to the case of a manifold of bands, we obtain

$$\varphi_{mn}^{i,i+1} = -\Im \log \langle \psi_m(\boldsymbol{\xi}_i) | \psi_n(\boldsymbol{\xi}_{i+1}) \rangle. \quad (10.77)$$

Clearly, the matrix  $M_{mn}^{\mathbf{k},\mathbf{b}}$ , Eq. (10.11), is a special case of the overlap  $\langle \psi_m(\boldsymbol{\xi}_i) | \psi_n(\boldsymbol{\xi}_{i+1}) \rangle$  used in Eq. (10.77), with the parameter  $\boldsymbol{\xi}$  chosen to be the  $\mathbf{k}$ -point and with the eigenvectors  $\psi_m(\boldsymbol{\xi})$  given as the lattice periodic parts  $u_{\mathbf{k}m}$ , which are eigenstates of the  $\mathbf{k}$ -dependent Hamiltonian  $\hat{H}_{\mathbf{k}}$ . The multi-band generalization of Eq. (10.76) is

$$\varphi_{1,1} = \sum_{i=1}^N \sum_m \varphi_{mm}^{i,i+1}. \quad (10.78)$$

A special case hereof is Eq. (10.17).

Making the discretization of the contour finer and finer the phase difference along the closed contour ultimately converges to a finite value known as the *Berry phase* [134, 135]:

$$\gamma = i \oint_{\mathcal{C}} \langle \psi(\boldsymbol{\xi}) | \nabla_{\boldsymbol{\xi}} \psi(\boldsymbol{\xi}) \rangle \cdot d\boldsymbol{\xi}. \quad (10.79)$$

The integrand  $i \langle \psi(\boldsymbol{\xi}) | \nabla_{\boldsymbol{\xi}} \psi(\boldsymbol{\xi}) \rangle$  is real valued and called the *Berry connection*. In contrast to the Berry phase the Berry connection is not gauge-invariant.

## 10.7 Ferroelectric Polarization

For finite samples the *electric dipole moment* is a well-defined quantity: From the core and valence electron densities,  $n_c(\mathbf{r})$  and  $n_v(\mathbf{r})$ , respectively, the *electronic contributions* to the dipole moment are obtained as follows:

$$\mathbf{d}_{\text{el}}^c = -|e| \int \mathbf{r} n_c(\mathbf{r}) d^3r \quad (10.80)$$

in the case of core electrons and

$$\mathbf{d}_{\text{el}} = -|e| \int \mathbf{r} n_{\text{v}}(\mathbf{r}) d^3 r \quad (10.81)$$

in the case of valence electrons. Likewise, the *nuclear contribution* to the dipole moment is given by:

$$\mathbf{d}_{\text{n}} = |e| \sum_{\mu} \boldsymbol{\tau}_{\mu} Z_{\mu}, \quad (10.82)$$

where  $Z_{\mu}$  denotes the nuclear number and  $\boldsymbol{\tau}_{\mu}$  the position of atom  $\mu$ . The total electric dipole moment is simply the sum of these three contributions:

$$\mathbf{d} = \mathbf{d}_{\text{el}}^{\text{c}} + \mathbf{d}_{\text{el}} + \mathbf{d}_{\text{n}}. \quad (10.83)$$

Defining the *core charge*  $Q_{\mu}$  of atom  $\mu$  as

$$Q_{\mu} = \int_{\text{MT}^{\mu}} n_{\text{c}}(\mathbf{r}) d^3 r \quad (10.84)$$

and the *ionic charge* as  $q_{\mu} = Z_{\mu} - Q_{\mu}$ , we introduce the *ionic contribution* to the dipole moment as

$$\mathbf{d}_{\text{ion}} = |e| \sum_{\mu} \boldsymbol{\tau}_{\mu} q_{\mu}. \quad (10.85)$$

We may now conveniently express the total dipole moment, Eq. (10.83), in terms of the ionic contribution and the electronic contribution due to the valence electrons:

$$\mathbf{d} = \mathbf{d}_{\text{el}} + \mathbf{d}_{\text{ion}}. \quad (10.86)$$

However, for a periodic solid Eq. (10.81) is not well-defined: The attempt to define the dipole moment of one unit cell,  $V$ , as

$$\mathbf{d} = \mathbf{d}_{\text{ion}} - |e| \int_V \mathbf{r} n_{\text{v}}(\mathbf{r}) d^3 r \quad (10.87)$$

fails because in general even a rigid shift of the entire integration volume  $V$  will change the value of  $\mathbf{d}$ , and consequently  $\mathbf{d}$  as given in Eq. (10.87) is *ill-defined*. A more mathematical way to understand this problem is to realize that the position operator, which enters in the second term on the right-hand side of Eq. (10.87) is not an observable in the Hilbert space of the wave functions of the crystal: The wave functions of the crystal satisfy Bloch's theorem, the product of the position operator with a wave function not. The position operator is even unbounded. It is important to note that Eq. (10.87) cannot be used as a definition of the dipole moment in a periodic system, because the second term on the right hand side changes *continuously*, when the unit cell is moved or deformed continuously. In contrast, the first term of the right hand side of Eq. (10.87) also exhibits an ambiguity, but

a *discrete* one: Consider the one-dimensional periodic arrangement of point charges  $+q$  at locations  $x_i^+$  and point charges  $-q$  at locations  $x_i^-$  given by

$$\begin{aligned} \dots, x_{-2}^+ &= -2.0a, x_{-1}^+ = -1.0a, x_0^+ = 0.0a, x_1^+ = 1.0a, x_2^+ = 2.0a, \dots, \\ \dots, x_{-2}^- &= -1.5a, x_{-1}^- = -0.5a, x_0^- = 0.5a, x_1^- = 1.5a, x_2^- = 2.5a, \dots \end{aligned} \quad (10.88)$$

If we choose the unit cell to go from  $-0.25a$  to  $0.75a$ , it encloses the points  $x_0^+$  and  $x_0^-$  and the resulting dipole is  $-qa/2$ . However, if we choose the unit cell to go from  $-0.75a$  to  $0.25a$ , it encloses the points  $x_{-1}^-$  and  $x_0^+$  and the resulting dipole is  $qa/2$ . We will see later that this discrete ambiguity necessitates consideration, but the actual problem that has to be solved concerns the electronic contribution rather than the ionic one: The electronic charge is smeared out and not concentrated like point charges. Consequently, the dipole due to the electronic charge does not change discretely but continuously, when the unit cell is moved.

For the *electric polarization* very similar problems arise regarding the question of its definition for a periodic solid, as we will see below. We first discuss a clear case: The definition of the electric polarization for a dilute gas. As the gas is dilute, we can apply Eq. (10.81,10.86) in order to calculate the electric dipole moment of individual molecules in the gas and

$$\alpha = \frac{2}{3} \sum_n \frac{|\langle 0 | e\hat{\mathbf{r}} | n \rangle|^2}{E_n - E_0} \quad (10.89)$$

to obtain the polarizability  $\alpha$  of the molecules. Assuming the gas to be composed of only one molecular species, the *dielectric constant*  $\epsilon$  and the *dielectric susceptibility*  $\chi$  of the gas may be determined from the *Clausius-Mossotti* relation,

$$\begin{aligned} \frac{\epsilon - 1}{\epsilon + 2} &= \frac{4\pi n}{3} \left( \alpha + \frac{d^2}{3k_B T} \right), \\ \chi &= \frac{n(\alpha + \frac{d^2}{3k_B T})}{1 - \frac{4\pi}{3} n(\alpha + \frac{d^2}{3k_B T})}, \end{aligned} \quad (10.90)$$

where  $k_B$  is Boltzmann's constant and  $n$  is the number of molecules per volume. In a finite electric field  $\mathbf{E}$  a polarization

$$\mathbf{P} = \chi \mathbf{E} \quad (10.91)$$

arises as a response to the applied electric field. In this example of a dilute gas the polarization  $\mathbf{P}$  may be understood as the effective macroscopic dipole moment per volume. In a periodic crystal this concept of the polarization as the effective dipole moment per volume suffers obviously from the problem to define the dipole moment, as Eq. (10.87) cannot be applied to a periodic crystal.

A solution to the problem of defining the polarization of a bulk crystal is given by the *modern theory of polarization* [24, 118, 119, 136], which allows to express *changes* of the polarization in terms of a Berry phase. For a *finite* system the position operator is bounded

and the following identity holds:

$$\langle \psi_i | \hat{\mathbf{r}} | \psi_j \rangle = -i \frac{\hbar}{m} \frac{\langle \psi_i | \hat{\mathbf{p}} | \psi_j \rangle}{E_i - E_j}, \quad i \neq j. \quad (10.92)$$

This is derived easily using the commutator

$$[\hat{H}, \hat{r}_i]_- = -\frac{i\hbar}{m} \hat{p}_i, \quad (10.93)$$

which follows from the commutator

$$[\hat{p}^2, \hat{r}_i]_- = -2i\hbar \hat{p}_i. \quad (10.94)$$

Interestingly, while it is not possible to take the thermodynamic limit of the left hand side of Eq. (10.92) this problem is absent for the right hand side. In fact, the operator of linear momentum  $\hat{\mathbf{p}}$  is a well-defined operator in a periodic crystal, in contrast to the position operator  $\hat{\mathbf{r}}$ . The strategy used by Resta [137] to arrive at an expression for the polarization of a periodic crystal is based on this observation. Of course, we cannot use Eq. (10.92) directly to recast the expression for the dipole moment, because of the restriction  $i \neq j$  in Eq. (10.92). To make progress, we consider the derivative of the polarization due to valence electrons with respect to the parameter  $\xi_i$  in a *finite* system:

$$\frac{\partial \mathbf{P}_{\text{el}}}{\partial \xi_i} = -\frac{|e|}{V} \sum_{n=1}^{N_{\text{occ}}} \left[ \left\langle \frac{\partial \psi_n}{\partial \xi_i} | \hat{\mathbf{r}} | \psi_n \right\rangle + \langle \psi_n | \hat{\mathbf{r}} | \frac{\partial \psi_n}{\partial \xi_i} \right], \quad (10.95)$$

where  $N_{\text{occ}}$  is the number of occupied states and  $V$  the volume of the system. Using first-order perturbation theory to express the derivatives of the wave functions in terms of the derivative of the potential ( $\partial \hat{H} / \partial \xi_i = \partial \hat{V} / \partial \xi_i$  is assumed),

$$\left| \frac{\partial \psi_n}{\partial \xi_i} \right\rangle = \sum_{m \neq n} \frac{|\psi_m(\boldsymbol{\xi})\rangle \langle \psi_m(\boldsymbol{\xi}) | \partial V(\boldsymbol{\xi}) / \partial \xi_i | \psi_n(\boldsymbol{\xi}) \rangle}{\epsilon_n(\boldsymbol{\xi}) - \epsilon_m(\boldsymbol{\xi})}, \quad (10.96)$$

allows us to make use of Eq. (10.92) and to take the thermodynamic limit. Consequently, following Ref. [137], we may argue that the first derivative of the polarization of a periodic crystal with respect to the parameter  $\xi_i$  of the Hamiltonian  $\hat{H}(\boldsymbol{\xi})$  is well defined and given by

$$\begin{aligned} \frac{\partial \mathbf{P}}{\partial \xi_i} &= \frac{i|e|\hbar}{NVm} \sum_{\mathbf{k}} \sum_{n=1}^{N_{\text{occ}}} \sum_{m \neq n} \left[ \frac{\langle \psi_{\mathbf{k}n}(\boldsymbol{\xi}) | \hat{\mathbf{p}} | \psi_{\mathbf{k}m}(\boldsymbol{\xi}) \rangle \langle \psi_{\mathbf{k}m}(\boldsymbol{\xi}) | \partial V(\boldsymbol{\xi}) / \partial \xi_i | \psi_{\mathbf{k}n}(\boldsymbol{\xi}) \rangle}{(\epsilon_{\mathbf{k}n}(\boldsymbol{\xi}) - \epsilon_{\mathbf{k}m}(\boldsymbol{\xi}))^2} - \text{c.c.} \right] \\ &= \frac{-2|e|\hbar}{NVm} \sum_{\mathbf{k}} \sum_{n=1}^{N_{\text{occ}}} \sum_{m \neq n} \Im \left[ \frac{\langle \psi_{\mathbf{k}n}(\boldsymbol{\xi}) | \hat{\mathbf{p}} | \psi_{\mathbf{k}m}(\boldsymbol{\xi}) \rangle \langle \psi_{\mathbf{k}m}(\boldsymbol{\xi}) | \partial V(\boldsymbol{\xi}) / \partial \xi_i | \psi_{\mathbf{k}n}(\boldsymbol{\xi}) \rangle}{(\epsilon_{\mathbf{k}n}(\boldsymbol{\xi}) - \epsilon_{\mathbf{k}m}(\boldsymbol{\xi}))^2} \right] \\ &= \frac{-2|e|\hbar}{NVm} \sum_{\mathbf{k}} \sum_{n=1}^{N_{\text{occ}}} \sum_{m=N_{\text{occ}}+1}^{\infty} \Im \left[ \frac{\langle \psi_{\mathbf{k}n}(\boldsymbol{\xi}) | \hat{\mathbf{p}} | \psi_{\mathbf{k}m}(\boldsymbol{\xi}) \rangle \langle \psi_{\mathbf{k}m}(\boldsymbol{\xi}) | \partial V(\boldsymbol{\xi}) / \partial \xi_i | \psi_{\mathbf{k}n}(\boldsymbol{\xi}) \rangle}{(\epsilon_{\mathbf{k}n}(\boldsymbol{\xi}) - \epsilon_{\mathbf{k}m}(\boldsymbol{\xi}))^2} \right], \end{aligned} \quad (10.97)$$



where  $N$  is the number of unit cells. Additionally, the change in the polarization under a finite adiabatic change of the Hamiltonian is well defined and given by

$$\Delta \mathbf{P}_{\text{el}} = \int \frac{\partial \mathbf{P}_{\text{el}}}{\partial \boldsymbol{\xi}} \cdot d\boldsymbol{\xi}. \quad (10.98)$$

Clearly, the derivative of the wave function  $|\psi_n(\boldsymbol{\xi})\rangle$  with respect to the parameter  $\boldsymbol{\xi}$  is not gauge invariant: If we re-define the wave function,

$$|\psi_n(\boldsymbol{\xi})\rangle \rightarrow e^{i\varphi(\boldsymbol{\xi})} |\psi_n(\boldsymbol{\xi})\rangle, \quad (10.99)$$

where  $\varphi(\boldsymbol{\xi})$  is an arbitrary real-valued smooth function of the parameter  $\boldsymbol{\xi}$ , the derivative of the wave function is modified:

$$\frac{\partial}{\partial \xi_i} |\psi_n(\boldsymbol{\xi})\rangle \rightarrow e^{i\varphi(\boldsymbol{\xi})} \frac{\partial}{\partial \xi_i} |\psi_n(\boldsymbol{\xi})\rangle + ie^{i\varphi(\boldsymbol{\xi})} \frac{\partial \varphi(\boldsymbol{\xi})}{\partial \xi_i} |\psi_n(\boldsymbol{\xi})\rangle. \quad (10.100)$$

We emphasize that Eq. (10.96) imposes a particular gauge. However, the derivative of the polarization, Eq. (10.95), is gauge invariant, as seen by inserting Eq. (10.100). Consequently, the derivative of the polarization may be calculated using the particular gauge imposed by Eq. (10.96).

In order to obtain an expression for  $\partial \mathbf{P}_{\text{el}} / \partial \xi_i$ , which does not depend on the unoccupied states, one changes from Bloch states  $|\psi_{\mathbf{k},n}(\boldsymbol{\xi})\rangle$  to the cell-periodic functions  $|u_{\mathbf{k},n}(\boldsymbol{\xi})\rangle$ . Using the identities

$$\begin{aligned} \langle \psi_{\mathbf{k},n}(\boldsymbol{\xi}) | \hat{p}_i | \psi_{\mathbf{k},m}(\boldsymbol{\xi}) \rangle &= \frac{m}{\hbar} \langle u_{\mathbf{k},n}(\boldsymbol{\xi}) | [\partial / \partial k_i, \hat{H}_{\mathbf{k}}(\boldsymbol{\xi})]_- | u_{\mathbf{k},m}(\boldsymbol{\xi}) \rangle, \\ \langle \psi_{\mathbf{k},n}(\boldsymbol{\xi}) | \partial V / \partial \xi_i | \psi_{\mathbf{k},m}(\boldsymbol{\xi}) \rangle &= \langle u_{\mathbf{k},n}(\boldsymbol{\xi}) | [\partial / \partial \xi_i, \hat{H}_{\mathbf{k}}(\boldsymbol{\xi})]_- | u_{\mathbf{k},m}(\boldsymbol{\xi}) \rangle \end{aligned} \quad (10.101)$$

one arrives at the expression [118]

$$\frac{\partial \mathbf{P}_{\text{el},\alpha}}{\partial \xi_i} = -\frac{2|e|}{8\pi^3} \int d^3k \sum_{n=1}^{N_{\text{occ}}} \Im [\langle \partial u_{\mathbf{k},n}(\boldsymbol{\xi}) / \partial k_\alpha | \partial u_{\mathbf{k},n}(\boldsymbol{\xi}) / \partial \xi_i \rangle]. \quad (10.102)$$

Choosing  $u_{\mathbf{k},n}(\boldsymbol{\xi})$  to satisfy

$$u_{\mathbf{k},n}(\mathbf{r}, \boldsymbol{\xi}) = e^{i\mathbf{G} \cdot \mathbf{r}} u_{\mathbf{k}+\mathbf{G},n}(\mathbf{r}, \boldsymbol{\xi}) \quad (10.103)$$

for all reciprocal lattice vectors  $\mathbf{G}$ , the change of the polarization, Eq. (10.98), along an adiabatic path from  $\boldsymbol{\xi}_1$  to  $\boldsymbol{\xi}_2$  is then given by

$$\Delta \mathbf{P}_{\text{el}} = \mathbf{P}_{\text{el}}(\boldsymbol{\xi}_2) - \mathbf{P}_{\text{el}}(\boldsymbol{\xi}_1), \quad (10.104)$$

with

$$P_{\text{el},\alpha}(\boldsymbol{\xi}) = -\frac{|e|}{8\pi^3} \int d^3k \sum_{n=1}^{N_{\text{occ}}} \Im [\langle \partial u_{\mathbf{k},n}(\boldsymbol{\xi}) / \partial k_\alpha | u_{\mathbf{k},n}(\boldsymbol{\xi}) \rangle]. \quad (10.105)$$

Due to the normalization  $\langle u_{\mathbf{k},n}(\boldsymbol{\xi}) | u_{\mathbf{k},n}(\boldsymbol{\xi}) \rangle = 1$  the argument of the imaginary part in Eq. (10.105) is purely imaginary:

$$\langle \partial u_{\mathbf{k},n}(\boldsymbol{\xi}) / \partial k_\alpha | u_{\mathbf{k},n}(\boldsymbol{\xi}) \rangle + \langle u_{\mathbf{k},n}(\boldsymbol{\xi}) | \partial u_{\mathbf{k},n}(\boldsymbol{\xi}) / \partial k_\alpha \rangle = 2\Re \langle u_{\mathbf{k},n}(\boldsymbol{\xi}) | \partial u_{\mathbf{k},n}(\boldsymbol{\xi}) / \partial k_\alpha \rangle = 0. \quad (10.106)$$

Exploiting the fact that  $\langle \partial u_{\mathbf{k},n}(\boldsymbol{\xi}) / \partial k_\alpha | u_{\mathbf{k},n}(\boldsymbol{\xi}) \rangle$  is purely imaginary, we may write Eq. (10.105) explicitly in the form of Eq. (10.79) to show that it is a Berry phase:

$$P_{\text{el},\alpha}(\boldsymbol{\xi}) = i \frac{|e|}{8\pi^3} \int d^3k \sum_{n=1}^{N_{\text{occ}}} \langle \partial u_{\mathbf{k},n}(\boldsymbol{\xi}) / \partial k_\alpha | u_{\mathbf{k},n}(\boldsymbol{\xi}) \rangle. \quad (10.107)$$

Strictly speaking, Eq. (10.79) is a circuit integral, while Eq. (10.107) is an integral along an open path. However, the end points of the open path are not arbitrary, but given by the Brillouin zone boundaries. In conjunction with the gauge condition Eq. (10.103) this ensures gauge-invariance of Eq. (10.107).

One can prove [118] that the polarization change along a closed loop can take only discrete values:

$$\oint \frac{\partial \mathbf{P}_{\text{el}}}{\partial \boldsymbol{\xi}} \cdot d\boldsymbol{\xi} = \frac{e\mathbf{R}}{V}, \quad (10.108)$$

where  $\mathbf{R}$  is a lattice vector. Thus, also an *absolute* polarization and not only polarization changes may be defined. In fact, one could use Eq. (10.105) as a definition for the absolute electronic polarization. However, according to Eq. (10.108), the absolute polarization can only be specified modulo  $e\mathbf{R}/V$ . While in practice only changes of the polarization can be measured, defining the absolute polarization can be useful, because this practice allows to assign absolute values to the various phases of a given material.

In order to obtain the total polarization, we have to add the electronic polarization, Eq. (10.105), and the ionic polarization, which is given by

$$\mathbf{P}_{\text{ion}} = \frac{|e|}{V} \sum_{\mu} \tau_{\mu} q_{\mu}. \quad (10.109)$$

Analogously to Eq. (10.98) the change of the total polarization  $\mathbf{P} = \mathbf{P}_{\text{el}} + \mathbf{P}_{\text{ion}}$  along the path  $\mathcal{C}$  in configuration space is well defined and given by:

$$\Delta \mathbf{P}_{\mathcal{C}} = \int_{\mathcal{C}} \frac{\partial \mathbf{P}}{\partial \boldsymbol{\xi}} \cdot d\boldsymbol{\xi}. \quad (10.110)$$

Thus, in order to calculate the ferroelectric polarization of a material, one may choose an adiabatic path  $\mathcal{C}$ , which connects an inversion symmetric configuration with the ferroelectric configuration. Everywhere along this adiabatic path  $\mathcal{C}$  the system has to be insulating. The inversion symmetric configuration is not ferroelectric and serves as a reference. In practice the continuous adiabatic path is replaced by a set of discrete points. The discrete points are connected by small fragments  $\mathcal{C}_i$  of the continuous adiabatic path  $\mathcal{C} = \sum_i \mathcal{C}_i$ . The ferroelectric polarization  $\mathbf{P}$  is then given by

$$\mathbf{P} = \Delta \mathbf{P}_{\mathcal{C}} = \sum_i \Delta \mathbf{P}_{\mathcal{C}_i}. \quad (10.111)$$

If the fragments  $\mathcal{C}_i$  are chosen sufficiently small one may evaluate the polarization changes  $\Delta\mathbf{P}_{\mathcal{C}_i}$  as differences between the absolute polarizations at the end points of the fragment  $\mathcal{C}_i$ . The fragments  $\mathcal{C}_i$  have to be so small that one can be sure that  $|\Delta\mathbf{P}_{\mathcal{C}_i}| < e \min[a, b, c]/V$ , which solves the problem that the absolute polarization may be defined only modulo  $e\mathbf{R}/V$ . For systems with a small polarization,  $|\mathbf{P}| < e \min[a, b, c]/V$ , it is sufficient to work with the end-points of the adiabatic path:

- Sum the electronic and ionic terms as evaluated in the ferroelectric phase of the material.
- Sum the electronic and ionic terms as evaluated for an inversion symmetric configuration of the system.
- Compute the difference  $\Delta\mathbf{P}$  of the two sums.
- Determine the lattice vector  $\mathbf{R}$ , which minimizes  $|\Delta\mathbf{P} - e\mathbf{R}/V|$ . Obtain the ferroelectric polarization as  $\mathbf{P} = \Delta\mathbf{P} - e\mathbf{R}/V$ .

However, unless one knows the approximate magnitude of the polarization, this procedure has to be followed with care, because one might miss a contribution  $e\mathbf{R}/V$ . This is the ambiguity we discussed in Eq. (10.88) and Eq. (10.108). Consequently, to be on the save side, it is sometimes necessary to evaluate the polarization also on intermediate points of the adiabatic path: If one finds that already in the middle of the adiabatic path the magnitude of  $\mathbf{P}$  is close to  $e \min[a, b, c]/V$ , it might well be that the true polarization at the end point of the adiabatic path is larger than  $e \min[a, b, c]/V$ .

### 10.7.1 Wannier Picture of Ferroelectric Polarization

Comparing Eq. (10.105) and Eq. (10.15) one realizes [118] that the electronic contribution to the polarization is related to the positions of the centers of the Wannier functions:

$$\mathbf{P}_{\text{el}} = -\frac{|e|}{V} \sum_n^{N_{\text{occ}}} \langle \mathbf{r} \rangle_n, \quad (10.112)$$

which may be interpreted as the polarization due to point charges of size  $-|e|$  at positions  $\langle \mathbf{r} \rangle_n$ . Thus, Wannier functions provide a very intuitive picture of ferroelectric polarization: As the adiabatic path is followed and the configuration of the crystal changes accordingly, ions and Wannier functions move giving rise to a current, which builds up the polarization. Obviously, if only the periodic charge density of the crystal is available, we cannot compute the electronic contribution to this current in general, because we cannot identify the corresponding charge carriers and their velocities. The complete expression for the ferroelectric polarization in the Wannier picture is:

$$\mathbf{P} = \mathbf{P}_{\text{el}} + \mathbf{P}_{\text{ion}} = \frac{|e|}{V} \left[ \sum_{\mu} \tau_{\mu} q_{\mu} - \sum_n^{N_{\text{occ}}} \langle \mathbf{r} \rangle_n \right]. \quad (10.113)$$

In the simplest point charge model of ferroelectric ionic crystals one assigns integer charges to the ions. This model misses in general the polarization due to the deformation of the electronic orbitals. This contribution is included in Eq. (10.113): The centers of the Wannier functions deviate in general from the nuclear positions. It can be useful to decompose the polarization into the contribution due to the deformation of the electronic orbitals and the contribution as obtained in the point charge model. To do this, each Wannier function is assigned to a host site in the inversion symmetric configuration of the crystal. A sensible choice for the host site of a given Wannier function is the position of the nucleus which has the smallest distance to the center of the Wannier function. Accordingly, we assign Wannier function  $n$  to atom  $\alpha(n)$  and obtain the polarization of the point charge model:

$$\mathbf{P}_M = \frac{|e|}{V} \left[ \sum_{\mu} \tau_{\mu} q_{\mu} - \sum_n^{N_{\text{occ}}} \tau_{\alpha(n)} \right]. \quad (10.114)$$

The contribution due to the deformation of the orbitals is

$$\mathbf{P}_W = \frac{|e|}{V} \sum_n^{N_{\text{occ}}} [\tau_{\alpha(n)} - \langle \mathbf{r} \rangle_n]. \quad (10.115)$$

For systems where  $\mathbf{P}_W$  is large and where the description in terms of the simple point charge model is unsatisfactory, Eq. (10.115) allows to track down this anomalous contribution to individual orbitals. Thus, in comparison to the Berry phase formulation of the previous section, the Wannier function formulation allows to decompose the complete polarization into the contributions of the individual orbitals, and to gain additional insight. Additionally, one can usually be sure that the individual displacements of the Wannier centers are smaller in magnitude than a lattice translation vector. When the Wannier centers are calculated they carry of course the ambiguity of a shift by a lattice translation vector. However, this ambiguity may be resolved easily by requiring that the magnitude of the Wannier center displacement be minimal. Hence, intermediate points on the adiabatic path are usually not needed, if the Wannier picture of ferroelectric polarization is applied. This is a big advantage over the Berry phase formulation, where intermediate points on the adiabatic path are necessary in general (see Eq. 10.111). One more example where the Wannier function formulation is superior to the Berry phase one is antiferroelectricity. An antiferroelectric has zero net polarization and consequently no information can be gained from a theory which only provides the net polarization. However, using Wannier functions it becomes possible to define the polarizations of the sub-systems as required for the description of antiferroelectricity. Similarly, in layered structures, one may introduce the concept of a layer-resolved polarization [121], which is based on the deviations of the centers of the Wannier functions from the host sites.

The advantages the Wannier picture has over the Berry phase formulation have a price: For the computation of the MLWFs the off-diagonal elements of the  $M_{mn}^{(\mathbf{k}, \mathbf{b})}$  matrix are needed. These off-diagonal elements do not influence the sum of the centers of the Wannier functions of an isolated group of bands, but they influence the total spread of the

corresponding set of MLWFs. As the Berry phase is equivalent to the sum of the centers of the WFs, only the diagonal elements of the  $M_{nn}^{(\mathbf{k},\mathbf{b})}$  matrix are needed for its calculation. Hence, the computational effort for the Berry phase is proportional to the number of bands, while it is proportional to the square of the number of bands for the MLWFs.

Besides Eq. (10.12) there are several finite difference formulations of Eq. (10.15), which all reduce to Eq. (10.15) in the thermodynamic limit. Clearly, it is an interesting question whether one particular finite difference formula is systematically the best concerning the convergence with respect to the number of  $k$ -points. It has been proposed [138] to replace Eq. (10.12) for the centers of the Wannier functions by a different finite difference equation to improve the convergence of the electronic part of the polarization with respect to the  $k$ -point set:

$$\langle \mathbf{r}_n \rangle = - \sum_{\mathbf{b}} w_{\mathbf{b}} \mathbf{b} \Im \ln \left[ \frac{1}{N} \sum_{\mathbf{k}} \tilde{M}_{nn}^{(\mathbf{k},\mathbf{b})} \right]. \quad (10.116)$$

Compared to Eq. (10.12) only the order of taking the logarithm and summing over  $k$ -points is reversed.

## 10.8 Examples of Wannier functions

### 10.8.1 Diamond

In the following we discuss MLWFs for diamond. The experimental lattice constant of 3.371 a.u. and the GGA exchange correlation potential of Perdew Burke and Ernzerhof [64] were used. We chose the muffin-tin radius to be 1.28 a.u. and a plane-wave cutoff of 4.6 a.u.<sup>-1</sup>. The band structure is shown in Fig. 10.2. The eight bands correspond to the eight atomic orbitals (two atoms in the primitive unit cell each of which has one 2s and three 2p orbitals). From the eight atomic  $sp^3$  orbitals four bonding states (black bands in Fig. 10.2) and four anti-bonding states (red bands in Fig. 10.2) arise.

Using an  $8 \times 8 \times 8$   $k$ -mesh, we constructed three sets of Wannier functions:

- 4 Wannier functions generated from the valence bands only (see Fig. 10.3(a)). They are bond-centered and may be interpreted as bonding orbitals formed by a superposition of the  $sp^3$  atomic orbitals of the two carbon atoms. In the mid-plane between the two carbon atoms the MLWF does not vanish. The mid-plane is a symmetry plane. Each of the 4 MLWFs has a spread of a.u.<sup>2</sup>.
- 4 Wannier functions generated from the conduction bands only (see Fig. 10.3(b)). They are bond-centered and may be interpreted as anti-bonding orbitals formed by a superposition of the  $sp^3$  atomic orbitals of the two carbon atoms. In the mid-plane between the two carbon atoms the MLWF vanishes. The mid-plane is a symmetry plane.
- 8 Wannier functions generated from the 4 valence and the 4 conduction bands (see Fig. 10.3(c)). They may be interpreted as the atomic  $sp^3$  orbitals. They are not

bond-centered and the mid-plane is not a symmetry plane. Each of the 8 MLWFs has a spread of 3.041 a.u.<sup>2</sup>.

The Wannier functions of each set are symmetry-related. As a consequence all Wannier functions within one set are characterized by the same spread. Clearly, there are two ways to generate MLWFs for the eight lowest bands of diamond: One may either calculate MLWFs separately for conduction and valence bands (Fig. 10.3(a) and Fig. 10.3(b)) or treat the group of eight bands together (Fig. 10.3(c)). In the latter case the MLWFs are stronger localized, because there are more degrees of freedom that may be exploited to localize the functions. The total spread of the eight orbitals is 24.33 a.u.<sup>2</sup> in the latter case and 34.82 a.u.<sup>2</sup> in the former case. In the former case the MLWFs of the valence bands contribute 10.93 a.u.<sup>2</sup> to the total spread and those of the conduction bands 23.89 a.u.<sup>2</sup>.

The construction of the MLWFs involves finding a minimum in a functional space, which may become rather large. Consequently, one may expect [19] that besides the global minimum also local minima exist and that in general the existence of local minima might make it more difficult to find the global minimum. Whether or not the minimization algorithm runs into a local minimum and gets stuck there depends of course on the quality of the first-guess Wannier functions. In many cases local minima may be avoided easily in practice by choosing the first-guess Wannier functions reasonably well. Nevertheless, the question of the existence and characteristics of Wannier functions corresponding to local minima of the spread is an interesting one. The MLWFs of the valence states shown in Fig. 10.3(a) have been obtained starting from first guesses, which resemble the atomic  $sp^3$  orbitals, with the lobes pointing in the directions of the bonds. Using first guesses the lobes of which point in the opposite directions, we obtain also four symmetry-related WFs, but the total spread of 15.81 a.u.<sup>2</sup> is now larger than for the MLWFs. These WFs correspond to a local minimum of the spread. In Fig. 10.4 we show the isosurface plot of the resulting orbital. Compared to the MLWF shown in Fig. 10.3(a) the local minimum WF has less symmetry: The mid-plane through the center of the bond is no longer a symmetry plane.

### 10.8.2 SrVO<sub>3</sub>

The transition-metal oxide SrVO<sub>3</sub> crystallizes in a perfectly cubic perovskite lattice with a lattice constant of 7.26 a.u.. The Sr ions are placed at the corners of a cube (see Fig. 10.6). The O ions are placed at the face centers and form an ideal octahedron in the center of which the V ion is located. SrVO<sub>3</sub> is a metal with an isolated group of three  $t_{2g}$  bands around the Fermi level, which are partially occupied by one  $d$ -electron (see Figure 10.5).

Within our GGA calculation we obtained a bandwidth of 2.5 eV for the  $t_{2g}$ -group. The experimental lattice constant (7.26 a.u.) was assumed in the calculation and the exchange-correlation potential of Perdew, Burke and Ernzerhof [64] was used. For Sr, V, and O muffin-tin radii of 2.8 a.u., 2.1 a.u. and 1.4 a.u. were used, respectively. Calculations were carried out with a plane wave cut-off of 4.5 a.u.<sup>-1</sup>. A uniform 16×16×16  $k$ -point mesh was used for the Wannier construction. For the three  $t_{2g}$  bands we constructed

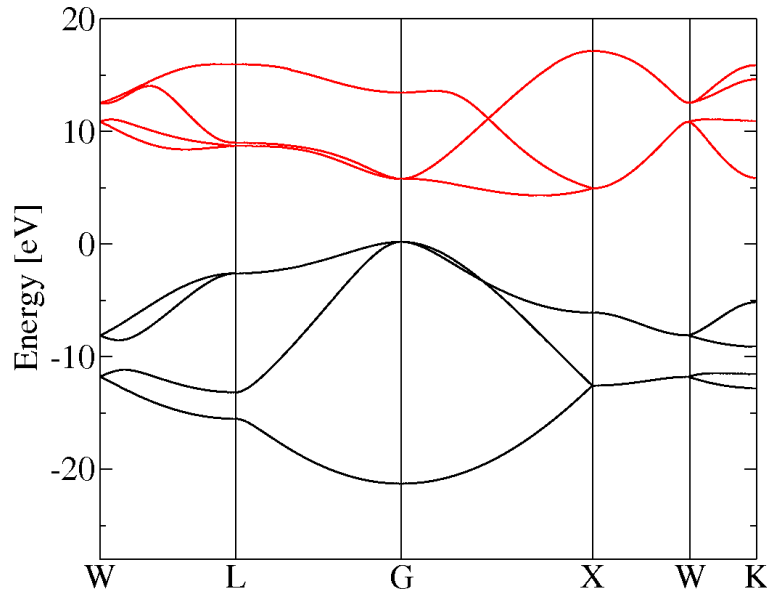


Figure 10.2: Band structure of diamond. Black bands: Valence bands. Red bands: Conduction bands.

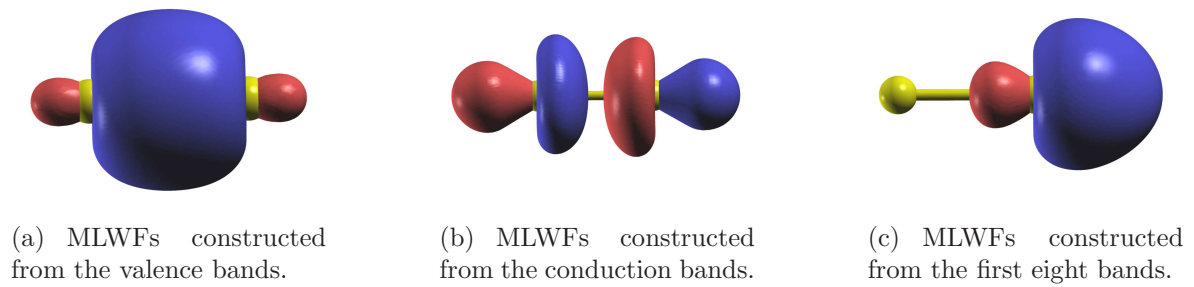


Figure 10.3: Wannier functions of diamond.

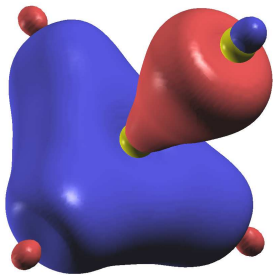
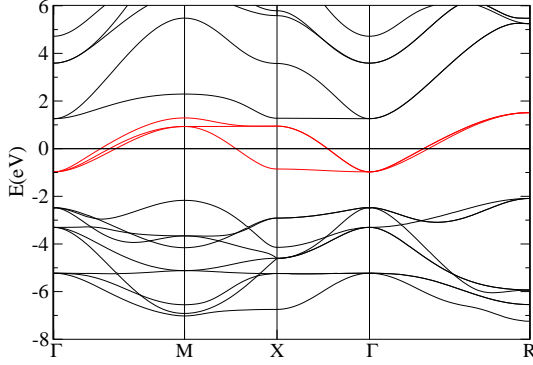


Figure 10.4: Wannier function constructed from the four valence bands. The WF shown here is not a MLWF, but corresponds to a local minimum of the spread.



Figure 10.5: Bandstructure of SrVO<sub>3</sub>. Red:  $t_{2g}$ -bands around the Fermi level.Table 10.2: Hopping Integrals for SrVO<sub>3</sub>. Energies are in meV.

$xyz$	001	010	011	101	110	111	002	020
$d_{xz}, d_{xz}$	-262.0	-27.0	5.8	-84.0	5.8	-5.7	7.6	0.2
$d_{xz}, d_{yz}$	0.0	0.0	0.0	0.0	9.2	3.6	0.0	0.0

three MLWFs,  $d_{xy}$ ,  $d_{yz}$  and  $d_{xz}$ , which are equivalent due to symmetry. The MLWFs are centered at the V site. The spread, Eq. (10.9), of the MLWFs was found to be 6.97 a.u.<sup>2</sup> for each of the three orbitals. The first-guess WFs are characterized by a spread which is only  $3 \cdot 10^{-4}$  a.u.<sup>2</sup> larger, showing that MLWFs and first-guess WFs are nearly identical in this case. To investigate the influence of spin-orbit coupling on the MLWFs a calculation including spin-orbit coupling was performed for the plots (see section 10.4). The spin-quantization axis, which defines the two spin-components of the spinor-valued MLWF, was chosen in [111] direction, to ensure that the spin components of the 6 spin-orbit MLWFs are related by symmetry. The spin-orbit MLWFs are complex-valued. The imaginary parts of the up and down-components of the  $d_{xy}$   $|\uparrow\rangle$ -dominated orbital, for example, are  $d_{x^2-y^2}$ -like plus an admixture of  $d_{yz}$ - $d_{xz}$ , while the real part of the down-component is  $(d_{yz} + d_{xz})$ -like. This result can be understood from the simple model in section 10.4 that leads to Eq. (10.61). The isosurface-plot for the  $d_{xy}$ -dominated orbital given in Fig. 10.6 clearly shows the hybridization between the V( $t_{2g}$ ) and O( $2p$ ) orbitals. The symmetry-inequivalent hopping integrals  $H_{m,m'}(\mathbf{R}_1 - \mathbf{R}_2)$ , Eq. (10.48), are listed in Table 10.2 and found to agree well with recently published WF-results [23, 116] on SrVO<sub>3</sub>. For reasons of symmetry the 1st-nearest-neighbor hopping integrals between different orbitals (e.g.  $d_{xz}$  and  $d_{yz}$ ) are zero in Table 10.2. However, there is a coupling between the  $d_{xz}$  orbital and the  $d_{yz}$  orbitals at the 110 and 111 sites, for example. Due to the dominance of the nearest-neighbor hopping the three MLWFs may, nevertheless, approximately be considered independent. The fast decay of the hoppings with distance furthermore indicates the short-range bonding in SrVO<sub>3</sub>. The dominance of the 001-hopping for the  $d_{xz}$ -orbital over the 010-hopping reflects the restriction of electron hopping to the  $xz$ -plane.

In order to study the convergence of the MLWFs with number of  $k$ -points we performed



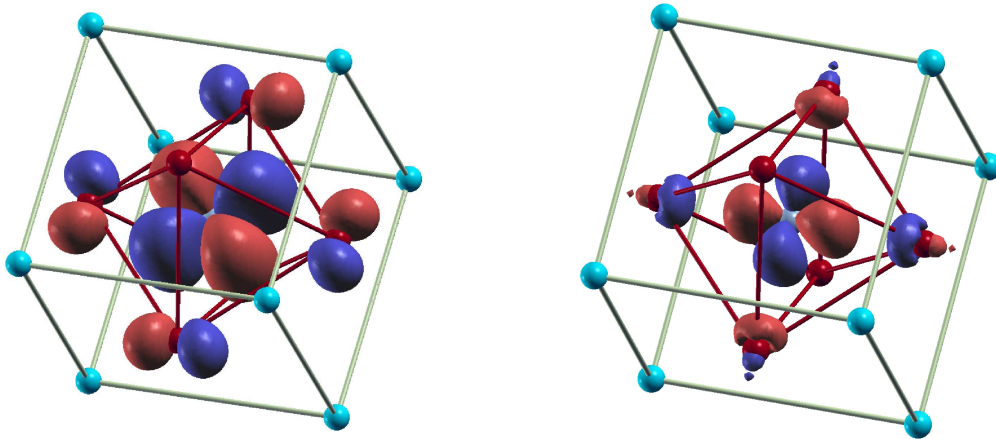


Figure 10.6: Isosurface plot of the  $t_{2g}$ -like MLWF  $d_{xy}$  for  $\text{SrVO}_3$  calculated with spin-orbit coupling. Left: Spin-up component (real part), isosurface= $\pm 0.05$ . Right: Spin-down component (imaginary part), isosurface= $\pm 0.001$ . The color of the isosurface refers to the sign: Positive for dark red and negative for dark blue. Red balls: O sites, cyan balls: Sr sites, V site at the center. The WFs were plotted using the program XCrySDen [139].

a second calculation using an  $8 \times 8 \times 8$ -mesh of  $k$ -points. This yielded hoppings identical to those of the previous calculation, but a slightly smaller spread of  $6.73 \text{ a.u.}^2$  per orbital. This latter difference is attributed to the fact that the spread was calculated via the finite difference formulae Eqns. (10.12, 10.13).

### 10.8.3 Graphene

A single layer of graphene was calculated within the FLEUR film mode. The muffin-tin radii and the plane wave cut-off were chosen to be  $1.28 \text{ a.u.}$  and  $4.6 \text{ a.u.}^{-1}$ , respectively. The C-C bond length was assumed to be  $2.72 \text{ a.u.}$ . We used the exchange-correlation potential of Perdew, Burke, and Ernzerhof [64]. MLWFs and first-guess WFs were constructed for the four valence bands using an  $8 \times 8$   $k_{\parallel}$ -mesh in the two-dimensional Brillouin zone. Graphene is a covalently bonded system. Consequently, one expects that the MLWFs are bond centered. Actually, the four valence bands do not constitute an isolated group of bands as they touch an unoccupied band at the  $\bar{K}$ -point. Avoiding the  $\bar{K}$ -point when choosing the uniform  $k_{\parallel}$ -mesh, disentangling is not necessary, however. For the construction of the first-guess WFs, two calculations were performed: In one calculation the localized functions  $|g_n\rangle$  corresponding to the  $sp^2$ -bonds were chosen to be restricted to the muffin-tin sphere of only one atom (FWF1), while they were restricted in the second calculation (FWF2) to the muffin-tins of the two atoms participating in the covalent bonding. The FWF2s were nearly identical with the MLWFs, having the same centers and negligibly different spreads, in particular. The FWF1s are not centered in the middle of the C-C-bond, the FWF2s are, however, centered. Irrespective of the starting point (i.e., either FWF1 or FWF2) we arrive at the same MLWFs, which are bond centered.

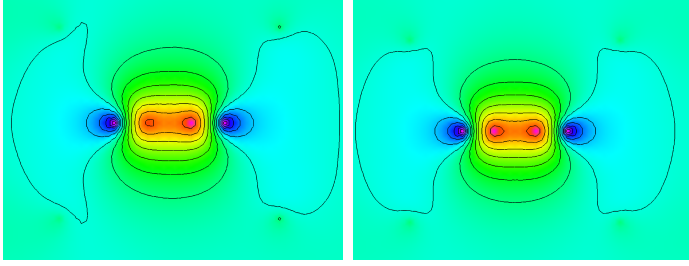


Figure 10.7: Contour plot of the FWF1 (left) and MLWF (right) of an  $sp^2$ -bond of graphene.

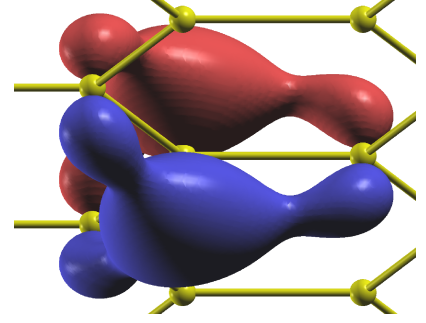


Figure 10.8: Isosurface plot of the  $\pi$ -orbital of graphene. Isosurface= $\pm 0.1$

Table 10.3: Centers and spreads of the first-guess (first row) and maximally localized (second row) WFs (atomic units).

	$x$	$y$	$z$	$\langle \mathbf{r}^2 \rangle$
FWF1 ( $sp^2$ )	2.038	1.169	0.000	2.184
FWF1 ( $sp^2$ )	2.038	-1.169	0.000	2.184
FWF1 ( $sp^2$ )	4.064	0.000	0.000	2.184
FWF1 ( $\pi$ )	2.714	0.000	0.000	10.526
MLWF ( $sp^2$ )	2.035	1.175	0.000	2.052
MLWF ( $sp^2$ )	2.035	-1.175	0.000	2.052
MLWF ( $sp^2$ )	4.070	0.000	0.000	2.052
MLWF ( $\pi$ )	2.714	0.000	0.000	10.075

Figure 10.7 shows the contour plot of one of the three  $sp^2$ -bonds for the first-guess FWF1 and for the MLWF. Figure 10.8 shows the  $\pi$ -orbital. Centers and spreads are given in Table 10.3. The initial spread of 17.08 a.u.<sup>2</sup> characterizing the first-guess FWF1 is reduced by the minimization procedure to a final total spread of 16.23 a.u.<sup>2</sup>.

The hopping matrix elements  $H_{m,m'}(\mathbf{R}_1 - \mathbf{R}_2)$ , Eq. (10.48), are listed in Table 10.4. There is no coupling between the  $\pi$  WFs and the  $sp^2$  WFs.

### 10.8.4 Platinum

In the following we discuss the MLWFs for a Platinum chain. Our calculations were performed with the one-dimensional version [140] of the FLEUR program and with spin-orbit coupling [141, 142, 143, 144]. The extensions necessary to treat the spin-orbit case have been described in section 10.4. The muffin-tin radii and the plane wave cut-off were chosen to be 2.22 a.u. and 3.7 a.u.<sup>-1</sup>, respectively. The RPBE [145] exchange-correlation potential was used. The relaxed Pt-Pt distance is given by 4.48 a.u.. We calculated 12 MLWFs corresponding to the  $s$ - and  $d$ -states of Platinum using 8  $k$ -points. The localized trial orbitals were chosen to be eigenstates of the  $z$ -projection of the spin operator. Both

Table 10.4: Hopping matrix elements of graphene. Energies are in meV. 00, 10, 11 and 20 denote the translations of the orbitals in units of the primitive translations.

	00	10	11	20
$sp^2(1), sp^2(1)$	-15038	560.7	6.6	51.3
$sp^2(1), sp^2(2)$	-2139	78.0	-21.5	7.4
$sp^2(1), sp^2(3)$	-2139	-144.1	2.5	-19.9
$sp^2(2), sp^2(1)$	-2139	-529.8	-21.5	-21.5
$sp^2(2), sp^2(2)$	-15038	-109.7	6.6	-6.7
$sp^2(2), sp^2(3)$	-2139	78.0	2.5	7.4
$sp^2(3), sp^2(1)$	-2139	-2139.1	78.0	-144.1
$sp^2(3), sp^2(2)$	-2139	-529.8	78.0	-21.5
$sp^2(3), sp^2(3)$	-15038	560.7	-16.4	51.3
$\pi, \pi$	-8329	-728.0	162.9	51.6

Table 10.5: Platinum chain: Spreads of the MLWFs (atomic units).

	$d_{xz}$	$d_{3x^2-r^2}$	$d_{xy}$	$sp$
$\langle \mathbf{r}^2 \rangle$	3.336	2.416	2.326	4.952

the direction of the chain and the spin-quantization axis are given by the  $z$ -direction. We chose the angular parts of the trial-orbitals for the  $d$ -bands to be  $d_{3x^2-r^2}$ ,  $d_{3y^2-r^2}$ , (i.e.,  $d_{3z^2-r^2}$  rotated to be coaxial with the  $x$ - and  $y$ -directions, respectively),  $d_{xy}$ ,  $d_{xz}$  and  $d_{yz}$ . The localized trial orbital corresponding to the  $sp$ -like WF was constructed as a linear combination of two localized  $s$ -orbitals on neighboring atoms. The MLWFs are spinor-valued and complex. 6 out of the 12 MLWFs are characterized by a dominance of the spin-up component while the spin-down component dominates the other 6 MLWFs. The two groups of spin-up and spin-down dominated WFs are symmetric by interchange of spins. Hence we will consider only the 6 spin-up dominated WFs in the following, unless explicitly stated. The angular dependencies of the real parts of the dominating spin-up components are approximately given by  $d_{xz}$  and  $d_{yz}$ ,  $d_{3x^2-r^2}$  and  $d_{3y^2-r^2}$ ,  $d_{xy}$ , and  $sp$ . The MLWFs  $d_{xz}$ ,  $d_{yz}$  and  $d_{3x^2-r^2}$ ,  $d_{3y^2-r^2}$  are symmetry equivalent, respectively. The  $sp$ -like WF is positioned bond-centered between two neighboring Pt-atoms. The angular functions that approximately describe the imaginary part of the spin-up component as well as the real and imaginary parts of the spin-down components agree very well qualitatively with the results of our simple model of section 10.4 given in Table 10.1. We found qualitative deviations only for the  $d_{3y^2-r^2}$ -orbital (and the symmetry-equivalent  $d_{3x^2-r^2}$ -orbital) shown in Figure 10.9: While Table 10.1 predicts the real part of the spin-down component belonging to the  $d_{3y^2-r^2}$ -orbital to vanish, it turns out to be non-vanishing and  $d_{xz}$ -like. This may be attributed to the fact that the actual  $d_{3y^2-r^2}$ -like orbital is not rotationally invariant around the  $y$ -axis, but rather squeezed in  $x$ -direction. The  $d_{xy}$ -like WF is shown in Figure 10.10. As there is no spin-orbit coupling for  $s$ -states the spin-down component of the  $sp$ -like WF, which is shown in Figure 10.11, is  $p$ -like.

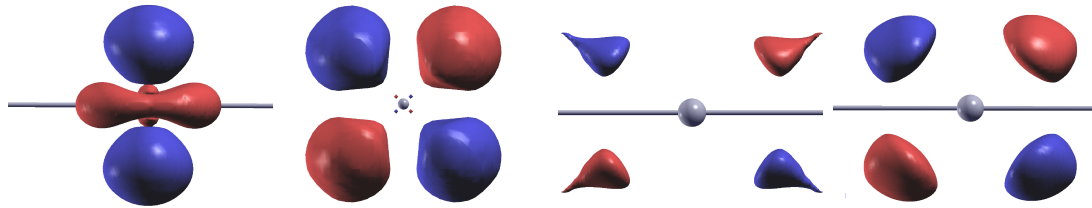


Figure 10.9:  $d_{3y^2-r^2}$ -like orbital of a one-dimensional Pt-chain. From left to right: Real part of spin-up component ( $d_{3y^2-r^2}$ , Isosurface= $\pm 0.1$ ), imaginary part of spin-up component ( $d_{xy}$ , Isosurface= $\pm 0.001$ ). Real part of spin-down component ( $d_{xz}$ , Isosurface= $\pm 0.00073$ ), imaginary part of spin-down component ( $d_{yz}$ , Isosurface= $\pm 0.0025$ ).

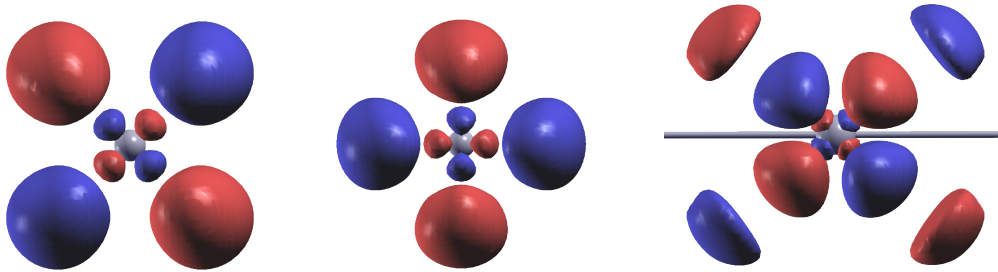


Figure 10.10:  $d_{xy}$ -like orbital of a one-dimensional Pt-chain. From left to right: Real part of spin-up component ( $d_{xy}$ , Isosurface= $\pm 0.2$ ), imaginary part of spin-up component ( $d_{x^2-y^2}$ , Isosurface= $\pm 0.005$ ), real part of spin-down component ( $d_{yz}$ , Isosurface= $\pm 0.001$ ).

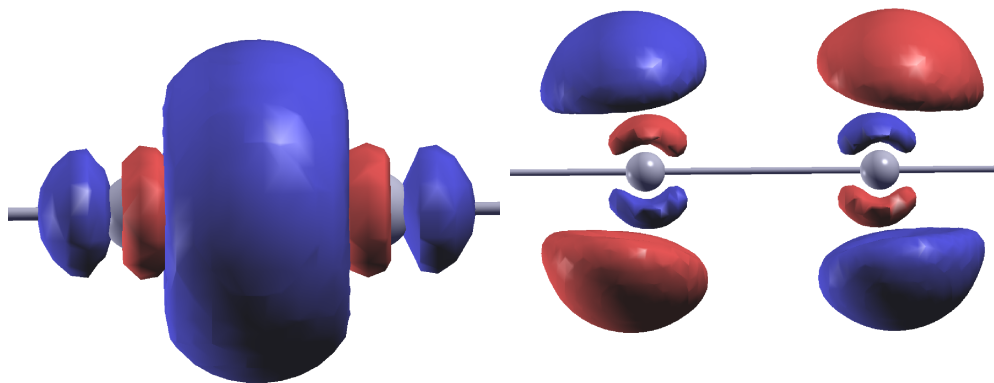


Figure 10.11:  $sp$ -like orbital of a one-dimensional Pt-chain. Left: real part of spin-up component ( $sp$ , Isosurface= $\pm 0.04$ ), Right: real part of spin-down component ( $p_x$ , Isosurface= $\pm 0.004$ ).

Table 10.6: Platinum chain: Spin-resolved nearest neighbor hopping matrix elements for the spin-up dominated MLWFs between identical orbitals (meV).

	$d_{xz}, d_{xz}$	$d_{3x^2-r^2}, d_{3x^2-r^2}$	$d_{xy}, d_{xy}$	$s, s$
$\uparrow, \uparrow$	1170.9	-548.8	-269.7	-2481.7
$\uparrow, \downarrow$	-0.1	0.4	-0.1	29.3
$\downarrow, \downarrow$	1.0	-0.6	-0.7	-21.3

Table 10.7: Platinum chain: Spin-resolved on-site hopping matrix elements between spin-up and spin-down dominated MLWFs (meV).

	$d_{xz}^\uparrow, d_{3x^2-r^2}^\downarrow$	$d_{3y^2-r^2}^\uparrow, d_{yz}^\downarrow$	$d_{xz}^\uparrow, d_{xy}^\downarrow$	$d_{xy}^\uparrow, d_{xz}^\downarrow$
$\uparrow, \uparrow$	-142	134	10	-6
$\uparrow, \downarrow$	460	460	268	268
$\downarrow, \uparrow$	0	0	0	0
$\downarrow, \downarrow$	134	-142	-6	10

Table 10.8: Platinum chain: Spin-resolved nearest neighbor hopping matrix elements between spin-up and spin-down dominated MLWFs (meV).

	$d_{xz}^\uparrow, d_{3x^2-r^2}^\downarrow$	$d_{3y^2-r^2}^\uparrow, d_{yz}^\downarrow$	$d_{xz}^\uparrow, d_{xy}^\downarrow$	$d_{xy}^\uparrow, d_{xz}^\downarrow$
$\uparrow, \uparrow$	33	0.8	5.6	-9.0
$\uparrow, \downarrow$	9.8	9.8	7.5	7.5
$\downarrow, \uparrow$	0	0	0	0
$\downarrow, \downarrow$	0.8	33	-9.0	5.6

Table 10.5 lists the spreads. The maximal localization procedure reduces the initial total spread of 195.72 a.u.<sup>2</sup> to a final total spread of 37.56 a.u.<sup>2</sup>.

In Table 10.6 we list the spin-resolved nearest neighbor hopping matrix elements for the spin-up dominated MLWFs between identical orbitals calculated according to Eq. (10.54). As the  $(\downarrow, \downarrow)$  components scale quadratically with the admixture of spin-down to the spin-up dominated WFs, they are small. Likewise the  $(\uparrow, \downarrow)$  components are found to be small: The angular distributions of the spin-down components of the WFs differ from those of the spin-up components, the admixture of spin-down is small, and the spin-orbit coupling, which couples the two spin-channels, is important only close to the nuclear cores and hence the coupling between functions well-localized on different atoms is small. For the on-site hopping matrix elements, however, the  $(\uparrow, \downarrow)$ - or  $(\downarrow, \uparrow)$ -components can dominate, because the two WFs are centered on the same atoms in this case, and their overlap close to the nuclear cores can be large. In Table 10.7 we list a selection of spin-resolved on-site hopping matrix elements that are dominated by hopping from spin-up into spin-down, which is mediated by spin-orbit coupling.  $d_{xz}^\uparrow$  is a spin-up dominated  $d_{xz}$ -like WF. According to Table 10.1 the spin-orbit interaction provides a coupling to  $d_{x^2-y^2}|\downarrow\rangle$ , which overlaps with  $d_{3x^2-r^2}^\downarrow$ . Analogously, there is a transition from  $d_{3y^2-r^2}^\uparrow$  to  $d_{yz}|\downarrow\rangle$ , which overlaps with  $d_{yz}^\downarrow$ . The other two examples in Table 10.7 are easily interpreted analogously on the basis of Table 10.1. The  $(\downarrow, \uparrow)$ -contributions in Table 10.7 are negligibly small, because the  $|\downarrow\rangle$ - and  $|\uparrow\rangle$ -components of the spin-up and spin-down dominated WFs are small, respectively. Table 10.8 is analogous to Table 10.6, but now for the nearest neighbor hoppings. The comparison of the two Tables shows that the  $(\uparrow, \downarrow)$ -contributions decay fastest, which is consistent with the facts that the spin-orbit coupling is strongest close to the nuclei, and that the WFs are well localized.

### 10.8.5 Ferroelectricity of BaTiO<sub>3</sub>

Thin films of BaTiO<sub>3</sub> may be grown epitaxially on SrTiO<sub>3</sub> [146] and are tetragonally distorted due to the in-plane epitaxial strain. We calculate the ferroelectric polarization of the corresponding tetragonally distorted phase of BaTiO<sub>3</sub>. The in-plane lattice constant is set to the lattice constant of SrTiO<sub>3</sub> ( $a = 7.46$  a.u.). The lattice constant perpendicular ( $c$ ) as well as the positions of all atoms in the unit-cell were determined by a series of force and total energy calculations. For Ba, Ti and O, muffin-tin radii of 2.2 a.u., 2.0 a.u. and 1.3 a.u. were used, respectively. The plane wave cut-off was chosen to be 4.8 a.u.<sup>-1</sup>. Using the exchange correlation potential of Perdew and Wang [147] we obtained a  $c/a$  ratio of 1.07, in reasonable agreement with experimental data [146]. The resulting atomic positions are given in Table 10.9 and the crystal structure of BaTiO<sub>3</sub> is illustrated in Figures 10.12 and 10.13. Compared to the cubic perovskite structure, the oxygen atoms are moved out of the face centers and the cube is elongated in  $z$ -direction.  $z$ -reflection symmetry is lost.  $\Delta\tau$  in Table 10.9 specifies the displacement in  $z$ -direction of the oxygen and titanium atoms from the symmetric positions in the face centers and the center of the cuboid, respectively. The displacements of the oxygen atoms are larger than those of titanium. The apical oxygen atoms exhibit a larger displacement than the basal ones.



We calculated MLWFs separately for the 9 oxygen  $p$ -bands, the 3 barium  $p$ -bands, the 3 oxygen  $s$ -bands, the one barium  $s$ -band, and the 3 titanium  $p$ -bands (the remaining electrons were treated as core electrons), which is possible as these five groups of bands are well separated in energy. A uniform  $k$ -point mesh of  $16 \times 16 \times 16$   $k$ -points was used. As final spread, Eq. (10.9),  $48.03 \text{ a.u.}^2$  were obtained for the 9 oxygen  $p$  MLWFs, while the spread of the first-guess WFs was  $48.08 \text{ a.u.}^2$ , suggesting that first-guess WFs and MLWFs are nearly identical for  $\text{BaTiO}_3$ . Figures 10.12 and 10.13 show the isosurfaces of the resulting MLWFs for the oxygen  $p$ -states. The MLWFs clearly reflect the broken  $z$ -reflection symmetry: Especially the apical oxygen  $p$ -orbitals are strongly distorted in  $z$ -direction. The apical O- $p$ -orbitals may be classified according to their symmetry with respect to the vertical Ti-O-Ti axis into one  $\sigma$  and two  $\pi$  orbitals. The  $\sigma$  orbital shows a strong hybridization with the titanium  $d_{z^2}$  orbital, while the two  $\pi$ -orbitals mainly hybridize with titanium  $d_{zx}$  and  $d_{yz}$  orbitals. Similarly, the basal oxygen  $p$ -orbitals mainly hybridize with the titanium  $d$ -states.

Table 10.10 lists the coordinates of the centers of the MLWFs along with their deviations  $\Delta z$  from the ion sites. According to Eq. (10.115) these deviations of the centers of the MLWFs determine the anomalous contribution to the polarization. As seen in table 10.10 the apical oxygen-MLWFs exhibit the largest response to the distortion of the crystal and the two  $\pi$ -orbitals are displaced stronger than the  $\sigma$ -orbital. Interestingly, not all orbitals contribute with the same sign to the anomalous contribution. In fact, the sum of positive Wannier center displacements is  $0.856 \text{ a.u.}$  while the sum of negative displacements is  $-0.165 \text{ a.u.}$ , showing that the total electronic polarization is the result of complex effects, which are partially compensating each other. The sum of displacements of the  $p$ -orbitals at the apical oxygen is  $0.657 \text{ a.u.}$ , while it is only  $0.003 \text{ a.u.}$  at the basal oxygens. Thus, the apical oxygen  $p$ -states contribute 95% to the anomalous contribution to the polarization. Applying Eq. (10.113) we find a polarization of  $48.9 \mu\text{C}/\text{cm}^2$  in excellent agreement with experimental data [146] of  $43 \mu\text{C}/\text{cm}^2$  for the case of thin  $\text{BaTiO}_3$  layers grown on  $\text{SrTiO}_3$ . The anomalous contribution (Eq. (10.115)) to the polarization due to the displacements of the centers of the MLWFs with respect to the centers of the atoms amounts to 36% of the total value of the polarization.

In order to assess convergence of the results with respect to the number of  $k$ -points a comparative calculation was performed using an  $8 \times 8 \times 8$   $k$ -point mesh. This calculation yielded a final spread of  $47.19 \text{ a.u.}^2$  for the MLWFs of the 9 oxygen  $p$  bands and a total polarization of  $48.6 \mu\text{C}/\text{cm}^2$ . We assume these small differences to be finite difference errors introduced by using formulae Eqns. (10.12, 10.13).

### 10.8.6 Ferroelectricity of $\text{PbTiO}_3$

In the following the ferroelectric polarization of bulk  $\text{PbTiO}_3$  in the cubic perovskite structure will be discussed. Muffin-tin radii of  $2.1 \text{ a.u.}$ ,  $1.95 \text{ a.u.}$  and  $1.35 \text{ a.u.}$  were used for Pb, Ti and O, respectively. The plane-wave cutoff was set to  $4.5 \text{ a.u.}^{-1}$  and the GGA of Wu and Cohen [148] was used. The FLAPW basis set was supplemented with local orbitals for the Ti- $p$  and the Pb- $d$  semicore states. The relaxed atomic coordinates are given in

Table 10.9: Positions of the Ba, Ti and O ions in the constrained ferroelectric perovskite BaTiO<sub>3</sub> (atomic units). For the O ions,  $\Delta\tau$  is the displacement from the face centers. For the Ti ion,  $\Delta\tau$  specifies the displacement from the center of the cuboid.

	$x$	$y$	$z$	$\Delta\tau$
Ba	0.000	0.000	0.000	0.000
Ti	3.730	3.730	3.901	-0.092
O	3.730	3.730	0.449	0.449
O	3.730	0.000	4.284	0.292
O	0.000	3.730	4.284	0.292

Table 10.10: BaTiO<sub>3</sub>: Coordinates, displacements and spreads of the MLWFs (atomic units).

	$x$	$y$	$z$	$\Delta z$	$\langle \mathbf{r}^2 \rangle$
O ( $pz$ )	3.730	3.730	0.629	0.181	4.75
O ( $px$ )	3.730	3.730	0.686	0.238	5.69
O ( $py$ )	3.730	3.730	0.686	0.238	5.69
O ( $pz$ )	3.730	0.000	4.296	0.012	5.69
O ( $px$ )	3.730	0.000	4.300	0.016	5.53
O ( $py$ )	3.730	0.000	4.255	-0.029	4.73
O ( $pz$ )	0.000	3.730	4.296	0.012	5.69
O ( $px$ )	0.000	3.730	4.255	-0.029	4.73
O ( $py$ )	0.000	3.730	4.300	0.016	5.53
Ba ( $pz$ )	0.000	0.000	-0.047	-0.047	6.03
Ba ( $px$ )	0.000	0.000	-0.011	-0.011	6.15
Ba ( $py$ )	0.000	0.000	-0.011	-0.011	6.15
O ( $s$ )	3.730	3.730	0.542	0.095	2.77
O ( $s$ )	3.730	0.000	4.305	0.021	2.64
O ( $s$ )	0.000	3.730	4.305	0.021	2.64
Ba ( $s$ )	0.000	0.000	0.000	0.000	3.20
Ti ( $pz$ )	3.730	3.730	3.863	-0.038	1.48
Ti ( $px$ )	3.730	3.730	3.905	0.003	1.47
Ti ( $py$ )	3.730	3.730	3.905	0.003	1.47

Table 10.11: Positions of the Pb, Ti and O ions in the ferroelectric perovskite PbTiO<sub>3</sub> (atomic units). For the O ions,  $\Delta\tau$  is the displacement from the face centers. For the Ti ion,  $\Delta\tau$  specifies the displacement from the center of the cuboid.

	$x$	$y$	$z$	$\Delta\tau$
Pb	0.000	0.000	0.000	0.000
Ti	3.667	3.667	4.152	0.235
O	3.667	0.000	4.778	0.862
O	0.000	3.667	4.778	0.862
O	3.667	3.667	0.783	0.783



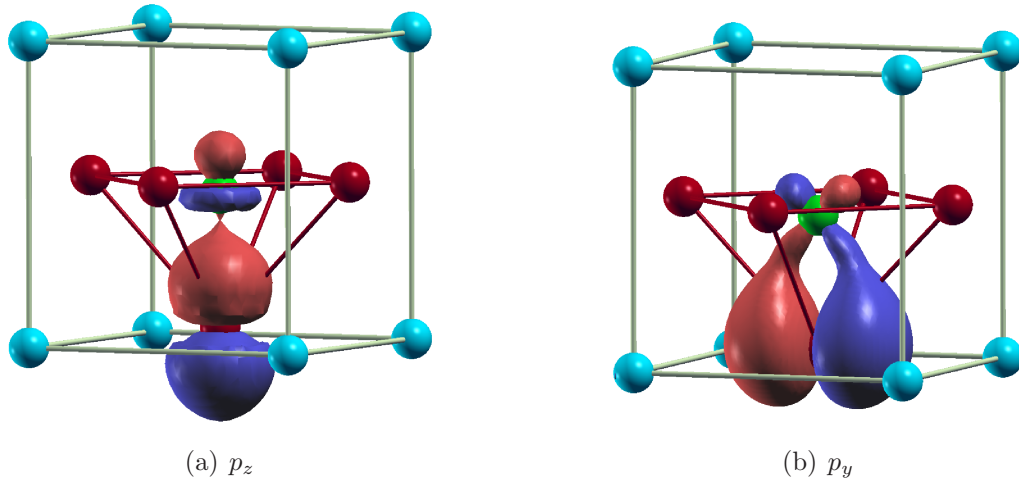


Figure 10.12: MLWFs  $O(p_z)$  and  $O(p_y)$  for the apical oxygen site close to  $xy$ -plane in  $\text{BaTiO}_3$ . Isosurface= $\pm 0.05$ . Red balls in the face centers: O sites, cyan balls at the corners: Ba sites, green ball at the center: Ti site. The O site above the upper face of the cuboid is not depicted. The hybridization of the oxygen  $p$ -orbitals with the titanium  $d$ -orbitals is clearly visible and results in a strong distortion of the MLWFs.

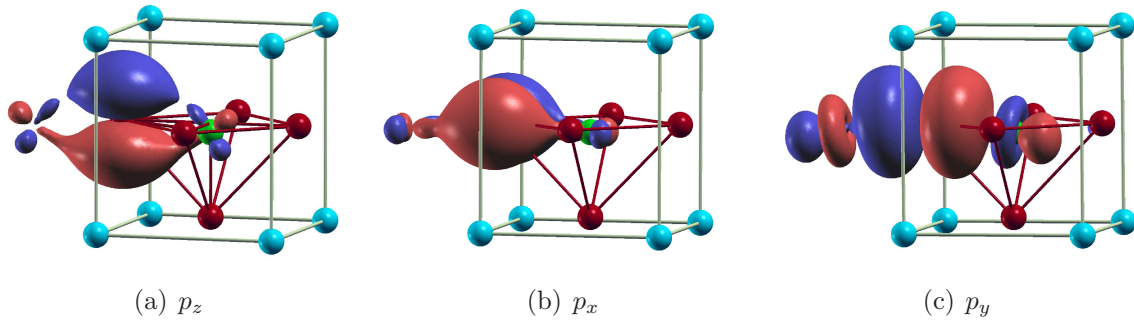


Figure 10.13: MLWFs  $O(p_z)$ ,  $O(p_x)$ , and  $O(p_y)$  for the basal oxygen sites close to  $xz$ -plane in  $\text{BaTiO}_3$ . Isosurface= $\pm 0.05$ . Red balls in the face centers: O sites, cyan balls at the corners: Ba sites, green ball at the center: Ti site.

Table 10.12: Contributions to the polarization of  $\text{PbTiO}_3$ .

	Ti- $p$	O- $s$	Pb- $d$	Pb- $s$	O- $p$	Ions	Total
$P[\mu\text{C}/\text{cm}^2]$	0.96	-16.58	13.47	12.41	-40.74	-55.41	-85.88

Table 10.11.

We calculated maximally localized Wannier functions for the following groups of bands, which are all well separated in energy from neighboring groups of bands: Ti-*p*, O-*s*, Pb-*d*, Pb-*s*, O-*p*. In table 10.12 we list the orbital contributions to the anomalous polarization. Like in BaTi<sub>3</sub> the dominant contribution to the anomalous polarization stems from the O-*p* orbitals. The Pb-*s* lone pair reduces the total polarization, because its sign is opposite to the sign of the total polarization. Likewise, the Pb-*d* semicore states reduce the total polarization. In order to calculate the ionic contribution to the polarization we assigned nominal charges of +4 to titanium, +2 to lead and -2 to oxygen. The anomalous contribution to the polarization is  $-30.48\mu\text{C}/\text{cm}^2$  and amounts to 35.5% of the total polarization of  $-85.88\mu\text{C}/\text{cm}^2$ .

### 10.8.7 Ferroelectricity of HoMnO<sub>3</sub>

Only phases which are not inversion symmetric can exhibit a spontaneous ferroelectric polarization. In our previous examples of ferroelectric polarization inversion symmetry was already violated by the geometry, i.e., the positions of the atoms. In magnetic systems, a spontaneous ferroelectric polarization may also occur even for an inversion symmetric geometry [149], if the magnetic structure violates inversion symmetry. In these cases the ferroelectricity is magnetically induced [150]. A special case of magnetically induced ferroelectricity occurs in cycloidal spin structures due to the spin-orbit interaction, e.g. in orthorhombic TbMnO<sub>3</sub> [151]. Of course, the violation of inversion symmetry by the magnetic structure has in general the consequence that the inversion symmetric configuration does not correspond to a minimum of the total energy of the crystal and is hence merely hypothetical. However, the deviation of the equilibrium geometry from the inversion symmetric one usually increases the spontaneous ferroelectric polarization. Furthermore, if ferroelectricity is magnetically induced the ionic contribution to the polarization is often smaller than the anomalous contribution.

As an example for magnetically induced ferroelectricity, we consider the orthorhombic manganite HoMnO<sub>3</sub>. We first consider the AFM-A phase, which is illustrated in Fig. 10.14. The AFM-A phase is inversion symmetric and does not exhibit a spontaneous ferroelectric polarization. As seen in Fig. 10.14 the intraplanar coupling is ferromagnetic. Neighboring planes are coupled antiferromagnetically. Each Mn-4*d*-shell is occupied by 4 electrons of the same spin. The charges of the ions within the point charge model are Ho:+3, Mn:+3, O:-2. We now rotate the magnetic moments into the magnetic configuration of the AFM-E phase while keeping the positions of the atoms fixed. The AFM-E phase shows in-plane FM zigzag chains antiferromagnetically coupled to the neighboring chains, as illustrated in Fig. 10.15. The interplanar coupling is AFM. As said before, we assume that the atoms have the coordinates of the AFM-A structure, and consequently this (hypothetical) geometry is invariant under space inversion. However, the magnetic structure does not exhibit inversion symmetry. For the calculation of this AFM-E configuration 8 formula units of HoMnO<sub>3</sub> are needed, i.e., the unit cell contains 40 atoms. In order to calculate the AFM-A phase, 4 formula units, i.e., 20 atoms, suffice. We may view the orientations of the magnetic

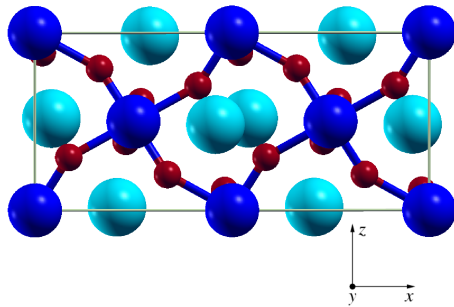


Figure 10.14: AFM-A phase of  $\text{HoMnO}_3$ . Blue balls: Mn with spin up. Red balls: O. Cyan balls: Ho. We show only one plane. The Mn are coupled ferromagnetically in each plane. In the AFM-A phase neighboring planes are coupled antiferromagnetically.

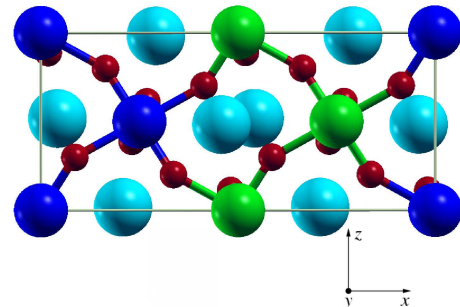


Figure 10.15: AFM-E phase of  $\text{HoMnO}_3$ . Blue balls: Mn with spin up. Green balls: Mn with spin down. Red balls: O. Cyan balls: Ho. The Mn atoms with spin up (blue) form one FM zigzag chain. Likewise, the Mn atoms with spin down (green) form a FM zigzag chain. We show only one plane. In the AFM-E phase neighboring planes are coupled antiferromagnetically.

moments to be described by the parameter  $\xi$  of the Hamiltonian, which was introduced in Eq. (10.73). Following the adiabatic path in  $\xi$ -space, which connects the AFM-A and AFM-E magnetic configurations, inversion symmetry is lost and a spontaneous ferroelectric polarization is induced. The mechanism behind the spontaneous polarization is the asymmetry of the hybridization of the states of a given atom with the states of neighboring atoms, which have different magnetic moments. This asymmetry of the hybridization leads to an asymmetry of the Wannier center displacement vectors, which gives rise to a spontaneous anomalous polarization according to Eq. (10.115). To see this we sketch the directions of the Wannier center displacement vectors for the AFM-A phase in Fig. 10.16 and for the AFM-E phase in Fig. 10.17. Only the displacements of the centers of oxygen- $p$ -orbitals are discussed in the figures. Due to the hybridization of the oxygen- $p$ -orbitals mainly with Mn- $d$ -states the centers of mass of the WF-orbitals are shifted away from the nuclear positions. In Fig. 10.16 the sum of displacements is zero, because the hybridization with the Mn- $d$ -states of neighboring atoms is symmetric. However, in Fig. 10.17 the sum of displacements is not zero, since the hybridization with the Mn- $d$ -states of neighboring atoms is asymmetric for those oxygens, which have one spin-up and one spin-down Mn atom as nearest neighbor. As suggested by the figure, the  $z$ -components of the displacement vectors do not cancel, and a net-displacement in  $z$ -direction results, which gives rise to an anomalous polarization in  $z$ -direction. Similarly, the sum of the centers of mass of the Mn- $d$ -orbitals may deviate from the nuclear position of Mn due to the asymmetric hybridization in the AFM-E phase.

We generated Wannier functions for the AFM-E phase of  $\text{HoMnO}_3$  using a  $8 \times 8 \times 8$

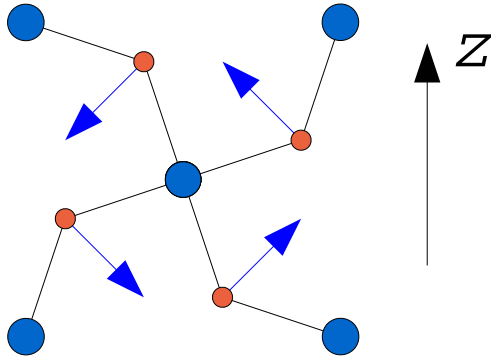


Figure 10.16: AFM-A phase of  $\text{HoMnO}_3$ . Blue balls: Mn. Mn atoms are coupled ferromagnetically in each plane. Red balls: O. We show only one plane. The Mn are coupled ferromagnetically in each plane. Blue arrows indicate the direction of the displacement vector of the Wannier centers of the oxygen- $p$ -orbitals with respect to the oxygen nuclear positions.

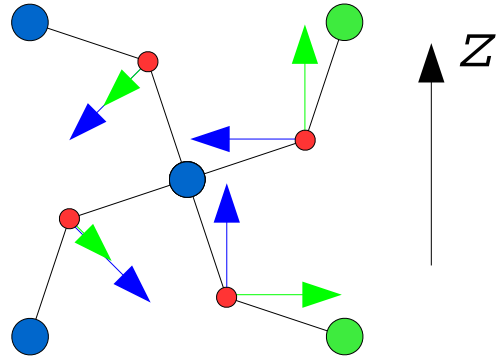


Figure 10.17: AFM-E phase of  $\text{HoMnO}_3$ . Blue balls: Mn with spin up. Green balls: Mn with spin down. Red balls: O. The Mn atoms with spin up (blue) form one FM zigzag chain. Likewise, the Mn atoms with spin down (green) form a FM zigzag chain. We show only one plane. Blue (green) arrows indicate the direction of the displacement vector of the Wannier centers of the spin-up (spin-down) oxygen- $p$ -orbitals with respect to the oxygen nuclear positions.

$k$ -mesh. The following groups of bands are separated in energy and for each group Wannier functions were calculated: 5p bands of Ho (24 Wannier functions per spin; 5p bands of Ho were treated as local orbitals). 2s bands of O (24 Wannier functions per spin). 2p bands of O (72 Wannier functions per spin). 4d  $t_{2g}$ -like bands of Mn (12 Wannier functions per spin). 4d  $e_g$ -like bands of Mn (4 Wannier functions per spin). In Table 10.13 we list the contributions of the 5 groups of orbitals to the anomalous polarization. If the atomic coordinates of AFM-A are used together with the magnetic configuration of AFM-E the largest contribution to the polarization stems from the Mn- $d(e_g)$  orbitals. Interestingly, the contributions of the Mn- $d(t_{2g})$  orbitals and the O- $p$  orbitals have the opposite sign and reduce the total polarization. For comparison we list the polarization of the relaxed AFM-E phase [150]. While the dominant contribution still comes from the Mn- $d(e_g)$  group, this contribution is now smaller and almost compensated by the contribution of the Mn- $d(t_{2g})$  group. The contribution of the O- $p$  group is larger in magnitude and has the same sign as the total anomalous polarization. In the case of the relaxed AFM-E structure the ionic contribution to the polarization is  $2.09 \mu\text{C}/\text{cm}^2$  and smaller than the anomalous contribution. Adding anomalous and ionic contributions, the total polarization for relaxed AFM-E is found to be  $5.61 \mu\text{C}/\text{cm}^2$ .

Table 10.13: Decomposition of the anomalous polarization into the contributions of groups of Wannier orbitals.  $P$ : Polarization of  $\text{HoMnO}_3$  in the AFM-E magnetic configuration, but with the atomic coordinates of AFM-A.  $P_{\text{relaxed}}$ : Polarization of  $\text{HoMnO}_3$  in the AFM-E magnetic configuration with the atomic coordinates of relaxed AFM-E.

	Ho- $p$	O- $s$	O- $p$	Mn- $d$ ( $t_{2g}$ )	Mn- $d$ ( $e_g$ )	Total (spin up)
$P[\mu\text{C}/\text{cm}^2]$	0.008	-0.048	-0.671	-1.226	3.136	1.20
$P_{\text{relaxed}}[\mu\text{C}/\text{cm}^2]$			1.51	-2.42	2.67	1.76

Table 10.14: Centers and spreads (atomic units) of the MLWFs corresponding to the  $p$ -bands of a Bismuth bilayer.

	$\langle x \rangle$	$\langle y \rangle$	$\langle z \rangle$	$\langle \mathbf{r}^2 \rangle$
1	-4.967	0.000	2.095	11.202
2	-4.822	0.000	1.723	12.662
3	-5.004	0.000	1.721	12.615
4	-4.967	0.000	2.095	11.202
5	-4.822	0.000	1.723	12.662
6	-5.004	0.000	1.721	12.615
7	4.967	0.000	-2.095	11.202
8	4.822	0.000	-1.723	12.662
9	5.004	0.000	-1.721	12.615
10	4.967	0.000	-2.095	11.202
11	4.822	0.000	-1.723	12.662
12	5.004	0.000	-1.721	12.615

Table 10.15: Centers and spreads (atomic units) of the MLWFs corresponding to the  $p$ -bands of a Bismuth bilayer.

	$\langle x \rangle$	$\langle y \rangle$	$\langle z \rangle$	$\langle \mathbf{r}^2 \rangle$
1	-5.100	0.291	1.812	12.204
2	-4.595	0.000	1.812	12.204
3	-5.100	-0.291	1.812	12.204
4	-5.100	0.291	1.812	12.204
5	-4.595	0.000	1.812	12.204
6	-5.100	-0.291	1.812	12.204
7	5.100	0.291	-1.812	12.204
8	5.100	-0.291	-1.812	12.204
9	4.595	0.000	-1.812	12.204
10	5.100	0.291	-1.812	12.204
11	5.100	-0.291	-1.812	12.204
12	4.595	0.000	-1.812	12.204

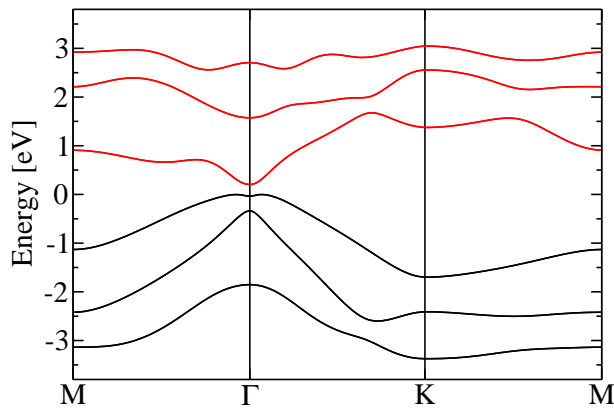


Figure 10.18: Band structure of a two-layer Bi-film

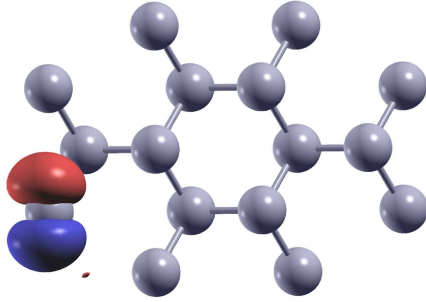


Figure 10.19: Wannier orbital of a  $p$ -state of Bi in a double layer of Bi(111). The Wannier orbital is an eigenstate of the symmetry operation of reflection at a mirror plane.

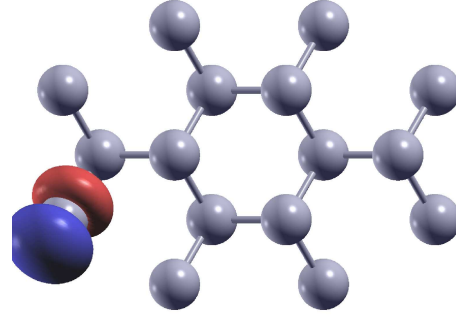


Figure 10.20: Wannier orbital of a  $p$ -state of Bi in a double layer of Bi(111). The Wannier orbital reflects the  $c_3$ -symmetry of the system.

### 10.8.8 Bi(111) Ultrathin Film: Topological Insulator

We calculated Wannier functions for an inversion symmetric two-layer Bi-film with a distance between the two layers of 3.15 a.u.. Fig. 10.19 illustrates the geometry. The in-plane lattice constant  $a$  of the hexagonal lattice was chosen to be 8.542 a.u.. The in-plane lattice vectors are  $a_1 = (\sqrt{3}/2, -1/2, 0)a$  and  $a_2 = (\sqrt{3}/2, 1/2, 0)a$ . The MT-radius was set to 2.5 a.u. and the plane-wave cutoff to 3.8 a.u.<sup>-1</sup>. The LDA exchange-correlation potential of Moruzzi, Janak and Williams [65] was used. Spin-orbit coupling was included in the calculation. We calculated 12 MLWFs corresponding to the valence  $p$  and conduction  $p$  bands. The 12 MLWFs were obtained from the 12 bands in one calculation, i.e., we did not split the computation into two, even though the conduction bands and the valence bands are separated by a gap. The centers and spreads are listed in Table 10.14. The total spread is 145.9 a.u.<sup>2</sup>. As seen in the Table, the centers and spreads of the Wannier functions reflect the inversion symmetry of the system. In Fig. 10.19 we show the real part of the spin-up component of one of the Wannier orbitals. The centers of all MLWFs lie in the  $y$ -plane and all MLWFs are eigenfunctions of the reflection at the  $y$ -plane. Clearly, the  $c_3$ -symmetry of the Bi-film is not reflected by this set of MLWFs. However, starting from first-guess WFs which reflect the  $c_3$ -symmetry of the system, the spread-minimization converges into a second different minimum. The corresponding WFs reflect the  $c_3$ -symmetry of the system, but the total spread of 146.4 a.u.<sup>2</sup> is slightly larger than for the previous set of WFs. In Table 10.15 we list the centers and spreads for this set of WFs. In Fig. 10.20 we show the real part of the spin-up component of one of the orbitals of this second set of Wannier functions. As the total spreads of the two sets are almost identical, one may expect that the decay properties of the hopping matrix elements are likewise very similar. The 12 MLWFs may be grouped into four sets containing each 3 MLWFs: MLWFs 1-6 are hosted on the first Bi-atom and MLWFs 7-12 on the second Bi-atom. MLWFs 1-3 are spin-up dominated while orbitals 4-6 are spin-down dominated. Likewise, MLWFs 7-9 are spin-up dominated while orbitals 10-12 are spin-down dominated.



In Fig. 10.18 we show the interpolated band structure of the insulating Bi-film, which we obtained from the hopping matrix elements, Eq. (10.48), by applying Eq. (10.50). We found the two sets of WFs, the c3-symmetric and the mirror-symmetric, to result in identical interpolated band structures. As stated before, we calculated the MLWFs for the entire group of twelve bands and did not split the group into two. In fact, calculating Wannier functions only for the 6 conduction bands or only for the 6 valence bands does not work reasonably well for the present system, even though valence and conduction bands are separated by a gap. For example, the convergence of the interpolated band structure to the correct band structure as the  $k$ -mesh is refined is much slower than in the calculation that treats both valence and conduction bands at the same time. The 6 valence  $p$  and the 6 conduction  $p$  bands have to be considered to form one composite group of bands, which cannot be split.

Besides the calculation of the interpolated band structure, another interesting application of the real-space Hamiltonian matrix, Eq. (10.48), is the computation of the  $Z_2$  topological number [67, 152, 153], which determines whether or not an insulator is a topological insulator. In inversion-symmetric systems the  $Z_2$  topological number may be evaluated from the parity eigenvalues of the Kramers pairs at the time-reversal-invariant momenta (TRIM) [154]. The TRIM  $\Gamma_i$  are  $k$ -points, which satisfy  $\Gamma_i = -\Gamma_i + \mathbf{G}$  for some reciprocal lattice vector  $\mathbf{G}$ . In two dimensions there are four such  $k$ -points. In time-reversal symmetric systems the bands are doubly degenerate at the TRIM. Of course, in inversion symmetric time-reversal symmetric systems the bands are doubly degenerate everywhere. In order to calculate the  $Z_2$  topological number of an inversion-symmetric two-dimensional system, one multiplies the parity eigenvalues of all occupied Kramers pairs at the four TRIM. If the result is +1 the  $Z_2$  topological number is 0. If the result is -1 the  $Z_2$  topological number is 1. For the Bi(111) ultrathin film the  $Z_2$  topological number is 1. Thus, it is a topological insulator. One may extract the parity eigenvalues at the TRIM conveniently [155] from the eigenvectors of the interpolated Hamiltonian, Eq. (10.50).

In inversion-asymmetric systems the determination of the  $Z_2$  topological number is more complicated [156]. Within a tight-binding framework the topological properties of insulators may be determined [155]. The transformation, Eq. (10.48), of the *ab initio* Hamiltonian into the Wannier function basis provides an optimal starting point for the construction of realistic tight-binding models.

## 10.9 Intrinsic anomalous Hall effect

The Hall resistivity of ferromagnetic materials depends on the external applied magnetic field and on the magnetization. The dependency of the Hall resistivity on the magnetization is due to two different effects. First, the magnetization contributes to the total magnetic induction. Second, the magnetization gives rise to an anomalous contribution to the Hall resistivity, which is often larger than the ordinary contribution. Depending on the material this anomalous contribution may be due to extrinsic or intrinsic mechanisms or both. Spin-dependent scattering of charge carriers at impurities or phonons gives rise to the extrinsic

contribution. In perfect crystals the anomalous contribution is an intrinsic scattering-free band-structure effect, which arises due to the spin-orbit interaction.

In the following we discuss the intrinsic anomalous Hall effect. In order to obtain an expression for the intrinsic anomalous Hall conductivity  $\Gamma_{xy}$  we calculate the current in  $x$ -direction, which arises due to a perturbing applied external electric field  $\mathcal{E}_y$  in  $y$ -direction. The current due to state  $|\tilde{\psi}_{\bar{\mathbf{k}},n}(\mathcal{E}_y)\rangle$  is given by

$$I_{x,\bar{\mathbf{k}},n}(\mathcal{E}_y) = \frac{e}{L_x} \langle \tilde{\psi}_{\bar{\mathbf{k}},n}(\mathcal{E}_y) | \hat{v}_x | \tilde{\psi}_{\bar{\mathbf{k}},n}(\mathcal{E}_y) \rangle = \frac{e}{L_x} \langle \tilde{\psi}_{\bar{\mathbf{k}},n}(\mathcal{E}_y) | \hat{p}_x | \tilde{\psi}_{\bar{\mathbf{k}},n}(\mathcal{E}_y) \rangle, \quad (10.117)$$

where  $L_x$  is the length of the unit cell in  $x$ -direction,  $e = -1$  is the charge of the electron and the velocity operator  $\hat{v}$  is equal to the momentum operator  $\hat{\mathbf{p}}$  due to the use of atomic units. Due to the presence of the electric field periodic boundary conditions are only used in the  $x$ - and  $z$ -directions. The corresponding two-dimensional Bloch vectors are labeled by  $\bar{\mathbf{k}}$ . The conductivity in the limit of zero electric field is given by

$$\Gamma_{xy} = \frac{1}{N} \frac{1}{L_y} \frac{1}{L_z} \sum_{\bar{\mathbf{k}}} \sum_n \frac{\partial I_{x,\bar{\mathbf{k}},n}(\mathcal{E}_y)}{\partial \mathcal{E}_y} \Big|_{\mathcal{E}_y=0}. \quad (10.118)$$

In first order with respect to the perturbing electric field  $\mathcal{E}_y$  the state  $|\tilde{\psi}_{\bar{\mathbf{k}},n}\rangle$  is related to the eigenstates  $|\psi_{\bar{\mathbf{k}},n}\rangle$  of the unperturbed Hamiltonian by

$$|\tilde{\psi}_{\bar{\mathbf{k}},n}\rangle = |\psi_{\bar{\mathbf{k}},n}\rangle + e\mathcal{E}_y \sum_{m \neq n} \frac{\langle \psi_{\bar{\mathbf{k}},m} | \hat{y} | \psi_{\bar{\mathbf{k}},n} \rangle}{E_{\bar{\mathbf{k}},n} - E_{\bar{\mathbf{k}},m}} |\psi_{\bar{\mathbf{k}},m}\rangle. \quad (10.119)$$

Using Eq. (10.119) to evaluate the conductivity, Eq. (10.118), we obtain:

$$\begin{aligned} \Gamma_{xy} &= \frac{e^2}{N} \frac{1}{V} \sum_{\bar{\mathbf{k}}} \sum_{n=1}^{N_{\text{occ}}} \sum_{m \neq n} \left[ \frac{\langle \psi_{\bar{\mathbf{k}},n} | \hat{p}_x | \psi_{\bar{\mathbf{k}},m} \rangle \langle \psi_{\bar{\mathbf{k}},m} | \hat{y} | \psi_{\bar{\mathbf{k}},n} \rangle}{E_{\bar{\mathbf{k}},n} - E_{\bar{\mathbf{k}},m}} + \frac{\langle \psi_{\bar{\mathbf{k}},n} | \hat{y} | \psi_{\bar{\mathbf{k}},m} \rangle \langle \psi_{\bar{\mathbf{k}},m} | \hat{p}_x | \psi_{\bar{\mathbf{k}},n} \rangle}{E_{\bar{\mathbf{k}},n} - E_{\bar{\mathbf{k}},m}} \right] \\ &= \frac{e^2}{N} \frac{2}{V} \Re \left\{ \sum_{\bar{\mathbf{k}}} \sum_{n=1}^{N_{\text{occ}}} \sum_{m \neq n} \frac{\langle \psi_{\bar{\mathbf{k}},n} | \hat{p}_x | \psi_{\bar{\mathbf{k}},m} \rangle \langle \psi_{\bar{\mathbf{k}},m} | \hat{y} | \psi_{\bar{\mathbf{k}},n} \rangle}{E_{\bar{\mathbf{k}},n} - E_{\bar{\mathbf{k}},m}} \right\} \\ &= \frac{e^2}{N} \frac{2}{V} \Re \left\{ \sum_{\bar{\mathbf{k}}} \sum_{n=1}^{N_{\text{occ}}} \sum_{m=N_{\text{occ}}+1}^{\infty} \frac{\langle \psi_{\bar{\mathbf{k}},n} | \hat{p}_x | \psi_{\bar{\mathbf{k}},m} \rangle \langle \psi_{\bar{\mathbf{k}},m} | \hat{y} | \psi_{\bar{\mathbf{k}},n} \rangle}{E_{\bar{\mathbf{k}},n} - E_{\bar{\mathbf{k}},m}} \right\}, \end{aligned} \quad (10.120)$$

where  $V$  is the volume of the unit cell. With the help of the commutator

$$[\hat{H}, \hat{y}]_- = -\frac{i\hbar}{m} \hat{p}_y \quad (10.121)$$

we may replace the position operator  $\hat{y}$  by the momentum operator  $\hat{p}_y$ , which allows us to



use periodic boundary conditions also in  $y$ -direction:

$$\begin{aligned}\Gamma_{xy} &= \frac{e^2}{N} \frac{2}{V} \Re \left\{ \sum_{\mathbf{k}} \sum_{n=1}^{N_{\text{occ}}} \sum_{m=N_{\text{occ}}+1}^{\infty} i \frac{\langle \psi_{\mathbf{k},n} | \hat{p}_x | \psi_{\mathbf{k},m} \rangle \langle \psi_{\mathbf{k},m} | \hat{p}_y | \psi_{\mathbf{k},n} \rangle}{(E_{\mathbf{k},n} - E_{\mathbf{k},m})^2} \right\} \\ &= -\frac{e^2}{N} \frac{2}{V} \Im \left\{ \sum_{\mathbf{k}} \sum_{n=1}^{N_{\text{occ}}} \sum_{m=N_{\text{occ}}+1}^{\infty} \frac{\langle \psi_{\mathbf{k},n} | \hat{p}_x | \psi_{\mathbf{k},m} \rangle \langle \psi_{\mathbf{k},m} | \hat{p}_y | \psi_{\mathbf{k},n} \rangle}{(E_{\mathbf{k},n} - E_{\mathbf{k},m})^2} \right\}.\end{aligned}\quad (10.122)$$

In order to eliminate the sum over excited states we use the identity

$$\langle \psi_{\mathbf{k},n} | \hat{p}_i | \psi_{\mathbf{k},m} \rangle = \frac{m}{\hbar} \langle u_{\mathbf{k},n} | \left[ \frac{\partial}{\partial k_i}, \hat{H}_{\mathbf{k}} \right]_- | u_{\mathbf{k},m} \rangle \quad (10.123)$$

and switch from Bloch functions to the lattice periodic parts. We obtain

$$\Gamma_{xy} = -\frac{e^2}{N} \frac{2}{V} \Im \sum_{\mathbf{k}} \sum_{n=1}^{N_{\text{occ}}} \left\langle \frac{\partial u_{\mathbf{k},n}}{\partial k_x} \middle| \frac{\partial u_{\mathbf{k},n}}{\partial k_y} \right\rangle. \quad (10.124)$$

The *Berry curvature*  $\mathcal{Y}_{n,xy}(\mathbf{k})$  is defined as two times the imaginary part of the overlap  $\langle \frac{\partial u_{\mathbf{k},n}}{\partial k_x} | \frac{\partial u_{\mathbf{k},n}}{\partial k_y} \rangle$ :

$$\mathcal{Y}_{n,xy}(\mathbf{k}) = 2\Im \left\langle \frac{\partial u_{\mathbf{k},n}}{\partial k_x} \middle| \frac{\partial u_{\mathbf{k},n}}{\partial k_y} \right\rangle. \quad (10.125)$$

If the gauge transformation

$$|u_{\mathbf{k}n}\rangle \rightarrow e^{i\varphi(\mathbf{k})} |u_{\mathbf{k}n}\rangle \quad (10.126)$$

is performed the overlap  $\langle \frac{\partial u_{\mathbf{k},n}}{\partial k_x} | \frac{\partial u_{\mathbf{k},n}}{\partial k_y} \rangle$  changes as follows:

$$\left\langle \frac{\partial u_{\mathbf{k},n}}{\partial k_x} \middle| \frac{\partial u_{\mathbf{k},n}}{\partial k_y} \right\rangle \rightarrow \left\langle \frac{\partial u_{\mathbf{k},n}}{\partial k_x} \middle| \frac{\partial u_{\mathbf{k},n}}{\partial k_y} \right\rangle - \frac{d\varphi(\mathbf{k})}{dk_y} \Im \left\langle \frac{\partial u_{\mathbf{k},n}}{\partial k_x} \middle| u_{\mathbf{k},n} \right\rangle + \frac{d\varphi(\mathbf{k})}{dk_x} \Im \left\langle u_{\mathbf{k},n} \middle| \frac{\partial u_{\mathbf{k},n}}{\partial k_y} \right\rangle. \quad (10.127)$$

Thus, the Berry curvature  $\mathcal{Y}_{n,xy}(\mathbf{k})$  is gauge invariant. Consequently, the conductivity  $\Gamma_{xy}$ , Eq. (10.124), is likewise gauge invariant:

$$\Gamma_{xy} = -\frac{e^2}{N} \frac{1}{V} \sum_{\mathbf{k}} \sum_{n=1}^{N_{\text{occ}}} \mathcal{Y}_{n,xy}(\mathbf{k}). \quad (10.128)$$

Of course, this proof of gauge invariance suffers from the fact that there may be degeneracies and band-crossings. At such points it is not clear how the band continues and the derivative with respect to  $k$  is not well-defined. However, these points have zero weight in the  $k$ -integration and hence do not influence the result theoretically. Practically, in an implementation based on finite differences and a  $k$ -mesh one would have to pay attention to this point. In fact, it is possible to write the Berry curvature of a subspace in a form which makes its invariance with respect to unitary transformations within this subspace

obvious. Thus, the Berry curvature is invariant in a more general sense and the difficulties due to considering the band-wise Berry curvature are avoided. To achieve this, we insert the identity operator:

$$\begin{aligned}
\mathcal{Y}_{xy}(\mathbf{k}) &= 2\Im \sum_{n=1}^{N_{\text{occ}}} \sum_{m=1}^{\infty} \left\langle \frac{\partial u_{\mathbf{k},n}}{\partial k_x} | u_{\mathbf{k},m} \right\rangle \left\langle u_{\mathbf{k},m} | \frac{\partial u_{\mathbf{k},n}}{\partial k_y} \right\rangle = \\
&= 2\Im \sum_{n=1}^{N_{\text{occ}}} \sum_{m=N_{\text{occ}}+1}^{\infty} \left\langle \frac{\partial u_{\mathbf{k},n}}{\partial k_x} | u_{\mathbf{k},m} \right\rangle \left\langle u_{\mathbf{k},m} | \frac{\partial u_{\mathbf{k},n}}{\partial k_y} \right\rangle = \\
&= 2\Im \sum_{n=1}^{N_{\text{occ}}} \sum_{m=N_{\text{occ}}+1}^{\infty} \left\langle \frac{\partial u_{\mathbf{k},m}}{\partial k_x} | u_{\mathbf{k},n} \right\rangle \left\langle u_{\mathbf{k},n} | \frac{\partial u_{\mathbf{k},m}}{\partial k_y} \right\rangle.
\end{aligned} \tag{10.129}$$

Clearly, this expression is invariant with respect to unitary transformations among the occupied bands.

The evaluation of the anomalous Hall conductivity requires very fine  $k$ -meshes of millions of  $k$ -points. To reduce the computational burden, Wannier interpolation [131, 132, 133] may be used. Two interpolation schemes have been discussed in the literature: First, the direct interpolation of the Berry curvature, Eq. (10.125), using a finite-difference method for the  $k$ -derivatives. Second, the  $k$ -derivatives are calculated from first-order perturbation theory. In the latter approach a Kubo-like formula in the Wannier function space has to be evaluated. We point out that Eq. (10.129) might serve as a better starting point to set up an interpolation scheme than Eq. (10.125): The Wannier function formalism allows to interpolate the Berry connection in a straightforward way without the need for  $k$ -derivatives. In comparison to the Kubo formula, in Eq. (10.129) there is no energy denominator which is difficult to deal with in the case of very small energy differences.

The Kubo formula for the spin Hall effect, the spin counterpart of the anomalous Hall effect, is obtained by replacing the current, Eq. (10.117), by the spin current:

$$\Gamma_{xy}^s = \frac{e^2}{N V} \Re \left\{ \sum_{\bar{\mathbf{k}}} \sum_{n=1}^{N_{\text{occ}}} \sum_{m=N_{\text{occ}}+1}^{\infty} \frac{\langle \psi_{\bar{\mathbf{k}},n} | \sigma_s \hat{p}_x | \psi_{\bar{\mathbf{k}},m} \rangle \langle \psi_{\bar{\mathbf{k}},m} | \hat{y} | \psi_{\bar{\mathbf{k}},n} \rangle}{E_{\bar{\mathbf{k}},n} - E_{\bar{\mathbf{k}},m}} \right\}, \tag{10.130}$$

where  $s$  labels the components of the spin vector operator. However, in contrast to the current, the spin current is not conserved in the presence of spin-orbit coupling. Thus, one may expect to obtain different results, when instead of the matrix element of the spin velocity the spin current through a surface is used to evaluate the conductivity. Assuming spin-orbit coupling to be small, we may consider the commutator between spin and Hamiltonian to vanish approximately. Consequently, one may expect that for small spin-orbit coupling the expression for the spin conductivity can be manipulated analogously to the case of the anomalous Hall effect, leading to the expression

$$\Gamma_{xy}^s = \frac{e^2}{N V} \Im \left\{ \sum_{\bar{\mathbf{k}}} \sum_{n=1}^{N_{\text{occ}}} \sum_{m=N_{\text{occ}}+1}^{\infty} \left\langle \frac{\partial u_{\mathbf{k},m}}{\partial k_x} | \sigma_s | u_{\mathbf{k},n} \right\rangle \left\langle u_{\mathbf{k},n} | \frac{\partial u_{\mathbf{k},m}}{\partial k_y} \right\rangle \right\}. \tag{10.131}$$

# Chapter 11

## Summary and Conclusions

In the first part of the thesis a novel order- $N$  implementation of the full-potential linearized augmented-plane-wave (FLAPW) method was developed to efficiently perform *ab initio* total energy and force calculations based on the density functional theory (DFT) of large layered structures and in particular of the electronic and spin transport properties of spin-valves and magnetic tunneling junctions (MTJs). The key ingredients of the implementation, which were described in detail, are (i) the Green function embedding formalism, (ii) the propagation of the embedding potentials, (iii) the introduction of the surface projector on the curvy embedding surfaces and (iv) the use of the Dyson equation and of the spectral representation of the Green function. Electronic transport properties are calculated within the Landauer formulation of ballistic transport, using the single-particle Kohn-Sham scattering wave functions. Various aspects of the implementation, e.g. its parallelization and the self-consistent calculation of the charge density in and out of equilibrium were discussed in detail. The parallelization with respect to both  $k$ -points and layers allows to run the program in parallel on several thousand processors with a high scalability. The method was validated for films, surfaces and the transport geometry. Applications of the method to surfaces, e.g. the (111)-surface of Sb and the (100)-surface of Co, and to electronic transport, e.g. in the Co/MgO/Co and the Fe/Co/MgO/Co/Fe MTJs, were shown. The order- $N$  implementation of the FLAPW method opens new prospects for the investigation of electronic transport in complex systems involving several hundred atoms per unit cell.

The method was extended with the purpose to calculate the elastic contribution to the spin torque. In the absence of spin-orbit coupling the spin torque is calculated from the change of the spin current as it traverses the free magnetic layer of the MTJ. The calculations are carried out using a non-collinear setup, where the magnetic quantization axes of the free and the fixed magnetic layers are rotated with respect to each other. The implementation allows a layer- and atom-resolved analysis of the contributions to the spin torque. In order to verify the implementation, calculations of the spin torque and the giant magnetoresistance (GMR) effect were performed for the Co/Cu/Co spin valve and the results were found to be in very good agreement to those of existing calculations obtained by the Korringa-Kohn-Rostoker (KKR) method for this system.

From the layer-resolved analysis of the elastic spin torque it is found that almost the

complete torque is deposited on the first few atomic layers of the free magnetic layer. Two components of the spin-torque have to be distinguished: (i) The in-plane torque, which is responsible for the current-induced switching and which can sustain dynamical modes of the free magnetic layer. (ii) The out-of-plane torque, which has a similar effect as an applied magnetic field. For thick free magnetic layers the out-of-plane torque is found to be very small, which is typical for all-metallic spin valves. The layer resolved in-plane torques due to left- and right-propagating states are found to be equal in magnitude but opposite in direction. In contrast, the layer resolved out-of-plane torques differ for left- and right-propagating states both in magnitude and distribution. It is expected that this bias-asymmetry has an impact on the current-induced magnetization dynamics in the case of nanopillars with a thin free magnetic layer, where the out-of-plane torque is not negligible. From the  $k$ -resolved calculation of the torque it is seen that states from the entire 2BZ contribute.

The spin-torque for the Fe/Ag/Fe spin valve was calculated. The in-plane torque and the resistance of the Fe/Ag/Fe spin valve are characterized by very large asymmetries. The two asymmetries agree rather well with Slonczewski's model. However, in contrast to Slonczewski's model, which predicts the two asymmetries to be exactly equal, the obtained *ab initio* results for the two asymmetries deviate. While the asymmetries between the *ab initio* calculation and Slonczewski's model agree well, the absolute values of torque and resistance are found to be different, suggesting that *ab initio* calculations of the spin torque provide additional valuable information that cannot be obtained from Slonczewski's model. For the Fe/MgO/Fe MTJ tunneling conductance and spin torque were investigated. The torque per current was found to be in very good agreement to recent experiments on CoFeB/MgO/CoFeB MTJs employing FeCoB as lead material. In comparison to recent similar *ab initio* calculations of the spin-torque in the Fe/MgO/Fe MTJ, a substantially larger out-of-plane torque was found, suggesting that (i) the out-of-plane torque depends very sensitively on the details of the MTJ and (ii) the impact of the out-of-plane torque on the current-induced switching may be strong if the MTJ is of very high quality. In order to compute the spin-torque in the presence of spin-orbit coupling, a second formulation of the spin-torque was implemented, which is based on the direct evaluation of the torque the non-equilibrium density experiences due to the exchange field. The two formulations are found to give identical results in the absence of spin-orbit coupling. The influence of spin-orbit coupling on the spin-torque was investigated for Fe/Au/Fe nanopillars. Especially the out-of-plane torque is found to be affected by spin-orbit coupling.

The last part of the thesis focuses on the implementation and use of first-guess and maximally localized Wannier functions. First-guess Wannier functions are obtained by projecting a set of functions, which are localized inside the MT-spheres, onto a set of Bloch functions. Maximally localized Wannier functions are constructed by minimizing the spread functional. The details of the implementation were presented for bulk, film and one-dimensional geometries. The implementation was validated for these geometries. While the computation of maximally localized Wannier functions is very efficient due to the exploitation of symmetries, the construction of first-guess Wannier functions is computationally much less demanding. For ionic oxides like SrVO<sub>3</sub>, first-guess Wannier functions

were found to be in very good agreement to maximally localized Wannier functions. For the covalent system graphene it is more difficult to obtain a good agreement between first-guess and maximally localized Wannier functions. A solution was presented which is based on the projection of Bloch functions onto linear combinations of localized functions in several MT-spheres. For diamond the question of the uniqueness of maximally localized Wannier functions was addressed: (i) Several local minima of the spread functional were shown to exist and (ii) maximally localized Wannier functions were shown to be different depending on whether they are constructed for the bonding states and the anti-bonding states separately or together. In the presence of spin-orbit coupling, Wannier-functions loose the property of real-valuedness and are spinor-valued. A simple model to understand the properties of Wannier-functions in the presence of spin-orbit coupling was developed and spinor-valued Wannier functions were constructed for  $\text{SrVO}_3$ , a one-dimensional Pt-chain and a double layer of Bi(111). Tight-binding parameters were computed for diamond, graphene,  $\text{SrVO}_3$ , a one-dimensional Pt-chain and a double layer of Bi(111) and the therewith interpolated band structures were found to be in excellent agreement with the true ones.

The relationships between the modern theory of ferroelectric polarization, the Berry phase, and the maximally localized Wannier functions were discussed in detail. The Berry phase formulation of ferroelectric polarization was compared to the Wannier function picture of ferroelectric polarization and the latter was found to be superior in two respects: (i) In many cases the Wannier function picture allows to avoid calculations for intermediate points on the adiabatic path joining the ferroelectric phase and the inversion symmetric phase and (ii) the Wannier function picture allows to define an orbital decomposition of the anomalous contribution to the polarization. The Wannier function picture of ferroelectric polarization was applied to the ferroelectric materials  $\text{BaTiO}_3$ ,  $\text{PbTiO}_3$  and the multiferroic  $\text{HoMnO}_3$  with excellent agreement to experiments where available.

Wannier functions turned out to be a powerful concept to relate sophisticated electronic structure methods to new physics. As a localized basis set they can be used in the field of many-body perturbation theory to describe ladder diagrams or the on-site Coulomb interaction or screened electron-hole and plasmon excitations. They allow to construct realistic model Hamiltonians from *ab initio* theory, which is applied to study e.g. the properties of strongly correlated materials. The implementation of spin-orbit Wannier functions opens the path to the investigation of the anomalous Hall and the spin-Hall effects.

In summary, electronic structure methods based on the density functional theory have been developed and applied that open a new vista for the theoretical investigation of electron and spin transport properties and processes in realistic spintronic devices.



# Appendix A

## Spherical Harmonics

The following definition of spherical harmonics is used:

$$Y_\ell^m(\theta, \varphi) = \sqrt{\frac{(2\ell+1)(\ell-m)!}{4\pi(\ell+m)!}} P_\ell^m(\cos\theta) e^{im\varphi}, \quad (\text{A.1})$$

where the Condon-Shortley phase is included in the associated Legendre polynomials  $P_\ell^m(x)$ . The spherical harmonics are orthonormal:

$$\int_{\theta=0}^{\pi} \int_{\varphi=0}^{2\pi} Y_\ell^m Y_{\ell'}^{m'*} d\Omega = \delta_{\ell\ell'} \delta_{mm'}. \quad (\text{A.2})$$

### A.1 Gaunt Coefficients

The Gaunt coefficients  $G_{l,l',l''}^{m,m',m''}$  are defined as overlap integral of three spherical harmonics:

$$G_{l,l',l''}^{m,m',m''} = \int d\Omega (Y_{l,m}(\hat{\mathbf{r}}))^* Y_{l',m'}(\hat{\mathbf{r}}) Y_{l'',m''}(\hat{\mathbf{r}}). \quad (\text{A.3})$$

In order to use the combined index  $L = (l, m)$  to label the angular momentum we introduce the alternative notation

$$G(L, L', L'') = G_{l,l',l''}^{m,m',m''}. \quad (\text{A.4})$$

The Gaunt coefficients are real-valued. They are zero unless all of the following conditions are satisfied:

- $l + l' + l''$  is even.
- The triangular condition  $|l - l'| \leq l'' \leq (l + l')$  is satisfied.
- $m = m' + m''$ .
- $|m| \leq l$ ,  $|m'| \leq l'$  and  $|m''| \leq l''$ .

## A.2 Wigner $D$ -matrix

The rotation operator  $\mathbf{R}(\alpha, \beta, \gamma)$  that corresponds to the Euler angles  $\alpha$ ,  $\beta$  and  $\gamma$  is given by

$$\mathbf{R}(\alpha, \beta, \gamma) = e^{-i\alpha\hat{L}_z} e^{-i\beta\hat{L}_y} e^{-i\gamma\hat{L}_z}. \quad (\text{A.5})$$

The Wigner  $D$ -matrix is a square matrix of dimension  $2l + 1$ . Its elements are

$$D_{m'm}^j(\alpha, \beta, \gamma) \equiv \langle lm' | \mathbf{R}(\alpha, \beta, \gamma) | lm \rangle = e^{-im'\alpha} d_{m'm}^l(\beta) e^{-im\gamma}, \quad (\text{A.6})$$

where

$$d_{m'm}^l(\beta) = \langle lm' | e^{-i\beta\hat{L}_y} | lm \rangle \quad (\text{A.7})$$

is known as Wigner's small  $d$ -matrix.



# Appendix B

## Coordinate Frame Transformations

### B.1 Definition of and need for local coordinate frames

For the implementation of spin-orbit coupling and non-collinear magnetism it is convenient to define for each atom  $\mu$  a local coordinate frame in which the local spin moment is aligned parallel to the local  $z$ -axis. We use two Euler angles,  $\alpha_\mu$  and  $\beta_\mu$ , to specify for each atom  $\mu$  the orientation of the local frame of reference with respect to the global one. Two Euler angles is the minimum number needed to be able to represent any given magnetization direction by a local frame of reference that has its  $z$ -axis parallel to the given magnetization direction. The inclusion of a third Euler angle would allow to specify also the orientation of the  $x$ - and  $y$ -axes of the local frame. However, we do not need this third Euler angle and the actual orientation of the  $x$ - and  $y$ -axes of the local frame is fixed by our specific choice of rotation matrices. The set of axes of the local frame is obtained from the set of axes of the global frame by successively performing the following two rotations on the set of axes of the global frame: First, a counterclockwise rotation by the angle  $\alpha_\mu$  around the  $z$ -axis of the global frame, second, a counterclockwise rotation by the angle  $\beta_\mu$  around the  $y$ -axis of the intermediate frame. The axes  $\hat{\mathbf{e}}_x^\mu$ ,  $\hat{\mathbf{e}}_y^\mu$ , and  $\hat{\mathbf{e}}_z^\mu$  of the local coordinate frame are then related to the axes of the global frame ( $\hat{\mathbf{e}}_x$ ,  $\hat{\mathbf{e}}_y$ , and  $\hat{\mathbf{e}}_z$ ) by the transformation

$$\begin{aligned}\hat{\mathbf{e}}_x^\mu &= \cos(\alpha_\mu) \cos(\beta_\mu) \hat{\mathbf{e}}_x + \cos(\beta_\mu) \sin(\alpha_\mu) \hat{\mathbf{e}}_y - \sin(\beta_\mu) \hat{\mathbf{e}}_z \\ \hat{\mathbf{e}}_y^\mu &= -\sin(\alpha_\mu) \hat{\mathbf{e}}_x + \cos(\alpha_\mu) \hat{\mathbf{e}}_y + 0 \hat{\mathbf{e}}_z \\ \hat{\mathbf{e}}_z^\mu &= \cos(\alpha_\mu) \sin(\beta_\mu) \hat{\mathbf{e}}_x + \sin(\alpha_\mu) \sin(\beta_\mu) \hat{\mathbf{e}}_y + \cos(\beta_\mu) \hat{\mathbf{e}}_z.\end{aligned}\tag{B.1}$$

## B.2 Transformation of cartesian vectors and cartesian vector operators

The transformation of the coordinates of vectors given with respect to the local frame into the coordinates of the global frame is provided by the transformation matrix

$$\mathbf{R}_\mu^{\text{global}} = \begin{pmatrix} \cos(\alpha_\mu) \cos(\beta_\mu) & -\sin(\alpha_\mu) & \cos(\alpha_\mu) \sin(\beta_\mu) \\ \cos(\beta_\mu) \sin(\alpha_\mu) & \cos(\alpha_\mu) & \sin(\alpha_\mu) \sin(\beta_\mu) \\ -\sin(\beta_\mu) & 0 & \cos(\beta_\mu) \end{pmatrix}. \quad (\text{B.2})$$

The transformation matrix which transforms the global coordinates into the local coordinates is given by the transpose of this matrix:

$$\mathbf{R}_\mu^{\text{local}} = \begin{pmatrix} \cos(\alpha_\mu) \cos(\beta_\mu) & \sin(\alpha_\mu) \cos(\beta_\mu) & -\sin(\beta_\mu) \\ -\sin(\alpha_\mu) & \cos(\alpha_\mu) & 0 \\ \cos(\alpha_\mu) \sin(\beta_\mu) & \sin(\alpha_\mu) \sin(\beta_\mu) & \cos(\beta_\mu) \end{pmatrix}. \quad (\text{B.3})$$

## B.3 Transformation of spinors

The transformation of spinors given in the local frame to spinors in the global frame is provided by the matrix

$$\mathbf{U}_\mu^{\text{global}} = \begin{pmatrix} e^{-\frac{i\alpha_\mu}{2}} \cos\left(\frac{\beta_\mu}{2}\right) & -e^{-\frac{i\alpha_\mu}{2}} \sin\left(\frac{\beta_\mu}{2}\right) \\ e^{\frac{i\alpha_\mu}{2}} \sin\left(\frac{\beta_\mu}{2}\right) & e^{\frac{i\alpha_\mu}{2}} \cos\left(\frac{\beta_\mu}{2}\right) \end{pmatrix}. \quad (\text{B.4})$$

The inverse transformation from the global frame to the local frame is given by the adjoint matrix:

$$\mathbf{U}_\mu^{\text{local}} = \begin{pmatrix} e^{\frac{i\alpha_\mu}{2}} \cos\left(\frac{\beta_\mu}{2}\right) & e^{-\frac{i\alpha_\mu}{2}} \sin\left(\frac{\beta_\mu}{2}\right) \\ -e^{\frac{i\alpha_\mu}{2}} \sin\left(\frac{\beta_\mu}{2}\right) & e^{-\frac{i\alpha_\mu}{2}} \cos\left(\frac{\beta_\mu}{2}\right) \end{pmatrix}. \quad (\text{B.5})$$

# Appendix C

## MPI subroutines

The MPI (message passing interface) library offers both point-to-point and collective communication subroutines. Point-to-point communication is optimal when small pieces of data need to be communicated from one process to a different process. If all processors need to communicate data at the same time, collective communication should be used instead of point-to-point communication. While it is theoretically possible to use point-to-point communication also in these cases, collective communication will be faster and problems like buffer overflow cannot occur. The parallelization of the propagation of the embedding potentials, which is described in section 7.3.2 requires the communication of big amounts of data (transfer matrices and embedding potentials) from all processes to all processes. Moreover, the data sent by process  $i$  to process  $j$  is different from the data sent by process  $i$  to process  $k$ . For this task the subroutine `MPI_ALLTOALL` has been designed. `MPI_ALLTOALL` is an extension of `MPI_ALLGATHER` to the case where each process sends distinct data to each of the receivers. `MPI_ALLTOALL` is called with a send buffer and a receive buffer. Both the send buffer and the receive buffer consist of blocks of equal size. The number of blocks both in the receive buffer and the send buffer is given by the total number of processes participating in the collective communication. The data that process  $i$  sends to process  $j$  is put into the  $j$ -th block of the send buffer. After the `MPI_ALLTOALL` operation has been performed, the  $i$ -th block of the receive buffer of process  $j$  contains the data sent by process  $i$ : The  $j$ -th block sent from process  $i$  is received by process  $j$  and is placed in the  $i$ -th block of the receive buffer.



# Appendix D

## JUGENE

Configuration of JUGENE (Juelicher Blue Gene/P): 72 Racks with 32 nodecards x 32 compute nodes (total 73728)

- Compute node: 4-way SMP processor
- Processortype: 32-bit PowerPC 450 core 850 MHz
- Processors: 294912
- Overall peak performance: 1 Petaflops
- Linpack: 825.5 Teraflops
- Main memory: 2 Gbytes per node (aggregate 144 TB)
- I/O Nodes: 600
- Networks:
  - Three-dimensional torus (compute nodes)
  - Global tree / Collective network (compute nodes, I/O nodes)
  - 10 Gigabit ethernet / Functional network (I/O Nodes)
- Power Consumption: max. 35 kW per rack



# Bibliography

- [1] G. Binasch, P. Grünberg, F. Saurenbach, and W. Zinn. Enhanced magnetoresistance in layered magnetic structures with antiferromagnetic interlayer exchange. *Phys. Rev. B*, 39:4828, 1989.
- [2] M. N. Baibich, J. M. Broto, A. Fert, F. N. V. Dau, F. Petroff, P. Etienne, G. Creuzet, A. Friederich, and J. Chazelas. Giant magnetoresistance of (001)Fe/(001)Cr magnetic superlattices. *Phys. Rev. Lett.*, 61:2472, 1988.
- [3] M. Jullière. Tunneling between ferromagnetic films. *Phys. Lett.*, 54A:225, 1975.
- [4] T. Miyazaki and N. Tekuza. Giant magnetic tunneling effect in Fe/Al<sub>2</sub>O<sub>3</sub>/Fe junction. *J. Magn. Magn. Mater.*, 139:L231, 1995.
- [5] J. S. Moodera, L. R. Kinder, T. M. Wong, and R. Meservey. Large Magnetoresistance at Room Temperature in Ferromagnetic Thin Film Tunnel Junctions. *Phys. Rev. Lett.*, 74:3273, 1995.
- [6] W. Wang, H. Sukegawa, R. Shan, S. Mitani, and K. Inomata. Giant tunneling magnetoresistance up to 330% at room temperature in sputter deposited Co<sub>2</sub>FeAl/MgO/CoFe magnetic tunnel junctions. *Appl. Phys. Lett.*, 95:182502, 2009.
- [7] L. Berger. Emission of spin waves by a magnetic multilayer traversed by a current. *Phys. Rev. B*, 54:9353, 1996.
- [8] J. C. Slonczewski. Current-driven excitation of magnetic multilayers. *J. Magn. Magn. Mater.*, 159:L1, 1996.
- [9] M. Tsoi, A.G.M. Jansen, J. Bass, W.C. Chiang, M. Seck, V. Tsoi, and P. Wyder. Excitation of a Magnetic Multilayer by an Electric Current. *Phys. Rev. Lett.*, 80:4281, 1998.
- [10] J.Z. Sun. *J. Magn. Magn. Mater.*, 202:157, 1999.
- [11] J. A. Katine, F. J. Albert, R. A. Buhrman, E. B. Myers, and D. C. Ralph. Current-Driven Magnetization Reversal and Spin-Wave Excitations in Co/Cu/Co Pillars. *Phys. Rev. Lett.*, 84:3149, 2000.

- [12] E. Tsymbal and H. Kohlstedt. Tunneling Across a Ferroelectric. *Science*, 313:181, 2006.
- [13] P. Hohenberg and W. Kohn. Inhomogeneous electron gas. *Phys. Rev.*, 136:B864, 1964.
- [14] W. Kohn and L. J. Sham. Self-consistent equations including exchange and correlation effects. *Phys. Rev.*, 140:A1133, 1965.
- [15] J. C. Slater. Wave functions in a Periodic Potential. *Phys. Rev.*, 51:846, 1937.
- [16] O. K. Andersen. Linear methods in band theory. *Phys. Rev. B*, 12:3060, 1975.
- [17] E. Wimmer, H. Krakauer, M. Weinert, and A. J. Freeman. Full-potential selfconsistent linearized-augmented-plane-wave method for calculating the electronic structure of molecules and surfaces: O<sub>2</sub> molecule. *Phys. Rev. B*, 24:864, 1981.
- [18] M. Weinert, E. Wimmer, and A. J. Freeman. Total-energy all-electron density functional method for bulk solids and surfaces. *Phys. Rev. B*, 26:4571, 1982.
- [19] N. Marzari and D. Vanderbilt. Maximally localized generalized Wannier functions for composite energy bands. *Phys. Rev. B*, 56:12847, 1997.
- [20] I. Souza, N. Marzari, and D. Vanderbilt. Maximally localized Wannier functions for entangled energy bands. *Phys. Rev. B*, 65:035109, 2001.
- [21] E. Pavarini, S. Biermann, A. Poteryaev, A. I. Lichtenstein, A. Georges, and O. K. Andersen. Mott Transition and Suppression of Orbital Fluctuations in Orthorhombic 3d<sup>1</sup> Perovskites. *Phys. Rev. Lett.*, 92:176403, 2004.
- [22] V. I. Anisimov, D. E. Kondakov, A. V. Kozhevnikov, I. A. Nekrasov, Z. V. Pchelkina, J. W. Allen, S.-K. Mo, H.-D. Kim, P. Metcalf, S. Suga, A. Sekiyama, G. Keller I. Leonov, X. Ren, and D. Vollhardt. Full orbital calculation scheme for materials with strongly correlated electrons. *Phys. Rev. B*, 71:125119, 2005.
- [23] F. Lechermann, A. Georges, A. Poteryaev, S. Biermann, M. Posternak, A. Yamasaki, and O. K. Andersen. Dynamical mean-field theory using Wannier functions: A flexible route to electronic structure calculations of strongly correlated materials. *Phys. Rev. B*, 74:125120, 2006.
- [24] R. Resta. Macroscopic polarization in crystalline dielectrics: the geometric phase approach. *Rev. Mod. Phys.*, 66:899, 1994.
- [25] J. E. Inglesfield. A method of embedding. *J. Phys. C: Solid State Phys.*, 14:3795, 1981.
- [26] S. Crampin, J. B. A. N. van Hoof, M. Nekovee, and J. E. Inglesfield. Full-potential embedding for surfaces and interfaces. *J. Phys.: Condens. Matter*, 4:1475, 1992.



- [27] D. Wortmann, H. Ishida, and S. Blügel. Ab initio Green-function formulation of the transfer matrix: Application to complex band structures. *Phys. Rev. B*, 65:165103, 2002.
- [28] D. Wortmann, H. Ishida, and S. Blügel. Embedded Green-function approach to the ballistic electron transport through an interface. *Phys. Rev. B*, 66:075113, 2002.
- [29] D. Wortmann. *An Embedding Green Function Approach for Electron Transport through Interfaces*. PhD thesis, RWTH-Aachen, 2003.
- [30] M. Di Ventra. *Electrical Transport in Nanoscale Systems*. Cambridge University Press, Cambridge, 2008.
- [31] T. L. Loucks. *Augmented Plane Wave Method*. W. A. Benjamin, Inc., New York, 1967.
- [32] S. Blügel and G. Bihlmayer. Full-Potential Linearized Augmented Planewave Method. In J. Grotendorst, S. Bügel, and D. Marx, editors, *Computational Nanoscience: Do It Yourself!*. John von Neumann Institute for Computing, Jülich, Jülich, Germany, 2006. NIC Series, Vol. 31, <http://www.fz-juelich.de/nic-series/volume31>.
- [33] D. Singh. Ground-state properties of lanthanum: Treatment of extended-core states. *Phys. Rev. B*, 43:6388, 1991.
- [34] G. K. H. Madsen, P. Blaha, K. Schwarz, E. Sjöstedt, and L. Nordström. Efficient linearization of the augmented plane-wave method. *Phys. Rev. B*, 64:195134, 2001.
- [35] See <http://www.flapw.de>.
- [36] Ph. Kurz. *Non-Collinear Magnetism at Surfaces and in Ultrathin Films*. PhD thesis, RWTH-Aachen, 2000.
- [37] W. Metzner and D. Vollhardt. Correlated Lattice Fermions in  $d = \infty$  Dimensions. *Phys. Rev. Lett.*, 62:324, 1989.
- [38] M. Jarrell. Hubbard model in infinite dimensions: A quantum Monte Carlo study. *Phys. Rev. Lett.*, 69:168, 1992.
- [39] A. Georges and G. Kotliar. Hubbard model in infinite dimensions. *Phys. Rev. B*, 45:6479, 1992.
- [40] A. Georges, G. Kotliar, W. Krauth, and M. J. Rozenberg. Dynamical mean-field theory of strongly correlated fermion systems and the limit of infinite dimensions. *Rev. Mod. Phys.*, 68:13, 1996.

- [41] G. Kotliar, S. Y. Savrasov, K. Haule, V. S. Oudovenko, O. Parcollet, and C. A. Marianetti. Electronic structure calculations with dynamical mean-field theory. *Rev. Mod. Phys.*, 78:865, 2006.
- [42] K. Held. Electronic structure calculations using dynamical mean field theory. *Adv. in Physics*, 56:829, 2007.
- [43] A. L. Fetter and J. D. Walecka. *Quantum Theory of Many-Particle Systems*. McGraw-Hill, San Francisco, 1971.
- [44] J. Schwinger. Brownian Motion of a Quantum Oscillator. *Journal of Mathematical Physics*, 2:407, 1960.
- [45] Y. Meir and N. S. Wingreen. *Phys. Rev. Lett.*, 68:2512, 1992.
- [46] T.-K. Ng. *Phys. Rev. Lett.*, 76:487, 1996.
- [47] A. Ferretti, A. Calzolari, R. Di Felice, and F. Manghi. First-principles theoretical description of electronic transport including electron-electron correlation. *Phys. Rev. B*, 72:125114, 2005.
- [48] J. E. Inglesfield. Embedding at surfaces. *Comp. Phys. Comm.*, 137:89, 2001.
- [49] M. Ye. Zhuravlev, J. D. Burton, A. V. Vedyayev, and E. Y. Tsymbal. A symmetric Green function for the non-collinear magnetic multilayer. *Journal of Physics A*, 38:5547, 2005.
- [50] F. Garcia-Moliner and V. R. Velasco. *Theory of Single and Multiple Interfaces*. World Scientific, Singapore, 1992.
- [51] J. E. Inglesfield, S. Crampin, and H. Ishida. Embedding potential definition of channel functions. *Phys. Rev. B*, 71:155120, 2005.
- [52] H. Ishida, D. Wortmann, and T. Ohwaki. First-principles calculations of tunneling conductance. *Phys. Rev. B*, 70:085409, 2004.
- [53] H. Ishida. Surface-embedded Green function calculation using non-local pseudopotentials. *Surf. Sci.*, 388:71, 1997.
- [54] H. Ishida. Surface-embedded Green-function method: A formulation using a linearized-augmented-plane-wave basis set. *Phys. Rev. B*, 63:165409, 2001.
- [55] K. Wildberger, P. Lang, R. Zeller, and P. H. Dederichs. Fermi-Dirac distribution in ab initio Green's-function calculations. *Phys. Rev. B*, 52:11502, 1995.
- [56] Y. Mokrousov. *Ab initio All-electron Full-potential Linearized Augmented Plane-wave Method for One-dimensional Systems*. PhD thesis, RWTH-Aachen, 2005.

- [57] M. Weinert. Solution of Poisson's equation: beyond Ewald-type methods. *J. Math. Phys.*, 22:2433, 1981.
- [58] J. M. Soler and A. R. Williams. Augmented-plane-wave forces. *Phys. Rev. B*, 42:9728, 1990.
- [59] R. Yu, D. Singh, and H. Krakauer. All-electron and pseudopotential force calculations using the linearized-augmented-plane-wave method. *Phys. Rev. B*, 43:6411, 1991.
- [60] J. M. Soler and A. R. Williams. Comment of "All-electron and pseudopotential force calculations using the linearized-augmented-plane-wave method". *Phys. Rev. B*, 47:6784, 1993.
- [61] M. Fähnle, C. Elsässer, and H. Krimmel. The Basic Strategy behind the Derivation of Various ab-initio Force Formulae. *physica status solidi (b)*, 191:9, 1995.
- [62] M. Brandbyge, J.-L. Mozos, P. Ordejón, J. Taylor, and K. Stokbro. Density-functional method for nonequilibrium electron transport. *Phys. Rev. B*, 65:165401, 2002.
- [63] S. K. Kim, C. Petersen, F. Jona, and P. M. Marcus. Ultrathin films of cobalt on Fe001 and the effect of oxygen. *Phys. Rev. B*, 54(3):2184–2190, 1996.
- [64] J. P. Perdew, K. Burke, and M. Ernzerhof. Generalized Gradient Approximation Made Simple. *Phys. Rev. Lett.*, 77:3865, 1996.
- [65] V. L. Moruzzi, J. F. Janak, and A. R. Williams. *Calculated Electronic Properties of Metals*. Pergamon Press, New York, 1978.
- [66] K. Sugawara, T. Sato, S. Souma, T. Takahashi, M. Arai, and T. Sasaki. Fermi Surface and Anisotropic Spin-Orbit Coupling of Sb(111) Studied by Angle-Resolved Photoemission Spectroscopy. *Phys. Rev. Lett.*, 96:046411, 2006.
- [67] Jeffrey C. Y. Teo, Liang Fu, and C. L. Kane. Surface states and topological invariants in three-dimensional topological insulators: Application to  $\text{Bi}_{1-x}\text{Sb}_x$ . *Phys. Rev. B*, 78:045426, 2008.
- [68] W. H. Butler, X.-G. Zhang, T. C. Schulthess, and J. M. MacLaren. Spin-dependent tunneling conductance of  $fe|mgo|fe$  sandwiches. *Phys. Rev. B*, 63(5):054416, Jan 2001.
- [69] S. Yuasa, T. Nagahama, A. Fukushima, Y. Suzuki, and K. Ando. *Nat. Mat.*, 3:868, 2004.
- [70] R. Matsumoto, A. Fukushima, T. Nagahama, and Y. Suzuki. Oscillation of giant tunneling magneto resistance with respect to tunneling barrier thickness in fully epitaxial Fe/MgO/Fe magnetic tunnel junctions. *Applied Physics Letters*, 90:252506, 2007.

- 
- [71] X.-G. Zhang and W. H. Butler. Large magnetoresistance in bcc Co/MgO/Co and FeCo/MgO/FeCo tunnel junctions. *Phys. Rev. B*, 70(17):172407, 2004.
- [72] Shinji Yuasa, Akio Fukushima, Hitoshi Kubota, Yoshishige Suzuki, and Koji Ando. Giant tunneling magnetoresistance up to 410% at room temperature in fully epitaxial Co/MgO/Co magnetic tunnel junctions with bcc Co(001) electrodes. *Applied Physics Letters*, 89(4):042505, 2006.
- [73] M. Lezaic and K. Rushchanskii. Private Communication.
- [74] C. H. Marrows. Spin-polarised currents and magnetic domain walls. *Adv. Phys.*, 54:585, 2005.
- [75] D. A. Allwood, G. Xiong, C. C. Faulkner, D. Atkinson, D. Petit, and R. P. Cowburn. Magnetic Domain-Wall Logic. *Science*, 309:1688, 2005.
- [76] M. Stiles and A. Zangwill. Anatomy of spin-transfer torque. *Phys. Rev. B*, 66:014407, 2002.
- [77] P. M. Haney, R. A. Duine, A. S. Nunez, and A. H. MacDonald. Current-induced torques in magnetic metals: Beyond spin-transfer. *J. Magn. Magn. Mater.*, 320:1300, 2008.
- [78] P. M. Haney, D. Waldron, R. A. Duine, A. S. Nunez, H. Guo, and A. H. MacDonald. Current-induced order parameter dynamics: Microscopic theory applied to Co/Cu/Co spin valves. *Phys. Rev. B*, 76:024404, 2007.
- [79] A. Manchon and S. Zhang. Theory of spin torque due to spin-orbit coupling. *Phys. Rev. B*, 79:094422, 2009.
- [80] A. Manchon and S. Zhang. Theory of nonequilibrium intrinsic spin torque in a single nanomagnet. *Phys. Rev. B*, 78:212405, 2008.
- [81] A. Matos-Abiague and R. L. Rodriguez-Suarez. Spin-orbit coupling mediated spin torque in a single ferromagnetic layer. *Phys. Rev. B*, 80:094424, 2009.
- [82] L. Berger. Precession of conduction-electron spins near an interface between normal and magnetic metals. *IEEE Trans. Magn.*, 31:3871, 1995.
- [83] J. C. Slonczewski. Conductance and exchange coupling of two ferromagnets separated by a tunneling barrier. *Phys. Rev. B*, 39:6995, 1989.
- [84] J. Xiao, A. Zangwill, and M. D. Stiles. Macrospin models of spin transfer dynamics. *Phys. Rev. B*, 72:014446, 2005.
- [85] J. C. Slonczewski. Currents and torques in metallic magnetic multilayers. *J. Magn. Magn. Mater.*, 247:324–338, 2002.

- [86] J. Grollier, V. Cros, A. Hamzic, J. M. George, H. Jaffres, A. Fert, G. Faini, J. B. Youssef, and H. Legall. Spin-polarized current induced switching in Co/Cu/Co pillars. *Appl. Phys. Lett.*, 78:3663, 2001.
- [87] F. J. Albert, J. A. Katine, R. A. Buhrman, and D. C. Ralph. Spin-polarized current switching of a Co thin film nanomagnet. *Appl. Phys. Lett.*, 77:3809, 2000.
- [88] C. Heiliger, M. Czerner, B. Y. Yavorsky, I. Mertig, and M. D. Stiles. Implementation of a non-equilibrium Green's function method to calculate spin-transfer torque. *J. Appl. Phys.*, 103:07A709, 2008.
- [89] M. D. Stiles and D. R. Penn. Calculation of spin-dependent interface resistance. *Phys. Rev. B*, 61:3200, 2000.
- [90] M. D. Stiles and J. Miltat. Spin-Transfer Torque and Dynamics. *Topics in Appl. Phys.*, 101:225, 2006.
- [91] H. Dasso, R. Lehdorff, D. E. Bürgler, M. Buchmeier, P. A. Grünberg, and C. M. Schneider. Normal and inverse current-induced magnetization switching in a single nanopillar. *Appl. Phys. Lett.*, 89:222511, 2006.
- [92] R. Lehdorff, M. Buchmeier, D. E. Bürgler, A. Kakay, R. Hertel, and C. M. Schneider. Asymmetric spin-transfer torque in single-crystalline Fe/Ag/Fe nanopillars. *Phys. Rev. B*, 76:214420, 2007.
- [93] R. Lehdorff, D. E. Bürgler, A. Kakay, R. Hertel, and C. M. Schneider. Spin-Transfer Induced Dynamic Modes in Single-Crystalline Fe-Ag-Fe Nanopillars. *IEEE Transactions on Magnetism*, 44:1951, 2008.
- [94] D. E. Bürgler. Spin-Transfer Torque Dynamics. In S. Blügel, D. Bürgler, M. Morgenstern, C. M. Schneider, and R. Waser, editors, *Spintronics - From GMR to Quantum Information*. Forschungszentrum Jülich, Zentralbibliothek, Jülich, Germany, 2009. Lecture Notes of the 40th IFF Spring School March 9-20, 2009.
- [95] Y. Huai, F. Albert, P. Nguyen, M. Pakala, and T. Valet. Observation of spin-transfer switching in deep submicron-sized and low-resistance magnetic tunnel junctions. *Appl. Phys. Lett.*, 84:3118, 2004.
- [96] G. D. Fuchs, N. C. Emley, I. N. Krivorotov, P. M. Braganca, E. M. Ryan, S. I. Kiselev, J. C. Sankey, D. C. Ralph, R. A. Buhrman, and J. A. Katine. Spin-transfer effects in nanoscale magnetic tunnel junctions. *Appl. Phys. Lett.*, 85:1205, 2004.
- [97] Jack C. Sankey, Yong-Tao Cui, Jonathan Z. Sun, John C. Slonczewski, Robert A. Buhrman, and Daniel C. Ralph. Measurement of the spin-transfer-torque vector in magnetic tunnel junctions. *Nature Physics*, 4:67–71, 2008.

- [98] A. A. Tulapurkar, Y. Suzuki, A. Fukushima, H. Kubota, H. Maehara, K. Tsunekawa, D. D. Djayaprawira, N. Watanabe, and S. Yuasa. Spin-torque diode effect in magnetic tunnel junctions. *Nature*, 438:339, 2005.
- [99] H. Kubota, A. Fukushima, K. Yakushiji, T. Nagahama, S. Yuasa, K. Ando, H. Maehara, Y. Nagamine, K. Tsunekawa, D. D. Djayaprawira, N. Watanabe, and Y. Suzuki. Quantitative measurement of voltage dependence of spin-transfer torque in MgO-based magnetic tunnel junctions. *Nature Phys.*, 4:37, 2008.
- [100] B. Georges, J. Grollier, V. Cros, A. Fert, A. Fukushima, H. Kubota, K. Yakushijin, S. Yuasa, and K. Ando. Origin of the spectral linewidth in nonlinear spin-transfer oscillators based on MgO tunnel junctions. *Phys. Rev. B*, 80:060404(R), 2009.
- [101] Y. Suzuki and H. Kubota. Spin-Torque Diode Effect and Its Application. *J. Phys. Soc. Jpn.*, 77:310021, 2008.
- [102] C. Heiliger and M. D. Stiles. Ab Initio Studies of the Spin-Transfer Torque in Magnetic Tunnel Junctions. *Phys. Rev. Lett.*, 100:186805, 2008.
- [103] J. C. Slonczewski and J. Z. Sun. Theory of voltage-driven current and torque in magnetic tunnel junctions. *J. Magn. Magn. Mater.*, 310:169–175, 2007.
- [104] E. Y. Tsymbal, O. N. Mryasov, and P. R. LeClair. Spin-dependent tunnelling in magnetic tunnel junctions. *J. Phys.: Condens. Matter*, 15:R109, 2003.
- [105] J. S. Moodera and G. Mathon. Spin polarized tunneling in ferromagnetic junctions. *J. Magn. Magn. Mater.*, 200:248, 1999.
- [106] J. C. Slonczewski. Currents, torques, and polarization factors in magnetic tunnel junctions. *Phys. Rev. B*, 71:024411, 2005.
- [107] I. Theodonis, N. Kioussis, A. Kalitsov, M. Chshiev, and W. H. Butler. Anomalous bias dependence of spin torque in magnetic tunnel junctions. *Phys. Rev. Lett.*, 97:237205, 2006.
- [108] P. M. Levy and A. Fert. Spin transfer in magnetic tunnel junctions with hot electrons. *Phys. Rev. Lett.*, 97:097205, 2005.
- [109] A. M. Deac. Bias-driven high-power microwave emission from MgO-based tunnel magnetoresistance devices. *Nature Physics*, 4:803, 2008.
- [110] Se-Chung Oh, Seung-Young Park, Aurelien Manchon, Mairbek Chshiev, Jae-Ho Han, Hyun-Woo Lee, Jang-Eun Lee, Kyung-Tae Nam, Younghun Jo, Yo-Chan Kong, Bernard Dieny, and Kyung-Jin Lee. Bias-voltage dependence of perpendicular spin-transfer torque in asymmetric MgO-based magnetic tunnel junctions. *Nature Physics*, 2009.

- 
- [111] C. Wang, Y.-T. Cui, J. Z. Sun, J. A. Katine, R. A. Buhrman, and D. C. Ralph. Bias and angular dependence of spin-transfer torque in magnetic tunnel junctions. *Phys. Rev. B*, page 224416, 2009.
  - [112] Y.-H. Tang, N. Kioussis, A. Kalitsov, W. H. Butler, and R. Car. Controlling the Nonequilibrium Interlayer Exchange Coupling in Asymmetric Magnetic Tunnel Junctions. *Phys. Rev. Lett.*, page 57206, 2009.
  - [113] J. Xiao, G. E. W. Bauer, and A. Brataas. Spin-transfer torque in magnetic tunnel junctions: Scattering theory. *Phys. Rev. B*, page 224419, 2008.
  - [114] G. H. Wannier. The Structure of Electronic Excitation Levels in Insulating Crystals. *Phys. Rev.*, 52:191, 1937.
  - [115] O. K. Andersen and T. Saha-Dasgupta. Muffin-tin orbitals of arbitrary order. *Phys. Rev. B*, 62:R16219, 2000.
  - [116] E. Pavarini, A. Yamasaki, J. Nuss, and O. K. Andersen. How chemistry controls electron localization in 3d<sup>1</sup> perovskites: a Wannier-function study. *New J. Phys.*, 7:188, 2005.
  - [117] E. Zurek, O. Jepsen, and O. K. Andersen. Muffin-Tin Orbital Wannier-Like Functions for Insulators and Metals. *ChemPhysChem*, 6:1934, 2005.
  - [118] R. D. King-Smith and D. Vanderbilt. Theory of polarization of crystalline solids. *Phys. Rev. B*, 47:1651, 1993.
  - [119] D. Vanderbilt and R. D. King-Smith. Electric polarization as a bulk quantity and its relation to surface charge. *Phys. Rev. B*, 48:4442, 1993.
  - [120] N. Marzari and D. Vanderbilt. Maximally-localized Wannier functions in perovskites: Cubic BaTiO<sub>3</sub>. In *First-Principles Calculations for Ferroelectrics: Fifth Williamsburg Workshop*, page 146. Springer Verlag, 1998.
  - [121] X. Wu, O. Diéguez, K. M. Rabe, and D. Vanderbilt. Wannier-Based Definition of Layer Polarizations in Perovskite Superlattices. *Phys. Rev. Lett.*, 97:107602, 2006.
  - [122] T. Thonhauser, D. Ceresoli, D. Vanderbilt, and R. Resta. Orbital Magnetization in Periodic Insulators. *Phys. Rev. Lett.*, 95:137205, 2005.
  - [123] D. Ceresoli, T. Thonhauser, D. Vanderbilt, and R. Resta. Orbital magnetization in crystalline solids: Multi-band insulators, Chern insulators, and metals. *Phys. Rev. B*, 74:024408, 2006.
  - [124] P. L. Silvestrelli, N. Marzari, D. Vanderbilt, and M. Parrinello. Maximally-localized Wannier functions for disordered systems: application to amorphous Silicon. *Solid State Communications*, 107:7, 1998.



- [125] K. S. Thygesen and K. W. Jacobsen. Molecular transport calculations with Wannier functions. *Chemical Physics*, 319:111, 2005.
- [126] A. Calzolari, N. Marzari, I. Souza, and M. B. Nardelli. Ab-initio transport properties of nanostructures from maximally-localized Wannier functions. *Phys. Rev. B*, 69:035108, 2004.
- [127] W. Kohn. Analytic Properties of Bloch Waves and Wannier Functions. *Phys. Rev.*, 115:809, 1959.
- [128] Wannier90 code. (See: <http://www.wannier.org/>).
- [129] X. Ren, I. Leonov, G. Keller, M. Kollar, I. Nekrasov, and D. Vollhardt. LDA+DMFT computation of the electronic spectrum of NiO. *Phys. Rev. B*, 74:195114, 2006.
- [130] D. R. Hamann. Semiconductor Charge Densities with Hard-Core and Soft-Core Pseudopotentials. *Phys. Rev. Lett.*, 42:662, 1979.
- [131] X. Wang, J. R. Yates, I. Souza, and D. Vanderbilt. Ab initio calculation of the anomalous Hall conductivity by Wannier interpolation. *Phys. Rev. B*, 74:195118, 2006.
- [132] J. R. Yates, X. Wang, D. Vanderbilt, and I. Souza. Spectral and Fermi surface properties from Wannier interpolation. *Phys. Rev. B*, 75:195121, 2007.
- [133] X. Wang, D. Vanderbilt, J. R. Yates, and I. Souza. Fermi-surface calculation of the anomalous Hall conductivity. *Phys. Rev. B*, 76:195109, 2007.
- [134] R. Jackiw. Three Elaborations on Berry's connection, curvature and phase. *Int. J. Mod. Phys. A*, 3:285, 1988.
- [135] M. V. Berry. Quantum Phase Factors Accompanying Adiabatic Changes. *Proc. R. Soc. London Ser. A*, 392:45, 1984.
- [136] R. Resta. Ab initio simulation of the properties of ferroelectric materials. *Modelling Simul. Mater. Sci. Eng.*, 11:R69, 2003.
- [137] R. Resta. Theory of the electric polarization in crystals. *Ferroelectrics*, 136:51, 1992.
- [138] M. Stengel and N. A. Spaldin. Accurate polarization within a unified Wannier function formalism. *Phys. Rev. B*, 73:075121, 2006.
- [139] A. Kokalj. Computer graphics and graphical user interfaces as tools in simulations of matter at the atomic scale. *Comp. Mater. Sci.*, 28:155, 2003. Code available from <http://www.xcrysden.org/>.



- 
- [140] Y. Mokrousov, G. Bihlmayer, and S. Blügel. Full-potential linearized augmented plane-wave method for one-dimensional systems: Gold nanowire and iron monowires in a gold tube. *Phys. Rev. B*, 72:045402, 2005.
- [141] A. Delin and E. Tosatti. Magnetic phenomena in 5d transition metal nanowires. *Phys. Rev. B*, 68:144434, 2003.
- [142] J. Velez, R. F. Sabirianov, S. S. Jaswal, and E. Y. Tsymbal. Ballistic Anisotropic Magnetoresistance. *Phys. Rev. Lett.*, 94:127203, 2005.
- [143] A. Delin, E. Tosatti, and R. Weht. Magnetism in Atomic-Size Palladium Contacts and Nanowires. *Phys. Rev. Lett.*, 92:057201, 2004.
- [144] Y. Mokrousov, G. Bihlmayer, S. Heinze, and S. Blügel. Giant Magnetocrystalline Anisotropies of 4d Transition-Metal Monowires. *Phys. Rev. Lett.*, 96:147201, 2006.
- [145] Y. Zhang and W. Yang. Comment on "Generalized Gradient Approximation Made Simple". *Phys. Rev. Lett.*, 80:890, 1998.
- [146] A. Petraru, N. A. Pertsev, H. Kohlstedt, U. Poppe, R. Waser, A. Solbach, and U. Klemradt. Polarization and lattice strains in epitaxial BaTiO<sub>3</sub> films grown by high-pressure sputtering. *J. App. Phys.*, 101:114106, 2007.
- [147] J. P. Perdew and Y. Wang. Accurate and simple analytic representation of the electron-gas correlation energy. *Phys. Rev. B*, 45:13244, 1992.
- [148] Z. Wu and R. E. Cohen. More accurate generalized gradient approximation for solids. *Phys. Rev. B*, 73:235116, 2006.
- [149] S. Picozzi, K. Yamauchi, B. Sanyal, I. A. Sergienko, and E. Dagotto. Dual Nature of Improper Ferroelectricity in a Magnetoelectric Multiferroic. *Phys. Rev. Lett.*, 99:227201, 2007.
- [150] K. Yamauchi, F. Freimuth, S. Blügel, and S. Picozzi. Magnetically induced ferroelectricity in orthorhombic manganites: Microscopic origin and chemical trends. *Phys. Rev. B*, 78:014403, 2008.
- [151] A. Malashevich and D. Vanderbilt. First Principles Study of Improper Ferroelectricity in TbMnO<sub>3</sub>. *Phys. Rev. Lett.*, 101:037210, 2008.
- [152] S. Murakami. Quantum Spin Hall Phases. *Prog. Theor. Phys. Suppl.*, 176:279, 2008.
- [153] S. Murakami. Phase transition between the quantum spin Hall and insulator phases in 3D: emergence of a topological gapless phase. *New Journal of Physics*, 9:356, 2007.
- [154] L. Fu and C. L. Kane. Topological insulators with inversion symmetry. *Phys. Rev. B*, 76:045302, 2007.

- 
- [155] S. Murakami and M. Wada. Private Communication.
- [156] T. Fukui and Y. Hatsugai. Topological aspects of the quantum spin-Hall effect in graphene:  $Z_2$  topological order and spin Chern number. *Phys. Rev. B*, 75:121403, 2007.
- [157] F. B. Mancoff, N. D. Rizzo, B. N. Engel, and S. Tehrani. Phase-locking in double-point-contact spin-transfer devices. *Nature*, 437:393, 2005.
- [158] S. Kaka, M. R. Pufall, W. H. Rippard, T. J. Silva, S. E. Russek, and J. A. Katine. Mutual phase-locking of microwave spin torque nano-oscillators. *Nature*, 437:389, 2005.
- [159] S. I. Kiselev, J. C. Sankey, I. N. Krivorotov, N. E. Emley, R. J. Schoelkopf, R. A. Buhrman, and D. C. Ralph. Microwave oscillations of a nanomagnet driven by a spin-polarized current. *Nature*, 425:380, 2003.
- [160] J. Rammer and H. Smith. Quantum field-theoretical methods in transport theory of metals. *Reviews of Modern Physics*, 58:323, 1986.
- [161] Kuang chao Chou, Zhao bin Su, Bai lin Hao, and Lu Yu. Equilibrium and Nonequilibrium Formalisms made unified. *Physics Reports*, 118:1, 1985.
- [162] D. C. Ralph and M. D. Stiles. Current Perspectives Spin Transfer Torques. *J. Magn. Magn. Mater.*, 320:1190, 2008.
- [163] C. Heiliger and M. D. Stiles. Ab Initio Studies of the Spin-Transfer Torque in Magnetic Tunnel Junctions. *Phys. Rev. Lett.*, 100:186805, 2008.
- [164] In the case of spin-orbit coupling, for example, the requirement of real-valuedness of the Wannier function cannot be fulfilled in general.
- [165] M. Posternak, A. Baldereschi, S. Massidda, and N. Marzari. Maximally localized Wannier functions in antiferromagnetic MnO within the FLAPW formalism. *Phys. Rev. B*, 65:184422, 2002.
- [166] G. Cangiani, A. Baldereschi, M. Posternak, and H. Krakauer. Born charge differences of  $\text{TiO}_2$  polytypes: Multipole expansion of Wannier charge densities. *Phys. Rev. B*, 69:121101, 2004.
- [167] M. Posternak, A. Baldereschi, E. J. Walter, and H. Krakauer. Wannier functions and Born charge tensors of brookite  $\text{TiO}_2$ . *Phys. Rev. B*, 74:125113, 2006.
- [168] H. Krakauer, M. Posternak, and A. J. Freeman. *Phys. Rev. B*, 19:1706, 1979.
- [169] M. Ehrhardt. Discrete Transparent Boundary Conditions for General Schrödinger-type Equations. *VLSI Design*, 9:325, 1999.

- 
- [170] J. E. Inglesfield and G. A. Benesh. Surface electronic structure: Embedded self-consistent calculations. *Phys. Rev. B*, 37:6682, 1988.
  - [171] J. E. Inglesfield. Time-dependent embedding. *J. Phys.: Condens. Matter*, 20:095215, 2008.
  - [172] E. Dix and J. E. Inglesfield. An embedding approach to electron waveguides. *J. Phys.: Condens. Matter*, 10:5923, 1998.
  - [173] E. Wimmer, H. Krakauer, M. Weinert, and A. J. Freeman. Full-potential selfconsistent linearized-augmented-plane-wave method for calculating the electronic structure of molecules and surfaces: O<sub>2</sub> molecule. *Phys. Rev. B*, 24:864, 1981.
  - [174] U. von Barth and L. Hedin. *J. Phys. C: Solid State Phys.*, 5:1629, 1972.



# Acknowledgement

I would like to thank Prof. Dr. Stefan Blügel for giving me the opportunity to conduct my Ph.D. studies in his group. He has been a great source of inspiration to me. Sometimes the inspiration was even too much, leaving me wondering which way to go. Some day I might explore some of these other routes.

I thank Prof. Dr. Dederichs for being the second evaluator of my thesis.

I profited from valuable discussions with and advice from many members of the institute for solid state research. Especially to the following ones I owe a thank you:

- Daniel Wortmann helped me to get familiar with the embedding method and electronic transport. Also, he helped me to improve my knowledge on the Fortran programming language.
- Gustav Bihlmayer is certainly the most valuable source of information on the use of the FLEUR program that exists in the world. His interest in the Sb(111) surface and topological insulators is the reason for some sections of this thesis.
- With Yuriy Mokrousov I had many good discussions on the Wannier functions and he contributed many good ideas and subroutines. I remember that when he was still in Hamburg and we had to share our experiences via e-mail I was sometimes typing one e-mail after the next. We had a great time on the CECAM Conference in Lyon. He read part of this thesis improving it with helpful suggestions. Also, he raised my interest in the anomalous Hall effect and the spin-Hall effect.
- Marjana Lezaic raised my interest in the Fe/Co/MgO/Co/Fe magnetic tunnel junction and many other (mainly nanoferronic) things. If she had not invented the word nanoferronic, I could not have used it in the title of my thesis. As a user of the Wannier functions she asked many good questions and complained about bugs, which was helpful in improving the code and its documentation.
- With Markus Heide I had some interesting discussions on non-collinear magnetism and spin-orbit coupling.
- Ersoy Şaşıoğlu had many nice suggestions for improving the Wannier function code.
- Frank Matthes supported Marjana Lezaic in raising my interest in the magnetic tunnel junction Fe/Co/MgO/Co/Fe.

- Daniel Bürgler raised my interest in the Fe/Ag/Fe nanopillars and he answered some of the questions a theoretician has when he learns something about an experiment.
- Phivos Mavropoulos explained to me – among other things – how the energy contour integration is performed within KKR and how the Fermi energy is determined there – concepts I took over.

In the course of my Ph.D. studies many guests visited the institute for solid state research to give interesting talks or to share their knowledge. To some of them I am particularly thankful:

- Silvia Picozzi and Kunihiro Yamauchi shared with me their knowledge on ferroelectricity in orthorhombic manganites.
- With Fumiyuki Ishii I had interesting discussions on the implementation of the electric field into DFT codes with the help of Wannier functions.
- From Shuichi Murakami I learned many things on the topological insulator.

My Ph.D. studies did not only profit from scientific discussions but also from the well-working organization of our group. Ute Winkler made sure that the organization was always working perfectly.

I am grateful to my friends and relatives for their support. Especially, I would like to thank my parents and my sister.

# Curriculum Vitae

## Personal Details

Name: Frank Freimuth  
Date of birth: 11.09.1980  
Place of birth: Simmern (Hunsrück, Germany)  
Address: Forschungszentrum Jülich, 52425 Jülich, Germany  
E-mail: f.freimuth@fz-juelich.de

## Education

1987-1991: Grundschule Rheinböllen  
1991-2000: Herzog-Johann-Gymnasium (Simmern)  
06.2000: Abitur  
09.2000-07.2001: Civil Service at German Red Cross  
10.2001-01.2006: Studies of Physics at Johannes-Gutenberg University Mainz  
04.2003: Vordiplom (sehr gut)  
01.2006: Diplom (mit Auszeichnung)  
Title of Thesis: Superfluidität fermionischer Atome im optischen Gitter  
06.2006-08.2009: Ph.D. student, Forschungszentrum Jülich  
since 09.2009: Postdoc, Forschungszentrum Jülich  
02.02.2011: Oral Ph.D. exam (mit Auszeichnung)

## Awards

04.1999-09.2005: German National Academic Foundation Scholarship  
06.1999: Günter Felke Award (Physics)  
07.1999: Honorary Mention for Participation at the  
30th International Physics Olympiad  
03.2000: German Physical Society Student Award  
06.2000: Herzog-Johann-Gymnasium Book Award  
06.2000: German Physical Society Book Award